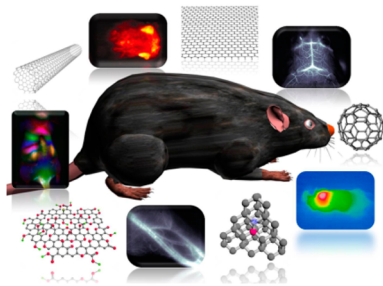


Carbon Nanomaterials for Biological Imaging and Nanomedicinal Therapy

Guosong Hong[†], Shuo Diao, Alexander L. Antaris, and Hongjie Dai*

Department of Chemistry, Stanford University, Stanford, California 94305, United States



CONTENTS

1. Introduction	10817	4.3.1. Carbon Nanomaterials for Two-Photon Fluorescence Imaging	10849
2. Carbon Nanomaterials	10818	4.3.2. Carbon Nanomaterials for Raman Imaging	10852
2.1. Zero-Dimensional (0D) Carbon Nanomaterial: Fullerene	10818	4.3.3. Carbon Nanomaterials for Transient Absorption Imaging	10854
2.2. One-Dimensional (1D) Carbon Nanomaterial: Carbon Nanotube	10819	4.4. Carbon Nanomaterials for Nonoptical Imaging Modalities	10856
2.3. Two-Dimensional (2D) Carbon Nanomaterial: Graphene	10819	4.4.1. Carbon Nanomaterials for Photoacoustic, Thermoacoustic, and Photothermal Imaging	10856
2.4. Carbon Dot	10820	4.4.2. Carbon Nanomaterials for X-ray Computed Tomography (CT), Magnetic Resonance Imaging (MRI), and Radionuclide Imaging with Loaded Contrast Agents	10857
2.5. Nanodiamond	10821	5. Carbon Nanomaterials for Nanomedicinal Therapy	10862
3. Surface Functionalization of Carbon Nanomaterials	10821	5.1. Carbon Nanomaterials for Drug Delivery	10862
3.1. Noncovalent Surface Functionalization	10822	5.2. Carbon Nanomaterials for Gene Delivery	10864
3.2. Covalent Surface Functionalization	10824	5.3. Carbon Nanomaterials for Photothermal Therapy	10866
4. Carbon Nanomaterials for Biological Imaging	10825	5.4. Carbon Nanomaterials for Photodynamic Therapy	10868
4.1. One-Photon Fluorescence Imaging of Carbon Nanomaterials in the Visible and First Near-Infrared (NIR-I) Windows	10825	5.5. Carbon Nanomaterials for In Vitro Sensing and Diagnostics	10871
4.1.1. Origin of Fluorescence of Fullerene, Graphene, Carbon Dot, and Nanodiamond	10825	6. Pharmacokinetics and Toxicology of Carbon Nanomaterials	10874
4.1.2. In Vitro Fluorescence Imaging with Fullerene, Graphene, Carbon Dot, and Nanodiamond	10827	6.1. In Vitro Cytotoxicity Study of Carbon Nanomaterials	10874
4.1.3. In Vivo Fluorescence Imaging with Fullerene, Graphene, Carbon Dot, and Nanodiamond	10830	6.2. In Vivo Pharmacokinetics and Toxicology of Carbon Nanomaterials	10876
4.2. One-Photon Fluorescence Imaging of Single-Walled Carbon Nanotubes (SWCNTs) in the Second Near-Infrared (NIR-II) Window	10831	7. Conclusions and Outlook	10880
4.2.1. Origin of Band-Gap NIR-II Fluorescence of SWCNTs	10831	7.1. What Are the Future Directions of Carbon Nanomaterial Based Biomedical Imaging and Therapy?	10880
4.2.2. SWCNTs for In Vitro NIR-II Fluorescence Imaging	10834	7.2. What Are the Main Hurdles We Need To Overcome before One Can Really Apply Carbon Nanomaterials for Clinical Applications?	10882
4.2.3. SWCNTs for In Vivo NIR-II Fluorescence Imaging	10839	7.3. What Insights Can We Gain from the Studies on Carbon-Nanomaterial-Based Imaging and Therapy, and How Do They Inspire New Research in the Fields of Chemistry and Biology?	10883
4.3. Carbon Nanomaterials for Other Optical Imaging Modalities	10849	Author Information	10884
		Corresponding Author	10884

Special Issue: Nanoparticles in Medicine

Received: January 5, 2015

Published: May 21, 2015

Present Address	10884
Author Contributions	10884
Notes	10884
Biographies	10884
Acknowledgments	10885
Abbreviations	10885
References	10886

1. INTRODUCTION

Carbon nanomaterials are a class of low-dimensional materials that have aroused a great deal of interest in the past 30 years since the spectacular debut of fullerene, the first member of this class reported by Smalley, Kroto, Curl et al. in 1985 at Rice University and University of Sussex.¹ The discoveries of two other allotropes, carbon nanotubes (CNTs) and graphene in 1991 and 2004, have also made a great sensation in science.^{2,3} While those three carbon nanomaterials are mainly comprised of sp^2 carbon atoms forming a seamless network of conjugated π -electrons, carbon dots with mixed sp^2 and sp^3 carbon atoms plus defects and heteroatoms, as well as nanodiamonds consisting of mostly sp^3 carbon atoms, have also received much attention (Figure 1).^{4,5} More recently, it has been reported that a new type

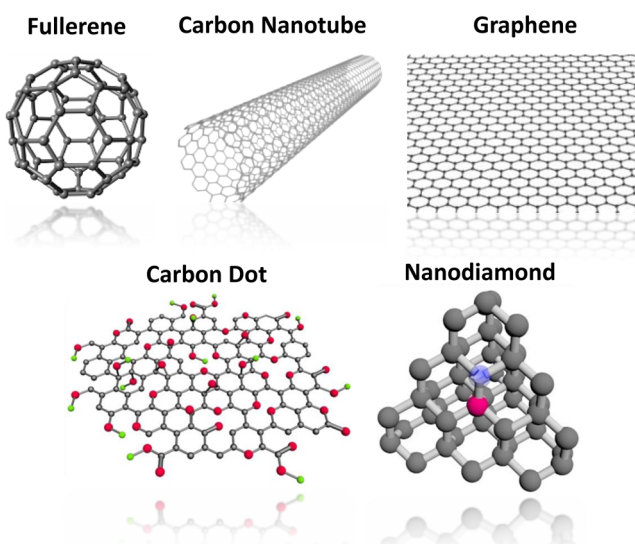


Figure 1. Carbon nanomaterials. Various carbon nanomaterials, including fullerene, carbon nanotube, graphene, carbon dot, and nanodiamond, have received a lot of interest in the past decade owing to their unique properties.

of one-dimensional (1D) nanostructures comprised of crystalline sp^3 carbon only, named carbon nanowire, can be synthesized via high-pressure solid-state polymerization reaction of benzene.⁶ These low-dimensional carbon nanomaterials have interesting properties that are not attainable in bulk carbon materials such as diamond and graphite, owing to the quantum confinement effect that leads to many unusual optical, electrical, magnetic, and chemical properties and useful applications in electronics, photonics, renewable energy, and biomedicine.^{7–10}

The past decade has witnessed a burst in biomedical research using carbon nanomaterials (Figure 2), which are advantageous primarily owing to small size, unique optical properties, and large surface area. The elegant marriage between nanoscience and biology originates from the similar dimensions between nanomaterials and many fundamental biomolecules that are

crucial to maintaining the basic functions of life. Carbon nanomaterials typically range from 1 nm to 1 μm in size, which is comparable to the sizes of proteins (1–100 nm) and DNA (2–3 nm in width) in biological environments, and the sizes of natural biological barriers *in vivo* including ion channels (a few nanometers) and the glomerular filtration barrier (5–10 nm).¹¹ The favorable sizes of carbon nanomaterials have made them ideal nanocapsules and nanocarriers to load and deliver drugs and genes to specific targets *in vivo*. Moreover, the optical properties unique to some carbon nanomaterials have also attracted a lot of interest for a variety of biomedical applications. The graphitic carbon nanomaterials such as CNTs and graphene usually have strong optical absorption in the traditional near-infrared window (NIR-I window, 750–1000 nm), leading to *in situ* photothermal effect for photoacoustic imaging and photothermal therapy.^{12,13} The unique intrinsic fluorescence emission of single-walled carbon nanotubes (SWCNTs) in the long-wavelength, second near-infrared window (NIR-II window, 1000–1700 nm) has allowed for deep-tissue fluorescence imaging using SWCNTs as fluorescent contrast agents owing to the reduced scattering of photons.^{14–16} The exceptionally long fluorescence lifetime of nanodiamond has allowed for time-gated fluorescence imaging to distinguish the nanodiamond labels from tissue autofluorescence.¹⁷ Furthermore, the large surface area of carbon nanomaterials and the π -electron conjugated surface have enabled supramolecular binding of hydrophobic molecules to the surface of SWCNTs and graphene through π – π interaction, which is the basis for efficient delivery of water-insoluble drug molecules in an aqueous biological environment.^{18–21} Besides the aforementioned features of carbon nanomaterials, SWCNTs and graphene with pristine carbon network and extended structures have superior mechanical properties that enhance the strengths of tissue scaffolds.^{22–26}

In this review paper we will cover the recent progress in biological imaging and nanomedicinal therapy using carbonaceous nanomaterials. A brief introduction on the structure and property of each carbon nanomaterial will be given (section 2), followed by the various surface functionalization methods to impart water solubility and biocompatibility to carbon materials (section 3). For carbon nanomaterial based biomedical imaging, we will discuss one-photon and multiphoton fluorescence imaging, Raman imaging, transient absorption microscopy, photoacoustic imaging, and other nonoptical imaging modalities (section 4), with a focus on the *in vivo* deep-tissue NIR-II fluorescence imaging using SWCNTs, which was pioneered by our group and is now explored by more and more groups (section 4.2). For therapeutic applications of carbon nanomaterials, we will highlight recent research on drug and gene delivery, photoacoustic and photodynamic therapy, as well as *in vitro* sensing and diagnostics applications of carbon nanomaterials (section 5). Reports on *in vitro* cytotoxicity and *in vivo* behavior with toxicology studies of various carbon nanomaterials will be briefly discussed to address some of the concerns on the biocompatibility of carbon nanomaterials (section 6). At the end, we will provide some insights on the future directions and foreseeable challenges for carbon-based biomedicine based on our own understanding of this field (section 7).

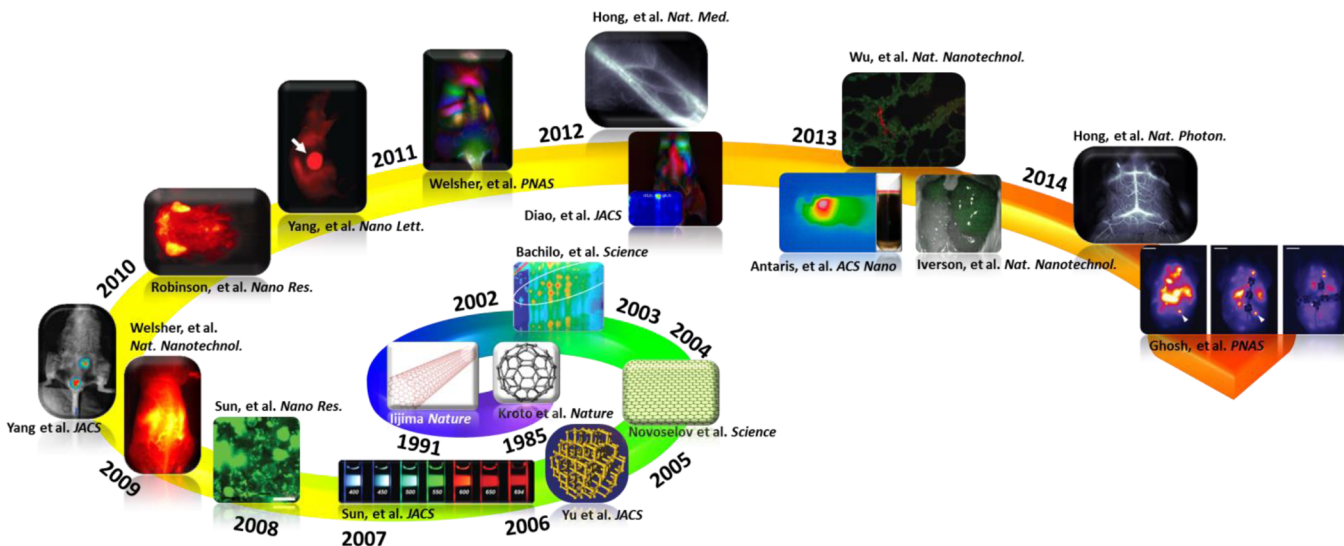


Figure 2. Timeline of major milestones in the field of carbon nanomaterial based biomedical imaging and therapy. This timeline includes the discoveries of fullerene (Kroto et al. *Nature*, 1985), carbon nanotubes (Iijima *Nature*, 1991), graphene (Novoselov et al. *Science*, 2004); the discovery of the intrinsic fluorescence of SWCNTs (Bachilo et al. *Science*, 2002) and carbon dots (Sun et al. *J. Am. Chem. Soc. (JACS)*, 2006); first in vitro fluorescence imaging with the intrinsic fluorescence of nanodiamonds (Yu et al. *JACS*, 2005) and graphene oxide (Sun et al. *Nano Res.* 2008); first in vivo fluorescence imaging with the intrinsic fluorescence of SWCNTs (Welsher et al. *Nat. Nanotechnol.*, 2009) and carbon dots (Yang et al. *JACS*, 2009); first dynamic contrast enhanced NIR-II fluorescence imaging with SWCNTs (Welsher et al. *Proc. Natl. Acad. Sci. U. S. A. (PNAS)*, 2011); first hind limb vascular imaging (Hong et al. *Nat. Med.*, 2012) and brain vascular imaging with SWCNTs (Hong et al. *Nat. Photon.*, 2014); first NIR-II based in vivo biosensing experiment with SWCNTs (Iverson et al. *Nat. Nanotechnol.*, 2013); first chirality-separated in vivo imaging with SWCNTs (Diao et al. *JACS*, 2012); first NIR-II imaging guided surgery with SWCNTs (Ghosh et al. *PNAS*, 2014); first in vivo photothermal therapy with SWCNTs (Robinson et al. *Nano Res.*, 2010) and graphene (Yang et al. *Nano Lett.*, 2010) and first chirality-separated in vivo photothermal therapy with SWCNTs (Antaris et al. *ACS Nano*, 2013). Images reprinted from ref 27, copyright 2004 American Chemical Society; ref 28, copyright 2006 American Chemical Society; ref 31, copyright 2009 American Chemical Society; ref 32, copyright 2010 American Chemical Society; ref 33, copyright 2012 American Chemical Society; ref 34, copyright 2013 American Chemical Society. Images reprinted with permission from ref 29, copyright 2008 Springer; ref 30, copyright 2009 Nature Publishing Group; ref 13, copyright 2010 Springer; ref 14, copyright 2011 National Academy of Sciences; ref 15, copyright 2012 Nature Publishing Group; ref 17, copyright 2013 Nature Publishing Group; ref 35, copyright 2013 Nature Publishing Group; ref 16, copyright 2014 Nature Publishing Group; ref 36, copyright 2014 National Academy of Sciences.

2. CARBON NANOMATERIALS

2.1. Zero-Dimensional (0D) Carbon Nanomaterial: Fullerene

Fullerene is the first carbon-based nanostructure that has received popular interest. Since the discovery of C₆₀ fullerene about three decades ago,¹ fullerene and many fullerene derivatives through rich covalent and noncovalent chemistry^{37,38} have been widely explored for energy, biosensing, and medicine applications owing to their remarkable physical, chemical, and biological properties.^{39–44} The Nobel Prize for Chemistry 1996, which was awarded to Smalley, Kroto, and Curl, has made fullerene at the center of the spotlight on the scientific stage. Although the popularity of the scientific pursuit of fullerene has somewhat subsided in recent years with the more rapid rise of carbon nanotubes and graphene, the ultrasmall size, uniform dispersity, and rich chemistry still attract much attention in a variety of fields of biomedical research, ranging from imaging to diagnostics and to therapeutics.⁴⁵

The C₆₀ molecule is a highly symmetrical sphere with a van der Waals diameter of 1.1 nm and comprised of solely carbon atoms. It can be synthesized by laser or heat induced evaporation of graphite,^{1,46} or direct bottom-up chemical synthesis from smaller aromatic molecules.⁴⁷ Although insoluble in water, C₆₀ molecules can be functionalized with hydrophilic surface groups to increase the water solubility and biocompatibility through covalent reactions with the carbon atoms in the sphere.^{48,49} On the other hand, C₆₀ molecules can also be noncovalently encapsulated inside cyclodextrins or micelles through supr-

molecular interactions between the hydrophobic C₆₀ guest molecule and the amphiphilic host molecules.^{50,51} The facile surface functionalization of C₆₀ molecules has allowed for bioconjugation with antibodies for selective targeting to certain biomarkers.⁵²

The nanometer size of the C₆₀ molecules can impart various unconventional capabilities to afford stealth nanoparticles for imaging and drug/gene delivery. First of all, the hollow cavity of the C₆₀ sphere can be used to load certain metal ions such as Gd³⁺ or ^{99m}Tc, resulting in contrast agents for magnetic resonance imaging (MRI) as well as nuclear medicine.^{53,54} Furthermore, it is found that the hydrophobic surface of the C₆₀ molecules binds strongly to oligodeoxynucleotide,⁵⁵ leading to efficient gene delivery vehicles that can pass through both the cell membrane and the nuclear membrane to improve the efficacy of gene therapy.^{56,57} Besides metal ions and DNA, C₆₀ molecules can also be used as drug carriers through surface functionalization, providing a drug delivery system that releases drug cargos in a slow, controlled manner that favors improved treatment efficacy.⁵⁸

Another unique photochemical property of C₆₀ is the photoexcitation capability of fullerene. Ground-state, singlet C₆₀ can absorb photon energy and become excited to the triplet C₆₀, which transfers its stored energy to the surrounding oxygen molecules and turns them into reactive oxygen species (e.g., singlet oxygen and oxygen free radicals) through both energy transfer and electron transfer.⁵⁹ These reactive species are highly

active in DNA cleavage and thus cytotoxic, leading to the use of C₆₀ molecules as a photosensitizer in photodynamic therapy.⁶⁰

Besides the aforementioned properties of C₆₀ molecules that have allowed for various imaging and therapeutic applications, there are also other miscellaneous applications of fullerenes based on their intrinsic photoluminescence for fluorescence imaging,^{61–64} protein activity inhibition for antiviral therapy,^{65,66} and anticancer activity for cancer treatment.^{67,68}

2.2. One-Dimensional (1D) Carbon Nanomaterial: Carbon Nanotube

Besides fullerenes that are comprised of sp² carbon atoms in a closed spherical shell, the sp² carbon atoms can also form single or multiple coaxial tubes of graphitic sheets called carbon nanotubes (CNTs). Since their discovery in the late 20th century,^{2,69–72} CNTs have stimulated a significant amount of interest from many different fields owing to their unique mechanical, chemical, electrical, and optical properties.⁷³ In the following sections of this review we will focus on the unique optical properties of CNTs that allow for biological imaging of living objects and photon-assisted therapeutics, and on their unusual mechanical and chemical properties that enable tissue scaffolding and drug delivery through biocompatible CNTs.

As 1D carbon nanomaterials, carbon nanotubes can be comprised of a single graphitic layer or multiple coaxial layers, resulting in single-walled carbon nanotubes (SWCNTs) and multiple-walled carbon nanotubes (MWCNTs). An SWCNT or each “wall” of an MWCNT can be viewed as a single graphene sheet with 2D honeycomb structure rolled up into a 1D nanocylinder, and the electronic properties of a “rolled-up” tube, such as being metallic or semiconducting, as well as its band gap energy, are determined by the direction along which the graphene sheet rolls up with respect to the 2D honeycomb lattice, and the diameter of the nanocylinder. As we will later see with more detailed discussion in section 4.2.1., two-thirds of all SWCNTs are semiconducting while the other one-third are metallic, depending on the “roll-up” directions in the 2D graphene lattice. Despite a band gap energy of zero for metallic nanotubes, a semiconducting nanotube has a band gap energy that is both predicted in theory and demonstrated in experiments to decrease with increasing tube diameter.^{74–76}

The electronic properties of CNTs have led to applications based on their band structures. Semiconducting SWCNTs have been demonstrated to function as field effect transistors (FETs) with their electrical resistance varying as a function of the gate voltage.⁷⁷ On the other hand, MWCNTs with diameters of 10 nm or larger tend to have smaller band gap energies and behave more like metallic nanotubes, thus losing FET properties with little or no gate action. Nevertheless, it has been found that structural deformations, such as in collapsed MWCNTs, can change the electronic properties and lead to FET behavior with gate response.⁷⁸ CNT-based FETs have not only found wide applications in semiconductor nanoelectronics, but also set the foundation for chemical and biomolecular sensing and diagnostics, in which the adsorption and desorption of analyte molecules effectively change the gate voltage of the CNT FET and result in measurable signals in device conductivity.^{79–81}

Field electron emission has been observed for SWCNTs when a thin film of SWCNTs made from electrophoretic deposition is applied with a dc voltage.⁸² The electron-emitting SWCNT film can be used as the cathode material in a cold-cathode X-ray tube, from which X-rays will be emitted for diagnostic medical imaging.⁸³ Compared to a conventional thermionic cathode

comprised of a metal filament, an SWCNT-based cold cathode has the benefits of a low operation temperature and a voltage-controllable output current. A number of biomedical imaging applications have been demonstrated for X-ray radiography,⁸⁴ microcomputed tomography (micro-CT),⁸⁵ and radiation therapy⁸⁶ using SWCNT-based field emission X-ray sources.

The existence of the band gap in semiconducting SWCNTs is also responsible for a variety of unique optical properties, based on which SWCNTs have found many interesting applications in biomedical imaging and therapeutics. Photons can be absorbed and emitted as fluorescence when interacting with SWCNTs. It is noteworthy that SWCNTs usually absorb photons in the visible (400–750 nm) and NIR-I (750–1000 nm) windows, followed by fluorescence emission in the NIR-II window (1000–1700 nm) and nonradiative relaxation of the absorbed photon energy in the form of heat.⁸⁷ Both NIR-I and NIR-II windows belong to the “biological transparent windows” due to the low absorption, reduced scattering, and minimum autofluorescence from biological tissues.⁸⁸ The unique optical properties of SWCNTs have made them promising candidates as photosensitizers for photothermal and photodynamic therapy,^{13,89} and as fluorophores for labeling and targeting structural and molecular features in living systems for deep tissue fluorescence imaging.^{14–16,30}

Aside from the unique electrical and optical properties of CNTs, they have also been reported to possess exceptional mechanical properties that allow for tissue scaffolding, and interesting chemical properties that make them efficient cargo carriers and delivery vehicles for shuttling drugs and other bioactive molecules such as DNA and RNA. It has been reported that both SWCNTs and MWCNTs exhibit remarkable flexibility and strength under mechanical duress, owing to the hexagonal network made of carbon atoms.^{90–92} The superior toughness and energy-absorbing capabilities of CNTs make them promising candidates as structure-supporting and strength-reinforcing agents in composite materials for tissue engineering.^{23,24,93} On the other hand, the abundant aromatic rings and delocalized π electrons on the outer wall of the CNTs enable them to form supramolecular conjugates with chemotherapy and gene therapy drugs through $\pi-\pi$ stacking between the CNT backbone and the bioactive molecules, which are otherwise usually difficult to deliver in the complex biological environment.^{18,19,94–96}

In this review paper we will cover the biological imaging and therapy applications of both SWCNTs and MWCNTs based on their exceptional electrical, optical, chemical, and mechanical properties with a focus on NIR-II fluorescence imaging and NIR-light based photothermal therapy in sections 4 and 5. The potential *in vitro* cytotoxicity as well as the *in vivo* toxicology and pharmacokinetics related to CNTs will also be discussed in this review.

2.3. Two-Dimensional (2D) Carbon Nanomaterial: Graphene

Compared to fullerene and carbon nanotube, graphene is a much newer member in the family of carbon materials.³ Graphene is an atomically thin film that consists of hexagonally arranged carbon atoms with sp² hybridization in two dimensions, which can be well isolated from its surrounding environment and thus becomes free-standing. This two-dimensional (2D) crystal of carbon can be synthesized by a number of means, including the early attempts of mechanical and chemical exfoliations,^{3,97–101} unzipping of carbon nanotubes,^{102–105} bottom-up epitaxial growth,^{106–113} and chemical synthesis.^{114,115} The band structure

of a single graphene sheet can be calculated by applying a tight-binding approach to the honeycomb hexagonal lattice of the 2D carbon crystal within the Hückel approximation, and one can find the valence band and conduction band of graphene touching at the six corners of the first Brillouin zone, resulting in a zero-gap semiconductor.¹¹⁶ As a result, electrons moving within the one-atom-thick layer of graphene behave like massless, and ultrarelativistic charge carries called Dirac fermions as opposed to the traditional Schrödinger fermions,¹¹⁷ leading to a myriad of unusual physical properties including high carrier mobility,^{118,119} superior thermal conductivity,¹²⁰ ambipolar electric field effect,³ and room-temperature quantum Hall effect.¹²¹

Besides these exotic physical properties of graphene that lead to the development of novel graphene-based nanoelectronics and nanophotonics,^{122–132} the large surface area, high mechanical flexibility, and capability of chemical functionalization of graphene and graphene derivatives have opened up a new horizon for biomedical research.^{8,133–136} There have been an increasing number of studies on the use of graphene and graphene oxide (GO) for various biological and medical applications including biosensing, imaging, and therapy.

The capability of graphene to be employed as a platform for sensing biologically relevant molecules comes from a few properties of graphene. First, the electric conductivity and/or capacity of graphene is sensitive to the biochemical environment, and can thus be modulated by certain chemical species that bind to the surface of the graphene sheet.^{137–144} Second, the high conductance of graphene makes it possible to record electrochemical reactions and measure the concentration of certain redox active species on a graphene-based electrode.^{141,145–147} Third, graphene has been reported to have surface-enhanced Raman scattering (SERS), allowing trace analyte molecules to be detected by amplifying the characteristic signature in the Raman spectrum.^{148–153} A wide spectrum of biomolecules, including glucose,^{137,138,141,146} glutamate,¹³⁷ DNA,^{139,141,152} dopamine,¹⁴⁸ thrombin,¹⁴⁰ and cholesterol,¹⁴⁷ have been successfully detected with high sensitivity and low detection limit by the graphene based biosensor.

Besides the electronic properties of graphene that have enabled high sensitivity detection of biomolecules, the distinctive optical properties of graphene oxide allow for biomedical imaging *in vitro* and *in vivo* using graphene oxide as the fluorescent tag. Although pristine graphene is a zero-gap semiconductor as aforementioned, due to the highly heterogeneous chemical and electronic structures of GO, strong fluorescence emission has been observed from GO in a broad spectrum ranging from the ultraviolet (UV) to near-infrared (NIR), the exact mechanism of which remains to be fully elucidated and has largely been believed to arise from the electronic transition between the nonoxidized, pristine sp^2 carbon domain and the oxidized boundaries of GO sheet.¹⁵⁴ Our group was the first to observe the NIR-I fluorescence up to ~1000 nm from both plain GO and PEGylated GO and to use the fluorescent GO as a fluorescent reporter for targeted cellular imaging.²⁹ Two-photon and multiphoton fluorescence imaging have been realized with GO for deep-tissue penetration microscopic imaging.¹⁵⁵ The absorbed photons can also be converted into acoustic waves by GO, making photoacoustic imaging possible with graphene.¹⁵⁶

The strong absorption of graphene derivatives including GO and reduced GO (rGO) opens up the possibility of employing graphene derivatives for photothermal therapy. Both *in vitro* and *in vivo* photothermal experiments have revealed that the tumor

cells and cancerous tissues can be selectively ablated by NIR light-induced heat from GO and rGO.^{32,157–162} In addition, it has also been reported that graphene oxide combined with NIR laser irradiation can be used for photothermal treatment of Alzheimer's disease.¹⁶³ Besides NIR light irradiation, nanographene oxide can also absorb focused ultrasound irradiation and generate enough heat for hyperthermia for brain tumor treatment.¹⁶⁴

The large surface area of graphene, which should be doubled compared to the SWCNT counterpart with the same number of carbon atoms owing to the accessibility to both sides of the graphene sheet, along with the delocalized π -electrons on its surface, have made graphene and its derivatives good candidates for loading and delivering drugs to certain cell types or desired regions in the body. Our group and others have shown that nanographene oxide is able to load water-insoluble anticancer drugs such as doxorubicin and SN38 and release the cargo drug molecules in a controllable manner.^{21,29,162,165–170} Besides chemotherapy drugs, graphene can also be used to deliver DNA and small interfering RNA (siRNA) for gene therapy.^{171–173} It has also been reported that, when combined with a photosensitizer, the photothermal conversion of graphene can facilitate the efficacy of photodynamic therapy.^{174,175}

Graphene also has excellent mechanical properties, including superior elasticity and high flexibility, allowing the graphene sheet to conform to any substrate with an arbitrary shape while providing structural support.^{176–178} It has been reported that graphene is among the strongest materials measured with exceptionally high Young's modulus, elastic stiffness, and intrinsic strength.¹⁷⁷ Therefore, graphene could be used as an ideal scaffolding material to effectively reinforce the structure and morphology of engineered tissues. To this end, a variety of studies have been carried out in which graphene and its chemical derivatives have been used as biocompatible substrates for the growth of neurons,¹⁷⁹ the differentiation of stem cells,^{25,26} as well as the proliferation and osteogenesis of osteoblast cells.^{26,180,181}

2.4. Carbon Dot

Carbon dot, also known as the carbon nanodot, carbon quantum dot or graphene quantum dot, represents another class of carbonaceous nanomaterial besides fullerene, carbon nanotube, and graphene. In terms of the chemical structure and physical properties, carbon dots in many ways resemble graphene oxide, and the distinction between carbon dots and graphene oxide mainly comes from the size difference, where carbon dots usually refer to the carbonaceous, graphitic nanoparticles with size below 10 nm.^{4,182} There is also a historical reason behind the distinction between graphene oxide and carbon dots. GO was first discovered in 1859 via harsh oxidative treatment of graphite¹⁸³ and then later modified via the Hummers method.¹⁸⁴ On the other hand, the research on carbon dots, which has just started receiving rising interest in the past decade, should be accredited to a serendipitous finding of fluorescent carbonaceous nanoparticles during a standard preparative electrophoresis experiment for purifying arc-discharged SWCNTs in 2004.¹⁸⁵ These fluorescent carbonaceous nanoparticles, which were later termed carbon dots, were identified and isolated from impure carbon soot from arc discharge synthesis of carbon nanotubes.¹⁸⁵ The research on carbon dots has become a hot topic in chemistry and many related fields ever since, starting from the various synthetic methods to make these carbon dots, and progressing toward the physicochemical understanding of the origin of their intrinsic

fluorescence and biomedical applications of carbon dots on imaging and therapy.^{182,186}

Carbon dots can be made by oxidation of the arc-discharged carbon soot with nitric acid, followed by base neutralization.¹⁸⁵ It has been found that surface passivation exists as a crucial step to obtain strong fluorescence emission from the carbon dots.²⁸ The precursor for making carbon dots can be graphite,^{28,187–191} fullerene,¹⁹² single-walled or multiwalled carbon nanotubes,^{185,190,193,194} graphene,^{195–197} carbon fibers,^{198,199} candle soot,²⁰⁰ glycerol,^{201–203} glucose,^{204,205} citrate,^{206–208} aromatic organic compounds,^{209–211} and many other bioorganic precursors including silk,²¹² orange juice,²¹³ banana juice,²¹⁴ honey,^{215,216} and even food waste.²¹⁷ To generate carbon dots from the carbon-containing precursors, a variety of physical and chemical means including both top-down^{28,185} and bottom-up strategies^{209–211} can be applied, including laser ablation,^{28,191} oxidative acid treatment,^{28,185,190,198,200,218} hydrothermal treatment,^{195,197,204,205,213,214} surfactant extraction,¹⁹⁴ electrochemical oxidation,^{187–189,193,199} ultrasound irradiation,^{201,202,217} microwave-assisted synthesis,²⁰³ electron-beam lithography,¹⁹⁶ and even rational organic synthesis.^{209–211}

The structure of carbon dots can be considered as a nanosized graphene with varying degrees of oxidation. The chemical composition of a carbon dot, although only composed of carbon, hydrogen, oxygen, and nitrogen, can vary from case to case for the percentage of each element, depending on the type of precursor and synthetic method.¹⁸² Nonetheless, highly crystalline lattices comprised of carbon atoms can be clearly seen from high resolution transmission electron microscopy (HRTEM) images of most reported carbon dots, confirming the graphitic nature of the carbon dots.⁴

Carbon dots have been identified as highly fluorescent in a broad range from deep ultraviolet,²⁰⁵ to visible,²⁸ to the near-infrared,^{219,220} making them a carbonaceous analogue of fluorescent semiconducting quantum dots.²²¹ The fluorescence of carbon dots has been found to be excitation-dependent, and the peak emission wavelength can be tuned in the entire visible window from 400 to 750 nm with progressively longer excitation wavelength.²⁸ Although still a matter of intensive debate, the origin of fluorescence of carbon dots has been attributed to the quantum confinement effect of emissive energy traps to the surface of the carbon dot nanoparticles,²⁸ excitonic transitions in nanosized carbon,^{193,222} and energy states related to edge defects.²²³ Besides normal one-photon, down-conversion fluorescence, carbon dots have also been reported to have two-photon and multiphoton fluorescence emission^{224–229} and upconversion fluorescence.^{223,230}

Owing to the versatile optical properties and the large surface area of carbon dots, they have been widely employed for a variety of biomedical applications including but not limited to the following: one-photon, down-conversion fluorescence imaging of cells in an *in vitro* setting (refs 197, 198, 201, 202, 212, 213, 218, and 230–246) and that of organs in live animals,^{31,190,215,220,247,248} multiphoton fluorescence imaging of cells and through tissue phantom to demonstrate the benefits of nonlinear optical microscopy with carbon dots,^{224–229} drug delivery,^{224,249–251} and photodynamic therapy.^{248,252} We will discuss the bioimaging and therapeutic applications of carbon dots in detail in the following sections.

2.5. Nanodiamond

Nanodiamonds are an emerging class of new carbonaceous nanomaterials with many intriguing optical, mechanical, and

chemical properties. Unlike all the other four classes of nanomaterials including fullerene, carbon nanotubes, graphene, and carbon dots, nanodiamond, being another allotrope of carbon-based nanomaterials, is not comprised of sp^2 graphitic carbon, but consists of sp^3 carbon atoms only. Nanodiamond is referred to diamond nanoparticles with sizes ranging from 2 to 10 nm, which are significantly smaller than bulk diamond and diamond abrasive powders, but larger than organic diamondoid molecules.⁵ Made from detonation of explosive compounds with a negative oxygen balance, nanodiamonds were first found in the detonation soot together with graphitic, nondiamond carbon.²⁵³

One unique feature of nanodiamonds, which distinguishes them from the other carbon allotropic nanomaterials, is the presence of fluorescent defect centers. Although different defect centers with tunable absorption and emission bands can be achieved, the most common defect center is the nitrogen–vacancy (N–V) defect center. There are two types of N–V centers: neutral N–V⁰ center with fluorescence emission at 576 nm and negatively charged N–V[−] center with emission at 638 nm.²⁵⁴ Both electronic transitions can be coupled with phonons to give a broad band at ~700 nm.^{255,256} With the fluorescence emission in a broad range from 500 to 800 nm, even a single N–V defect center can be visualized by scanning confocal microscopy.^{256–258}

For bioimaging and therapy purposes, which are the two focuses of this review paper, nanodiamond has several advantages: first, nanodiamond is a highly photostable fluorophore that is almost nonphotobleachable, allowing for long-time imaging without concerns of signal decay;²⁵⁵ second, the fluorescence quantum efficiency is surprisingly high, usually ranging from 0.7 to 1, significantly higher than molecular fluorophores with similar emission wavelengths;^{255,259} third, nanodiamond has been reported to be highly biocompatible and nontoxic to biological tissues and organisms;²⁵⁵ fourth, the abundant dangling bonds on the surface of nanodiamonds allow for easy surface functionalization via both covalent and noncovalent means without affecting the intrinsic optical properties of the N–V centers in the core, rendering them readily applicable for various biomedical application.^{5,260,261} Owing to these benefits, nanodiamonds have been intensively employed as fluorescent labels for *in vitro* imaging of subcellular structures and certain biomarkers,^{17,254,255,261–266} *in vivo* whole animal imaging,^{267–269} drug and gene delivery,^{264,270–275} and tissue engineering.^{276,277}

3. SURFACE FUNCTIONALIZATION OF CARBON NANOMATERIALS

As for any nanomaterial to be used in living organisms, water solubility and biocompatibility need to be achieved. Different carbon nanomaterials require different strategies of surface functionalization to make them soluble in aqueous environment and compatible with cells and tissues. As a brief note, fullerenes are typically covalently functionalized through chemical reactions directly with the carbon atoms in the sp^2 carbon shell, and a library of standard chemical reactions have been developed for fullerene chemistry. Carbon nanotubes and graphene, both of which feature continuous graphitic honeycomb structures expanding over submicrometer to micrometer scales, can be either covalently or noncovalently functionalized to impart water solubility, depending on the need for specific biological applications. Carbon dots are by nature rich in –OH and –COOH functional groups, which can easily form hydrogen bonds with water molecules and thus endow carbon dots with

good solubility in aqueous environment; nonetheless, it is still desired to further functionalize them with PEG or other functional groups to increase biocompatibility. Nanodiamond, on the other hand, is similar to carbon nanotubes and graphene in that both noncovalent and covalent functionalizations have been reported to increase their water solubility and biocompatibility. In this section we will focus on the different surface functionalization methods for various carbon nanomaterials, which are discussed in two major categories of noncovalent and covalent surface treatments.

3.1. Noncovalent Surface Functionalization

Noncovalent surface functionalization works by supramolecular interactions between the pristine carbon nanomaterial and the coating molecules/polymers, which impart minimum structural damage and disturbance to the intrinsic properties of the functionalized carbon nanomaterials. The supramolecular interactions employed for noncovalent surface functionalization include $\pi-\pi$ stacking and hydrophobic interactions.

With SWCNT as an example, noncovalent functionalization retains the pristine honeycomb structure comprised of sp^2 graphitic carbon atoms, and thus maintains the many desired electronic and optical properties of SWCNTs, in particular the NIR-II fluorescence emission. Owing to the intrinsic excitonic nature of the NIR-II fluorescence of semiconducting SWCNTs (see section 4.2.1. for more details), the quantum efficiency of giving off NIR-II photons by a semiconducting SWCNT highly depends on the diffusion length and the fate of excitons, which are closely related to the length and the surface defects of SWCNTs. It has been reported that SWCNT, regardless of its chirality, has an exciton diffusional range of approximately 90 nm, suggesting lower NIR-II fluorescence quantum efficiency with shorter nanotubes on the ~100 nm scale. Nanotubes with defects that act as discontinuities along the length of the conjugated system will also show lower quantum yield. Both the tips and the defect sites in an SWCNT can cause nonradiative recombination of diffusing excitons as they travel along the length of the nanotube.²⁷⁸ Therefore, noncovalently coated and solubilized SWCNTs are desired especially for NIR-II fluorescence imaging applications with SWCNTs to avoid the disruption of the π -network of pristine carbon nanotubes.

SWCNTs and graphenes can be wrapped by surfactants, polymers, DNA, proteins, and even viruses to achieve noncovalent surface functionalization. The first stable aqueous solution of SWCNTs that allowed for direct measurement of band gap fluorescence from individual SWCNTs was made by vigorous sonication of high pressure CO (HiPco) decomposed CNTs in the presence of sodium dodecyl sulfate (SDS) surfactant.⁸⁷ When the surfactant concentration is higher than the critical micelle concentration (cmc) of SDS, the SDS molecules form columnar micelles spontaneously in water with a hydrophobic core encapsulating SWCNTs through hydrophobic interactions and a hydrophilic shell providing solvation of SWCNTs in an aqueous environment (Figure 3a). Under sonication, the hydrophobic and van der Waals interactions between micelle and carbon nanotube rival those between bundled nanotubes, leading to debundling into individual, micelle-wrapped SWCNTs that have a lower density than the bundled SWCNTs. This density difference allows for separation of individually dispersed SWCNTs from large bundles and aggregates. Besides SDS, many other small molecule surfactants, including anionic surfactants such as sodium dodecylbenzenesulfonate (SDBS),²⁷⁹ sodium cholate,³⁰ sodium deoxycholate,²⁸⁰

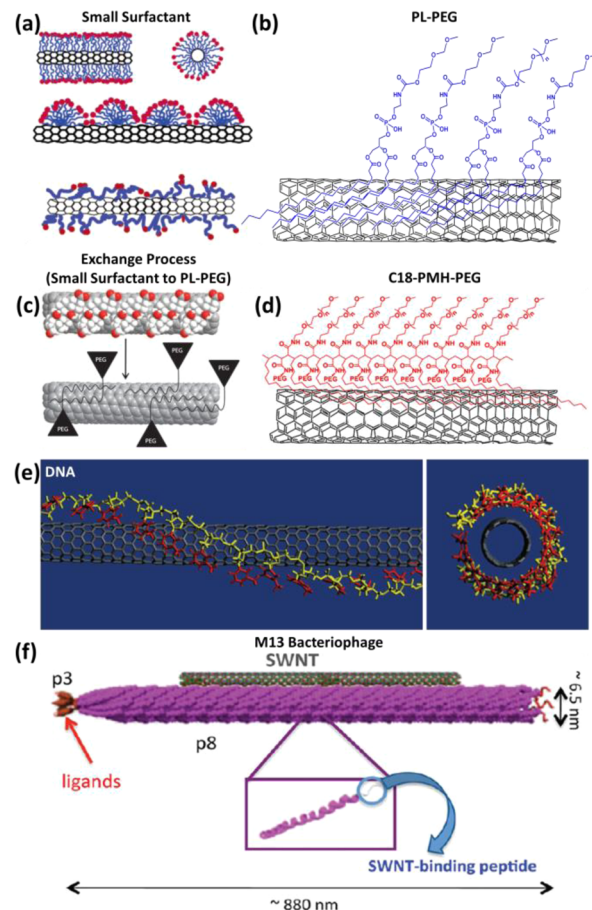


Figure 3. Different noncovalent surface functionalization methods for SWCNTs. (a) Schematics showing the proposed structures of surfactant-solubilized SWCNTs, which can be wrapped in a columnar micelle (top), in multiple semimicelles (middle) or with random surface adsorption (bottom). Reprinted from ref 326. Copyright 2004 American Chemical Society. (b) Schematic drawing showing the proposed structure of an SWCNT solubilized by the supramolecular interaction between the nanotube sidewall and the hydrophobic alkyl chains of the PL-PEG molecules. (c) Schematic showing the surfactant exchange process in which cholate coating (shown as white and red balls) on the SWCNT is eventually replaced by PL-PEG (black triangles) to afford biocompatibility with minimum structural damage to the nanotube. Reprinted with permission from ref 30. Copyright 2009 Nature Publishing Group. (d) Schematic of an SWCNT solubilized by branched C18-PMH-mPEG polymer. Reprinted from ref 298. Copyright 2012 American Chemical Society. (e) Binding model of a single strand DNA-wrapped SWCNT showing the helical structures of the DNA extending along the length of the nanotube. The sugar-phosphate backbone is shown in yellow while the nucleobases are shown in red in both the top view (left) and the side view (right). Reprinted with permission from ref 306. Copyright 2003 Nature Publishing Group. (f) Schematic drawing showing the M13-SWCNT bioconjugate where the carbon nanotube is stabilized and dispersed by the SWNT-binding peptide on p8, the major coat protein in the M13 bacteriophage. Reprinted from ref 321. Copyright 2012 American Chemical Society.

sodium taurodeoxycholate,²⁸⁰ cationic surfactants such as cetyltrimethylammonium bromide (CTAB),²⁸¹ imidazolinium halides,²⁸² cetylpyridinium chloride,²⁸⁰ and nonionic surfactants such as Triton X-100²⁸³ and Tween 20,²⁸⁴ have also been used to noncovalently disperse and stabilize SWCNTs in an aqueous solution through micellar solubilization. Owing to the similar graphitic structure of graphene to CNTs, many of the

aforementioned surfactants have also been used as noncovalent surface stabilizing agents for GO and rGO.^{285,286}

Although micelle-stabilized SWCNTs and graphene can be stable in an aqueous solution for several months, the soapy surfactant molecules are usually highly toxic and raise biocompatibility concerns for biomedical imaging and therapy applications.²⁸⁷ Another major disadvantage of micellar stabilization based on small surfactant molecules is the difficulty of removing excessive, free surfactant molecules that are not physisorbed on the SWCNTs, due to the fact that small molecule stabilization relies on the formation of micelles and the surfactant concentration needs to be higher than the cmc to maintain the dynamic equilibrium between free surfactants and micellar surfactants. The difficulty of removing excessive, free surfactants places an obstacle for further conjugation of the solubilized SWCNT complexes with other imaging labels or bioactive molecules such as targeting ligands, since conjugation will take place on both nanotube-bound surfactants and free surfactants, leading to undesired nonspecific labeling and conjugation of the SWCNTs.

To overcome the aforementioned problem associated with small molecule surfactants, our group has pioneered the use of phospholipid–polyethylene glycol (PL–PEG) as a surface coating agent for solubilization of SWCNTs while also imparting further surface functionalization ability through the terminal groups available at the end of the PEG chain, including $-\text{NH}_2$ and $-\text{COOH}$ groups.^{95,288,289} To make a stable aqueous solution of SWCNTs, raw SWCNT powder needs to be sonicated in the presence of PL–PEG in water, where the hydrophobic PL chain sticks to the surface of SWCNTs through hydrophobic interaction and tears bundled nanotubes apart into SWCNT–PL–PEG complexes each loaded with single or a few nanotubes. Although PL–PEG can also be considered as a surfactant due to the existence of a hydrophobic PL chain and a hydrophilic PEG chain, it solubilizes and stabilizes SWCNTs in water based on a different mechanism than the small molecule surfactants. PL–PEG forms a strong supramolecular complex with SWCNT, and the solution stability does not rely on the formation of free micelles in the solution (Figure 3b). An important implication of this solubilization mechanism is that excessive free PL–PEG molecules in the aqueous solution can be removed by repetitive centrifugal filtration without affecting the aqueous stability of the already-formed SWCNT–PL–PEG complexes, thus allowing for specific biochemical conjugation to the PEG chains on the nanotube surface.²⁹⁰ Taking advantage of this property, our group has shown successful solubilization and conjugation of SWCNTs to arginine-glycine-aspartic acid (RGD) peptide, which remain highly stable in both PBS and full fetal bovine serum, for in vivo targeting to $\alpha_v\beta_3$ integrin positive tumors. We have also found that a larger molecular weight of PEG or more branched PEG favors longer blood circulation time and lower liver uptake, indicating a better “stealth effect” of PEG on the nanotubes to prevent fast immune response and opsonization of the intravenously administered SWCNTs.²⁹¹ In a similar manner, we have shown that the FeCo/graphene nanoparticles can be noncovalently functionalized with improved water solubility by physisorption of PL–PEG molecules onto the graphitic shell on these nanoparticles.^{20,292,293}

Despite the advantages of PL–PEG surfactants for SWCNT solubilization, which has been widely adopted by many groups to make biocompatible carbon nanotubes for a variety of applications,^{12,94,294,295} one major drawback of the PL–PEG assisted solubilization process of SWCNTs is that, during

sonication, PL–PEG causes significant damage to the carbon nanotube backbone, leading to short segments of nanotubes chopped down to 50–300 nm and a large number of defects evidenced by the increased D band in Raman spectroscopy.^{30,291,296} Given the mean exciton diffusion distance of ~ 90 nm for SWCNTs, the shortened length and increased number of defect sites on the SWCNTs significantly increase the chance of quenching the NIR-II photoluminescence by capturing a traveling exciton before it radiatively recombines. Therefore, SWCNTs solubilized by directly sonicating solid powder of nanotubes in a PL–PEG solution do not have sufficient NIR-II fluorescence and are thus unsuitable for imaging applications that require bright NIR-II fluorophores. To solve this problem, we have come up with a surfactant exchange method by replacing the surfactant molecules of sodium cholate solubilized SWCNTs, which have relatively less damage to the graphitic structure and higher NIR-II fluorescence quantum yield, with the more biocompatible and stable PL–PEG molecules using a mild dialysis method instead of direct sonication to preserve the NIR-II fluorescence (Figure 3c). We have shown a minimum loss of $<20\%$ quantum yield during the exchange process, as opposed to a dramatic 30-fold decrease of quantum yield during the direct sonication process, in order to achieve noncovalent PEGylation of the SWCNTs.³⁰ This method has allowed for in vivo whole-body NIR-II fluorescence imaging and intravital NIR-II microscopy with SWCNTs for the first time, and has also laid the foundation for all follow-up works on in vivo NIR-II fluorescence imaging with the exchanged SWCNTs coated with PL–PEG.^{14–16}

Although PL–PEG functionalized SWCNTs have shown satisfactory biocompatibility, relatively long blood circulation time (of a few hours for 5 kDa PEG), and low RES uptake, a branched PEG polymer, poly(maleic anhydride-*alt*-1-octadecene)-methoxy poly(ethylene glycol) [C18-PMH-mPEG], has shown improved PEGylation and surface passivation of SWCNTs, evidenced by a very long circulation half-life of 20–30 h, depending on the degree of polymerization and molecular weight of the branched PEG polymer (Figure 3d).^{297,298} As will be discussed in later sections, this long blood circulation half-life favors higher nonspecific tumor uptake for in vivo NIR-II fluorescence imaging of the tumor,²⁹⁸ as well as minimized complement activation of the immune system.²⁹⁹ The branched C18-PMH-mPEG polymer can also be used to noncovalently functionalize and solubilize rGO,^{157,300} which has much fewer available $-\text{COOH}$ groups for covalent functionalization than GO.

In 2001, our group reported strong noncovalent binding of pyrene moieties to the sidewalls of SWCNTs due to π – π stacking, useful for functionalization of nanotubes for biological applications. The π -stacking chemistry has been widely utilized in the past decade for functionalization of not only nanotubes, but also various forms of graphene.^{301–305} Besides nonbioactive molecules, polymeric biomolecules such DNA and proteins have also been employed for solubilization of SWCNTs. Single-stranded DNA (ssDNA) was used to assist the dispersion and suspension of SWCNTs in water by helically wrapping to the surface of the nanotube, as first reported by Zheng et al.³⁰⁶ It was suggested that strong π – π stacking between nanotube surface and the aromatic bases of ssDNA is responsible for the formation of hybrid between nanotube and DNA, which is elegant since DNA is a molecule of central importance in biology and the carbon nanotube represents an artificial 1D carbon nanocrystal.³⁰⁶ In the DNA–SWCNT hybrid complex, the nitrogenous bases point

toward the carbon nanotube backbone, while the hydrophilic, phosphate–deoxyribose backbone of DNA points toward water to impart water solubility to the functionalized SWCNTs (Figure 3e). The noncovalent wrapping of ssDNA on the SWCNT surface is found to be sequence-dependent based on a systematic screening of the ssDNA library with different base compositions, and SWCNTs with different diameters and electronic properties can be separated by performing anion exchange chromatography of the ssDNA-wrapped SWCNTs.^{307,308} Single semiconducting chiralities of SWCNTs have also been successfully separated from the starting HiPco mixture by designing short DNA sequence motifs that can recognize and fold selectively on each specific chirality and performing chromatographic purification of the DNA-functionalized SWCNTs.^{309–312} DNA-wrapped SWCNTs also allow for length separation of SWCNTs based on size-exclusion chromatography.³¹³ More interestingly, since DNA is a chiral polymer, it can wrap around a certain chirality of SWCNTs with selected handedness, leading to observed circular dichroism activity from a racemic mixture of SWCNTs dispersed with DNA.³¹⁴ Owing to the endogenous nature of DNA molecules, DNA-functionalized SWCNTs have shown good biocompatibility and low toxicity when introduced to cells and live animals,^{96,315} while providing good dispersion of individual SWCNTs with minimum degree of bundling and aggregation. Our group has shown that the DNA-wrapped SWCNTs can be employed as an intracellular transporter of DNA via an endocytotic internalization pathway.^{95,96}

Proteins have been found to adsorb nonspecifically on the sidewall of SWCNTs and on graphene sheets. Similar to the DNA–nanotube conjugate, protein-functionalized SWCNTs have allowed us to make intracellular protein transporters.^{96,316} Amphiphilic proteins such as hydrophobins have been used for exfoliation and functionalization of graphene sheets as they detach from graphite.³¹⁷ GO decorated with bovine serum albumin (BSA) through the stable protein adsorption has been used as a universal adhesive nanoplatform for controlled assembly of a variety of nanoparticles in one study³¹⁸ and as a model nanoparticle to study the size dependent cell internalization pathway in another study.³¹⁹

Recently, the Belcher group developed a new method to noncovalently functionalize SWCNTs using a virus called M13 bacteriophage, which allows for multivalent interaction with 1D nanomaterials such as SWCNTs with benefits from its filamentous shape. The M13 bacteriophage binds to the surface of carbon nanotubes through π – π stacking between the aromatic histidine residue and the graphitic sidewall of SWCNTs (Figure 3f). A typical surfactant exchange procedure, similar to the aforementioned exchange method to replace sodium cholate with PL–PEG, is used to make stable SWCNT–M13 bioconjugate via pH-controlled dialysis.³²⁰ Owing to the larger size of M13 bacteriophage than an SWCNT, each M13 bacteriophage with a diameter of ~6.5 nm and length of ~880 nm can load multiple SWCNTs without compromising their NIR-II fluorescence, allowing for *in vivo* NIR-II fluorescence imaging with this inorganic–biological hybrid probe.^{321,322} Unlike PL–PEG where the targeting ligands are attached to the terminal groups in the PEG chain to afford specific targeting capability, the minor coat protein p3 located at the tip of each M13 bacteriophage can be engineered to express either a certain peptide ligand that can directly bind to a biomarker on its own, or some peptide handles for further site-specific conjugation with antibodies.^{36,321,322} The M13 bioconjugate virus can also enhance the colloidal dispersion stability of graphene sheets

through noncovalent coating of multiple filamentous viruses on one continuous single-layer graphene sheet.³²³ As a genetically engineered peptide display platform, M13 bacteriophage provides sufficient available sites for incorporating many different functional nanoparticles (SWCNTs, magnetic nanoparticles)³²⁴ and peptide motifs (targeting peptides, antibodies, and dye-labeled proteins) into one single carrier, which are promising versatile nanostructures with both imaging and therapeutic functions.³²⁵

3.2. Covalent Surface Functionalization

Most carbon nanomaterials are insoluble in water due to their hydrophobic surfaces made of sp^2 carbon atoms. Covalent surface functionalization introduces heteroatoms (mostly O and N) and functional groups to the pristine carbon nanostructures and thus increases water solubility. The functional groups also provide handles for further conjugation with other functional molecules to improve biocompatibility and impart certain functions to the original carbon nanomaterials.

Fullerenes can react with electrophiles due to the rich delocalized π -electrons on the surface of the fullerene spheroid. A number of organic reactions, including radical additions, nucleophilic additions, cycloadditions, oxidations, and many other reactions, can occur to the double bonds made of sp^2 carbon atoms to impart functional groups that allow for further chemical and biochemical functionalizations.³²⁷ Typical products including pyrrolidinofullerenes (with a nitrogen-containing five-membered ring on the fullerene surface) in the 1,3-dipolar cycloaddition reaction,³²⁸ methanofullerenes (with a three-membered ring on the fullerene) in the nucleophilic addition Bingel reaction,³²⁹ and fullerenols (with many hydroxyl groups on the fullerene) in the radical addition reaction with nitrogen dioxide radicals.³³⁰ The rich fullerene chemistry and a library of fullerene derivatives have allowed for the synthesis of many different types of water-soluble fullerene bioconjugates, including fullerene-containing amino acids, peptides,³³¹ and carbohydrates,³³² as well as PEGylated fullerene nanoparticles^{61,333} for various biomedical applications including imaging, photodynamic and photothermal therapies, as well as drug and gene delivery.^{42,334}

Carbon nanotubes can be covalently functionalized with the same chemical reactions as fullerenes since they bear similar graphitic structures on the sidewalls. For example, 1,3-dipolar cycloaddition to azomethine (i.e., the Prato reaction) can occur on the sidewalls of SWCNTs, resulting in carbon nanotubes with the surface covalently functionalized with pyrrolidine rings.³³⁵ A more widely accepted methodology for the covalent functionalization of carbon nanotubes and graphenes is through controlled oxidation in the presence of various oxidizing agents such as $KMnO_4$, H_2SO_4 , and HNO_3 . Smalley et al. have shown that a mixture of H_2SO_4 and HNO_3 can cut raw carbon nanotube materials into shorter fragments ranging from 100 to 300 nm in length, and the carboxylic groups at the open ends of the chopped short SWCNTs can be utilized for further conjugation to other functional groups.²⁸³ Haddon et al. report the derivatization of the open-ended SWCNTs with thionyl chloride and octadecylamine, allowing for solubilization and spectroscopic study of the alkyl-functionalized SWCNTs in organic solvents.³³⁶ Our group has expanded the covalent surface functionalization of SWCNTs to afford water solubility via conjugation with hydrophilic molecules such as proteins and PEG.^{316,337} The –COOH groups at the open ends and sidewalls of the oxidized SWCNTs can link to the amine groups in proteins

or amine-terminated PEG molecules through standard EDC-catalyzed amidation reaction with high yield.^{337–339} Amidation between the nanotube-bound carboxyl groups and amine groups from other functional water-soluble molecules can also be achieved by treating the –COOH groups with thionyl chloride to achieve activation of the carboxyl group, followed by adding the amine-group rich molecules.³⁴⁰ Although covalent functionalization of CNTs provides a broad selection of chemical approaches for solubilization and conjugation, it is worth mentioning that the damage to the conjugated π network is a big concern, especially for NIR-II fluorescence imaging applications, due to the higher likelihood of nonradiative recombination of excitons at the defect site and decreased fluorescence quantum efficiency. Therefore, to the best of our knowledge, none of the SWCNT-based *in vitro* and *in vivo* NIR-II fluorescence imaging works reported so far is done with covalently solubilized and functionalized SWCNTs. Nonetheless, recently the Wang group at University of Maryland has reported that, as opposed to defect-induced quenching, the NIR-II fluorescence brightness can be enhanced by introduction of controlled sp^3 defect sites into semiconducting SWCNTs, resulting in red-shifted photoluminescence with significantly enhanced emission intensity and opening up possibilities of NIR-II fluorescence imaging with greater sensitivity.^{341,342}

In a similar way to the covalently functionalized CNTs, graphite materials can also be treated with oxidizing agents to make GO with abundant functional groups such as –OH and –COOH, which allow for further conjugation with PEG or bioactive molecules.³⁴³ Unlike in the case of SWCNTs, since the fluorescence of GO does not rely on the intactness of the graphitic structures but may rather originate from defect states, the introduction of covalent functional groups to graphene would rather increase the fluorescence intensity. We have shown that expandable graphite can be treated with a modified Hummers method to form nanoGO sheets, which are further linked with branched PEG molecules through EDC cross-linking reaction to afford great water solubility and biocompatibility for *in vitro* cell imaging and drug delivery experiments.²⁹ The EDC-assisted functionalization of bioactive molecules on GO has been widely adopted by many other groups, including the conjugation of GO with folic acid,¹⁶⁷ DNA,¹³⁹ and chitosan.³⁴⁴ Besides direct oxidation of graphene sheet to generate carboxylic acid groups, azo coupling reaction has also been employed to functionalize graphene edges with sulfonic acid groups to improve water solubility. Samulski et al. have reported the treatment of graphene with 4-diazoniobenzenesulfonate to introduce multiple sulfonic acid groups that are highly hydrophilic and can significantly increase the water solubility of graphene.³⁴⁵

Since carbon dots are typically synthesized by treating organic precursors with oxidizing agents, carbon dots are usually rich in carboxyl groups that afford intrinsically high water solubility and easy covalent functionalization. Condensation of –COOH groups with PEG molecules is usually used as surface passivation to enhance intrinsic fluorescence emission, as reported by Sun et al.²⁸ Besides PEG, many other small molecules, such as ethylenediamine, octadecylamine, and 2-(2-aminoethoxy)-ethanol, can be covalently linked to the surface of carbon dots through an amide bond, resulting in hydrophilic and hydrophobic carbon dot nanoparticles depending on the chemical properties of the capping molecules.^{206,346}

Nanodiamonds after air or ozone purification are intrinsically functionalized with carboxyl groups, allowing for further surface modifications to impart different biochemical functionalities.

Treating the carboxyl functionalized nanodiamonds with different gases and/or chemicals is an efficient way to modify the surface hydrophobicity and functionalities. For example, nanodiamonds can be heated up in hydrogen atmosphere to reduce all –COOH groups to hydrogen, leading to hydrophobic nanodiamonds.³⁴⁷ For most biomedical applications, a hydrophilic and biocompatible surface is needed. It has been reported that the as-purified nanodiamonds without any further treatment can readily be internalized into cells without causing appreciable cellular toxicity.²⁵⁵ Nonetheless, under some circumstances it is desired to tag nanodiamonds with peptides, DNA, or fluorophores. Taking advantage of the abundant –COOH groups available on the surface of nanodiamonds, the coupling reaction between carboxyl group and amine group is usually employed to link amine-terminated molecules to the surface of nanodiamonds.⁵ Ando et al. report the surface functionalization of –COOH group coated nanodiamonds with thymidine through thionyl chloride catalyzed condensation between the carboxyl group of nanodiamond and the 5' hydroxyl group of thymidine, followed by the subsequent grafting of DNA through base pair recognition.³⁴⁸ Krueger demonstrate surface functionalization of amino acids, and even the formation of a peptide sequence can be achieved on the surface of nanodiamond particles, imparting biological activities to the nanodiamonds.²⁶¹ The same group has also shown that different fluorescent dye molecules can be conjugated to nanodiamond through click chemistry using the Cu-catalyzed azide–alkyne coupling reaction.³⁴⁹

4. CARBON NANOMATERIALS FOR BIOLOGICAL IMAGING

4.1. One-Photon Fluorescence Imaging of Carbon Nanomaterials in the Visible and First Near-Infrared (NIR-I) Windows

4.1.1. Origin of Fluorescence of Fullerene, Graphene, Carbon Dot, and Nanodiamond. One-photon, down-conversion fluorescence, which is the most common type of photoluminescence with normal Stokes shift, has been reported as an intrinsic optical property, for all carbon nanomaterials covered in this review paper, including fullerene, carbon nanotube, graphene, carbon dot, and nanodiamond. However, it is worth pointing out that, although they all exhibit red-shifted fluorescence emission upon excitation at a shorter wavelength, the fluorescence of carbon nanotubes is quite unique with wavelengths mainly in the second near-infrared window (NIR-II window, 1000–1700 nm) and distinguishes them from all others with fluorescence wavelengths in the much shorter wavelengths of visible (400–750 nm) and traditional near-infrared windows (750–1000 nm). Owing to the salient advantages of longer-wavelength NIR-II fluorescence over shorter-wavelength fluorescence, we will discuss the NIR-II fluorescence with its imaging applications of carbon nanotubes in a separate section (section 4.2) while combining all other materials with similar fluorescence properties in this section (section 4.1). Nonetheless, it should be admitted that the other carbonaceous materials, although all exhibiting fluorescence in the 400–1000 nm window, absorb light and emit fluorescence photons from completely different mechanisms than SWCNTs, which will be discussed in great detail in later paragraphs.

A fullerene nanoparticle is made of a closed shell of graphene that contains conjugated double bonds. Taking the C₆₀ molecule as an example, one can find 30 double bonds with π -electrons

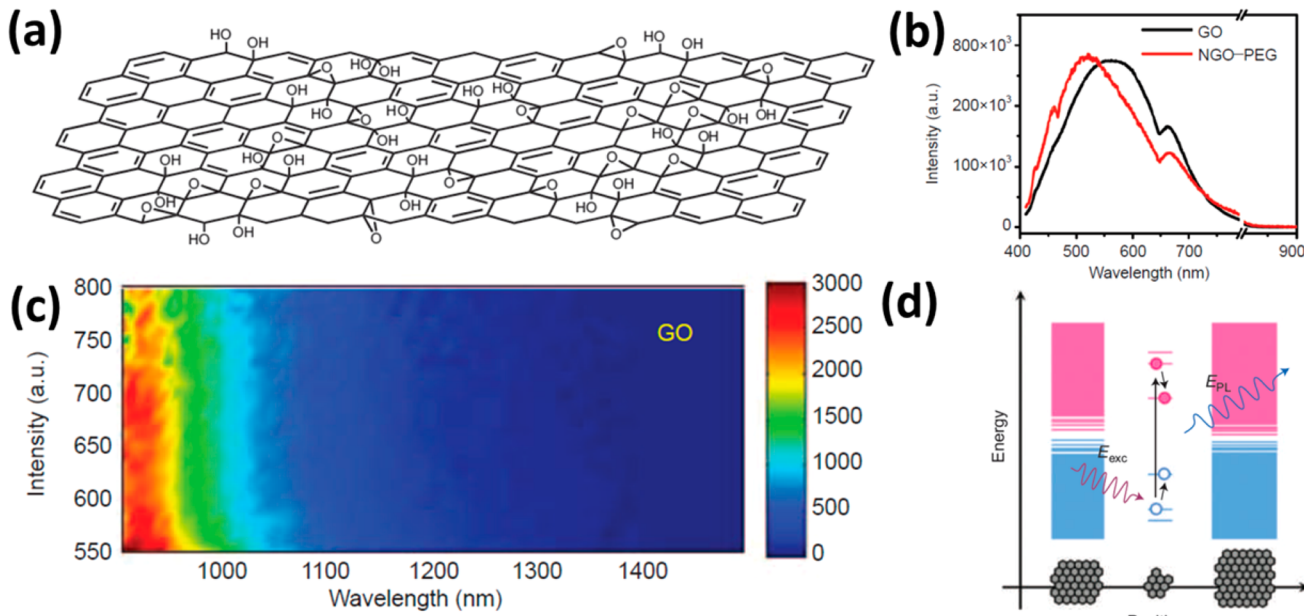


Figure 4. Structure and fluorescence of GO. (a) Proposed chemical structure of GO based on the Lerf–Klinowski model. Reprinted with permission from ref 124. Copyright 2010 Nature Publishing Group. (b) Fluorescence spectra of GO (black curve) and PEGylated nanoGO (termed NGO–PEG, red curve) in the visible and NIR-I range (400–1000 nm) under 400 nm excitation. Reprinted with permission from ref 29. Copyright 2008 Springer. (c) Photoluminescence versus excitation (PLE) map of GO, highlighting the falling edge of fluorescence emission in the NIR-II window (1000–1700 nm). Reprinted with permission from ref 29. Copyright 2008 Springer. (d) Proposed energy diagram of GO, showing larger band gap associated with smaller aromatic domain size. Reprinted with permission from ref 124. Copyright 2010 Nature Publishing Group.

highly delocalized over all the conjugated double bonds. Therefore, electronic transitions are expected to take place between the HOMO and LUMO of the large π -conjugated system, corresponding to strong absorption mostly in the ultraviolet (UV) region (<400 nm), which should be followed by fluorescence emission in the visible window. However, the fluorescence quantum yield of unmodified, pristine fullerene is very low, on the order of 10^{-5} – 10^{-4} , and the photoluminescence decreases at increasing temperature with very weak emission at room temperature due to nonradiative recombination of excited nanoparticles coupled with phonons.^{350–352} Nonetheless, it has been reported that covalent surface functionalization³⁵³ and structural defects,³⁵⁴ both of which break the structural symmetry of the pristine fullerene molecule, can be used as a strategy to enhance the fluorescence emission of fullerene, making it bright enough as a fluorescent label for imaging applications.³⁵⁵

A pristine, infinitely large graphene sheet is a zero band gap semiconductor with the conduction band and valence band touching at the K points and should thus be nonfluorescent.^{117,356} However, when the size of the graphene sheet shrinks and functional groups are introduced to the edges of graphene, band gap opening is predicted and experimentally confirmed due to quantum confinement and edge effects,^{116,357,358} and as a result fluorescence can be observed across the band gap of narrow graphene nanoribbons and oxidized graphene sheets (i.e., graphene oxide or GO).^{29,359} Owing to the facile chemical synthesis of GO in solution phase, GO is the most common type of fluorescent graphene materials widely used for biomedical imaging. The highly complex and heterogeneous structure of GO (Figure 4a) leaves an open question as to the origin of fluorescence from GO, and a handful of mechanisms have been proposed to account for this long-debated question. Our group has suggested the many nanometer-sized aromatic

domains with lateral dimensions ranging from 1 to 5 nm in a GO sheet as the origin of the observed broad fluorescence emission spanning over the visible and NIR-I ranges (Figure 4b,c).²⁹ Similar mechanisms have been proposed by Chhowalla and Chen et al.,^{360,361} with proposed band diagrams of GO showing the domain size dependent energy gap (Figure 4d) and a continuous distribution of sp^2 carbon domain sizes that lead to the broad emission band and excitation-dependent emission of GO.¹⁵⁴ Ajayan et al. have attributed the pH-dependent fluorescence emission of GO to the presence of quasi-molecular fluorophores formed by the strong electronic coupling between the carboxyl groups located at the edges and the neighboring sp^2 graphitic carbon π -electrons.³⁶² In a similar argument but expanding to all oxygen-containing functional groups including carboxyl, carbonyl, and alkoxy groups, Gurzadyan et al. proposed another mechanism where the electronic transitions between the nonoxidized, pristine sp^2 graphitic carbon regions and oxidized carbon regions at the boundaries are attributed as the origin of GO fluorescence.¹⁵⁴ Besides these aforementioned mechanisms, there are also other explanations including bond distortions and localized electronic states at the oxidation sites.^{363,364}

Carbon dots, which can be seen as nanosized graphene or graphene oxide with <10 nm size, bear much resemblance to GO in optical, in particular fluorescence, properties. For example, the photoluminescence spectra of carbon dots exhibit broad emission peaks that are dependent on the excitation wavelengths,²⁸ indicative for the presence of a multiple fluorophore system similar to GO.^{154,365} The emission wavelengths of carbon dots can be tuned in a broad range from 400 to 750 nm by changing the size, suggesting quantum confinement of the graphitic domain is an important contributor to the photoluminescence of carbon dots.^{200,243,366} Besides, the modification of surface states by heteroatoms (such as O, N, P, and S) in the carbon dots also plays a crucial role in determining the

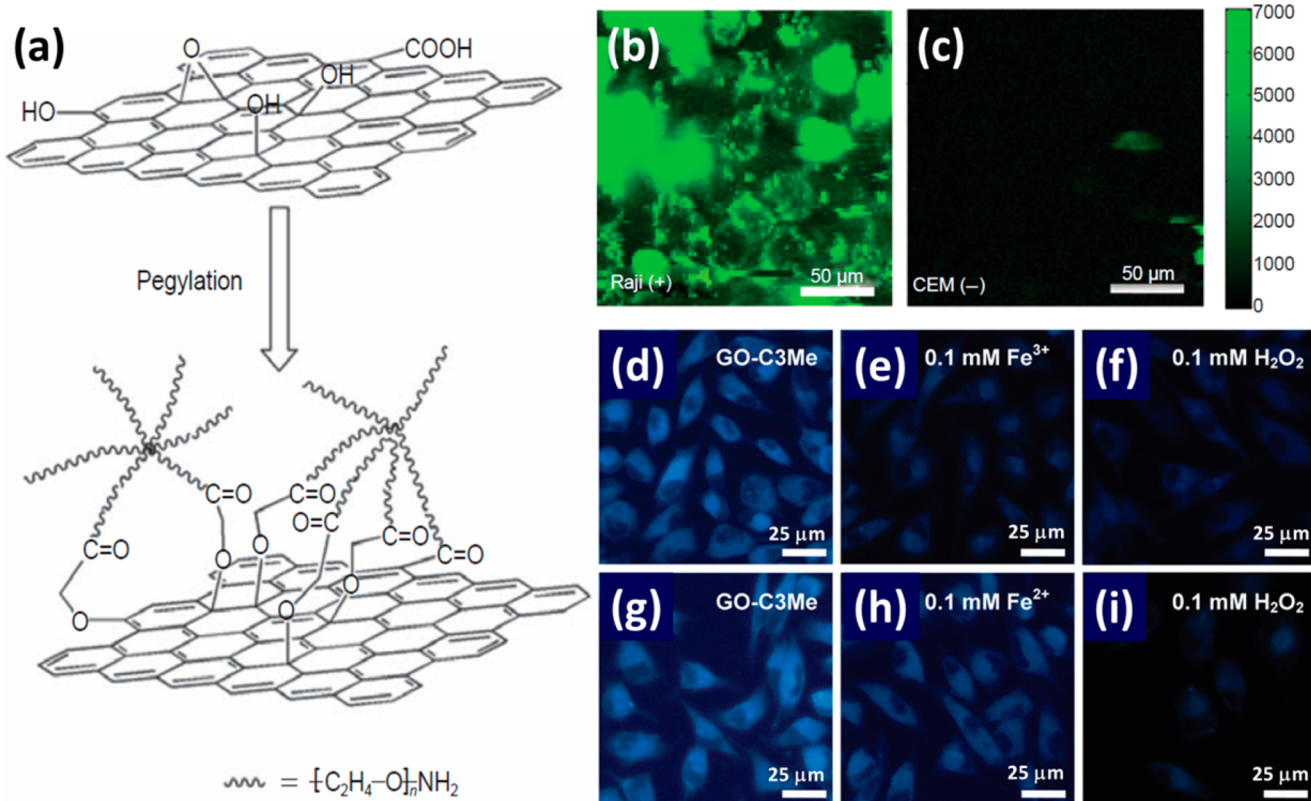


Figure 5. In vitro one-photon fluorescence imaging of cells with the intrinsic photoluminescence of GO. (a) Schematic showing the PEGylation of GO through the coupling between the carboxyl groups on GO and the amine groups in the PEG-star molecule. (b) NIR-I fluorescence image of CD20 positive Raji B-cells stained with NGO-PEG-anti-CD20 bioconjugate. (c) NIR-I fluorescence image of CD20 negative CEM T-cells stained with NGO-PEG-anti-CD20 bioconjugate. (a–c) Reprinted with permission from ref 29. Copyright 2008 Springer. (d–f) Fluorescence images of human lung carcinoma A549 cells incubated with *n*-butylamine modified GO (termed GO-C3Me) without Fe^{3+} (d), with 0.1 mM Fe^{3+} (e), and with both 0.1 mM Fe^{3+} and 0.1 mM H_2O_2 (f). (g–i) Fluorescence images of A549 cells incubated with GO-C3Me without Fe^{2+} (g), with 0.1 mM Fe^{2+} (h), and with both 0.1 mM Fe^{2+} and 0.1 mM H_2O_2 (i). (d–i) Reprinted with permission from ref 370. Copyright 2012 Royal Society of Chemistry.

nonradiative decay rate and even the band gap,^{241,243} as evidenced by fluorescence enhancement after surface passivation^{28,205} and color tuning by surface functionalization with different functional groups.^{199,205,223} Experimental results agree with theoretical studies on the band gap of carbon dots, where a combination of tight-binding and Hartree–Fock methods have been applied to reveal the dependence of carbon dot band gap on size, edge structure, and shape.²²²

Due to the lack of sp^2 graphitic carbon, nanodiamond emits fluorescence based on a completely different mechanism, arising from the presence of the defect centers. Defect centers are point defects commonly found in diamond, among which the most well-studied one is the N–V center owing to its unique and useful photoluminescence in the visible window.^{256,367} The fluorescence emission spectrum of the N–V centers in nanodiamond is usually composed of three peaks: a peak located at 576 nm assigned to the zero-phonon line (ZPL) of neutral N–V center ($\text{N}-\text{V}^0$), a peak located at 638 nm assigned to the ZPL of negatively charged N–V center ($\text{N}-\text{V}^-$), and another broad peak centered at \sim 700 nm assigned to the phonon-coupled sideband.²⁵⁴ In addition to the green and red fluorescence of nanodiamond, Gogotsi et al. have also synthesized a new type of nanodiamond with unusual blue fluorescence with an emission peak located at 450 nm, expanding the palette of available colors afforded by nanodiamond.³⁶⁸ The fluorescence of nanodiamonds is very robust against photobleaching, making them

an ideal fluorescence label for long-term tracking of interesting biomarkers and cells.^{17,369}

4.1.2. In Vitro Fluorescence Imaging with Fullerene, Graphene, Carbon Dot, and Nanodiamond. A myriad of publications have been focused on using the aforementioned carbon nanomaterials for in vitro cell imaging and tissue staining by optically exciting and detecting one-photon, Stokes fluorescence from these fluorescent tags. Fullerene and its derivatives have relatively less bright fluorescence compared to the others, and the photodynamic property of fullerene also raises concern on generating active oxygen species after photoexcitation and affecting the cell viability. Nonetheless, there are a handful of reports on using C_{60} and C_{70} as fluorescent biomarkers. Prasad et al. have studied the internalization of 750 nm fluorescence emitting C_{60} aggregates into the cytoplasm of MCF10A cells, which are normal human mammary epithelial cells, with fluorescence costaining of F-actin using FITC-phalloidin.⁶² A C_{60} –silica composite has been synthesized and studied for its photoluminescence at 600 nm under a 488 nm excitation, which was found to be proportional to the concentration of C_{60} in the silica matrix and used for staining macrophages. The fluorescence of the C_{60} –silica composite was localized in the cytoplasm, leaving a dark, unstained nuclear region and showing greater photostability than Alexa 488, a commercial molecular dye with a similar excitation profile.⁶³ Similar photostability has been found by Ke et al., who have used a 540 nm fluorescence emitting C_{70} –gallic acid bioconjugate to

stain Chinese hamster ovary (CHO) cells, living water flea tissue, and living mantle tissue and shown immunity to photobleaching under prolonged illumination and excitation compared to a commercial live cell labeling dye, calcein AM.⁶⁴ With the tunable fluorescence color of C₆₀-tetraethylene glycol (C₆₀-TEG) that has been found to depend on the concentration of C₆₀-TEG in the solution, cell staining and imaging have been performed by Chung et al. to demonstrate fluorescence imaging of HeLa cells in different excitation/emission channels with distinct colors.⁶¹

Our group has pioneered in biomedical imaging using graphene derivatives, in particular nanosized graphene oxide (NGO). In 2008, Sun et al. published the first paper on targeted cell imaging by employing the intrinsic NIR fluorescence of PEGylated NGO (named NGO-PEG, Figure 5a).²⁹ The starting material in this work, submicrometer-sized GO sheets, is broken down into much smaller pieces during PEGylation of the carboxyl functional groups that are abundant at the edges of the GO sheets, resulting in NGO-PEG with an average lateral size of ~20 nm. A much increased absorption over the entire visible and NIR range and a blue-shifted emission peak are observed during PEGylation and fragmentation of the GO sheets (Figure 4b), which can be attributed to the change of functional groups in the GO sheets as well as the reduction of average size of the NGO nanoparticles. Owing to the broad emission band of the NGO-PEG, part of the emission tail even extends to ~1000 nm in the NIR-I region (Figure 4c). To afford cell type specific fluorescence imaging, the as-made NGO-PEG is conjugated with a B-cell specific antibody Rituxan (anti-CD20) and applied for molecular imaging on both the CD20 positive Raji B-cells and the CD20 negative CEM T-cells. Fluorescence microscopic images taken in the NIR window of both cell lines clearly reveal a high degree of intrinsic NIR fluorescence from NGO-PEG selectively on the surfaces of the positive Raji B-cell (Figure 5b) and a much lower signal on the negative CEM T-cells (Figure 5c), with a positive-to-negative ratio of over 20.²⁹ The high selectivity of targeted fluorescence imaging using NGO-PEG reflects the distinct degrees of expression of CD20 on both cell lines and suggests the fluorescent NGO can be used for molecular phenotyping with sufficient sensitivity.

Zhang et al. have made a “smart” fluorescent probe with response to the concentration of Fe³⁺ ions by employing the selective fluorescence quenching properties of GO in the presence of Fe³⁺ ions.³⁷⁰ Based on this interesting property of GO, a combinational logic gate has been realized to discriminate Fe³⁺ and Fe²⁺ ions in live human lung carcinoma A549 cells. When A549 cells are stained with GO intracellularly, strong blue fluorescence at 440 nm can be found in the cell cytoplasm; strong fluorescence quenching is observed when Fe³⁺ is added to the cell incubation medium (Figure 5d–f), while cells incubated with Fe²⁺ do not show fluorescence quenching of GO until H₂O₂ is added to oxidize the Fe²⁺ ions into Fe³⁺ (Figure 5g–i).³⁷⁰ Thus, GO can not only be used as a molecular imaging probe for certain membrane receptors,²⁹ but can also afford intracellular functional imaging capability to sense the concentration of certain metal ions.³⁷⁰

With similar fluorescence emission to GO, carbon dots have also been widely applied for in vitro cell imaging. Sarkar et al. report labeling Ehrlich ascites carcinoma (EAC) cells with fluorescent carbon dots and performing microscopic imaging of the labeled cells by collecting fluorescence of the carbon dots under both UV and blue light illuminations. They find that the carbon dots exhibit strong dependence of emission wavelength on the excitation, in that the carbon dots labeled cells appear

blue-green under the UV illumination and yellowish under blue light excitation.²¹⁸ Similar excitation dependency has been found by several other groups in their cell fluorescence imaging experiments applying carbon dots derived via different physiochemical routes as intracellular fluorescent labels (Figure 6a–d).^{201,212,213,232,240,371,372} On the excitation wavelength

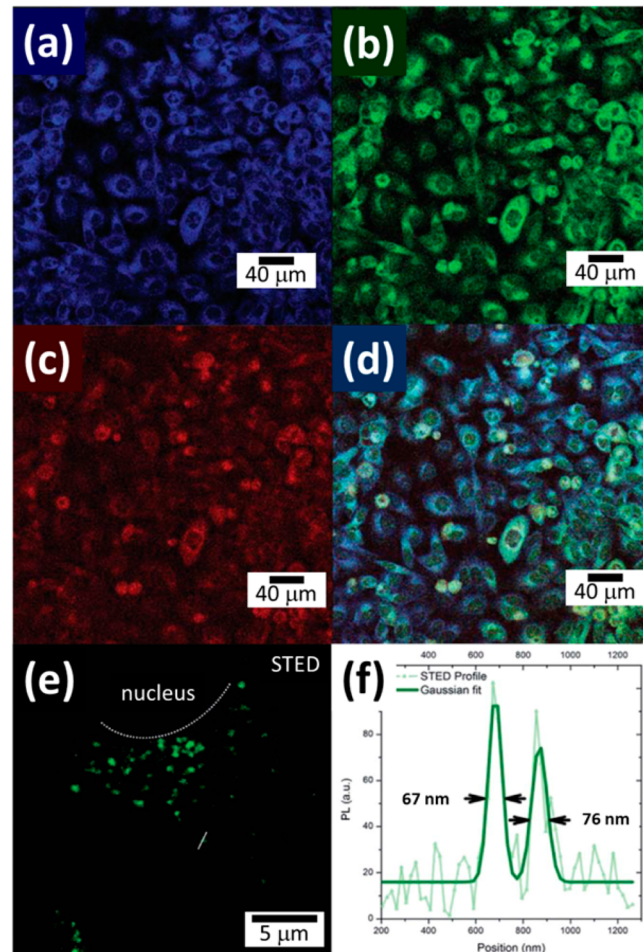


Figure 6. In vitro one-photon fluorescence imaging of cells with the intrinsic photoluminescence of carbon dots. (a–d) Laser scanning confocal microscopic fluorescence images of carbon dots labeled human hepatocellular carcinoma HepG-2 cells under excitations of 405 (a), 488 (b), and 543 nm (c). (d) Overlaid image of (a), (b) and (c). (a–d) Reprinted with permission from ref 201. Copyright 2011 Royal Society of Chemistry. (e) STED fluorescence image showing the distribution of fluorescent carbon dots in a human breast cancer MCF-7 cell. (f) Line cross-section intensity profile (light green) along the white solid line in (e) with Gaussian fitted peaks (dark green) showing the peak widths of 67 and 76 nm, respectively. (e) and (f) Reprinted with permission from ref 244. Copyright 2014 Royal Society of Chemistry.

dependent photoluminescence of graphitic carbon dots, a recent paper by Wu et al. carefully studies this phenomenon and attributes this unusual behavior to the “giant red-edge effect” resulting from the slow solvation dynamics on the same time scale as the fluorescence lifetime that is specific to the local environment of oxidized graphitic structures.³⁷³

Carbon dots can also be modified to have fluorescence responses to specific metal ions. Tian et al. report a conjugate consisting of both carbon dots and Cu²⁺-chelating molecules that gradually loses its blue fluorescence at ~500 nm with

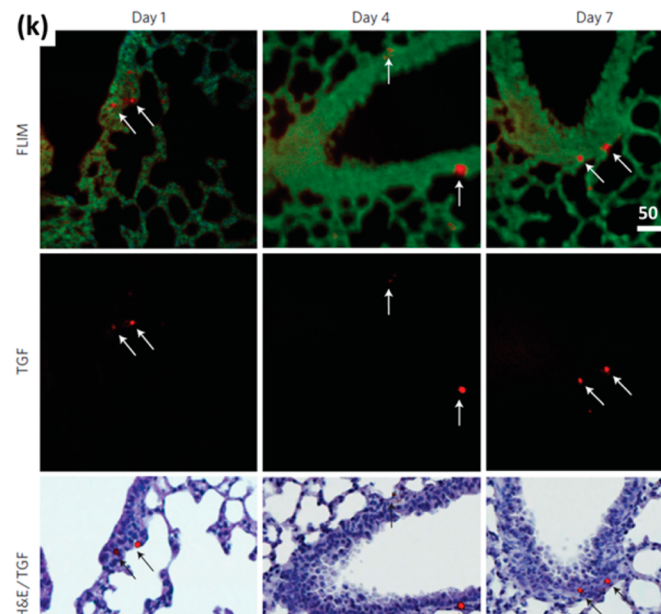
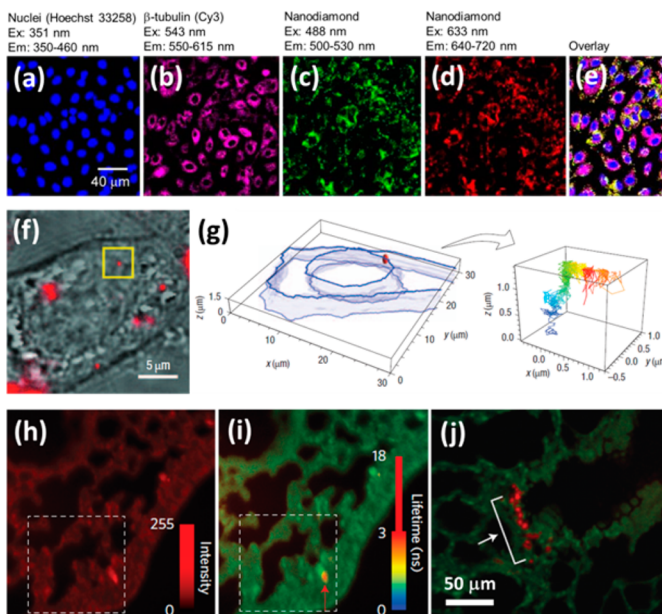


Figure 7. In vitro one-photon fluorescence imaging of cells and tissues with the intrinsic photoluminescence of nanodiamonds. (a–e) Laser scanning confocal fluorescence images of human lung carcinoma A549 cells stained with carboxylated nanodiamond with an average size of 100 nm and an incubation concentration of 100 $\mu\text{g}/\text{mL}$. Images were taken in the Hoechst 33258 channel to show the nuclei (a), in the Cy3 channel to show the β -tubulin (b), and in two other channels to reveal the distribution of nanodiamond (c, d). (e) Overlaid image of (a)–(d). (a–e) Reprinted with permission from ref 263. Copyright 2007 Elsevier. (f) Wide-field overlaid image of the bright-field optical image and fluorescence image of a live HeLa cell with 35 nm fluorescent nanodiamond particles (shown as red dots) inside the cell. (g) Three-dimensional trajectories of a single fluorescent nanodiamond particle (right) inside the yellow box in (f), with respect to the cell coordinates showing the boundaries of both the cytoplasm and the nucleus (left). (f) and (g) Reprinted with permission from ref 262. Copyright 2008 Nature Publishing Group. (h) Confocal fluorescence image of an uninjured lung tissue section showing fluorescence signal coming from both the tissue and the nanodiamond. (i) FLIM image of the same tissue section in (h), showing the nanodiamond (red dot, long fluorescence lifetime) can be distinguished from the autofluorescence background by their different lifetimes. (j) FLIM image of an injured lung tissue section, showing the engraftment of the transplanted lung stem cells labeled with nanodiamond, evidenced by the clustering of the red dots. (k) Time course FLIM (first row), TGF (second row), and H&E (third row) staining images of uninjured lung tissue sections over the course of 7 days (different columns) post transplantation of nanodiamond-labeled lung stem cells, revealing the nanodiamond-labeled lung stem cells are mainly located in the subepithelium of bronchiolar airways (indicated by white and black arrows). (h–k) Reprinted with permission from ref 17. Copyright 2013 Nature Publishing Group.

progressively increasing Cu^{2+} concentrations in the cytoplasm of cells.²³⁵ When hybridized with a stably fluorescent CdSe/ZnS core/shell quantum dot nanostructure whose red fluorescence is inert to the Cu^{2+} cations, the nanohybrid can form a dual-emission ratiometric fluorescent sensor that changes color from blue (dominated by carbon dots) to red (dominated by CdSe quantum dots) upon addition of the Cu^{2+} ions.³⁷⁴ Similar ratiometric intracellular fluorescent probes for Zn^{2+} , Fe^{3+} , S^{2-} , and superoxide (O_2^-) ions have been developed.^{375–378} Selective targeting and molecular imaging of folate receptors on the surface of cancer cells have also been made possible with folic acid conjugated carbon dots, showing intense fluorescence on the folate receptor expressing HeLa cells but not on the underexpressing normal fibroblast cells.²³⁷ Transferrin-conjugated carbon dots have shown selective targeting to HeLa cells for in vitro detection and diagnosis of cancer cells with certain phenotypes.³⁷⁹ Aptamer-conjugated carbon dots have also been reported to target and selectively label cancer cell lines while leaving the normal healthy cells largely unstained.²⁰²

Besides regular fluorescence microscopic imaging, super-resolution imaging can also be performed on carbon dot stained cells. In a recent work by Pompa et al., for the first time stimulated emission depletion (STED) microscopy is applied to reveal the subdiffraction limit distribution of fluorescent carbon dots surrounding the cell nucleus with 60–80 nm feature size (Figure 6e,f).²⁴⁴ Since thus far carbon dots have not been found

to be photoswitchable, the other super-resolution microscopy techniques such as photoactivated localization microscopy (PALM)³⁸⁰ and stochastic optical reconstruction microscopy (STORM)³⁸¹ have not been made possible on carbon dot labeled samples, but the possibility of synthesizing photoswitchable fluorescent carbon dots remains and could potentially make carbon dots more useful for biologists.

Carbon dots are considered as promising fluorescent tags based on the following reasons: First, similar to other carbonaceous nanofluorophores, carbon dots are highly photo-stable and resistive to photobleaching, as revealed by carbon dot labeled cell fluorescence imaging under prolonged illumination.²³⁴ Second, compared to semiconductor quantum dots with comparable fluorescence wavelength tunability, carbon dots do not contain any toxic elements such as heavy metals and chalcogens, eliminating the toxicity concerns for staining and imaging live organisms with carbon dots.³⁸² Third, a recent study by Sun et al. argues the size similarity between carbon dots (~ 5 nm) and fluorescent proteins (FPs, ~ 4 nm), advocating carbon dots as ultracompact fluorescent probes with extremely small footprints.³⁸³

The strong and stable fluorescence of nanodiamonds has allowed people to use them to stain cells and tissues, and to track the intracellular trafficking of each individual nanodiamond particle. One of the early works on intracellular nanodiamond imaging incubates the ~ 700 nm emitting nanodiamond with

293T human kidney cells and performs 3D fluorescence-based optical sectioning of a single cell with fluorescence confocal microscopy to confirm the intracellular uptake of nanodiamond particles.²⁵⁵ Excitation dependent fluorescence emission has also been found in a nanodiamond-stained cell imaging experiment (Figure 7a–e), suggesting possibly a similar cause as for carbon dots.²⁶³ Owing to the superior photostability with minimum photobleaching under continuous excitation, single fluorescent nanodiamond particles can be tracked to give 2D in-plane trajectories and 3D volumetric trajectories, revealing the Brownian diffusion motion inside the cell cytoplasm (Figure 7f,g).^{254,262} Based on fluorescence staining of early endosomes and colocalization analysis, Treussart et al. conclude that the cellular uptake pathway of 25 nm nanodiamonds may not be endosome-associated endocytosis, but that of 46 nm nanodiamonds is mainly via clathrin-mediated endocytosis.^{265,266} This finding has been confirmed by studying the trajectory of a single nanodiamond particle as it interacts with the cell.³⁸⁴

In a more recent study, Chang and Yu et al. have shown fluorescent nanodiamonds can be used for labeling, identifying, and tracking transplanted lung stem/progenitor cells over a course of 7 days, exploiting the photostable fluorescence of nanodiamond in the >590 nm range under an excitation of 515–560 nm.¹⁷ Moreover, the fluorescence lifetime of nanodiamond is significantly longer (up to 20 ns) than those of many endogenous and exogenous fluorophores (<10 ns), allowing for straightforward identification of nanodiamond from background tissue autofluorescence and other fluorescent immunostains using fluorescence lifetime microscopy (FLIM) and time-gated-fluorescence (TGF) imaging (Figure 7h,i). The transplanted lung stem cells labeled with nanodiamond are successfully identified in highly differentiated lung tissues, where they are found to be mainly located in the subepithelium of bronchiolar airways (Figure 7k) and form clustered engraftment in injured lung tissues (Figure 7j).¹⁷ The same TGF imaging by exploiting the long fluorescence lifetime has been used for imaging nanodiamond-labeled cancer cells in both a microfluidic device and mouse ear blood vessels.³⁶⁹

4.1.3. In Vivo Fluorescence Imaging with Fullerene, Graphene, Carbon Dot, and Nanodiamond. Reports on in vivo fluorescence imaging using fullerene and its derivatives as fluorescent labels are few to the best of our knowledge, presumably due to the relatively low fluorescence quantum yields of fullerenes as well as their potential toxicity to the administered organism. Lee et al. have reported on using hyaluronated C₆₀ particles for tumor targeting and in vivo fluorescence imaging on tumor-bearing mice. They have found that hyaluronate can bind to overexpressed CD44 receptors on certain cancer cells, and the hyaluronate–C₆₀ bioconjugate allows targeted in vivo tumor fluorescence imaging by detecting the deep red fluorescence of hyaluronated C₆₀ at 710 nm under an excitation of 635 nm. The targeting effect is demonstrated as a higher fluorescence signal from the CD44 positive HCT-116 tumor (a human colorectal carcinoma model) than the CD44 negative KB tumor (a human cervical cancer model).³³²

Sun et al. report the first in vivo fluorescence imaging in live mice using their photoluminescent carbon dots.³¹ With subcutaneously injected carbon dots under the dorsal skin, bright fluorescence within the injected region can be clearly visualized as both green (525 nm) and red (620 nm) colors under 470 and 545 nm excitations, respectively. Migration of intradermally injected carbon dots to axillary lymph nodes can be observed after injection into the front extremity by tracking the

fluorescence of carbon dots.^{31,247} When the photoluminescent carbon dots are administered intravenously, the injected carbon dots are found in the bladder and urine at merely 3 h post injection, indicating an excretion pathway of renal clearance for these small carbon dots with an average diameter of 4–5 nm, which is smaller than the renal filtration cutoff size (Figure 8a–

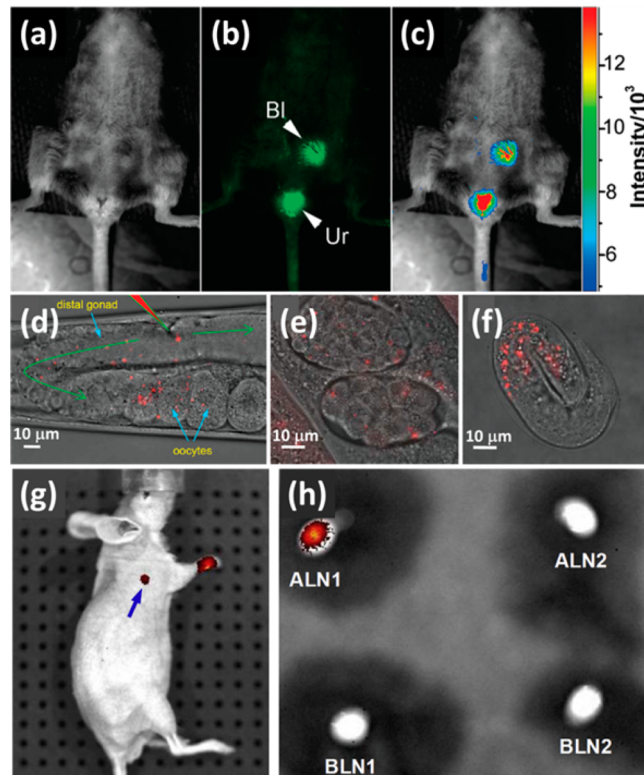


Figure 8. In vivo one-photon fluorescence imaging of mice and *C. elegans* with the intrinsic photoluminescence of carbon dots and nanodiamonds. (a–c) White light (a), fluorescence (b), and color-coded overlaid (c) images of a mouse intravenously injected with fluorescent carbon dots. Fluorescence from carbon dots can be observed in the bladder (Bl) and the urine (Ur). (a–c) Reprinted from ref 31. Copyright 2009 American Chemical Society. (d–f) Epifluorescence and differential interference contrast (DIC) overlaid images of *C. elegans* after microinjection of fluorescent nanodiamonds. The injection site is shown as the red triangle and the migration paths of injected nanodiamonds are shown as green arrows in the lower magnification image (d), while higher magnification images of the early (e) and late (f) embryos exhibit obvious fluorescence from the migrated nanodiamonds. (d–f) Reprinted from ref 267. Copyright 2010 American Chemical Society. (g) White-light and fluorescence overlaid image of a mouse intradermally injected with NIR emitting nanodiamonds in the right front paw. Fluorescence can be observed from both the injection site and the proximal right axillary lymph node (indicated by a blue arrow). (h) Ex vivo fluorescence images of dissected right axillary lymph node (ALN1), left axillary lymph node (ALN2), right brachial lymph node (BLN1), and left brachial lymph node (BLN2), showing fluorescence only found in the dissected right axillary lymph node (ALN1). (g) and (h) Reprinted with permission from ref 269. Copyright 2012 Elsevier.

c).³⁸⁵ In a similar way, renal excretion of carbon dots with average sizes of 2–5 nm has been found by Liu et al., where carbon dots are derived from MWCNTs by mixed acid treatment.¹⁹⁰

Besides visible fluorescence emitting carbon dots, Lee et al. synthesized NIR fluorescent carbon dots with an emission wavelength of ~800 nm from exfoliation and acid treatment of carbon fibers, and used the NIR emitting carbon dots for deep

tissue *in vivo* fluorescence imaging of a mouse intravenously administered with these carbon dots. Fluorescence signals from deep tissues and organs can be observed from the side and front views of the injected animal, and the accumulation of carbon dots in the kidney and liver evidenced by an increased signal in these organs agrees with previous reports on the pharmacokinetic pathway of these materials.²²⁰ NIR emitting carbon dots have also been used to track their migration to popliteal lymph node post injection of the carbon dots into the hind paw.²¹⁵

In vivo fluorescence imaging of nanodiamond was first performed in living *Caenorhabditis elegans* (*C. elegans*) rather than mammals, owing to the simple and well-defined anatomy of *C. elegans*, as well as the high transparency of its body throughout its life cycle that allows easy interrogation of the nanodiamond distribution by fluorescence microscopy. In a study performed by Chang et al.,²⁶⁷ *C. elegans* worms are fed with fluorescent nanodiamonds, and the nanodiamonds can be tracked down the digestive system and are found primarily in the intestinal cells. Continuous fluorescence imaging and tracking of microinjected nanodiamond into the gonad of an adult hermaphrodite reveal the downstream migration and delivery of injected nanodiamond into the distal gonad, oocytes, and early and late stage embryos sequentially (Figure 8d–f). This finding suggests that the injected nanodiamonds can be passed down to the next generation without causing detectable stress to the worms.²⁶⁷ In another study done by the same group,²⁶⁹ fluorescent nanodiamonds were injected intraperitoneally into a live mouse and the distribution of the injected nanodiamonds inside the peritoneal cavity can be tracked over time by monitoring the fluorescence emission in the NIR window at 780 ± 10 nm. Axillary lymph nodes light up and become visible as well owing to migration of nanodiamonds from the intradermal injection site at the front paw of a live mouse (Figure 8g,h).²⁶⁹ Shirakawa et al. devised a new imaging system called selective imaging²⁶⁸ based on the unique property of the N–V center in nanodiamond that the fluorescence of the N–V center highly depends on the ground state spin configuration, which is regulated by electron spin magnetic resonance, while the background fluorescence does not. By using this new technique, long-term background-free fluorescence imaging of *C. elegans* and mouse has been realized with a greater signal-to-background ratio.²⁶⁸

In summary, all aforementioned carbonaceous nanomaterials exhibit fluorescence in the visible and traditional NIR windows from one-photon excitation and down-converted emission. It is worth mentioning that the mechanisms accounting for the fluorescence emission are different for these materials, where the fluorescence of fullerenes originates from the molecular orbitals of delocalized π -electrons over the entire closed spherical shell, the fluorescence of graphene oxide and carbon dots is from quantum confinement of nanosized graphitic domains as well as the edge states, and that of nanodiamonds is a direct result of the presence of many N–V centers. The fluorescence emission has allowed for various *in vitro* and *in vivo* fluorescence imaging applications. However, the relatively short fluorescence emission wavelengths of these materials make them mostly applicable for *in vitro* imaging of cultured cells and thin tissue sections, whereas *in vivo* fluorescence imaging is hampered by the strong scattering associated with these shorter-wavelength fluorescence photons. As a result, most of the *in vivo* imaging examples performed with these materials are limited to *C. elegans* owing to its transparency and small size, and mice with superficial penetration depth and suboptimal imaging resolution. Nonetheless, in section 4.2 we will focus on the one-photon, down-converted fluorescence of

SWCNTs in the much longer wavelength, NIR-II window, which allows for much deeper penetration and crisper imaging resolution of *in vivo* live mouse fluorescence imaging.

4.2. One-Photon Fluorescence Imaging of Single-Walled Carbon Nanotubes (SWCNTs) in the Second Near-Infrared (NIR-II) Window

4.2.1. Origin of Band-Gap NIR-II Fluorescence of SWCNTs. As we have discussed earlier, CNTs can be categorized as SWCNTs and MWCNTs. Since the electronic and optical properties of all CNTs are primarily determined by covalent intralayer bonding between carbon atoms rather than multilayer interactions between different graphitic walls, an MWCNT can be considered as a coaxial bundle of multiple SWCNTs.³⁸⁶ Therefore, in this section SWCNTs will be taken as an example for the discussion of their unique band gap fluorescence in the NIR-II window (that is, a subregion in the electromagnetic spectrum with wavelengths ranging from 1000 to 1700 nm) and the related biological imaging applications.^{14,15,87}

A single-walled carbon nanotube can be pictured as a single graphene sheet rolled up seamlessly into a nanocylinder with its diameter ranging from less than 1 nm to a few nanometers.^{387,388} Due to the quantum confinement along the transverse direction of a single carbon nanotube, which can be considered as a quasi-one-dimensional nanomaterial, SWCNTs feature very sharp maxima of electronic density of states (DOS) called van Hove singularities in their energy band diagrams.³⁸⁹ The energies of van Hove maxima of SWCNTs in a band diagram are mainly dependent on the diameter of the nanotube and the chiral angle at which the specific nanotube is rolled up from a single graphene sheet with 2D honeycomb structure (Figure 9a). Rolling up the graphene sheets with different chiral angles results in nanotubes

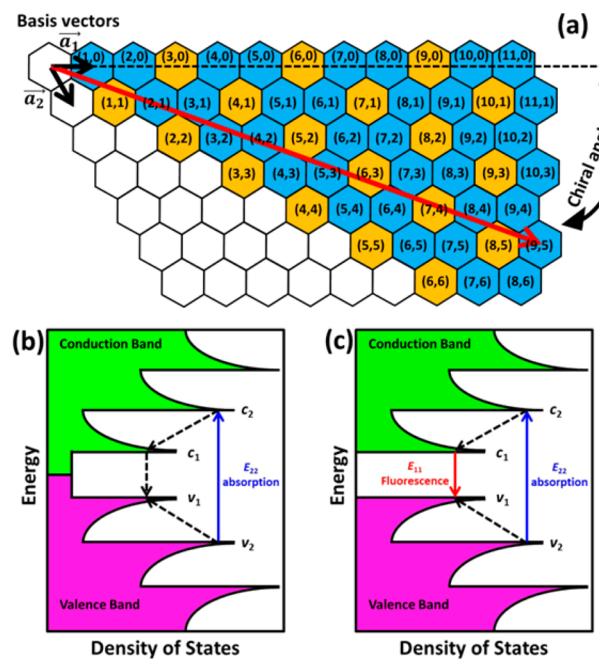


Figure 9. Physical and electronic band structures of SWCNTs. (a) Honeycomb structure of graphene showing different roll-up vectors (red arrow) result in different (n,m) indices, or chiralities (numbers labeled in each hexagon). (b) Band diagram of a metallic SWCNT, showing no fluorescence emission due to the continuous DOS near the Fermi level. (c) Band diagram of a semiconducting SWCNT, showing fluorescence emission after excitation.

with different chiralities, which are determined by two indices n and m that define the roll-up vector as follows:²⁷

$$\text{roll-up vector } (n, m) = n\vec{a}_1 + m\vec{a}_2$$

where the length of the roll-up vector is the circumference of the nanotube. Based on simple geometry, one can derive the diameter of a nanotube based on its chirality (n, m):

$$d = \frac{\sqrt{3} d_{\text{C-C}}}{\pi} \sqrt{n^2 + nm + m^2}$$

where $d_{\text{C-C}}$ denotes the bond length between a pair of neighboring carbon atoms in the hexagonal graphitic lattice and is ~ 0.142 nm.

Different chiralities also result in semiconducting [$(n - m) \bmod 3 = 1, 2$] and metallic SWCNTs [$(n - m) \bmod 3 = 0$], while only semiconducting SWCNTs have photoluminescence upon photon absorption. This is because for metallic SWCNTs the density of states is not zero at the Fermi level, so the excited state after absorbing a photon can relax nonradiatively to the valence band (Figure 9b).²⁷ From the color coding in Figure 9a, it can be seen that two-thirds of all SWCNT chiralities are semiconducting and thus fluorescent (Figure 9c). Since only semiconducting SWCNTs have the electronic structures that support the photoluminescence process, for biomedical fluorescence imaging in the NIR-II window we will only focus on semiconducting SWCNTs. Nonetheless, as we will discuss in section 4.3.3, metallic SWCNTs can also have sufficient imaging contrast for biological imaging using transient absorption microscopy.³¹⁵

The band diagram of a semiconducting SWCNT shown in Figure 9c is worth revisiting in greater detail to fully understand the NIR-II photoluminescence process, which can be described in three consecutive steps:

1. First, an SWCNT absorbs a photon with the photon energy matching the band gap of the E_{22} transition, which is the difference in energy between the second valence band v_2 and the second conduction band c_2 . The absorption of this excitation photon leads to the excitation of an electron (blue arrow in Figure 9c), which used to be in the second valence band, to the second conduction band, while leaving a hole behind. The excited electron and the remaining hole form a bound pair called an exciton that is held by the exciton binding energy, which is usually around 400 meV for semiconducting carbon nanotubes.³⁹⁰

2. Second, after the excitation process and the separation of an electron and a hole to form a bound exciton, both the electron and the hole undergo rapid nonradiative relaxations to the lowest level in both valence and conduction bands, i.e., the v_1 and c_1 bands in Figure 9c.³⁹¹

3. Lastly, the bound pair of electron and hole travel together along the length of the nanotube through diffusion until they recombine radiatively to give off a fluorescence photon with its energy corresponding to the band gap across E_{11} minus the exciton energy; alternatively, this electron/hole pair can encounter a defect on the sidewall or a chemically induced hole before it radiatively recombines, and the energy will be released in a nonradiative Auger process, resulting in quenching of the fluorescence.²⁷⁸ Given the measured exciton excursion range is ~ 90 nm for semiconducting carbon nanotubes independent of the chirality, in order to afford sufficiently bright fluorescence emission for imaging purposes, there should be minimum structural disruption to the pristine SWCNTs during

surface functionalization of carbon nanotubes, as has been pointed out in section 3.1.

According to the preceding description of the photoluminescence process, we know that the absorbed photons should have energy matching the band gap of the E_{22} transition and the emitted photons matching that of the E_{11} transition. The fact that band gap energy mainly depends on the diameter and chirality of an SWCNT allows us to engineer the desired absorption and fluorescence wavelengths of the SWCNT fluorophores by growing nanotubes with different diameter distributions. The photoluminescence-versus-excitation plot (PLE plot) allows us to study the number of distinct semiconducting chiralities in a mixture of synthesized SWCNTs and their diameter distribution with reference to band gap energies in wavelength. In a typical PLE plot, each individual circle has a unique excitation wavelength and a unique emission wavelength, which correspond to the E_{22} transition energy and the E_{11} transition energy, respectively (Figure 10). SWCNTs

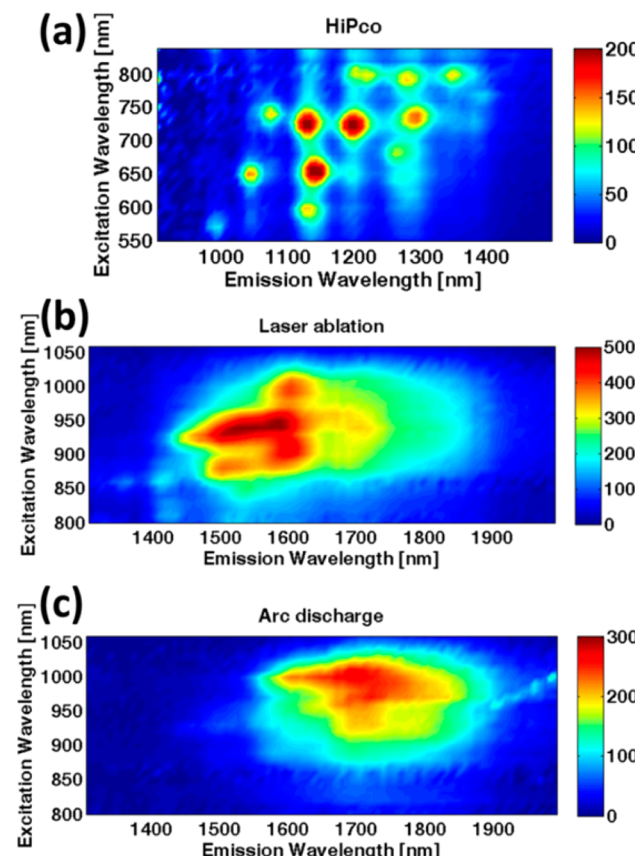


Figure 10. PLE plots of HiPco (a), laser ablation (b), and arc discharge (c) SWCNTs, with progressively increasing diameter distribution.

from different synthetic routes have different ranges of diameter distribution, resulting in different ranges of photoluminescence wavelengths of 900–1400 nm for high-pressure CO (HiPco) decomposed SWCNTs (Figure 10a), 1500–1700 nm for laser ablation SWCNTs (Figure 10b), and 1600–1900 nm for arc discharge SWCNTs (Figure 10c). This optical property with unusual emission wavelengths has made SWCNTs the first practical materials with NIR-II fluorescence for biomedical imaging, ushering in a new era of NIR-II imaging with a variety of materials later.^{392–396} Owing to the relatively higher fluorescence quantum yield of HiPco SWCNTs than laser ablation SWCNTs,

as well as the easier dispersion and surface functionalization of HiPco SWCNTs, HiPco SWCNTs have been the most commonly used CNTs for NIR-II fluorescence imaging.^{15,30,294,397} Nonetheless, the larger diameter SWCNTs such as laser ablation SWCNTs with longer fluorescence emission wavelengths are preferable for biological imaging owing to lower scattering³⁹⁸ and less interference with tissue autofluorescence,³⁹⁹ using photodetectors or cameras with sufficient quantum efficiency in the range of 1500–1900 nm.

As discussed above, the fluorescence of SWCNTs is excitonic in nature and the exciton diffusion can be arrested by surface defect sites and become nonradiative.²⁷⁸ This excitonic nature of SWCNT fluorescence makes it sensitive to its chemical environment as well as the length of the nanotube. Owing to the many factors that could lead to fluorescence quenching of SWCNTs, SWCNTs generally exhibit a low quantum yield on the order of 0.1–1%,^{87,400,401} significantly lower than organic synthetic dyes, fluorescent proteins (FPs), and quantum dots (QDs) in the shorter-wavelength, visible, and NIR-I regions.⁴⁰² To determine the fluorescence quantum yield of SWCNTs in the long-wavelength, NIR-II window, polymethine dyes such as IR-26 and Styryl-13 with similar emission wavelengths are usually used as the reference. However, for both IR-26 and Styryl-13 dyes, their absolute quantum yields have been disputed (2.0%⁴⁰³ vs 11%⁴⁰⁴ for Styryl-13; and 0.5%⁴⁰⁵ vs 0.05%⁴⁰⁶ for IR-26). It is recommended to use IR-26 as the reference NIR-II fluorophore with a reported quantum yield of 0.1% in a recent thorough study.⁴⁰⁷ In this case, it is worth noting that previous quantum yield measurements of SWCNTs based on higher reported values for IR-26 need to be scaled back by a factor of 5. Even in this case, the low autofluorescence background in the NIR-II window has readily allowed fluorescence imaging with nanotubes and other fluorophores by us and others. A major intrinsic factor contributing to the low fluorescence quantum yield of SWCNTs is the optically forbidden nature of the lowest-energy “dark” exciton that has even symmetry in wave function and is thus nonradiative.^{400,408} Extrinsic factors accounting for the low quantum yields include bundling of photoluminescent semiconducting nanotubes with metallic ones,⁴⁰⁹ defects on the sidewalls and the short lengths,^{30,278,410} conductive and semiconductive substrates in contact with nanotubes,⁴¹¹ external electric field,⁴¹² and potential fluctuations in their environments (e.g., single-molecule reactive species such as acid, base, oxygen, and diazonium compounds,^{278,404,413,414} or trapped charges on insulating substrates⁴¹⁵). The presence of metallic SWCNTs in bundles causes effective nonradiative decay of photon-excited electron/hole pairs.⁴⁰⁹ Shortened length of SWCNTs and increased number of defect sites on the sidewalls of the carbon nanotube can increase the chance of nonradiative recombination of excitons due to its mean diffusion distance of ~90 nm.^{30,278} External electric field can reversibly decrease the fluorescence emission of SWCNTs, with the quenching efficiency dependent on the specific nanotube structure and chirality.⁴¹² Although the conversion efficiency of absorbed photons into emitted fluorescence photons remains quite low for SWCNTs,⁸⁷ the strong absorption of light in the NIR-I window by SWCNTs and the highly efficient photothermal conversion of SWCNTs resulting from nonradiative decay of absorbed photon energy have led to photosensitizers in the NIR window for efficacious photothermal therapy.^{13,34,416}

In order to make SWCNTs suitable for fluorescence imaging with sufficient NIR-II photoluminescence emission, a considerable amount of effort has been paid to enhance the intrinsic

fluorescence emission of SWCNTs by applying field enhancement near the surface of metal substrate,^{417–419} removing the possible quencher from the surface of nanotubes^{404,420} and reducing the degree of bundling.⁴⁰⁹ We have mentioned in section 3.1. that the surfactant exchange method helps avoid direct damage to the nanotube sidewalls during the PL–PEG assisted sonication process, resulting in biocompatible, PEGylated SWCNTs with fewer defect sites, longer lengths, and most importantly, significantly higher fluorescence quantum yield in the NIR-II window (Figure 11a).³⁰ We have found that bundling of SWCNTs results in nonradiative energy transfer to nonfluorescent metallic CNTs in a similar way to the aromatic stacking effect that quenches the fluorescence of the host molecule. Density gradient centrifugation has enabled efficient debundling of photoluminescent, semiconducting SWCNTs from metallic nanotubes and allowed us to extract SWCNTs with on average longer length distribution, better individualization, and higher fluorescence quantum yield (Figure 11b,c).⁴⁰⁹ Liu et al. have successfully shown the blocking of substrate-induced nonradiative decay of nanotube excitons and the recovery of NIR-II fluorescence of SWCNTs by separating the SWCNTs from the quenching substrate by a self-assembly monolayer.⁴²¹ To avoid single-molecule oxidative quenching species such as the oxygen molecules, the Papadimitrakopoulos group synthesized an aliphatic (dodecyl) analogue of flavin mononucleotide, FC12, as an oxygen-excluding capping agent that can form helical ribbons wrapping on the sidewalls of semiconducting SWCNTs.⁴⁰⁴ Due to the tight helical wrapping of FC12 molecules around an individualized SWCNT, the chemisorbed oxygen species become energetically unfavorable (Figure 11d–g), and as a result the SWCNT retains its strong intrinsic photoluminescence with a measured quantum yield of ~20% in the NIR-II window without significant quenching from the oxygen molecules,⁴⁰⁴ which are known to be strong quenchers of SWCNTs in acidic or neutral environment.^{413,422} Despite the record-high fluorescence quantum yield achieved by excluding the oxygen molecules, this method based on the use of hydrophobic FC12 capping molecules does not allow for making a brightly emissive solution of water-soluble SWCNTs for biological applications. A different method aiming at reducing the oxidative potential near the surface of SWCNTs via the use of strong reductants, such as dithiothreitol (DTT) and Trolox, has been employed to consume the oxygen molecules and donate electrons to hole-dominated trap sites while brightening the intrinsic NIR-II fluorescence of DNA-wrapped SWCNTs dispersed in water (Figure 11h,i).⁴²⁰

Besides the strategy of minimizing various exogenous factors that lead to the fluorescence quenching of SWCNT, there have also been methods of enhancing the apparent fluorescence quantum yields via external modulation of the local electric field and the radiative decay rate of carbon nanotubes. Our group reports the first working example of metal-enhanced NIR-II fluorescence of SWCNTs by placing the PEGylated HiPco SWCNTs on a plasmonic gold film comprised of gold island nanostructures.^{417,423} An increase of apparent fluorescence quantum efficiency of up to 10-fold has been found (Figure 12a–d) and attributed to the radiative lifetime shortening of SWCNTs as a result of resonance coupling between the nanotube emission in the NIR-II window and the plasmon modes supported by the gold substrate, which is also the strongest in the NIR-II window. To our surprise, study of the distance dependence of the NIR-II fluorescence enhancement reveals a short quenching distance for SWCNTs, and the bare

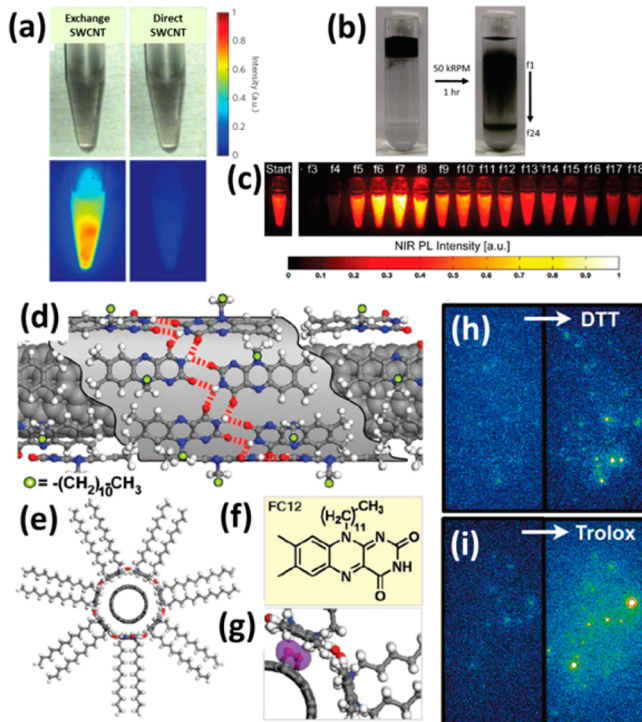


Figure 11. Brightening of the intrinsic NIR-II fluorescence of SWCNTs by eliminating various quenching factors. (a) A surfactant exchange method gives rise to PL-PEG coated biocompatible SWCNTs with bright NIR-II fluorescence emission owing to longer average length and fewer defects (bottom left), in comparison to SWCNTs directly sonicated with PL-PEG (bottom right). Note that both solutions were concentration-balanced, exhibiting similar darkness that indicates similar carbon content (top row). Reprinted with permission from ref 30. Copyright 2009 Nature Publishing Group. (b, c) A density gradient centrifugation method (b) allows for extraction of more efficiently debundled and individualized SWCNTs in fractions f6 to f8 with higher NIR-II fluorescence quantum yields (c). (b, c) Reprinted from ref 409. Copyright 2010 American Chemical Society. (d–g) Brightening of SWCNT fluorescence in organic solvent using an oxygen-excluding capping molecule, FC12. The top view and size view of FC12 molecules wrapping on the sidewall of an SWCNT in a helical pattern are shown in (d) and (e), with (f) showing the chemical structure of one FC12 molecule and (g) showing the unfavorable formation of 1,4-endoperoxide on the nanotube sidewall after oxidation due to the tight adsorption of the FC12 molecules. Hydrogen bonding between neighboring FC12 molecules is shown as red dashed lines while the hydrophobic, alkyl side chains are shown as green spheres. Carbon, hydrogen, nitrogen, and oxygen atoms are shown in gray, white, blue, and red, respectively. (d–g) Reprinted with permission from ref 404. Copyright American Association for the Advancement of Science. (h, i) Brightening of the NIR-II fluorescence of DNA-wrapped SWCNTs immobilized on a quartz coverslip and immersed in an aqueous solution, showing obvious recovery of NIR-II fluorescence upon addition of reducing agents including DTT (h) and Trolox (i). (h, i) Reprinted from ref 420. Copyright 2011 American Chemical Society.

gold film without any additional spacer coating turns out to afford the highest fluorescence enhancement for PL-PEG coated SWCNTs (Figure 12e,f),⁴¹⁷ in good agreement with the short exciton quenching distance independently found by Peng et al.⁴²⁴ Besides the metal substrates that afford NIR-II fluorescence enhancement of SWCNTs, Kato et al. have reported the use of a photonic crystal nanocavity for strong enhancement of nanotube photoluminescence with an estimated enhancement factor between 50 and 200.⁴²⁵ While the plasmonic

films and photonic crystals can only afford NIR-II fluorescence enhancement on a solid substrate, Setaro et al. have achieved up to 20-fold NIR-II fluorescence enhancement in a suspension of SWCNTs by using micelle-stabilized gold nanorods, affording the capability of facilely integrating the NIR-II fluorescence enhanced SWCNTs into a biological environment (Figure 12g).⁴¹⁹ Another free-standing fluorescence enhancing method has been reported by Pichler et al. by selectively filling ferrocene molecules into the cavity of size-matching chiralities such as (8,6) and (9,5).⁴²⁶

With much improved quantum yields through the various aforementioned means, the NIR-II fluorescence emitting SWCNTs have shown great potential as contrast agents in a wide variety of in vitro and in vivo biological applications. In vitro fluorescence imaging using SWCNTs as extracellular and intracellular labels^{294,427,428} has the benefits of resistance to photobleaching, low autofluorescence background, and the large Stokes shift. It is worth highlighting that the exceptionally large Stokes shift of hundreds of nanometers for SWCNTs helps avoid the detection channel crosstalk and makes laser line cleanup much less of a problem than organic fluorophores in the visible and NIR-I windows. This benefit has allowed for much easier implementation of an NIR-II microscopy setup with SWCNTs using filters with lower stop-band optical density and less sharp cutoff edge. In vivo fluorescence imaging in the NIR-II region benefits mainly from the much longer emission wavelengths than the traditional fluorophores, leading to the much reduced light scattering, lower endogenous autofluorescence, and improved imaging contrast with deeper tissue penetration.^{14,15} In sections 4.2.2 and 4.2.3 we will focus on the unique applications offered by SWCNTs for in vitro and in vivo biomedical imaging.

4.2.2. SWCNTs for In Vitro NIR-II Fluorescence Imaging.

As discussed above, SWCNTs have great promise for use as effective biomarkers for cell imaging due to their excellent properties such as low cytotoxicity, high photostability, absence of quenching, and photobleaching in cells if functionalized properly.^{95,297,298,429} Although SWCNTs covalently conjugated with organic fluorophores of shorter emission wavelengths had been imaged with confocal fluorescence microscopy in cells,^{337,430} a groundbreaking piece of work demonstrating cell imaging by detecting the intrinsic fluorescence of SWCNTs was achieved for the first time by Weisman et al., who incubated the Pluronic surfactant stabilized SWCNTs with macrophages and successfully imaged the intracellular distribution of fluorescent SWCNTs that were phagocytosed into the cell cytoplasm during the incubation (Figure 13a).⁴³¹ The intracellular distribution of internalized SWCNTs has been found as many bright, highly localized regions in the NIR-II fluorescence image, which are believed to be small phagosomes inside the cells. This finding provides a great opportunity for observing biological interactions between SWCNTs and biological systems through the direct detection of the intrinsic fluorescence of SWCNTs. The same group has shown that the intrinsic fluorescence of SWCNTs can be used to map the distribution of intravenously injected SWCNTs inside ex vivo rabbit liver tissues after euthanizing the rabbits and collecting the organs.⁴³²

With the pioneering works by the Weisman group showing SWCNTs as potential NIR-II labels for biological imaging via nonspecific binding (NSB), in order to turn SWCNTs into a fluorescent tag for molecular imaging, the NSB nature has to be suppressed⁴³³ while the surface of SWCNTs has to be modified with specific targeting ligands. To this end, our group shows for the first time that through noncovalent surface functionalization

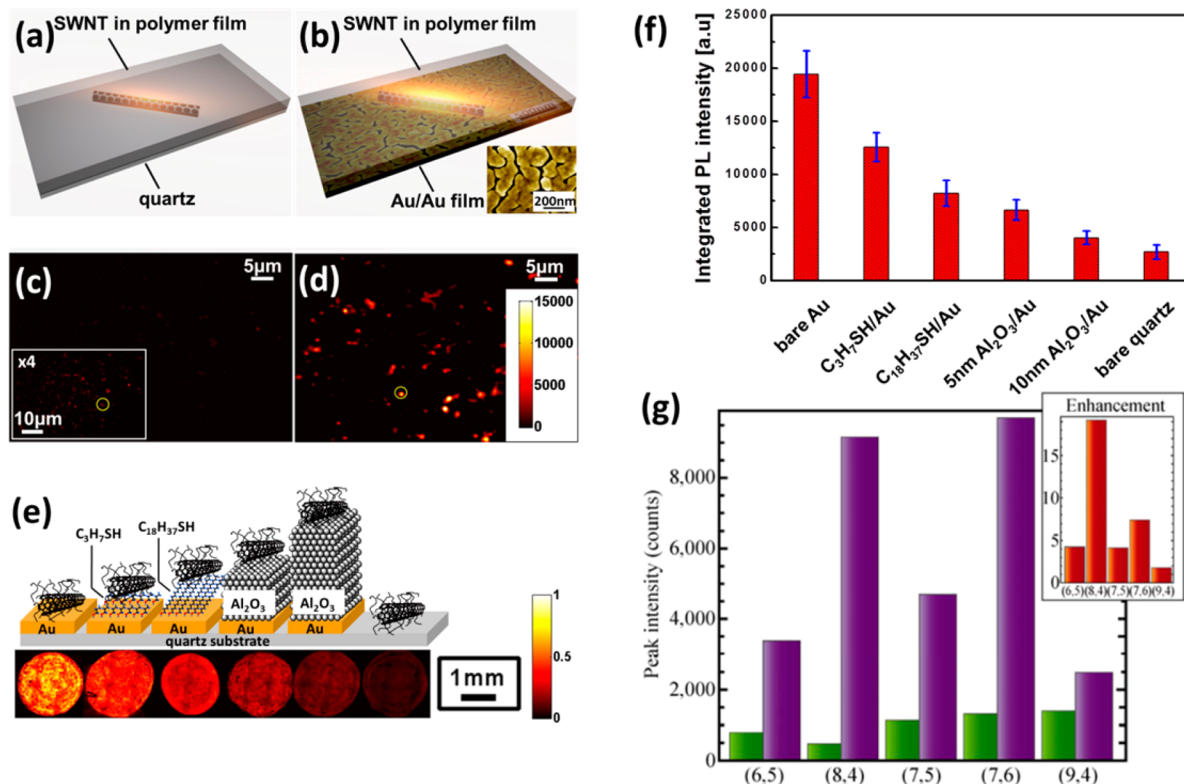


Figure 12. Enhancement of the intrinsic NIR-II fluorescence of SWCNTs by plasmonic nanomaterials. (a–f) NIR-II fluorescence enhancement of SWCNTs on gold substrates. NIR-II photoluminescence images of PL–PEG functionalized SWCNTs spin-coated on the gold plasmonic film (d) show much higher fluorescence intensity than those on the bare quartz substrate (c), as illustrated in the respective schematic drawings (b, a). NIR-II fluorescence enhancement of PEGylated SWCNTs on the gold substrate is found to decay monotonically versus the nanotube–gold distance (f), as illustrated by the schematic in (e). (a–f) Reprinted from ref 417. Copyright 2010 American Chemical Society. (g) Measured NIR-II fluorescence intensity of various nanotube chiralities for CTAB-solubilized SWCNTs (green bars) and the SWCNT–Au nanorod complexes (purple bars) in aqueous suspension. The inset shows the calculated enhancement factors for all measured chiralities. Reprinted with permission from ref 419. Copyright 2013 Springer.

of SWCNTs with PL–PEG(5400 Da)–NH₂, the PEG chain sufficiently blocks the NSB while rendering the nanotubes water-soluble (see section 3.1 for more details on the noncovalent PEGylation method developed by our group), and the free amine group allows for further conjugation with different targeting ligands such as Rituxan and Herceptin, which specifically target the CD20 and HER2 receptors, respectively (Figure 13b).²⁹⁴ NIR-II fluorescence imaging of B-cell lymphoma Raji cells (CD20 positive) and T-cell lymphoma CEM cells (CD20 negative) has clearly revealed the uniformly stained Raji cells with strong NIR-II fluorescence, and by strong contrast, barely stained CEM cells with little NIR-II signal (Figure 13c,d). A positive/negative ratio of ~55 has been found with the SWCNT–Rituxan conjugate, suggesting high specificity of the nanotube-based molecular fluorescence imaging probe and successfully blocked NSB of the SWCNTs. Similarly, the HER2 positive BT-474 cells and HER2 negative MCF-7 cells both incubated with SWCNT–Herceptin bioconjugate exhibit a staining specificity of ~20, revealed by the NIR-II fluorescence images of both cell lines (Figure 13e,f). This work, for the first time, proves the concept that properly functionalized SWCNTs can be used as NIR-II fluorescent tags decreased signal and an increased noise up the possibility of using SWCNTs for various *in vitro* biological imaging applications.

To improve the sensitivity of NIR-II fluorescence-based molecular imaging and lower the detection limit of certain biomarkers using functional SWCNTs, our group has applied the

fluorescence brightening and enhancement methods as aforementioned in section 4.2.1. for cell imaging. Welsher et al. have conjugated the brightly fluorescent SWCNTs prepared via the surfactant-exchange method with arginine-glycine-aspartic acid (RGD) peptide, which specifically targets the $\alpha_1\beta_3$ integrins on the human brain glioblastoma U87-MG cells.³⁰ Both the $\alpha_1\beta_3$ integrin positive U87-MG cells and the $\alpha_1\beta_3$ integrin negative MDA-MB-468 cells are treated with RGD-conjugated exchange SWCNTs and directly sonicated SWCNTs, and NIR-II fluorescence microscopy of different cell lines treated with SWCNTs prepared with different methods reveals a high positive NIR-II signal from the $\alpha_1\beta_3$ integrin positive U87-MG cells treated with SWCNT–RGD conjugate (Figure 13g), while all other combinations show negligible NIR-II fluorescence under the same imaging conditions (laser power, magnification, and exposure time) due to low expression level of $\alpha_1\beta_3$ integrins, low fluorescence quantum yield, or both (Figure 13h–j). As a further step, Hong et al. have applied the plasmonic enhancing gold substrate for specifically targeted cell imaging also using the brightly fluorescent SWCNT–RGD conjugate.⁴²⁷ A good selectivity has been found between the $\alpha_1\beta_3$ integrin positive U87-MG cells and the $\alpha_1\beta_3$ integrin negative, human breast cancer MCF-7 cells (Figure 13k,l), while the nanostructured gold film, when in touch with the SWCNTs binding to the receptors on the outside of the cell membrane, enhances the NIR-II fluorescence signals by about 9-fold compared to the bare quartz film (Figure 13m,n).⁴²⁷ This strong NIR-II fluorescence

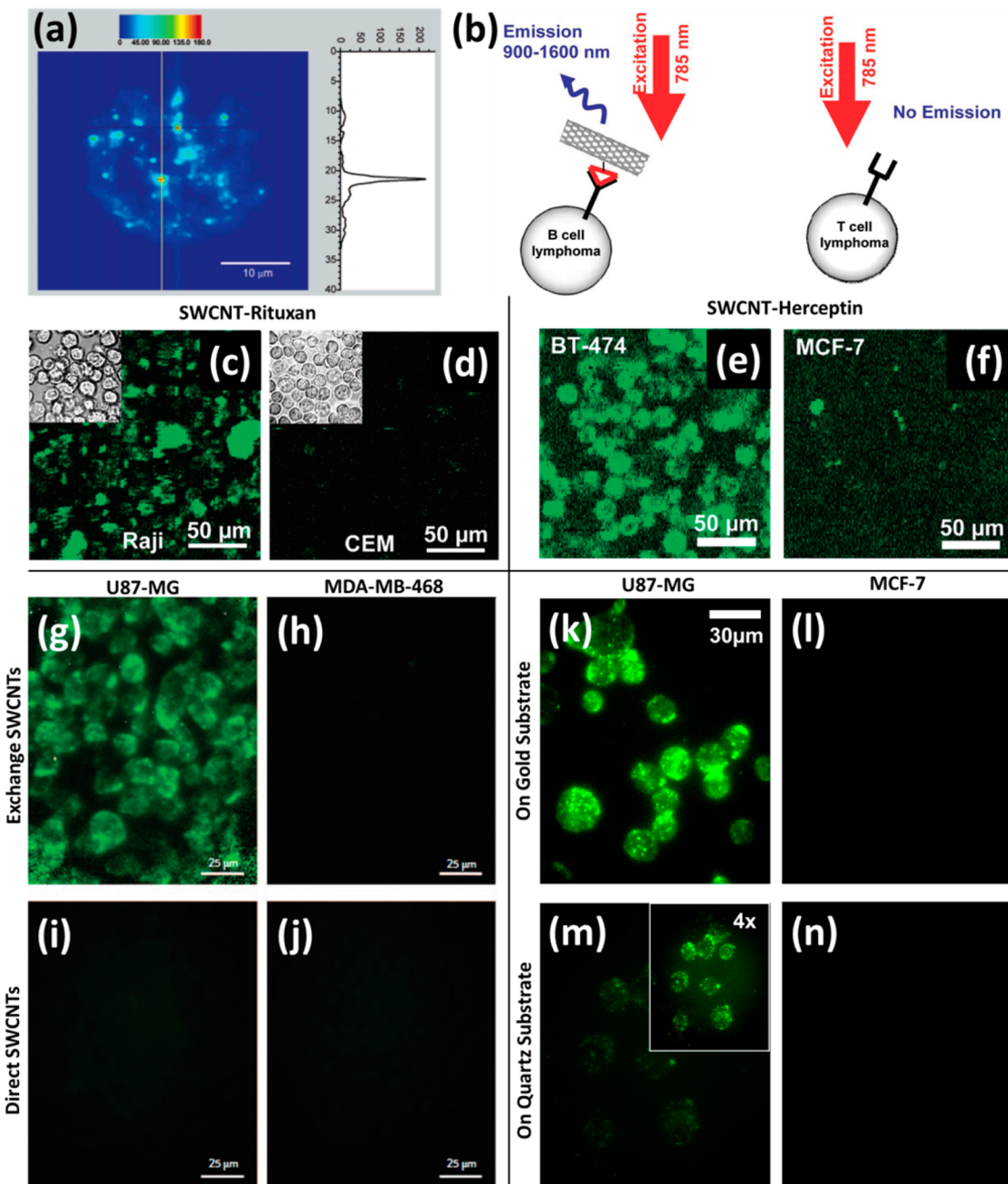


Figure 13. In vitro NIR-II fluorescence imaging of cells with SWCNTs. (a) Microscopic image of a macrophage cell after incubating with SWCNTs solubilized by Pluronic surfactant. Strong NIR-II fluorescence is detected as localized bright spots in the macrophage cell, suggesting efficient uptake of SWCNTs by the cell. Reprinted from ref 431. Copyright 2004 American Chemical Society. (b) Schematic drawing showing that the SWCNT–Rituxan conjugate can selectively bind to the CD20 expressing B-cell lymphoma Raji cells for fluorescence detection in the NIR-II window while leaving the CD20 negative T-cell lymphoma CEM cells unstained. (c, d) NIR-II fluorescence images of CD20 positive Raji cells (c) and CD20 negative CEM cells (d) both incubated with SWCNT–Rituxan, by detecting the intrinsic band gap NIR-II fluorescence emission from SWCNTs. (e, f) NIR-II fluorescence images of HER2 positive BT-474 cells (e) and HER2 negative MCF-7 cells (f) both incubated with SWCNT–Herceptin, by detecting the intrinsic band gap NIR-II fluorescence emission from SWCNTs. (b–f) Reprinted with permission from ref 294. Copyright 2008 American Chemical Society. (g–j) NIR-II fluorescence images of $\alpha_1\beta_3$ integrin positive U87-MG cells (g, i) and $\alpha_1\beta_3$ integrin negative MDA-MB-468 cells (h, j) incubated with SWCNT–RGD conjugates made from the surfactant exchange method (g, h) and the direct sonication method (i, j). (g–j) Reprinted with permission from ref 30. Copyright 2009 Nature Publishing Group. (k–n) NIR-II fluorescence images of $\alpha_1\beta_3$ integrin positive U87-MG cells (k, m) and $\alpha_1\beta_3$ integrin negative MCF-7 cells (l, n) incubated with SWCNT–RGD conjugates and placed on the plasmonic gold substrates (k, l) and bare quartz substrates (m, n). The inset of (m) shows the same field of view as (m) with the intensity scaled up by 4-fold. (k–n) Reprinted with permission from ref 427. Copyright 2011 John Wiley & Sons.

enhancing effect is attributed to the close proximity of the membrane-bound SWCNTs to the surface of the gold plasmonic film, allowing us to acquire microscopic cell fluorescence images with better image contrast and quality under an even shorter

exposure time (300 ms with gold enhancement versus 1–3 s without gold). The much shorter exposure time provides a great opportunity of using SWCNTs for high-frame-rate dynamic imaging with fast feedback in an *in vitro* setting by coating the cell

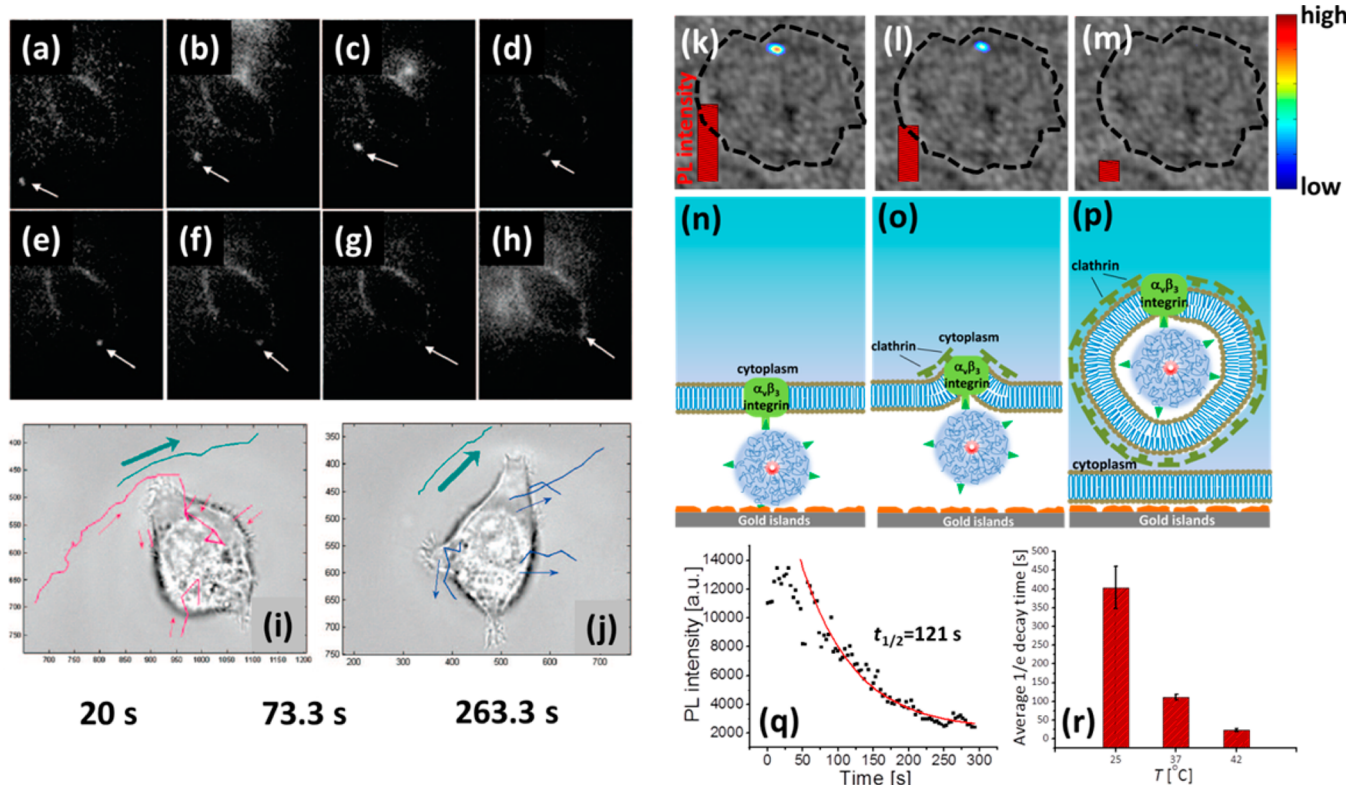


Figure 14. In vitro tracking and imaging of SWCNTs interacting with cells using NIR-II fluorescence. (a–h) NIR-II fluorescence microscopy images showing the interaction of a single nanotube (indicated by the white arrow) with a live NIH-3T3 fibroblast cell (the outline of the cell can be seen from the negative contrast). (i, j) Selected trajectories showing endocytosis (red curves in (i)), exocytosis (blue curves in (j)), and convective diffusion driven by the perfusion system (green curves in both images). The arrows with corresponding colors indicate the direction of the motion in each trajectory. (a–j) Reprinted from ref 447. Copyright 2008 American Chemical Society. (k–p) NIR-II fluorescence/bright-field overlaid images (k–m) and corresponding schematic drawings (n–p) showing the endocytosis process of a single carbon nanotube (SWCNT–RGD) bound on the membrane of a U87-MG cell through the strong interaction between the RGD moiety on the nanotube conjugate and the $\alpha_5\beta_3$ integrin on the cell plasma membrane. The NIR-II images were taken at 20 (k), 73.3 (l), and 263.3 s (m) after the temperature increased to 37 °C and endocytosis started, with the corresponding schematic drawings (n–p) underneath each NIR-II image. (q) NIR-II fluorescence intensity of this particular single carbon nanotube plotted as a function of time (black squares), with a 1/e decay time of 121 s based on fitting to a first-order exponential decay (red curve). (r) Bar chart showing the average exponential decay time of the single nanotube NIR-II fluorescence at three different temperatures, suggesting the internalization process is energy-dependent. (k–r) Reprinted with permission from ref 449. Copyright 2012 Nature Publishing Group.

culture and imaging chamber with a nanostructured gold film. Owing to the improved sensitivity of NIR-II fluorescence-enhanced molecular imaging afforded by the gold substrate, the detection limit is significantly reduced from 1.2 nM to 48 pM for the staining concentration of SWCNTs, corresponding to an estimated total of ~10 SWCNTs per cell for unambiguous identification of the positive U87-MG cells.⁴²⁷

Understanding the cellular uptake pathway and the intracellular trafficking mechanism of nanomaterials is of central importance for in vitro applications involving the use of nanomaterials for efficient drug and gene delivery.^{434–437} CNTs have been widely employed as intracellular transporters for delivering a wide variety of cargo molecules including proteins,³¹⁶ siRNA,^{288,438} DNA,^{96,316} and drug molecules,^{18,439} as we will discuss in more detail in section 5. Despite the efficacious delivery of cargo molecules using SWCNTs, how each individual carbon nanotube enters the cell cytoplasm remains a long-debated open question in the scientific community. There have been two distinct live cell internalization pathways for the cellular uptake of CNTs in general, including the energy-dependent clathrin/receptor mediated endocytosis,^{95,96,288,316,337,440–443} and the energy-independent insertion/diffusion process across the cell plasma mem-

brane.^{430,444–446} The intrinsic NIR-II emission of SWCNTs under wide-field fluorescence microscopy has provided an elegant way of tracking the internalization process of each individual nanotube, taking advantage of the stable NIR-II fluorescence of SWCNTs that barely photobleaches under prolonged excitation and imaging, and the low fluorescence background in the NIR-II window from endogenous intracellular species that may interfere with the detection of fluorophores with shorter emission wavelengths. Strano et al. studied the interaction of individual SWCNTs in a perfusing solution with immobilized NIH-3T3 fibroblast cells adhering to the Petri dish. By tracking the stable fluorescence of SWCNTs over time, they have recorded trajectories of over 10 000 individual SWCNTs involved in cellular uptake in real time (Figure 14a–h), which allowed identification of internalization steps of SWCNT including membrane adsorption, confined diffusion, endocytosis (Figure 14i), convective diffusion during intracellular trafficking, exocytosis (Figure 14j), and desorption.⁴⁴⁷ These different mechanical steps comprising the complete nanotube–cell interaction pathway have been identified and investigated using the single particle tracking (SPT) method by analyzing the in-plane 2D mean squared displacement (MSD) versus time, which has characteristic power-law dependence on the lag time for

different types of motion. This work presents the first direct observation of the cell internalization process of individualized SWCNTs based on dynamic NIR-II microscopy and reveals the cell internalization pathway as membrane receptor mediated endocytosis evidenced by the distinct dynamic signatures of confined diffusion followed by active intracellular transport.⁴⁴⁷ In a later work done by the same group, endocytosis rates of SWCNTs were evaluated as a function of both the nanotube length and the incubation time.⁴⁴⁸ The endocytosis rate was shown to be size-dependent with a maximum rate achieved by SWCNTs with an average length of ~320 nm and an effective radius near 25 nm, with a measured endocytosis rate constant of 10^{-3} min⁻¹, significantly higher than that of gold nanoparticles (10^{-6} min⁻¹). Based on these findings the authors have developed a quantitative model that explains the correlation between endocytosis rate and geometric influence of nanoparticles using the NIR-II fluorescence assisted single particle tracking method.⁴⁴⁸

In addition to the 2D in-plane tracking of individual SWCNTs as demonstrated by the Strano group, our group has exploited the ultrasensitive dependence of gold-enhanced NIR-II fluorescence of SWCNTs on the distance between nanotubes and the plasmonic gold surface.⁴¹⁷ We have shown in Figure 12f that, owing to the short quenching distance of nanotubes and the efficient resonance coupling between the nanotube excitons and the gold surface plasmons, the surface-enhanced NIR-II fluorescence of SWCNTs decays rapidly as the nanotube–gold distance increases by only a few nanometers, providing us with a “nanoscopic ruler” that measures nanometer displacement away from the gold surface. Since the thickness of the cell plasma membrane (~10 nm) is on the same order of magnitude as the exponential decay distance of the fluorescence enhancement of SWCNTs (~6 nm), the plasmonic ruler allows us to probe the transmembrane motion of single CNTs with nanometer accuracy in the axial direction, which is perpendicular to and points away from the surface of the plasmonic substrate.⁴⁴⁹ We have shown that, in a typical experiment, a single, membrane-bound SWCNT is sandwiched between the cell membrane and the underlying gold film and can be identified with polarization dependence measurement of its photoluminescence intensity.⁴⁵⁰ Upon the increase of incubation temperature from 4 to 37 °C, the transmembrane motion of this particular nanotube can be tracked in real time by recording its fluorescence enhancement change as a function of time (Figure 14k–p). The decrease of the NIR-II fluorescence reflects the motion of SWCNT moving away from the underlying gold film, while the time constant of the fluorescence decay indicates the internalization rate of the nanotube (Figure 14q). We have found that the internalization rate is temperature-dependent (Figure 14r) with an extracted activation barrier of 120 ± 37 kJ mol⁻¹ for the transmembrane motion, suggesting the endocytic pathway for the cellular entry process of single carbon nanotubes.

The exceptionally stable NIR-II fluorescence and negligible autofluorescence background in the NIR-II window have made SWCNTs unique fluorescent labels suitable for the study of intracellular dynamics of certain motor proteins of interest, allowing biologists to make new findings that are otherwise impossible with traditional fluorophores. Recently a collaborative study between two European groups and a research group in the United States has achieved high-resolution imaging of intracellular fluctuations via detection of NIR-II fluorescence from SWCNTs.⁴²⁸ In this work, the NIR-II luminescent SWCNTs are targeted to kinesin-1 motor proteins in fibroblast-like COS-7

cells through the covalent interaction between SWCNTs wrapped with the short DNA oligonucleotides and the kinesin motor protein extended by a C-terminal HaloTag that specifically binds to its counterpart in nanotube-sidewall-bound DNA (Figure 15a). The SWCNT-labeled kinesins move along the microtubule tracks, which form an interconnected network embedded in the actin cytoskeleton. Therefore, by tracking the trajectories of NIR-II fluorescent SWCNTs, it is possible to interrogate the dynamics of cytoskeleton driven by myosins (Figure 15b). High-resolution microscopic imaging is performed

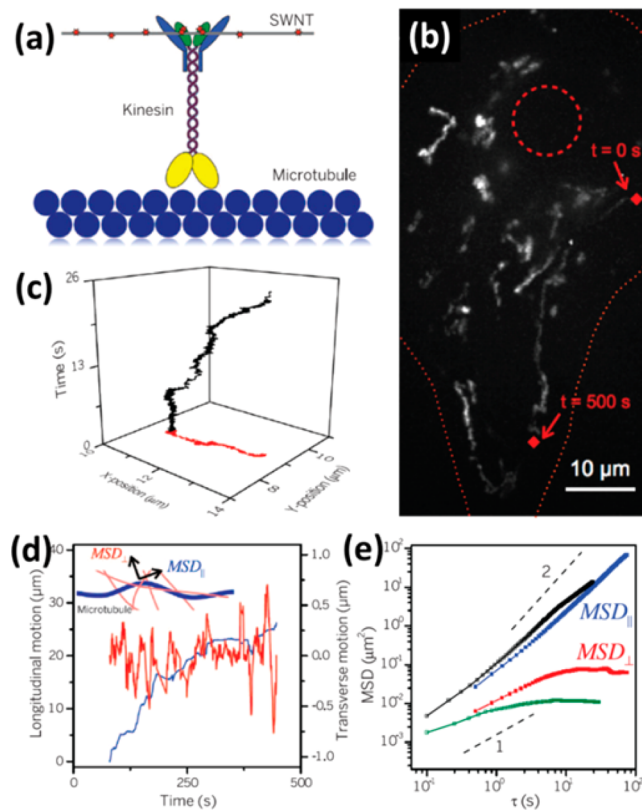


Figure 15. In vitro tracking and imaging of SWCNT-labeled kinesin motor proteins in living cells using NIR-II fluorescence. (a) Schematic showing a single carbon nanotube bound to the kinesin motor protein through covalent interaction with the HaloTag (red stars). Kinesins move along the microtubule filaments unidirectionally. (b) A 2D maximum intensity projection showing the trajectories of SWCNT-labeled kinesin motor proteins obtained by NIR-II fluorescence microscopy. The red diamonds mark the start and end positions of a 500-s trajectory. The nucleus and cell peripheries are marked by the red dashed lines. (c) Trajectory of an SWCNT-labeled kinesin with a high temporal resolution of 5 ms. The black trajectory shows the location of this particular kinesin in 2D (x and y axes) as a function of time (z axis), while the red trajectory is a 2D projection of the black trajectory to the 2D x–y plane. (d) Kinesin motor trajectory decomposed into longitudinal (blue curve) and transverse (red curve) motions, where the longitudinal motion shows obvious unidirectional transport along the microtubule filament, while the transverse motion shows random fluctuation due to the myosin-driven cytoskeletal stirring. (e) MSD analysis of the longitudinal motion (blue squares) and transverse motion (red squares) of SWCNT-labeled kinesin motor proteins in untreated cells, and that of the longitudinal motion (black squares) and transverse motion (green squares) of kinesin in cells treated with 50 mM blebbistatin to block the myosin activity. Reprinted with permission from ref 428. Copyright 2014 American Association for the Advancement of Science.

to track the motions of the kinesin-1 motor proteins inside the cytoplasm with an unprecedented temporal resolution of 5 ms per frame (Figure 15c). The authors claim that the nonblinking and nonphotobleaching nature of the NIR-II fluorescence of SWCNTs is the key to the acquisition of ultrashort time dynamics, since it is possible to increase the excitation power without causing any degradation of the NIR-II signal from SWCNTs up to hours of illumination. Dynamic NIR-II fluorescence microscopy allows the authors to observe both the active transport of kinesin motor proteins along the microtubule filaments and the random fluctuation of the cytoskeleton caused by “stirring” of cytoplasmic myosins, via decomposition of the observed SWCNT trajectory into the longitudinal convective diffusion (with a power-law exponent of 2) and the transverse random walk (with a power-law exponent of 1) (Figure 15d,e).

From the aforementioned examples showing the *in vitro* cell imaging applications with SWCNTs, one can see that SWCNTs with intrinsic fluorescence emission in the NIR-II window have many unrivaled advantages compared to traditional fluorophores such as small organic molecules. The superior photostability without any blinking or photobleaching has allowed for long-term imaging and tracking of single carbon nanotubes or SWCNT-labeled biomolecules. The rich surface chemistry offered by noncovalent PEGylation has enabled molecular cell imaging using functionalized SWCNTs with low background and high sensitivity. The only shortcoming of the NIR-II fluorescent SWCNTs comes from the low fluorescence quantum efficiency, which can be partly overcome by elimination of quenchers and introducing fluorescence enhancing species. Potential future directions of SWCNTs as cell fluorescent labels include multicolor molecular imaging with different chiralities of carbon nanotubes that have spectrally resolvable emission wavelengths in the NIR-II window,^{33,34} super-resolution NIR-II fluorescence imaging by introducing photoswitchable quenchers for SWCNTs,^{451,452} and molecular phenotyping of intracellular proteins and membrane biomarkers combined with the use of plasmonic enhancing substrate or nanoparticles to achieve high specificity and sensitivity.^{453–455}

4.2.3. SWCNTs for *In Vivo* NIR-II Fluorescence Imaging.

For fluorescence-based *in vivo* imaging of live animals, the penetration depth and imaging clarity are usually limited by the intrinsic optical properties of the turbid biological tissue, the spectral features of the fluorescent labels, and the interaction between the fluorescence emitters and the biological tissue. Three main factors contribute to the decreasing contrast-to-noise ratio (CNR, sometimes referred to as signal-to-noise ratio, SNR, or signal-to-background ratio, SBR) of fluorescence imaging as the depth increases: photon scattering, photon absorption, and tissue autofluorescence. Scattering happens as the fluorescence photons deviate from the original paths in a turbid biological medium, converting some of the signal photons to noise. Absorption occurs when the traveling fluorescence photons are captured by water or endogenous chromophores in the tissue without reemission, leading to a decreased amount of signal photons. Tissue autofluorescence comes from endogenous fluorophores that spontaneously emit photons upon illumination, leading to an increased amount of noise photons. As one can see, all these three factors lead to a decreased signal and an increased noise, and thus a lower CNR.

The large Stokes shift allows SWCNTs to be excited in the first biological transparent window (the NIR-I window, 750–1000 nm) and detected in the second transparent window (the NIR-II

window, 1000–1700 nm). There are several salient benefits offered by the NIR-II fluorescence of SWCNTs, which come threefold:

1. Owing to the inverse power law relationship between the wavelength and scattering of photons, the NIR-II fluorescence photons have much less scattering than traditional fluorescence in the visible and NIR-I windows. The empirical formulas for reduced scattering coefficients of different tissue types versus wavelength are shown as follows, where all of them exhibit an inverse power law relationship while the exponent varies for different tissues and tissue phantom (Figure 16a):^{456–460}

$$\mu'_s(\text{skin})/\text{mm}^{-1} = 0.11(\lambda/\mu\text{m})^{-4} + 1.61(\lambda/\mu\text{m})^{-0.22}$$

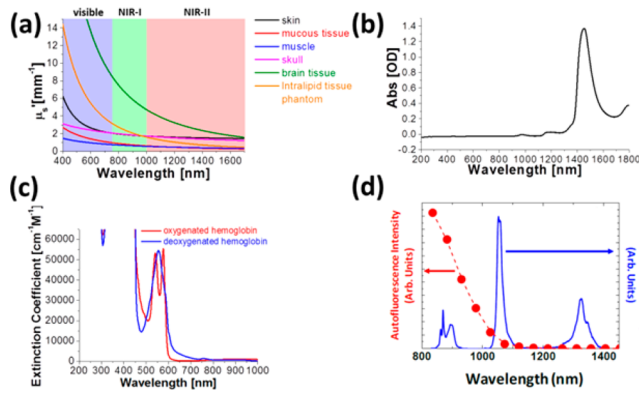


Figure 16. Challenges of deep tissue fluorescence imaging and the call for NIR-II window. (a) The reduced scattering coefficient, μ'_s , is plotted as a function of wavelength in the range of 400–1700 nm for various tissue types including the skin (black), the mucous tissue (red), muscle (blue), skull (pink), the brain tissue (green), and the tissue phantom, Intralipid (orange). Please note that the plots for skin, mucous tissue, muscle, and skull are derived from human samples, while that for brain is derived from mouse sample.^{456–460} The ranges of visible, NIR-I, and NIR-II windows in the spectrum are also shaded in light blue, green, and red, respectively. (b) Absorption spectrum of water (H_2O) in a cuvette with a 1 mm path length, featuring strong vibrational overtone absorption bands in the 1400–1500 nm region and the >1700 nm region. (c) Absorption spectra of oxygenated hemoglobin (red) and deoxygenated hemoglobin in the range of 200–1000 nm, showing minimum absorbance beyond 650 nm. (d) Autofluorescence spectrum of mouse food pellet under an 808 nm excitation (red curve), showing negligible autofluorescence beyond 1100 nm. This autofluorescence spectrum is compared with the fluorescence emission spectrum of neodymium-doped strontium fluoride nanoparticles (blue curve), showing the NIR-II fluorescence of certain nanomaterials is the key to helping achieve truly autofluorescence-free *in vivo* fluorescence imaging. (d) Reprinted with permission from ref 399. Copyright 2015 Springer.

(where the two terms are attributed to Rayleigh scattering and Mie scattering, respectively; human)

$$\mu'_s(\text{mucous tissue})/\text{mm}^{-1} = 0.61(\lambda/\mu\text{m})^{-1.62} \quad (\text{human})$$

$$\mu'_s(\text{muscle})/\text{mm}^{-1} = 0.56(\lambda/\mu\text{m})^{-1.045} \quad (\text{human})$$

$$\mu'_s(\text{skull})/\text{mm}^{-1} = 1.72(\lambda/\mu\text{m})^{-0.65} \quad (\text{human})$$

$$\mu'_s(\text{brain tissue})/\text{mm}^{-1} = 4.72(\lambda/\mu\text{m})^{-2.07} \quad (\text{mouse})$$

$$\mu'_s(\text{tissue phantom})/\text{mm}^{-1} = 1.6(\lambda/\mu\text{m})^{-2.4} \quad (\text{Intralipid})$$

There are a few conclusions we can draw from these formulas: First, for all biological tissues and the tissue phantom (1% Intralipid), the amount of scattering decreases as a function of wavelength, due to the negative exponents on wavelength. Second, the larger the absolute amplitude of the exponent, the greater the dependence of scattering on wavelength. Therefore, one can see that the brain tissue has a much greater dependence of scattering on wavelength than other tissues such as the muscle, indicated by a much larger amplitude of the wavelength exponent (-2.07) than the muscle (-1.045) in the empirical formulas of scattering coefficients. Therefore, compared to imaging in other tissues and organs, deep tissue imaging in the brain by collecting fluorescence in the NIR-II window is expected to benefit from a much greater reduction of scattering. Third, the 1% Intralipid mimics the brain tissue better than other tissues, evidenced by a similar wavelength exponent (-2.07 for brain tissue and -2.4 for Intralipid), which can also be testified by comparing the shape of scattering curves for Intralipid (orange) and brain tissue (green) in Figure 16a.

2. The NIR-II window has low photon absorption by the endogenous chromophores. The main contributors to the endogenous absorption of photons are water and hemoglobins (including both oxygenated and deoxygenated hemoglobins). Water molecules have strong absorption in the 1400–1500 and >1700 nm regions due to the vibrational overtones (Figure 16b),⁴⁶¹ and the high percentage of water in almost any living organism precludes imaging in these two spectral windows. On the other hand, hemoglobin molecules, being the most abundant chromophores in mammals, absorb intensely in the visible window with multiple absorption bands extending to ~ 650 nm (Figure 16c).⁴⁶² Therefore, two optically transparent windows can be identified purely based on the absorption properties of the biological tissue, the 650–1400 nm range, and the 1500–1700 nm range, which cover the red end of the visible window, the NIR-I window, and part of the NIR-II window.

3. The chance for endogenous biological molecules to have autofluorescence decreases monotonically with increasing wavelengths.⁴⁶³ Autofluorescence is most commonly found in the major internal organs and bodily fluids, which contain a significant amount of fluorescent biomolecules such as chlorophyll, NAD(P)H, flavins, porphyrins, and collagen.^{464–466} In a recent work by Jaque García et al., the autofluorescence spectrum of a chlorophyll-containing diet is studied to reveal a monotonic decrease of autofluorescence intensity as wavelength increases (Figure 16d). It has been found that the food intake induced autofluorescence becomes negligible beyond 1100 nm, and *in vivo* imaging with significantly reduced autofluorescence can be performed on mice with NIR-II fluorophores emitting at 1340 nm.³⁹⁹

Due to strong scattering and absorption of emitted fluorescence photons as well as the severe interference from autofluorescent photons, it remains a big challenge for the traditional fluorescence imaging method to reach a penetration depth of $>150\ \mu\text{m}$ with sufficient resolving power.⁴⁶⁷ The discussion in the preceding paragraphs has pointed out the necessity of using longer-wavelength fluorescence to probe fine anatomical structures and interrogate the exquisite functions in living organisms by reducing the amount of scattering, absorption, and autofluorescence. Single-walled carbon nanotube, being the first material with practical NIR-II fluorescence emission, has been utilized in small animal imaging experiments to demonstrate the power of NIR-II fluorescence imaging.

Our group was the first to apply biocompatible SWCNTs for *in vivo* live mouse imaging in the NIR-II window.³⁰ A few major concerns that limited the applicability of SWCNTs had to be addressed to impart these NIR-II fluorescent labels with desired optical and biological properties. First, both the NIR-II fluorescence quantum yield and the *in vivo* pharmacokinetics are highly dependent on the method and degree of surface functionalization, calling for the use of proper capping agents to prepare the suitable SWCNT solution for *in vivo* administration. Second, as-made SWCNTs are a mixture of semiconducting and metallic nanotubes with various chiralities, with the metallic and off-resonance chiralities not contributing to the overall fluorescence signal. Third, the fluorescence quantum efficiency is generally low compared to many commercial fluorophores in the shorter-wavelength regions. Our lab has been taking on these challenges over the past few years, paving a way for the emerging field of *in vivo* NIR-II fluorescence imaging.

Our efforts on improving the surface functionalization of water-soluble and biocompatible SWCNTs have led to the first report on NIR-II *in vivo* fluorescence imaging in mice using SWCNTs. Before our work the Weisman group reported on NIR-II fluorescence imaging of SWCNTs inside *Drosophila* larvae, which were raised on food containing disaggregated SWCNTs.⁴⁶⁸ Although SWCNTs with strong NIR-II fluorescence signals are found in the gut, the blood system, and the central nervous system, the tiny size of *Drosophila* larvae fails to show the deep-penetrating NIR-II fluorescence of SWCNTs, since a regular microscopy imaging setup of <900 nm is sufficient to probe the entire body of such a small and transparent organism. The SWCNTs used in this study were directly sonicated and suspended in the presence of bovine serum albumin (BSA), which was believed to significantly decrease the fluorescence quantum yield due to the formation of defects in the nanotube sidewalls. As a result, whole-body fluorescence imaging of relatively large experimental animals such as mice remained unattainable until biocompatible and yet highly fluorescent SWCNTs were developed by our group in 2009.³⁰ In this work, Welsher et al. developed a surfactant exchange method to preserve the NIR-II fluorescence quantum efficiency during the PEGylation process while maintaining the favorable blood circulation behavior offered by the PEG chains.³⁰ As a result, whole-animal fluorescence imaging in NIR-II window using SWCNTs was achieved for the first time, leading to an appreciation of the deep-tissue capability of NIR-II imaging and opening up the possibility of using SWCNTs as effective fluorophores for *in vivo* imaging. It has been found that a low dose of 17 mg/L (200 μL) exchanged SWCNTs is sufficient to afford a bright fluorescence signal inside the mouse body with clear visualization of deep inner organs such as liver and spleen, while a dose of 260 mg/L (200 μL) directly sonicated SWCNTs shows less sharp imaging contrast despite the dose being 15 times higher than that of exchanged SWCNTs (Figure 17a–f). Moreover, the brightly fluorescent SWCNTs have allowed for high-resolution intravital imaging of blood vessels inside a xenograft tumor below the skin of the mouse. With a 50 \times microscopic objective and an injected carbon nanotube dose of 170 mg/L (300 μL), small capillary vessels inside a tumor can be clearly visualized with down to a few micrometers spatial resolution without the need of a dorsal chamber or a surgical imaging window (Figure 17g–j). The unique NIR-II fluorescence of SWCNTs has for the first time shown its capability of monitoring the biodistribution of injected nanotubes in live

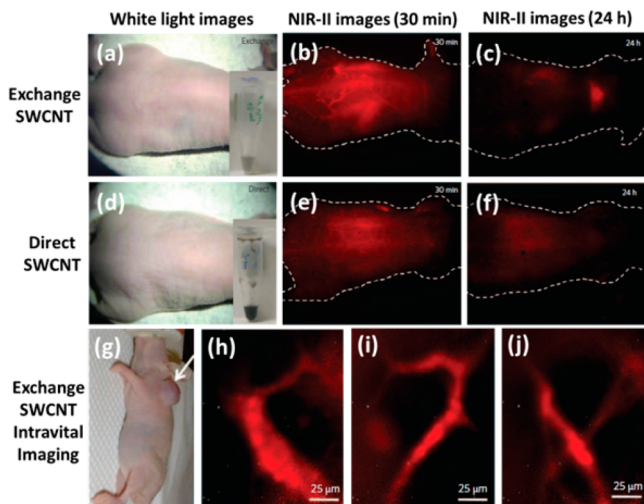


Figure 17. In vivo NIR-II fluorescence imaging of mice. (a, d) White light optical images of mice injected with exchange SWCNTs at a dose of 17 mg/L (200 μ L) (inset, a) and with direct SWCNTs at a dose of 260 mg/L (200 μ L) (inset, d). (b, e) NIR-II fluorescence images of the same animals at 30 min after injection of the exchange SWCNTs (b) and the direct SWCNTs (e). (c, f) NIR-II fluorescence images of the same animals at 24 h after injection of the exchange SWCNTs (c) and the direct SWCNTs (f). (g) White light optical image showing the location of the xenograft tumor, which is inoculated on the shoulder of the mouse (indicated by a white arrow). (h–j) Selected intravital NIR-II fluorescence images showing the vasculature with widths down to a few micrometers inside the tumor in (g) through the relatively thick shoulder skin. Reprinted with permission from ref 30. Copyright 2009 Nature Publishing Group.

animals and angiogenesis inside the tumor with minimum autofluorescence interference.³⁰

With the same formulation of SWCNTs that offers sufficient brightness of NIR-II fluorescence, video-rate NIR-II fluorescence imaging with a short exposure time of 50 ms and a high temporal resolution of \sim 14 frames/s has been achieved for imaging the blood flow dynamics and tracking the whole-body blood circulation labeled by NIR-II fluorescent SWCNTs.¹⁴ Carried by the circulating blood, the injected SWCNTs flow through different inner organs in a highly orchestrated manner. This has allowed us to visualize the appearance of various organs including lungs, kidneys, liver, and spleen that show up sequentially after injection with unprecedented clarity and sharpness (Figure 18a–h). By applying principal component analysis (PCA), which is a powerful mathematical tool first employed by Hillman et al. for fluorescence-mediated organ registration using an NIR-I fluorophore ICG (emission at \sim 800 nm),⁴⁶⁹ Welsher et al. have achieved anatomical registration of the mouse inner organs with dynamically enhanced contrast of major organs from video-rate NIR-II imaging (Figure 18i). PCA works by grouping pixels in a 2D image that exhibit similar variance in time into a single, unique principal component. Since all pixels comprising the same organ in an image should have similar time variance and different organs appear at different times, PCA is able to group pixels that belong to the same organ or the same type of tissue into one single principal component and discriminate different organs into orthogonal principal components. The PCA-assisted dynamic NIR-II fluorescence imaging has salient advantages over the previous work in the NIR-I window with significantly improved anatomical resolving power as a result of reduced photon scattering. Owing to the crisp anatomical resolution

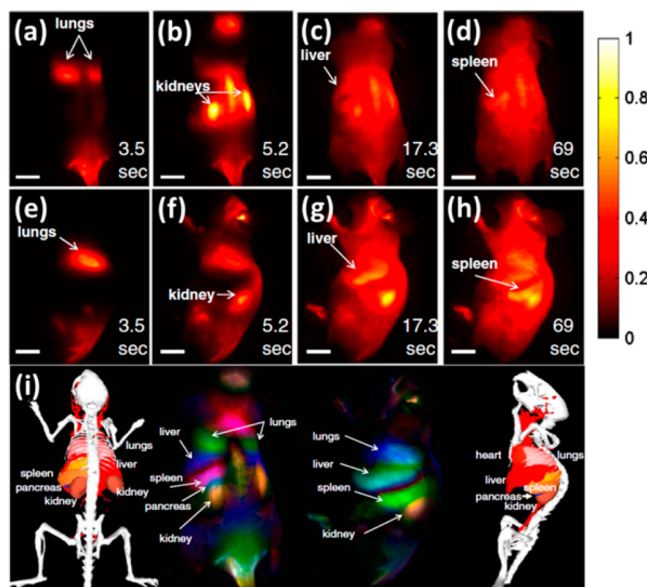


Figure 18. Dynamic contrast enhanced NIR-II fluorescence imaging of mice. (a–d) Time course NIR-II fluorescence images of a live mouse showing the entire body in the prone position immediately after intravenous injection of SWCNTs. (e–h) Time course NIR-II fluorescence images of another mouse showing the left side of the body after intravenous injection of SWCNTs. (i) Dynamic contrast enhanced images through PCA showing major features with temporal distinction based on NIR-II videos taken on both prone-lying and side-lying mice. Reprinted with permission from ref 14. Copyright 2011 National Academy of Sciences.

afforded by in vivo NIR-II imaging and the dynamically enhanced contrast offered by PCA, an important organ with a relatively small size, pancreas, was successfully resolved from PCA (Figure 18i). It is noteworthy that the pancreas is not resolvable either by NIR-I dynamic imaging or from raw NIR-II time-course images, suggesting PCA analysis synergistically improves the resolving power of NIR-II fluorescence imaging. Therefore, the deep penetration NIR-II video-rate imaging together with PCA analysis provides a powerful tool for the identification and differentiation of anatomical features not only based on the structural difference but also by taking the hemodynamic distinction into account.

Proper surface functionalization of SWCNTs not only leads to a higher fluorescence quantum yield and brighter NIR-II emission as discussed above, but should also offer more favorable in vivo pharmacokinetics including slower opsonization, longer blood circulation half-life, and desirable biodistribution. A later work by our group has shown that, through noncovalent surface coating of SWCNTs with a branched PEG-based polymeric surfactant, amphiphilic poly(maleic anhydride-*alt*-1-octadecene)-methoxy poly(ethylene glycol) [C18-PMH-mPEG(90k)] (see section 3.1 and Figure 3d for more information), an increased blood circulation of SWCNTs in the mouse body after intravenous administration can be achieved.²⁹⁸ The long blood circulation with a half-life of \sim 30 h (Figure 19a) allows for multiple passes of the circulating blood carrying SWCNTs through the fenestrated tumor vasculature and continuous accumulation of SWCNTs in the tumor, owing to the enhanced permeability and retention (EPR) effect.^{470,471} When the SWCNTs functionalized with C18-PMH-mPEG(90k) surfactants are injected into the tail vein, the venous blood first travels to the lungs to be oxygenated (Figure 19b), before the kidneys

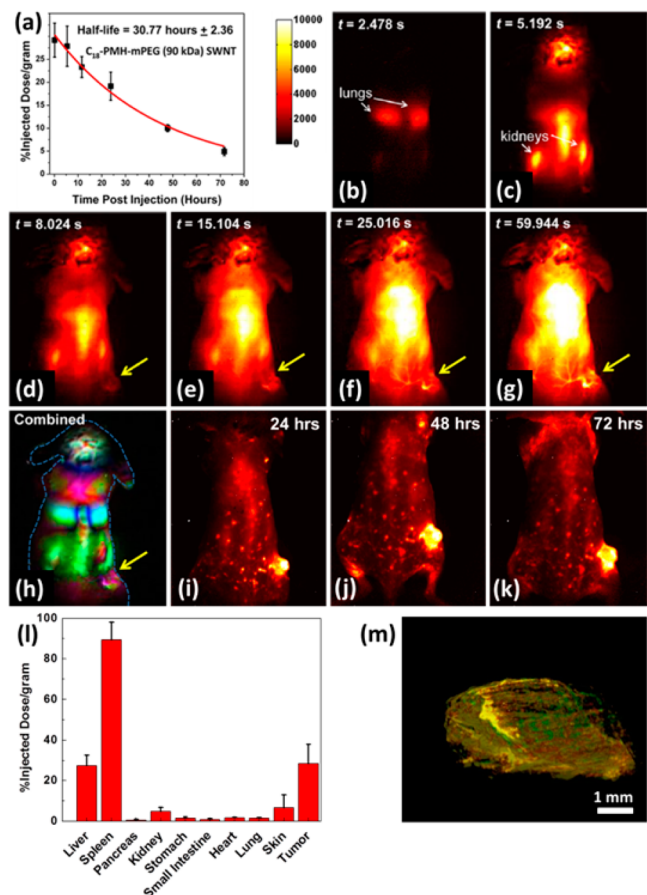


Figure 19. In vivo NIR-II fluorescence imaging of mouse xenograft tumor using the branched PEGylated SWCNTs. (a) Plot showing the SWCNT concentration in blood circulation as a function of time post injection (black squares), which is fitted to a first-order exponential decay with an extracted half-life of 30.77 ± 2.36 h for the C18-PMH-mPEG(90k) coated SWCNTs. (b–g) Time course whole-body NIR-II fluorescence images of a 4T1 tumor-bearing nude mouse in the first minute after intravenous injection of the C18-PMH-mPEG(90k) coated SWCNTs. The tumor is indicated by yellow arrows in (d)–(g). (h) Dynamic contrast enhanced image showing the overlaid positive and negative principal components after PCA analysis. The tumor body (indicated by a yellow arrow) is color-coded in chartreuse and overlaid with the tumor vasculature color-coded in magenta. (i–k) NIR-II fluorescence images of the same animal at 24, 48, and 72 h post injection of SWCNTs, showing the obvious contrast of the tumor due to the passive tumor accumulation of injected nanotubes. (l) Bar chart showing the biodistribution of the injected SWCNTs in different organs and tissues from a mouse sacrificed at 100 h post injection of the C18-PMH-mPEG(90k) coated SWCNTs. (m) A 3D reconstructed and rendered image of the tumor with high SWCNT uptake, where the SWCNT is shown in red, vessels are shown in green, and their colocalization is shown in yellow. Reprinted from ref 298. Copyright 2012 American Chemical Society.

and the tumor show up in NIR-II fluorescence imaging as the oxygenated arterial blood carrying SWCNTs flow through the renal and tumoral vasculature in the systemic circulation (Figure 19c,d). It is noteworthy that, due to the rich tumor vasculature that is more tortuous than in the normal tissue, the NIR-II fluorescence intensity in the tumor region continues to increase in the first minute after injection (Figure 19e–g), making the tumor tissue distinguishable from its surrounding normal tissue via principal component analysis (Figure 19h). Besides dynamically resolving the tumor from other organs, time course

NIR-II fluorescence images of the same mouse at 24–72 h post injection show obvious accumulation of the injected SWCNTs inside the tumor, evidenced by the prominent NIR-II signal from the tumor that forms a striking contrast to the low background signal in the surrounding skin and normal tissue, affording unambiguous identification of the tumor (Figure 19i–k). At approximately 100 h post injection, a surprisingly high tumor uptake of ~30% injected dose per gram (ID/g) with very low uptake in the skin and many other organs is found after the injected mice are euthanized and the organs are collected (Figure 19l). Meanwhile, due to the exceptionally high tumor uptake, NIR-II fluorescence based 3D reconstruction of the tumor is performed to reveal the distribution of SWCNTs inside of the tumor and a high degree of colocalization of the SWCNTs with blood vessels (Figure 19m). This novel functionalization method has made SWCNTs ideal probes for cancer diagnosis and imaging applications.

With the well-functionalized SWCNTs showing in vivo stability and bright NIR-II fluorescence, we demonstrated the benefits of NIR-II fluorescence imaging in a side-by-side comparison with imaging in the NIR-I window,¹⁵ which used to give the highest imaging quality for traditional fluorescence imaging in vivo.^{463,472} In this work, Hong et al. examined NIR-I and NIR-II imaging of the same mouse hind limb vasculatures simultaneously by intravenously injecting a bicolor fluorophore conjugate comprised of the NIR-I fluorescence emitting IRDye-800 molecules covalently linked to PEG chains that coated on the surface of the NIR-II fluorescence emitting SWCNT backbone (Figure 20a).¹⁵ With this bicolor fluorophore conjugate that fluoresces strongly in both the NIR-I window (~800 nm) and the NIR-II window (1100–1400 nm) under a 785 nm laser excitation (Figure 20b), mouse hind limb vascular images are taken at different magnifications in the two NIR subregions, revealing crisp angiographic images of high-order vascular branches in the NIR-II images with striking contrast to the indistinct, blurry images in the NIR-I window (Figure 20c–h). We attribute the greater in vivo imaging clarity to the much reduced scattering of longer-wavelength NIR-II photons and the negligible tissue autofluorescence in the NIR-II window. In addition, we also compare the resolution limits between the SWCNT-enabled NIR-II fluorescence imaging and micro-CT, which is a commonly used imaging modality for 3D reconstruction of anatomical features based on the deeply penetrating X-ray. It has been found that NIR-II fluorescence imaging, which is essentially an optical imaging method with the spatial resolution only limited by diffraction, is able to resolve small hind limb vessels with widths down to ~35 μm , approximately 3 times smaller than the resolution limit of micro-CT, which cannot resolve any features less than 100 μm in size (Figure 20i,j).

More importantly, the quick feedback of NIR-II fluorescence imaging allows video-rate recording that not only resolves vascular anatomy but also provides hemodynamic information. Utilizing the aforementioned dynamic contrast enhanced imaging via PCA, Hong et al. successfully differentiate arterial vessels from venous vessels in the mouse hind limb based on the early frames of NIR-II video-rate imaging during intravenous injection of SWCNTs (Figure 20k,l). Although showing up differently in time, the arteries and the veins are difficult to discriminate by inspection of the raw NIR-II images due to the spatial proximity of these vessels. PCA analysis extracts the temporal contrast from the video and aids easy differentiation of vessel types and quick detection of vascular anomalies.¹⁵ Another

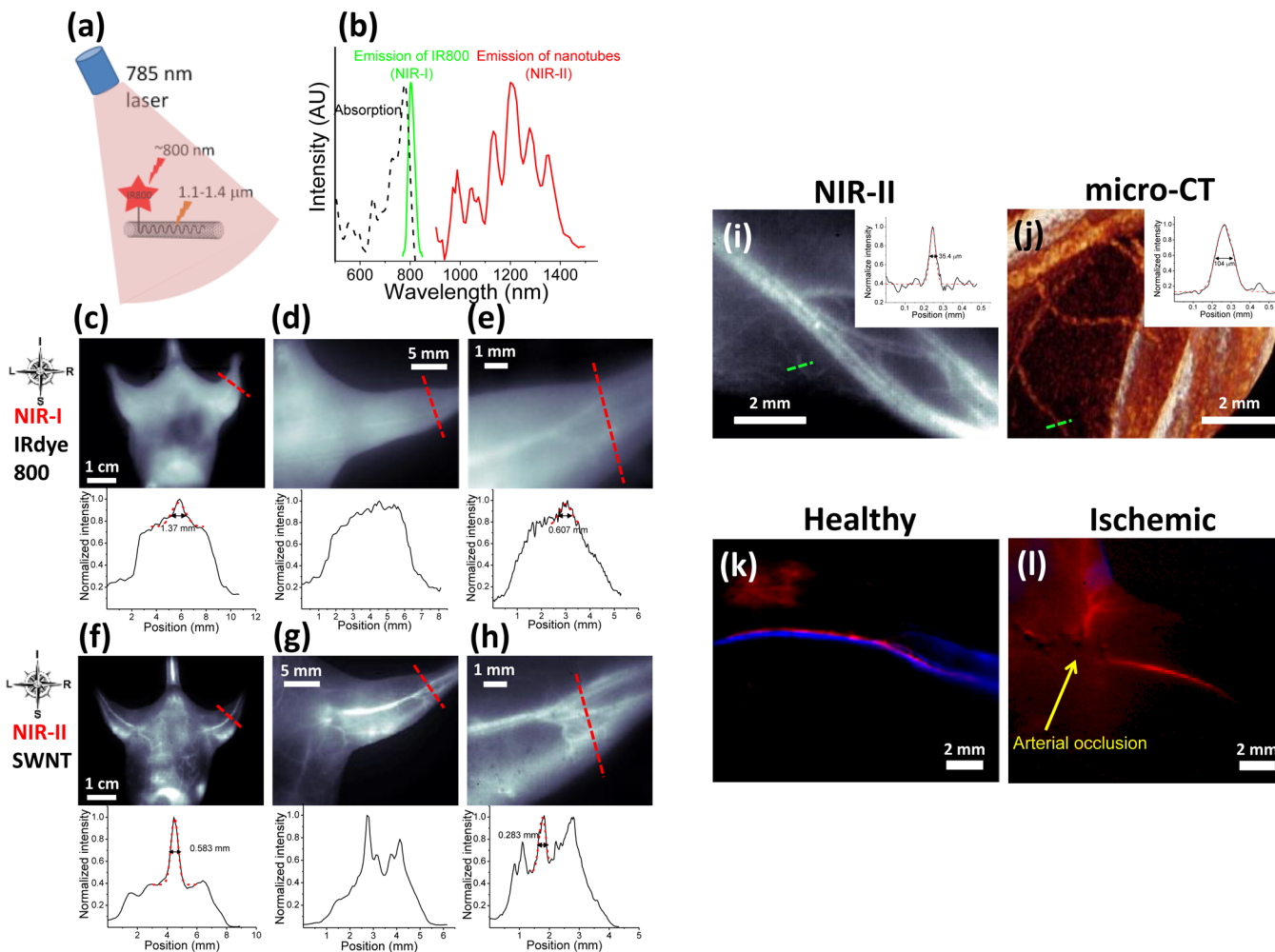


Figure 20. In vivo NIR-II fluorescence imaging of mouse hind limb vasculature. (a) Schematic drawing showing the structure of the SWCNT-IRDye-800 bicolor fluorophore conjugate, which simultaneously emits NIR-I fluorescence at 800 nm wavelength and NIR-II fluorescence in the 1100–1400 nm wavelength region upon excitation of a 785 nm laser. (b) Absorption (black dashed curve), NIR-I emission (green solid curve), and NIR-II emission (red solid curve) spectra of the SWCNT-IRDye-800 bicolor fluorophore conjugate. (c–e) The top row shows in vivo NIR-I fluorescence images of a mouse injected with SWCNT-IRDye-800 under progressively increasing magnifications. The bottom row shows the corresponding cross-sectional intensity profiles (black solid curve) along red dashed bars in the top row images, which are fitted to Gaussian functions (red dashed curve) for the extraction of the vessel widths. (f–h) The top row shows in vivo NIR-II fluorescence images of a mouse intravenously injected with SWCNT-IRDye-800 under progressively increasing magnifications. The bottom row shows the corresponding cross-sectional intensity profiles (black solid curve) along red dashed bars in the top row images, showing much narrower peaks and smaller Gaussian-fitted widths (red dashed curve) owing to the reduced scattering of photons. (i, j) Side-by-side comparison of mouse hind limb angiography obtained by NIR-II fluorescence imaging (i) and micro-CT imaging (j) of the same mouse. The inset shows the line intensity profile along the green dashed bar in each image. (k, l) PCA overlaid images showing the arteries (red) and veins (blue) based on video-rate NIR-II fluorescence imaging of a healthy mouse hind limb (k) and an ischemic mouse hind limb (l). Reprinted with permission from ref 15. Copyright 2012 Nature Publishing Group.

unique feature of dynamic NIR-II fluorescence imaging is the capability of quantifying blood velocity in vessels. We have found a 30 times lower blood velocity in the ischemic femoral artery due to surgery-induced occlusion than in the normal healthy femoral artery based on dynamic NIR-II fluorescence imaging, giving consistent measurements of blood velocity with ultrasonography in the Doppler mode. It is noteworthy that the blood velocity of ischemic hind limb is too slow to be quantified with Doppler measurement, while dynamic NIR-II imaging provides a broader dynamic range with a much lower detection limit of the blood velocity. Therefore, this work has shown that NIR-II imaging incorporates high spatial resolution, deep tissue penetration, fast imaging feedback, vessel differentiation capability, and quantitative hemodynamic measurement into one single imaging modality and achieves what is typically accomplished by multiple

traditional imaging modalities such as micro-CT and ultrasound.¹⁵

With NIR-II fluorescence angiography, we have demonstrated SWCNTs can be used to track the revascularization process in mouse hind limb as a natural response to experimentally induced acute hind limb ischemia, which is a murine model of peripheral arterial diseases.³⁹⁷ Through video-rate NIR-II fluorescence imaging of the entire mouse body in the supine position immediately after injection of SWCNTs, dynamic tissue perfusion measurement is achieved by monitoring the NIR-II signal increase in both the healthy, control hind limb and the ischemic hind limb (Figure 21a,b), revealing a progressively increasing relative tissue perfusion in the ischemic hind limb tissue over the course of recovery. The NIR-II fluorescence based tissue perfusion measurement agrees in trend with laser Doppler

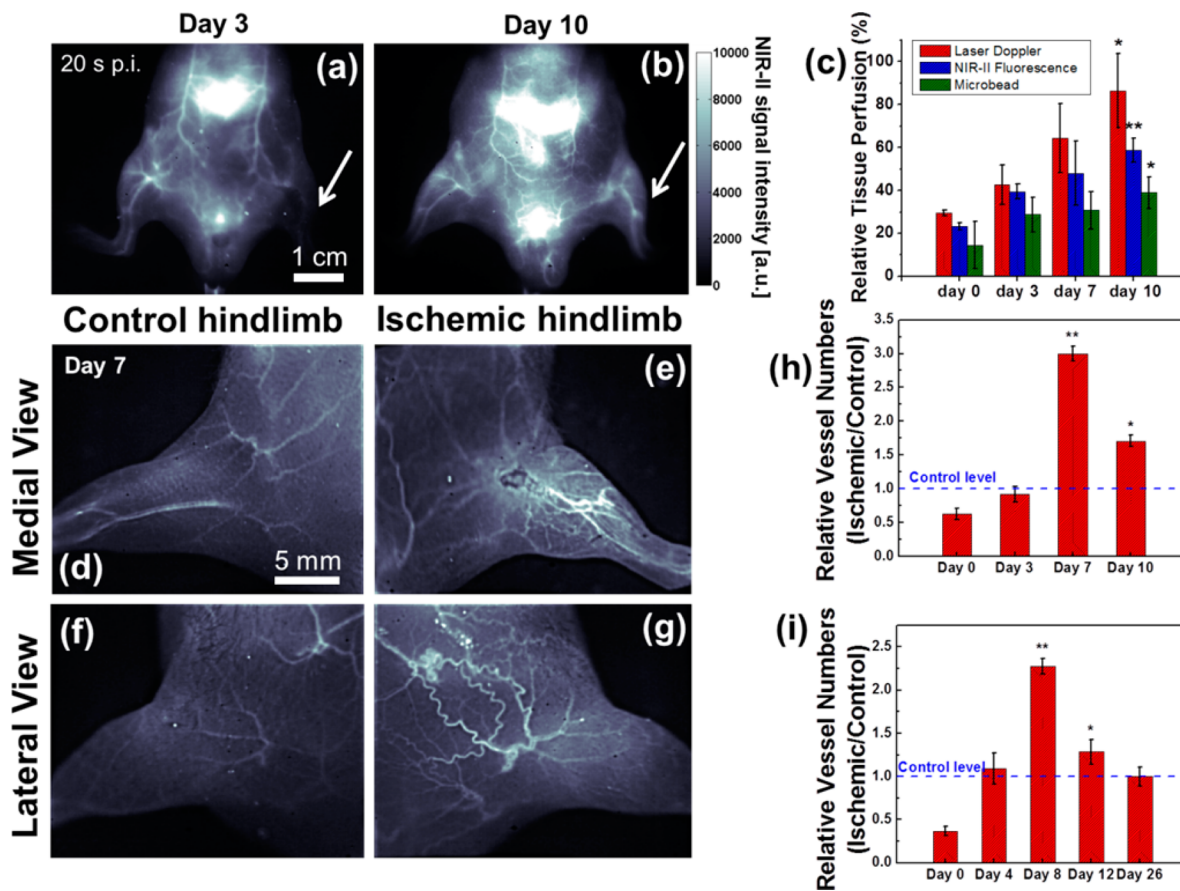


Figure 21. In vivo NIR-II fluorescence imaging of mouse hind limb revascularization. (a, b) NIR-II fluorescence images of the same mouse on day 3 and day 10 after surgery-induced acute limb ischemia, showing improved tissue perfusion evidenced by a higher NIR-II signal in the ischemic hind limb (indicated by the white arrow) on day 10 than on day 3. These images were taken at 20 s after intravenous injection of SWCNTs. (c) Bar chart showing the relative tissue perfusion in the ischemic hind limb (normalized against that in the control, untreated hind limb) on days 0, 3, 7, and 10, measured by laser Doppler blood flowmetry (red bars), NIR-II fluorescence method (blue bars), and microbead-based perfusion measurement (green bars). (d–g) NIR-II fluorescence images of the control, untreated hind limbs (d, f) and the ischemic hind limbs (e, g) in medial view (d, e) and lateral view (f, g) from two different mice, showing a significantly increased number of microvessels in the ischemic hind limbs. (h, i) Trends of the relative vessel numbers, which are defined as vessel number in the ischemic hind limb over that in the control hind limb, showing a temporal increase of microvessels in the hind limb tissue at ~1 week after the surgery followed by vessel regression. Reprinted with permission from ref 397. Copyright 2014 Wolters Kluwer Health.

blood flowmetry and microbead-based perfusion measurement (Figure 21c), while the NIR-II method provides a greater probing depth into the tissue in a noninvasive way. Moreover, the high resolving power of NIR-II fluorescence imaging with deep tissue penetration enables us to quantify structural changes in the hind limb vascular anatomy over a course of up to 26 days, with interesting observations showing an initial burst of newly recruited collateral branches on ~1 week post surgery (Figure 21d–g), followed by regression of these collateral vessels and a gradual return of microvascular density to normal levels (Figure 21h,i). This surprising finding made by the noninvasive NIR-II fluorescence imaging is confirmed by the invasive immunohistochemical staining of blood vessels in hind limb tissue slices.³⁹⁷ The nonphotobleachable and deep tissue penetrating NIR-II fluorescence of SWCNTs makes NIR-II imaging a powerful tool for monitoring anatomic and dynamic changes over a long time course in various disease models.

Although the optimized functionalization methods allow for production of biocompatible SWCNTs without destroying their intrinsic NIR-II fluorescence, the coexistence of semiconducting and metallic SWCNTs, as well as the presence of many off-resonance chiralities that have little contribution to the

fluorescence emission, makes the SWCNT mixture less ideal for in vivo fluorescence imaging. As one can see from Figure 10, the three widely used SWCNT growth methods (chemical vapor deposition, laser ablation, and electric arc discharge) generally produce a mixture of various SWCNT species with a wide range of diameters and chiralities. Since the optical properties of SWCNTs are strongly correlated to their diameters and chiralities, the raw mixture of nanotubes exhibits a wide variation of excitation and emission wavelengths, making it impossible to excite all chiralities with equal efficiency using a single wavelength excitation source. Most of the as-reported NIR-II imaging experiments have been performed under an 808 nm excitation to afford maximum penetration of the excitation light in the first biological transparent window (i.e., the NIR-I window).^{14–16} However, due to the inhomogeneity of SWCNTs, only 9% of the raw SWCNT mixture made from the HiPco method can be resonantly excited using an 808 nm laser.³³ Since the majority of the raw HiPco SWCNTs are off-resonant, an unnecessarily high injection dose is typically needed to provide sufficient NIR-II fluorescence signal, raising toxicity concerns when exploring SWCNTs for in vivo uses. Therefore, there is a

need for isolating a single chirality of SWCNTs for NIR-II imaging applications.

To this end, our group has utilized gel chromatography and density gradient centrifugation methods to separate (12,1) and (11,3) chiralities, as well as a single (6,5) chirality, both from the raw HiPco mixture.^{33,34} Gel chromatography has been applied for both electronic type separation and single chirality separation;^{473–477} however, in order to be able to use the separated SWCNTs for *in vivo* imaging, a sufficient quantity of the separated nanotubes needs to be produced with biocompatibility. Diao et al. developed a simple separation technique based on gel chromatography to isolate (12,1) and (11,3) chiralities in strong optical resonance with the 808 nm excitation, which is widely used for *in vivo* NIR-II fluorescence imaging (Figure 22a).³³ The gel chromatography is performed using a suspension of SWCNTs in sodium cholate as opposed to the widely used sodium dodecyl sulfate (SDS)^{474,475} to retain the NIR-II fluorescence quantum yield. Owing to the well-matched E₂₂ resonance absorption bands of (12,1) and (11,3) (\sim 800 nm) with the 808 nm excitation laser, the chirality separated SWCNTs are found to have 5-fold higher brightness in the

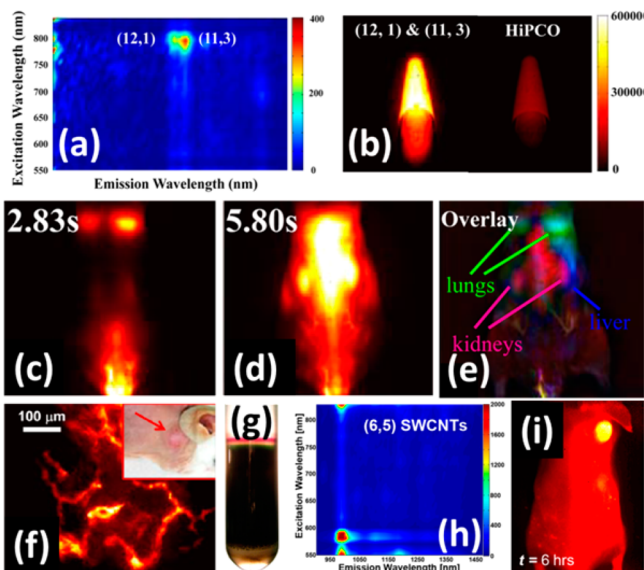


Figure 22. *In vivo* NIR-II fluorescence imaging using chirality-separated SWCNTs. (a) Photoluminescence versus excitation (PLE) map of the gel-separated chirality-pure (12,1) and (11,3) SWCNTs. (b) NIR-II fluorescence image showing the chirality-pure SWCNTs are 5 times brighter than the raw HiPco SWCNT mixture in the NIR-II window when both samples are normalized to the same mass concentration. (c, d) Time course NIR-II fluorescence images showing the entire body of a nude mouse after injection of the chirality-pure (12,1) and (11,3) SWCNTs. (e) PCA overlaid image based on dynamic NIR-II fluorescence recording for the nude mouse injected with chirality-pure (12,1) and (11,3) SWCNTs, showing the anatomical registration of different internal organs. (f) Intravital NIR-II fluorescence image showing rich vasculature inside the tumor, with the vascular contrast enhanced by the chirality-pure (12,1) and (11,3) SWCNTs. (a–f) Reprinted from ref 33. Copyright 2012 American Chemical Society. (g) White-light digital photograph showing the separation of the (6,5) chirality (shown as the purple band) at the top of the centrifuge tube after density gradient centrifugation. (h) PLE map of the (6,5) chirality. (i) *In vivo* fluorescence image showing the high accumulation of (6,5) SWCNTs inside the tumor, evidenced by the bright circle located on the right shoulder of this tumor-bearing mouse. (g–i) Reprinted from ref 34. Copyright 2013 American Chemical Society.

NIR-II window than the mass-balanced, pristine HiPco mixture (Figure 22b). The high NIR-II fluorescence brightness with emission wavelength centered at \sim 1200 nm allows for high-performance dynamic *in vivo* imaging of the entire mouse body (Figure 22c–e) with a much lower injection dose (0.16 mg/kg body weight vs previously 1.0 mg/kg body weight) of nanotubes. The chirality enriched, resonantly excited SWCNTs have also been used as vascular contrast agents for intravital imaging of tumor angiogenesis, resolving capillary vessels inside the tumor with less than 10 μ m widths at millimeter depths (Figure 22f).³³ Besides gel chromatography, density gradient centrifugation is another powerful tool for separation of SWCNTs.^{478,479} Our group has successfully used chirality enriched (6,5) SWCNT derived from density gradient ultracentrifugation (Figure 22g,h) for xenograft tumor imaging and photothermal therapy, taking advantage of the high passive tumor uptake due to the EPR effect (Figure 22i). These examples have demonstrated the chirality-separated SWCNTs as single-color fluorophores with the potential of multiplexed, multicolor *in vivo* NIR-II fluorescence imaging at much lower injection doses than needed for the unseparated, heterogeneous mixture of nanotubes.

With the advances in optimizing the surface functionalization, emission wavelength, chirality composition, and fluorescence quantum yield of SWCNTs, *in vivo* NIR-II fluorescence imaging has been explored in recent years for a variety of biomedical applications, including *in vivo* lymphatic vessel imaging,⁴⁸⁰ *in vivo* detection of nitric oxide,³⁵ imaging guide tumor surgery,³⁶ *in vivo* imaging of bacterial infection,³²² and noninvasive through-scalp/skull brain vascular imaging.¹⁶

Not only can SWCNTs be used as contrast agent for imaging blood vessels in the NIR-II window, recently our group and Liu's group have shown in a collaboration that SWCNTs can also be afforded as lymphatic vascular contrast to track the path of tumor metastasis by intratumoral injection of PEGylated SWCNTs.⁴⁸⁰ Cancer lymphatic metastasis can significantly decrease the cancer survival rate, and imaging guided identification and therapy hold a key to eradicating metastatic cancers. At merely 20 min after injection of SWCNTs into the tumor inoculated on the hind paw, an NIR-II signal can be clearly seen in the closest sentinel lymph node on the popliteal site, indicating the translocation of SWCNTs from the original injection site in the primary tumor to the neighboring sentinel lymph node through the lymphatic vessels. The lymphatic drainage and translocation of SWCNTs is believed to be through the same pathway for the primary tumor to metastasize. Compared to traditional fluorescence methods for imaging of sentinel lymph nodes,^{482–488} NIR-II imaging benefits from low autofluorescence and reduced light scattering, affording a much higher signal-to-background ratio (lymph node to surrounding tissue) useful for the accurate identification and surgical excision of the metastasized sentinel lymph node.⁴⁸⁰

Besides structural imaging in the NIR-II window, the NIR-II fluorescent SWCNTs have been intensively studied as optical biosensors by the Strano group, showing detection specificity to certain molecular species such as hydrogen peroxide (H_2O_2) and nitric oxide (NO).^{481,489–491} In a recent study by the Strano group, SWCNTs wrapped with DNA oligonucleotides and functionalized with PEG (Figure 23a) have been developed as an *in vivo* nitric oxide sensor based on their NIR-II fluorescence emission, which shows strong fluorescence quenching effect in the presence of NO free radicals (Figure 23b).³⁵ Facilitated by a liquid crystal tunable grating and the spatial-spectral imaging deconvolution algorithm, the authors are able to successfully remove the tissue autofluorescence and background signals from

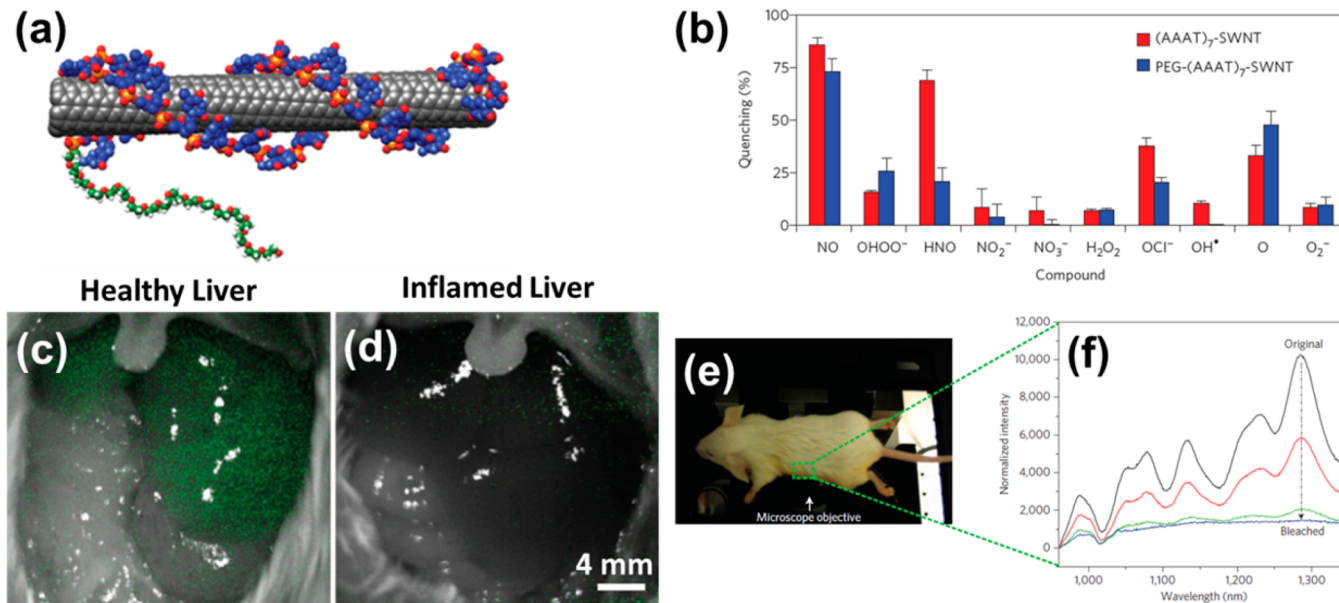


Figure 23. In vivo nitric oxide sensor based on SWCNTs. (a) Schematic drawing showing the SWCNT-based NO sensor, which is comprised of the nanotube backbone (gray cylinder), DNA oligonucleotide (helices made of red and blue balls), and PEG (the chain with tiny green balls). (b) Bar chart showing the percent quenching of unPEGylated SWCNTs [(AAAT)₇-SWNT] and PEGylated SWCNTs [PEG-(AAAT)₇-SWNT] following the exposure of SWCNTs to various reactive nitrogen species and reactive oxygen species, showing the perfect selectivity of PEG-(AAAT)₇-SWNT to NO. (c, d) In situ NIR-II fluorescence images (color coded in green) of mouse liver overlaid on top of the white-light optical images for a healthy, untreated mouse (c) and a mouse injected with RcsX tumor cells to cause liver inflammation (d). Reprinted with permission from ref 35. Copyright 2013 Nature Publishing Group. (e, f) Microscopic fluorescence spectroscopy of SWCNTs in the mouse abdominal cavity (e), showing gradually decreasing fluorescence intensity after injection of a 60 μ M NO solution (f). (e, f) Reprinted with permission from ref 481. Copyright 2009 Nature Publishing Group.

the characteristic NIR-II signals of the SWCNT reporters based on their spectral differences. The spectrally unmixed NIR-II fluorescence imaging allows the authors to selectively detect local nitric oxide concentration in the liver of a live mouse, which is injected with RcsX tumor cells to cause liver inflammation and *in situ* generation of NO molecules in the liver. In vivo NIR-II fluorescence imaging of the exposed mouse liver through a cut in the abdominal cavity exhibits much lower NIR-II fluorescence from the inflamed liver than the healthy, untreated liver, due to the NO-induced strong fluorescence quenching of SWCNTs (Figure 23c,d). Spectral measurements reveal a drastic drop in fluorescence intensity of the SWCNTs in the presence of NO (Figure 23e,f).⁴⁸¹ The in vivo NO sensor based on the NIR-II fluorescence of SWCNTs has proven to be a useful tool for the quantification of tissue NO concentration and the study of inflammation signaling pathway in animal models.

The Belcher group has developed a novel method to solubilize and functionalize SWCNTs with the M13 bacteriophage viruses (see section 3.1 for more details on the M13-assisted surface functionalization of SWCNTs).³²⁰ Using the M13–SWCNT bioconjugate as a fluorescent label in the NIR-II window, Belcher et al. have imaged the biodistribution of intravenously injected M13–SWCNTs, and found that the liver, spleen, and spine showed high NIR-II signals owing to the high uptake of SWCNTs (Figure 24a).³²¹ Owing to the long wavelength NIR-II fluorescence emission, the M13–SWCNT probes can be detected in tissue-like phantom with up to 2.5 cm depth. Recently, it has been reported by the same group that the SPARC (secreted protein, acidic and rich in cysteines) binding peptide (SBP) functionalized M13–SWCNTs can be used to selectively target the SPARC-expressing tumors *in vivo*.³⁶ An orthotopic mouse model of human ovarian cancer is used in this study, and

the SBP-functionalized M13–SWCNTs are injected intraperitoneally into the tumor-bearing mice. The authors have shown that SWCNTs with NIR-II fluorescence emission have higher signal-to-noise performance than fluorophores in the visible and NIR-I windows (FITC and AlexaFluor750), in that only NIR-II fluorescence imaging with SBP-functionalized M13–SWCNTs allows for delineation of the disseminated tumor nodules in the abdomen while SBP-functionalized shorter-wavelength fluorophores fail to exhibit distinguishable contrast of the tumor nodules over the background (Figure 24b). Owing to the selective targeting to the tumor nodules and the high imaging sensitivity of SBP-functionalized M13–SWCNTs, submillimeter tumor nodules can be detected to depths as great as 9.7–18.2 mm with NIR-II fluorescence imaging, and imaging-guided surgery has been performed to show more complete removal of overall tumor burden in the mouse abdomen than unguided tumor excision (Figure 24c). This work has suggested M13–SWCNTs as effective NIR-II fluorescent labels with engineered targeting ligands for high-contrast *in vivo* molecular imaging, early stage tumor diagnosis, and guided surgical excision of disseminated ovarian tumors with sizes down to submillimeters.³⁶

Taking advantage of the natural binding affinity of the M13 bacteriophage to certain bacterial strains such as *E. coli*, the same group has shown *in vivo* targeted imaging of bacterial infection using the NIR-II fluorescence emitting M13–SWCNTs.³²² In this work, F' positive *E. coli* is injected intramuscularly into the right flank of a mouse to cause bacterial infection while PBS is injected into the left flank as a control. After M13–SWCNTs are injected intravenously into the mouse, the right flank with *E. coli* induced bacterial infection shows a significantly higher NIR-II fluorescence signal than the left flank, which only received PBS

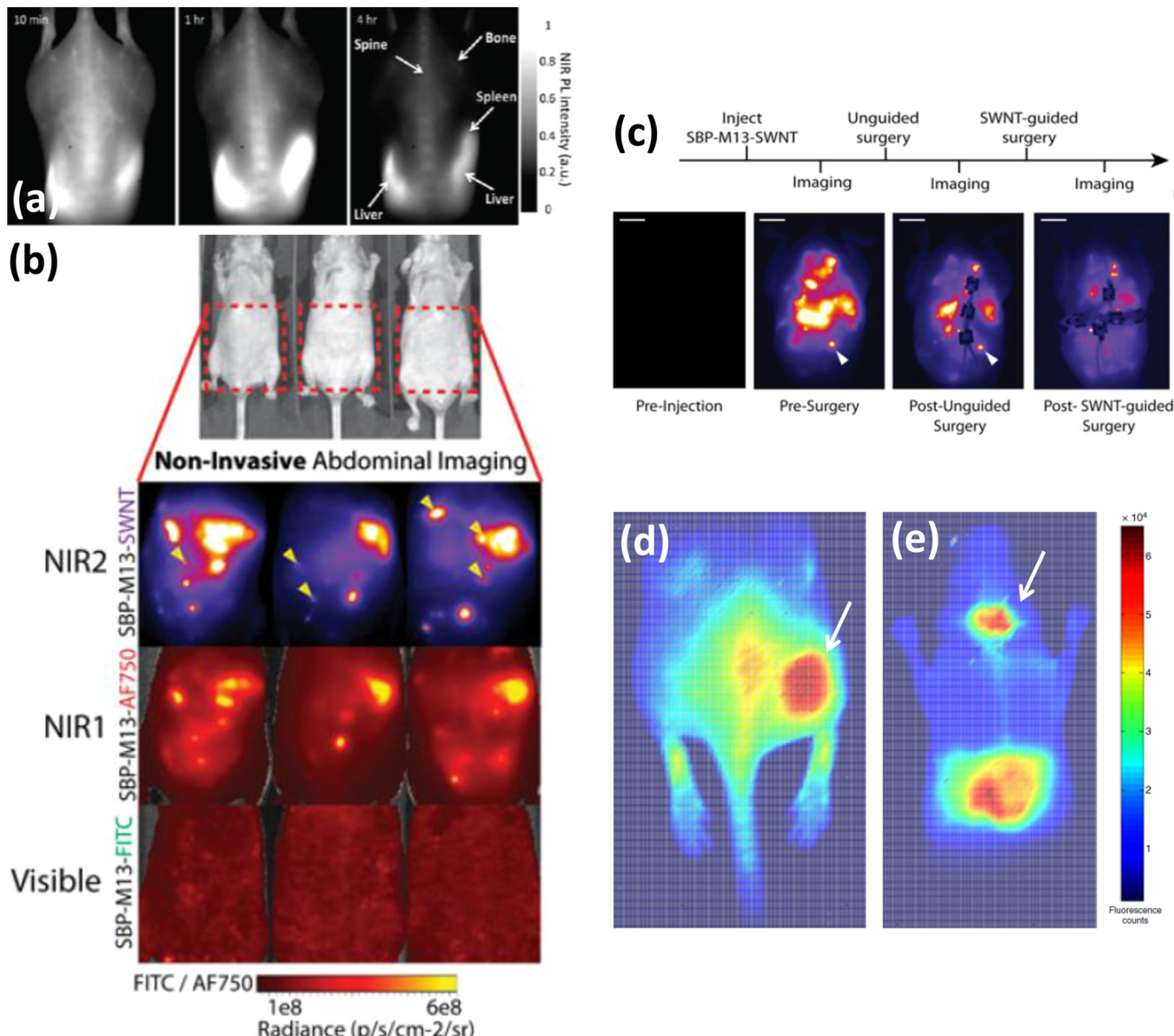


Figure 24. In vivo NIR-II fluorescence imaging with M13 bacteriophage conjugated SWCNTs. (a) Whole-body NIR-II fluorescence images of a mouse at 10 min (left), 1 h (middle), and 4 h (right) post injection of M13–SWCNTs. Reprinted from ref 321. Copyright 2012 American Chemical Society. (b) In vivo abdominal imaging of disseminated ovarian tumors, replicated on three animals (the row of white-light optical images). The fluorescence images are taken in the NIR-II window with SBP-functionalized M13–SWCNTs (top row), in the NIR-I window with SBP-functionalized M13–AlexaFluor750 (middle row), and in the visible window with SBP-functionalized M13–FITC (bottom row). The disseminated ovarian tumor nodules are indicated by the yellow triangles and can only be observed in the NIR-II fluorescence images. (c) NIR-II fluorescence based abdominal images showing the removal of the ovarian tumor nodules before surgery, after unguided surgery, and after NIR-II imaging guided surgery. (b, c) Reprinted with permission from ref 36. Copyright 2014 National Academy of Sciences. (d) NIR-II fluorescence image of a mouse infected with F'-positive *E. coli* strain JM109 in the right flank and intravenously injected with M13–SWCNTs, showing specificity of M13–SWCNTs to the bacteria infected site (indicated by the white arrow). (e) NIR-II fluorescence image of a mouse infected with *S. aureus* strain Xen-29 to cause endocarditis in the heart and intravenously injected with anti-*S. aureus*–M13–SWCNTs that target the bacteria infected site (indicated by the white arrow). (d, e) Reprinted with permission from ref 322. Copyright 2014 Nature Publishing Group.

(Figure 24d). M13–SWCNTs can also be conjugated with the anti-*S. aureus* antibody and used for in vivo targeted imaging of *S. aureus* induced endocarditis in the heart (Figure 24e).³²² These examples have demonstrated that the NIR-II fluorescence of SWCNTs can not only afford anatomical imaging, but also allow for functional and molecular imaging with specificity.

The central role of the brain and the complex network comprised of interconnected neurons with exquisite functions in the brain urge the emergence of novel imaging tools for better

understanding of the most sophisticated and delicate organ in all mammals.^{492,493} Structural and molecular interrogation of the brain has long been limited by current brain imaging techniques, which either lack enough penetration depth to probe the inner cerebral structures and functions,^{494,495} or do not have sufficient resolving power to identify small structures on a cellular or even molecular level.^{496,497} To this end, our group has applied NIR-II fluorescence imaging, which has many salient advantages as demonstrated in preceding paragraphs, for noninvasive brain

vascular imaging through the intact scalp and skull for the first time.¹⁶ To afford the maximum tissue penetration depth with the highest possible spatial resolution, we rationally choose a subregion in the NIR-II window from 1300 to 1400 nm (named the NIR-IIa window), using diameter-sorted HiPco SWCNTs with enriched semiconducting chiralities that have bright fluorescence emission biased toward the longer wavelength NIR-IIa region. The NIR-IIa window is located as an absorbance minimum in the water absorption spectrum, while rejecting all shorter wavelength NIR-II photons of <1300 nm to minimize scattering. To show the benefits of the NIR-IIa window, *in vivo* brain imaging through intact scalp skin and cranial bones is performed on the same mouse in the NIR-I (850–900 nm), NIR-II (1000–1700 nm), and NIR-IIa windows (1300–1400 nm) by intravenously injecting the mouse with SWCNT–IRDye-800 conjugates. One can see that the brain image taken in the NIR-IIa window exhibits the sharpest cerebrovascular structures with the greatest clarity and contrast (Figure 25a–d), due to the reduced photon scattering in this longer wavelength window. As a result, several major cortical vessels including the inferior cerebral vein, superior sagittal sinus, and transverse sinus together with many small, higher-order cerebral branches can be clearly resolved at an imaging depth of 1–2 mm in the NIR-IIa region without any craniotomy. Another advantage of NIR-IIa imaging is that it allows for high-magnification microscopic fluorescence imaging through the intact scalp and skull, affording the capability of spatially resolving <10 μm cerebral capillary vessels at >2 mm depths underneath the scalp skin (Figure 25e–h).

Moreover, similar to the aforementioned NIR-II hind limb imaging, NIR-IIa brain imaging is explored to study hemodynamic difference between the control, healthy brain and the diseased brain with middle cerebral arterial occlusion (MCAO) in a mouse model of stroke (Figure 26a–l). Video-rate imaging and tracking of circulating SWCNTs based on their NIR-IIa fluorescence emission clearly reveal dramatically reduced cortical blood perfusion in the left cerebral hemisphere of a mouse, which has been surgically occluded in the middle cerebral artery, compared to the intact, right hemisphere with normal cortical blood perfusion (Figure 26g–l). The dynamic NIR-IIa fluorescence imaging also allows for quantitative assessment on the degree of hemodynamic impairment in the mouse cortex, showing good agreement with a well-established, but more invasive method based on laser Doppler blood flowmetry (Figure 26m–o). This work presents a completely noninvasive fluorescence imaging method of mouse cerebral vasculatures without craniotomy by detecting intrinsic fluorescence of chemically purified SWCNTs in the 1.3–1.4 μm region, which is the longest wavelength ever used for fluorescence brain imaging thus far. The high spatial resolution (down to sub-10 μm cerebral capillaries), superior penetrating power (through intact scalp and skull), and fast acquisition rate (dynamic blood flow imaging) of NIR-IIa fluorescence imaging have opened up new horizons leading to the understanding of brain neurovascular functions on both cortical and subcortical levels in animal models.^{16,498,499}

Being the first practical material with intrinsic NIR-II fluorescence emission, the use of SWCNTs for *in vitro* and *in vivo* biomedical imaging has stimulated the search for other fluorescent agents in NIR-II. Inspired by the many salient advantages of SWCNT-based NIR-II fluorescence imaging, including reduced photon scattering, minimum tissue absorption, negligible endogenous autofluorescence, deep tissue

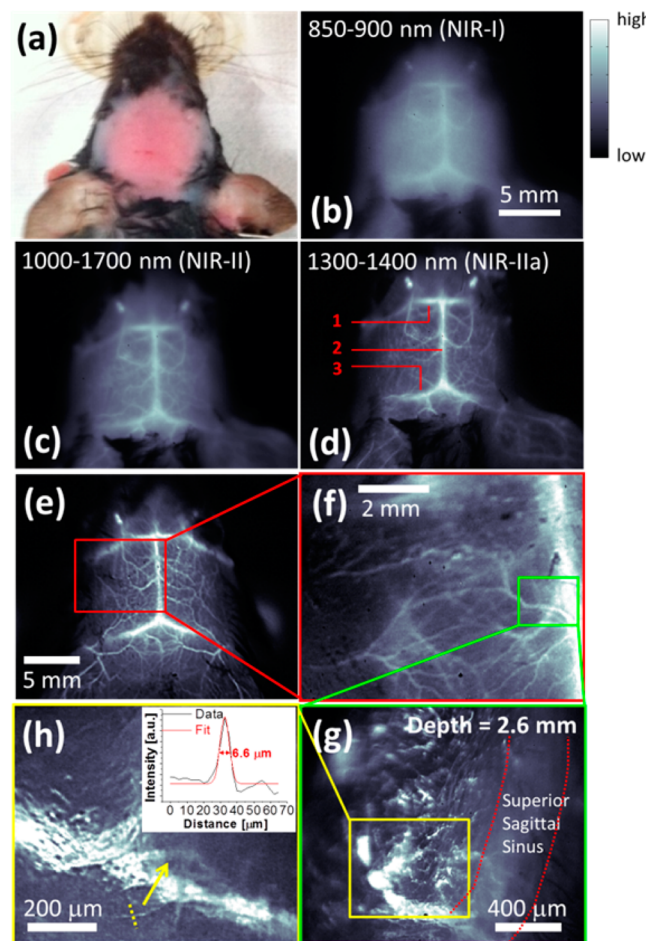


Figure 25. Noninvasive through-skull brain vascular imaging in the NIR-IIa window using SWCNTs. (a) White-light photograph showing a C57Bl/6 mouse with its hair removed for brain imaging. (b–d) Brain fluorescence images of the same mouse head shown in (a), taken in the NIR-I (b), NIR-II (c), and NIR-IIa (d) windows. Some major cerebral vessels are labeled in (d) as 1, inferior cerebral vein; 2, superior sagittal sinus; and 3, transverse sinus. (e–h) NIR-IIa fluorescence images of the brain vasculature with progressively increasing magnification from (e) to (h). Cerebral capillary vessel intersected by the yellow dashed line in (h) is found to have a measured width of 6.6 μm by fitting the line cross-section intensity profile (black curve, h inset) to a Gaussian function (red curve, h inset). Reprinted with permission from ref 16. Copyright 2014 Nature Publishing Group.

penetration, resistance to photobleaching, sufficient spatial resolution, and fast imaging feedback, in recent years, our group, among many other independent research groups, has expanded the toolbox of NIR-II fluorophores beyond SWCNTs. A handful of inorganic nanomaterials and organic molecules, including chalcogenide quantum dots (e.g., Ag₂S, Ag₂Se, and PbS),^{392,395,497,500–507} rare-earth-doped nanoparticles,^{394,399,508,509} conjugated copolymers,³⁹⁶ and organic small molecules,³⁹³ have been synthesized with sufficient photoluminescence in the NIR-II window for *in vivo* NIR-II fluorescence imaging of xenograft tumor,^{392,394,501,503,504,507} blood vasculature,^{393,395,396,497} lymphatic vasculature,^{503,505,509} and cell migration.^{502,506} With an increasing number of highly efficient NIR-II fluorophores developed down the road, it is anticipated that NIR-II fluorescence imaging will find more and more applications in answering fundamental and practical questions in biology and medicine.

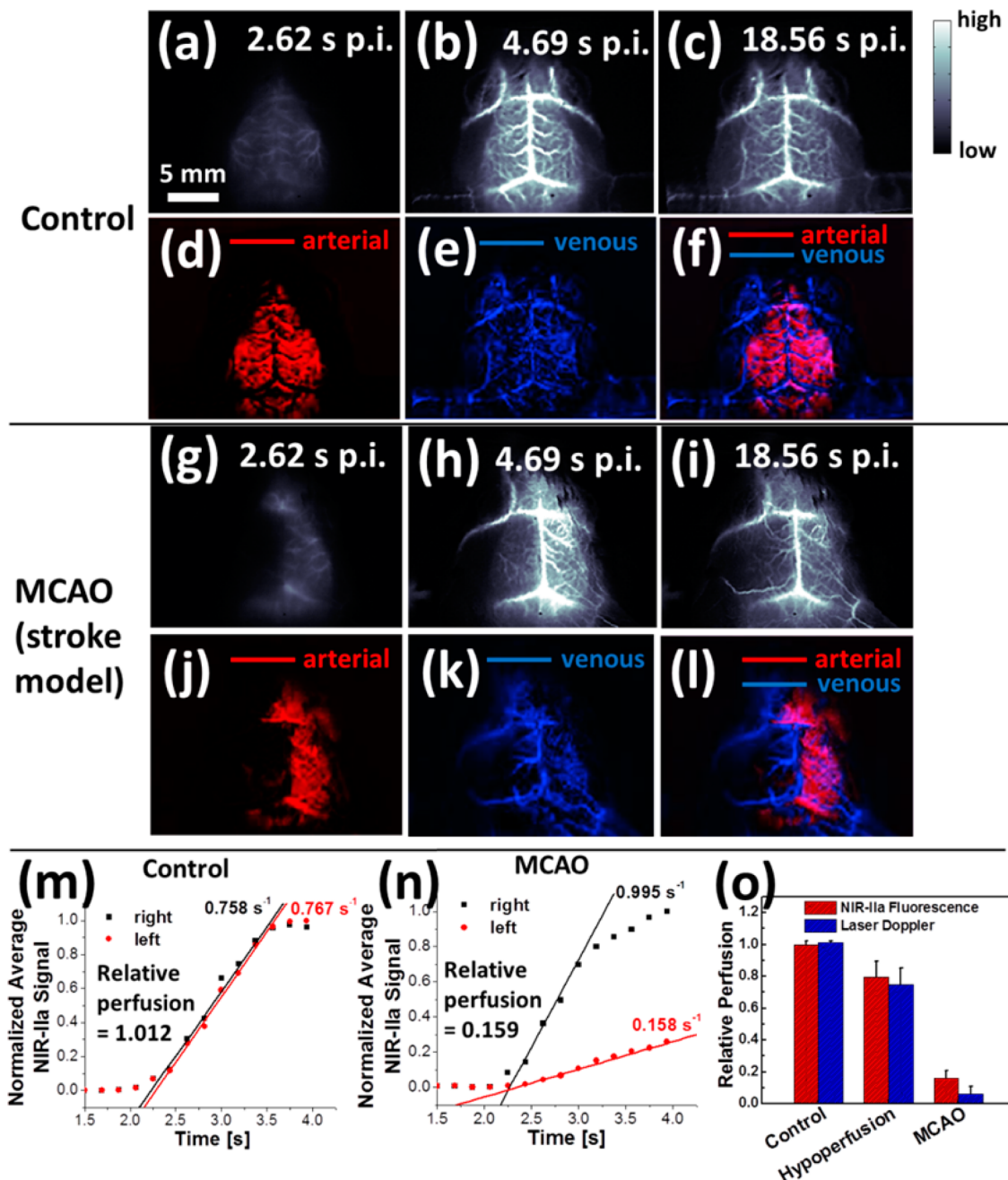


Figure 26. Dynamic NIR-IIa fluorescence imaging of the mouse cerebral blood perfusion. (a–c) Time course NIR-IIa fluorescence images of a control, healthy mouse brain immediately after tail vein injection of SWCNTs. (d–f) PCA overlaid images of the healthy mouse brain showing the arterial (d), venous (e) and both (f) principal components. (g–i) Time course NIR-IIa fluorescence images of a diseased mouse brain with surgery-induced stroke in the left hemisphere. (j–l) PCA overlaid images of the diseased mouse brain showing the arterial (j), venous (k), and both (l) principal components. A much reduced number of arterial vessels can be seen in the left, occluded hemisphere due to stroke in the left middle cerebral artery that blocks arterial blood inflow to the left hemisphere. (m, n) Normalized NIR-IIa fluorescence signals in the left (red) and right (black) hemispheres plotted as functions of time post injection of SWCNTs for the control, healthy mouse (m) and the diseased mouse with MCAO in the left hemisphere (n). (o) Bar chart showing the relative cortical blood perfusion of the left cerebral hemisphere measured by dynamic NIR-IIa fluorescence imaging (red bars) and laser Doppler method (blue bars), for the control group ($n = 3$), the cerebral hypoperfusion group ($n = 4$), and the MCAO group ($n = 4$). Reprinted with permission from ref 16. Copyright 2014 Nature Publishing Group.

4.3. Carbon Nanomaterials for Other Optical Imaging Modalities

4.3.1. Carbon Nanomaterials for Two-Photon Fluorescence Imaging. Two-photon laser scanning fluorescence microscopy was first invented by Denk, Webb, and co-workers in 1990.⁵¹⁰ In a two-photon excitation process, the fluorophore absorbs two photons simultaneously and is excited to a higher

energy state, after which the absorbed energy is released by emitting only one photon with a shorter wavelength (i.e., higher energy) than the absorbed photons as the molecule returns to the ground state (Figure 27a). The nonlinear two-photon excitation of a traditionally one-photon excited fluorophore results in anti-Stokes fluorescence emission that increases quadratically with the power density of the excitation, and thus has many benefits

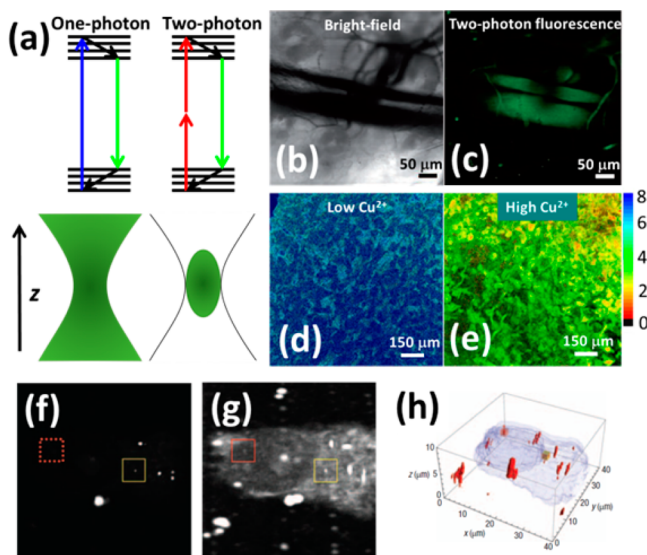


Figure 27. Two-photon fluorescence imaging using carbon nanomaterials. (a) Jablonski diagrams showing the process of one-photon excitation with Stokes fluorescence (upper left) and two-photon excitation with anti-Stokes fluorescence (upper right). Due to difference in excitation power dependency of one- and two-photon fluorescence, one-photon fluorescence can be excited in an extended volume including the beam waist (bottom left) while two-photon fluorescence can only be efficiently excited within a much smaller epifocal region at the beam waist (bottom right). (b, c) Bright-field (b) and two-photon fluorescence (c) images of ear blood vessels of a mouse intravenously injected with GO. The images are taken at 1 h post injection of GO. (b, c) Reprinted with permission from ref 155. Copyright John Wiley & Sons. (d, e) Ratiometric two-photon fluorescence images of lung cancer tissue slices with lower (d) and higher (e) Cu^{2+} concentrations. The images are plotted using the color map (with the scale bar on the right) that reflects the ratio of the two-photon fluorescence intensity in the blue channel (450–600 nm) to that in the red channel (620–700 nm). (d, e) Reprinted with permission from ref 520. Copyright 2013 Nature Publishing Group. (f) Two-photon fluorescence image of a fixed HeLa cell with 140 nm nanodiamonds internalized inside the cell. The excitation is an 875 nm femtosecond pulsed Ti:sapphire laser. (g) One-photon confocal fluorescence image of the same HeLa cell at the same focal depth as in (f). The excitation is a 532 nm continuous-wave laser. (h) A 3D image of the same cell as in (f) and (g), where the nanodiamond signal is based on two-photon fluorescence imaging and the cell body signal is based on the one-photon fluorescence imaging. (f–h) Reprinted with permission from ref 262. Copyright 2008 Nature Publishing Group.

for biomedical imaging. First, the probability of excitation and fluorescence emission in a two-photon or multiphoton process is supralinearly proportional to the photon flux (i.e., the power density), which can be equivalently expressed as $P \propto I^n$, where n is 2 for two-photon and $n > 2$ for other multiphoton cases.⁵¹¹ As a result, when the excitation beam penetrates through a deep tissue, only the fluorophores located at the beam waist of the excitation beam can get excited while the probability of exciting an out-of-focus fluorophore falls off quadratically or with an even higher order power relationship (Figure 27a). This allows for optical sectioning through a tissue volume by focusing and imaging the distribution of fluorophores layer by layer without the need of a pinhole. Second, unlike confocal microscopy that also allows for optical sectioning and achieves it by rejecting all the out-of-focus light, since only fluorophores located at the perifocal region are excited, two-photon microscopy avoids unnecessary photobleaching of unexcited fluorophores that are

located outside of the perifocal region. Third, two-photon fluorescence microscopy has a better chance of imaging features at greater depths inside a turbid biological tissue, owing to the efficient rejection of the interfering, scattered photons. This is because two-photon excitation and fluorescence emission only occur in the tightly focused beam waist; any scattered photons will not be able to reach nearly as high photon flux and power density as the focus of the excitation beam. Therefore, the scattered photons that deviate from the original path will not generate any fluorescence, reducing the amount of blurry background in traditional one-photon fluorescence imaging. Owing to these benefits, two-photon fluorescence microscopy has been widely used in neurobiology,^{512–515} oncology,⁴⁶⁷ and embryology⁵¹⁶ to interrogate structural and molecular features deep inside a living organism.

Carbon nanomaterials have been reported to have large two-photon absorption cross sections,^{225,517} allowing them to be used for two-photon fluorescence imaging in cells, tissue sections, and even live animals. It has been reported that, when one-photon fluorescent molecules are converted into inorganic carbon dot nanoparticles, the two-photon fluorescence intensity increases dramatically.²²⁷ Carbon nanotubes have been reported to have two-photon absorption followed by NIR-II fluorescence emission for different chiralities in an experiment designed to measure the exciton binding energies,⁵¹⁸ but to the best of our knowledge there has been no report on two-photon excited NIR-II fluorescence imaging in either in vitro or in vivo settings, partly due to the limited availability of infrared laser pulses with $>2\text{ }\mu\text{m}$ wavelengths (note that the two-photon excitation should be roughly double the emission wavelength). Nonetheless, other carbon nanomaterials including graphene, carbon dots, and nanodiamonds have been widely used as fluorescent dyes for in vitro and in vivo two-photon fluorescence imaging, owing to their short emission wavelengths in the visible window and thus convenient excitation wavelengths in the NIR-I or NIR-II windows.

Wang and Gu et al. have stained gastric cancer AGS cells with transferrin-conjugated and PEGylated graphene oxide, which shows strong fluorescence in the range 400–650 nm when excited by NIR pulsed lasers at ~ 800 nm. Two-photon fluorescence imaging of the stained cells is carried out, showing a much lower excitation power for efficient fluorescence imaging than a conventional molecular dye, fluorescein isothiocyanate (FITC), owing to a higher two-photon excitation cross section of graphene oxide.⁵¹⁹ He et al. performed in vivo intravital two-photon microscopy imaging of graphene oxide by injecting PEGylated graphene oxide intravenously. When the mouse ear blood vessels are imaged through a microscope objective, two-photon fluorescence signals under an NIR excitation of 810 nm are found to colocalize well with the blood vessels, indicating the traveling of fluorescent GO with the blood circulation (Figure 27b,c), while one-photon excitation at 405 nm does not show any meaningful fluorescence signal due to limited penetration depth of short-wavelength, one-photon fluorescence. The traveling velocity of an individual red blood cell (RBC) is measured by performing a line scan along the trajectory of that RBC using two-photon fluorescence microscopy owing to the shadow projected by the RBC in the blood flow. In vivo two-photon fluorescence imaging of the brain has also been performed in a live mouse after craniotomy surgery and injection, and depth-resolved 3D imaging and reconstruction are achieved up to a depth of 420 μm inside the mouse brain, taking advantage of the

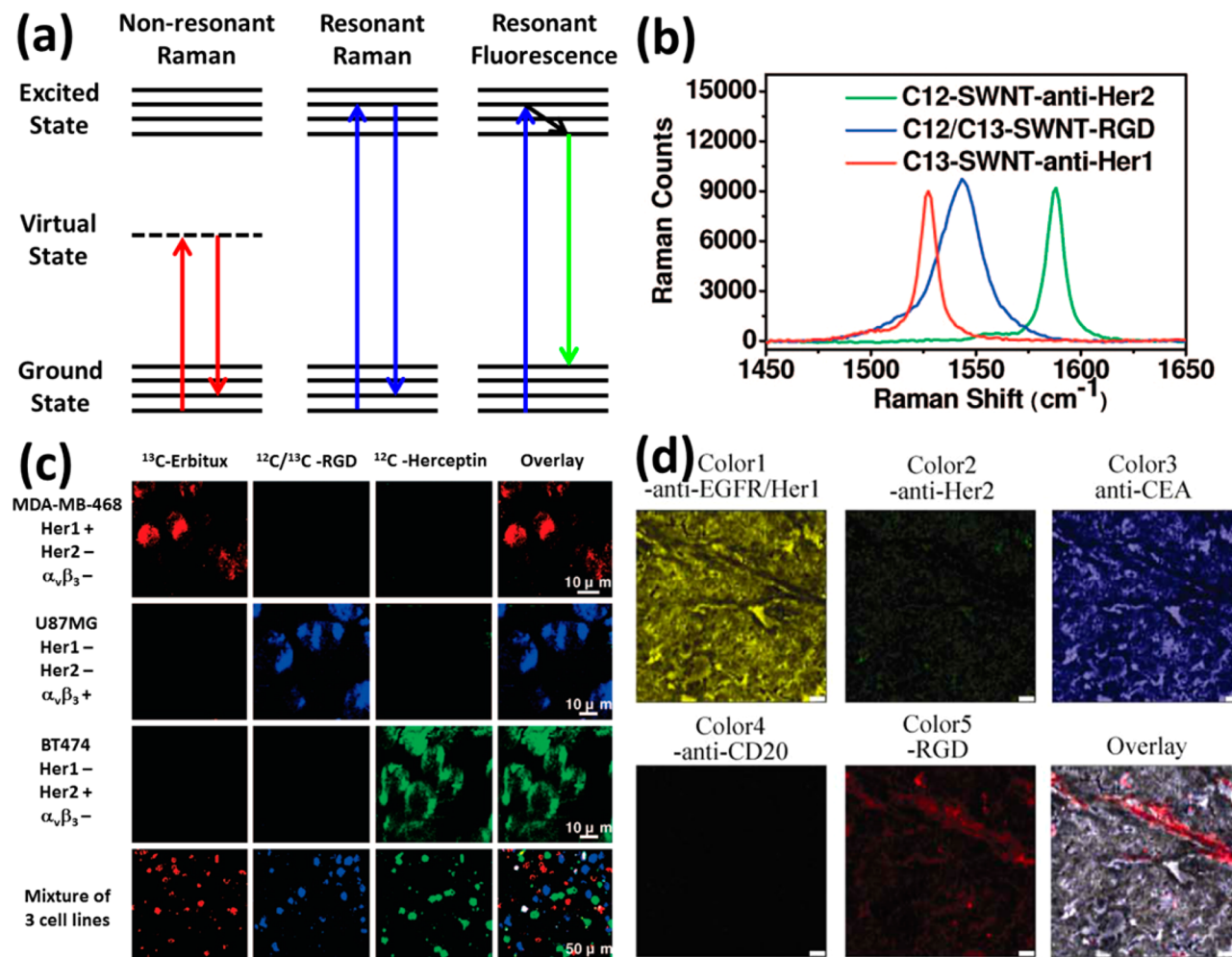


Figure 28. Resonant Raman imaging using carbon nanomaterials in an in vitro setting. (a) Jablonski diagrams showing the processes of nonresonant Raman scattering (left), resonant Raman scattering (middle), and resonant fluorescence (right). (b) Resonant Raman spectra of three SWCNT probes with different $^{12}\text{C}/^{13}\text{C}$ ratios taken in solution phase under a 785 nm laser excitation, exhibiting different G-band positions that allow for multicolor Raman imaging. (c) Multicolor Raman microscopic imaging using the three SWCNT probes (as shown in (b)) conjugated with different targeting ligands. The first three rows correspond to the Raman images of three different cell lines, with only one cell line stained at a time; the last row shows the Raman images of a mixture of cell lines stained together. The first three columns correspond to spectrally deconvolved, pseudocolored Raman images in three channels based on the G-band position while the last column is an overlaid image of the three channels. (b, c) Reprinted from ref 533. Copyright 2008 American Chemical Society. (d) Multicolor Raman microscopic imaging of an LS174T tumor slice using a five-color mixture of SWCNT Raman probes. The first five images are spectrally deconvolved Raman images in each individual channel based on the G-band peak position, while the last image represents an overlaid image of all five channels. Reprinted with permission from ref 534. Copyright 2010 Springer.

deep penetration and optical sectioning capability of two-photon fluorescence microscopy.¹⁵⁵

The two-photon excitation and fluorescence microscopic imaging of carbon dots can be dated back to 2007, when the Sun group reported on the observation of fluorescence emission at 400–500 nm under a two-photon excitation of 800 nm.²²⁵ Human breast cancer MCF-7 cells with internalized carbon dots are imaged under the two-photon fluorescence microscope, revealing the carbon dots are mostly located in the cytoplasm.²²⁵ Since then a handful of other groups have independently reported two-photon fluorescence imaging using carbon dots in a variety of settings. Tian et al. synthesized an in vitro pH sensor that responds to H^+ in a solution by changing its two-photon fluorescence intensity at ~ 520 nm, allowing real-time monitoring of $\text{Na}^+ - \text{H}^+$ exchange and cytosolic pH balance in live cells.²²⁹ In a more recent work done by the same group, another fluorophore, Nile blue, with constant two-photon fluorescence at 675 nm is covalently conjugated to the 465 nm emitting

carbon dot to afford a two-photon, bicolor ratiometric imaging probe for the detection of Cu^{2+} ions in live cells and tissues.⁵²⁰ Since the carbon dots used in this work lose their two-photon blue fluorescence at progressively increasing Cu^{2+} concentration while the internal reference molecule Nile blue with red fluorescence is inert to the environmental Cu^{2+} ion concentration, the overall fluorescence of the dual-fluorophore conjugate changes from blue (dominated by carbon dot) to yellow (dominated by both fluorophores) upon an increase of Cu^{2+} ion concentration. This ratiometric biosensor has been applied to live cells and tumor slices for functional imaging of local Cu^{2+} concentrations with sensitive color change upon two-photon excitation (Figure 27d,e).

Zheng et al. designed a drug-delivery system based on carbon dots and combined the two-photon fluorescence of carbon dots with Förster resonance energy transfer (FRET) between the cargo doxorubicin molecules and the drug carrier carbon dots to monitor the process of cargo release.²²⁴ The two-photon excited

fluorescence of carbon dots at ~ 500 nm becomes quenched in the presence of physisorbed doxorubicin molecules, leading to energy transfer and fluorescence emission of doxorubicin at ~ 600 nm. In addition, the physisorbed doxorubicin molecules can be unloaded under acidic pH, resulting in the recovery of the two-photon fluorescence of carbon dots. Therefore, by visualizing the fluorescence color of the carbon dot drug carrier, one can monitor the degree of drug release in real time.²²⁴ Another example by Gong et al. shows that two-photon fluorescence imaging of nitrogen-doped carbon dots is capable of deep tissue imaging at 1.8 mm depth inside a tissue phantom, which is not attainable by one-photon fluorescence imaging on the same sample.²²⁶ Besides two-photon excitation, three-photon fluorescence of carbon dots has been reported under an NIR-II excitation at 1028 nm, which allows cell imaging with internalized carbon dots.²²⁸

Nanodiamonds have been demonstrated to exhibit stable luminescence under two-photon excitation of the N–V centers. Fann et al. report that when a femtosecond pulsed laser operated at 875 nm is used to excite the nanodiamonds, the N–V⁰ center gets excited preferentially over the N–V[−] center owing to the better match between the excitation photon energy and the absorption band of the N–V⁰ center, resulting in a blue-shifted emission peak located at ~ 620 nm compared to the regular one-photon fluorescence of nanodiamonds at ~ 700 nm.^{262,521} Two-photon fluorescence of nanodiamonds shows significant benefits over one-photon fluorescence of the same material in a reduced background signal and improved contrast for *in vitro* 3D cell imaging. A 3D reconstructed image of a single cell with internalized nanodiamonds has been made possible by pinpointing the locations of nanodiamonds based on two-photon fluorescence signals and reconstructing the entire cell body based on one-photon fluorescence signals that include cell autofluorescence and scattering (Figure 27f–h).²⁶²

Although a substantial amount of work has been done to prove the concept of *in vitro* and even *in vivo* two-photon fluorescence imaging with a variety of carbon-based nanomaterials, we envisage some important future directions for carbon-nanomaterial-enabled two-photon and multiphoton fluorescence imaging. First, with the development of mid-infrared pulsed lasers providing 2–3 μm excitation lines and InGaAs camera for detection of NIR-II photons in the 1.0–1.7 μm window, two-photon fluorescence imaging of SWCNTs and other NIR-II emitting fluorophores should be made available for deep tissue fluorescence imaging that might afford unprecedented penetration depth owing to both long-wavelength excitation and emission. It has been reported that three-photon fluorescence microscopy with an excitation of a 1700 nm NIR-II pulsed laser can achieve a penetration depth of 1.4 mm for *in vivo* imaging of cerebrovasculature and neuronal network in live mouse brain, representing the longest excitation wavelength for fluorescence imaging despite the short emission wavelength of ~ 600 nm.⁴⁵⁶ It is anticipated that using longer wavelengths for both excitation and emission should further improve the imaging depth for noninvasive structural and molecular interrogation of the intact mouse brain owing to further reduced photon scattering of the emitted light, owing to the inversely proportional relationship of scattering versus wavelength.^{14,16,457} Second, the superior photostability of two-photon active carbon nanomaterials makes it possible to perform long-term imaging, tracking, and monitoring of specific biomarkers and cells labeled with two-photon fluorescence, such as in the cases for imaging the formation of connectomes and neural plasticity in live animals

during long-term learning and training experiences.^{513,522} Last but not least, the distinguishable two-photon fluorescence of carbon nanomaterials from the autofluorescence background bodes well for histological imaging and molecular phenotyping of the otherwise highly autofluorescent samples such as liver tissue sections, allowing for greater staining and detection sensitivity and higher signal-to-background ratio for such imaging purposes.⁵²³

4.3.2. Carbon Nanomaterials for Raman Imaging.

Raman scattering is an inelastic scattering process of a photon that gains or loses energy during the process, where the Stokes Raman process involves a loss in photon energy while a gain in energy is associated with anti-Stokes Raman process. Depending on if the absorbed photon energy matches that of the optical transition of the probed molecules or materials, Raman scattering can be subdivided into nonresonant Raman scattering and resonant Raman scattering, where in the former case an electron is excited to a virtual state before relaxation, and in the latter case an electron is excited to a real electronic state with the excitation energy corresponding to an optical transition (Figure 28a). Resonant Raman scattering has gained a significant amount of interest owing to the much higher Raman scattering cross sections.⁵²⁴ Graphitic carbon nanomaterials such as CNT, graphene, and carbon dot exhibit Raman scattering peak at the graphitic band (G-band), which is characteristic of all graphitic carbon-based materials.^{525–529} For pristine SWCNTs, another signature band in Raman scattering spectrum is the radial breathing mode (RBM) due to the radial expansion and contraction motions of the nanotube, based on which each chirality of small-diameter SWCNTs can be uniquely assigned.^{530,531} In a similar manner layer breathing mode (LBM) and interlayer coupling mode (C mode) can exist for fewer layer graphenes.⁵³² SWCNTs can exhibit strong resonance Raman scattering due to its 1D nature and sharp electronic transitions between van Hove singularities. The extremely large Raman scattering cross sections of SWCNTs have made them promising Raman labels and probes for *in vitro* and *in vivo* biomedical imaging,^{533–537} along with other Raman active nanomaterials based on surface-enhanced Raman scattering (SERS) of Raman reporter molecules by Au and Ag nanoparticles.^{538–544}

The first example of cell imaging by detecting the Raman RBM signals of SWCNTs was given by Strano et al., who incubated 3T3 fibroblast and myoblast cells in the presence of DNA-functionalized SWCNTs.⁵³⁵ Strong Raman signals are found in cells for up to 8 days of incubation, and the Raman RBM band is used to map out the distribution of internalized SWCNTs inside the cells. Our group has performed *in vitro* molecular imaging of cells using Raman active optical labels based on SWCNTs. We have reported Raman imaging of cells based on the G-band of SWCNTs to find out the degree of SWCNT uptake and molecular delivery ability as a function of surface coating on the nanotubes.⁴³⁸ However, these aforementioned examples have only “one color” for Raman imaging since all SWCNTs used as Raman probes will have highly similar Raman spectra, limiting the ability of using Raman imaging to probe different biomarkers or different cell types in spectrally resolved multiple channels.

To realize “multicolor” Raman imaging in a similar way to multicolor fluorescence imaging,⁵⁴⁵ our group has developed a novel strategy to generate spectral shift of the nanotube G-band by introducing the ¹³C isotope to the SWCNT composition with well-controlled ¹²C/¹³C ratios.^{533,534} This has been made possible by mixing ¹³C-methane with ¹²C-methane, which is the precursor of synthesizing SWCNTs via chemical vapor

deposition (CVD). Due to the isotope effect, the Raman G-band of SWCNTs can be shifted in a controllable way from 1590 cm^{-1} for pure ^{12}C -SWCNTs to 1528 cm^{-1} for pure ^{13}C -SWCNTs, leaving the spectral region between these two ends tunable by changing the $^{12}\text{C}/^{13}\text{C}$ ratio (Figure 28b). We first show that three spectrally distinguishable Raman probes, ^{12}C -SWCNT, $^{12}\text{C}/^{13}\text{C}$ -SWCNT, and ^{13}C -SWCNT, can be conjugated to different targeting ligands, Herceptin (anti-Her2), arginine-glycine-aspartic acid (RGD), and Erbitux (anti-Her1), respectively. These three-color ligand-SWCNTs are mixed and allowed to stain a mixture of three different cell lines, MDA-MB-468, U87MG, and BT474 cells with overexpressed Her1, $\alpha_v\beta_3$ integrin, and Her2 receptors, respectively. Raman imaging of the mixed cells reveals multiplexed imaging of different molecular phenotypes in different cell lines with little or no crosstalk, evidenced by minimum color overlapping in the overlaid pseudocolor Raman images (Figure 28c).⁵³³ In a follow-up work,⁵³⁴ we have expanded the three-color Raman imaging probes to five-color multiplexed molecular imaging with five different $^{12}\text{C}/^{13}\text{C}$ compositions in the SWCNT Raman probes. All five different colors of the SWCNTs can be excited by the same 785 nm laser and resolved by spectral deconvolution, and the palette of multicolor Raman probes enables us to perform molecular imaging that reveals the different expression levels of five biomarkers, Her1 receptor, Her2 receptor, $\alpha_v\beta_3$ integrin, carcinoembryonic antigen (CEA), and B-lymphocyte antigen CD20, in cells and tumor sections via Raman microscopic imaging (Figure 28d). An upregulated expression of Her1 and CEA has been found in the LS174T tumor slice with overexpressed $\alpha_v\beta_3$ integrins on the endothelial cells that form the blood vessels in the tumor.⁵³⁴

Gold and silver nanoparticles with surface plasmon resonance (SPR) have been widely used for enhancing the Raman scattering intensity of molecules adsorbed on their surface via the local electric field amplification.^{546,547} SWCNTs with Raman enhancing films comprised of plasmonic Au nanoparticles have been used as labels for detection of a variety of analytes with high sensitivity and low detection limit.^{548,549} A nanocomposite made of SWCNT and Au nanoparticles should thus provide a higher Raman intensity for imaging. To this end, Liu et al. have modified the DNA-coated SWCNTs with Au and Ag nanoparticles via solution phase synthesis, and have demonstrated Raman imaging of cells specifically labeled with the PEGylated and folate-functionalized SWCNT–metal bioconjugate. Compared to traditional Raman-based cell imaging with SWCNTs alone, the introduction of SERS-active noble metal nanoparticles helps capture Raman images with a significantly shortened period of time (0.1 s integration time per pixel with enhancement versus 1–2 s without enhancement) owing to the enhanced signal and thus improved SNR.⁵⁵⁰ Besides the SWCNT–metal nanocomposite, Li et al. reported the synthesis of GO/Au hybrid nanoparticles and studied the cell internalization pathway of the GO/Au hybrid by performing Raman imaging of cells incubated with the hybrid nanoparticles at different temperatures, where a much stronger Raman signal from GO has been observed in the presence of Au.⁵³⁷ A similar GO/Ag hybrid nanostructure has also been reported for Raman-based cell imaging with higher Raman signals.⁵⁵¹

In vivo Raman imaging is also pursued independently by multiple research groups. Our group and the Gambhir group explore in vivo Raman imaging using SWCNTs conjugated with RGD peptide in an $\alpha_v\beta_3$ integrin positive U87MG tumor model in living mice. We find a strong, increasing Raman signal over a

72-h period from the xenograft U87MG tumor in the mice injected with RGD conjugated SWCNTs and little to no signal from the control mice injected with plain SWCNTs (Figure 29a,b).^{536,542} With in vivo Raman microscopy, Liu et al. have

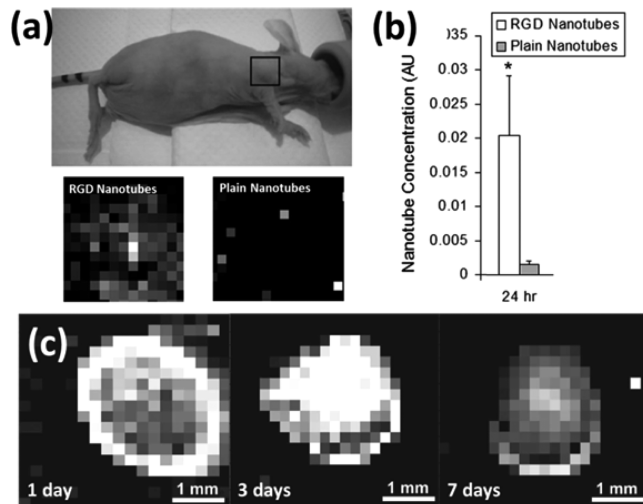


Figure 29. Resonant Raman imaging using carbon nanomaterials in an in vivo setting. (a) White-light digital photograph (top) of a U87MG tumor-bearing mouse with the in vivo Raman images of tumors from two mice, one injected with RGD conjugated SWCNTs showing the accumulation of SWCNTs in the tumor (bottom left) and the other injected with plain SWCNTs as a negative control (bottom right). The Raman images are taken 24 h post injection of the SWCNTs with a step size of $750\text{ }\mu\text{m}$ corresponding to each pixelated square in both images. (b) Bar chart summarizing the concentrations of RGD conjugated SWCNTs and plain SWCNTs inside the U87MG tumor based on the measured Raman intensities from in vivo Raman imaging. (a, b) Reprinted with permission from ref 542. Copyright 2008 National Academy of Sciences. (c) In vivo Raman images of subcutaneously transplanted hMSCs labeled with SWCNTs in the back of a mouse, suggesting SWCNTs can be used as labels for long-term in vivo tracking. Reprinted with permission from ref 552. Copyright 2012 John Wiley & Sons.

successfully tracked the human mesenchymal stem cells (hMSCs) labeled with SWCNTs after subcutaneous transplantation into the back of the mice (Figure 29c).⁵⁵² These findings suggest in vivo Raman imaging as a sensitive and noninvasive approach for molecular and cellular interrogation in living subjects. However, there are still several major drawbacks of in vivo Raman imaging that limit its potential for broader applications. First of all, so far only bare SWCNTs without any metal nanoparticle decoration or any Raman enhancement have been used for in vivo Raman imaging, which is unfavorable for in vivo structural and molecular interrogation given severe tissue attenuation that worsens the weak Raman intensities. To this end, graphitic nanomaterials coated with noble metals may be delivered in vivo assuming the introduction of metal nanostructures does not alter the pharmacokinetics of the original Raman probes. Moreover, so far most in vivo Raman studies are performed with NIR-I laser excitation at a wavelength of 785 nm. If the G-band of graphitic nanomaterials is probed for imaging, the equivalent wavelength of Raman scattering photons would be around 900 nm, still in the NIR-I window. One can see from the preceding sections on NIR-II fluorescence imaging that imaging with NIR-I photons has shallow penetration depth and blurry features due to the strong photon scattering by thick

biological tissues. The indistinct features observed in Figure 29 indeed reflect the severe scattering associated with the short-wavelength photon emission and can be improved by using longer-wavelength excitation in the Raman process. Another disadvantage of Raman-based *in vivo* imaging compared to fluorescence-based *in vivo* imaging lies in the instrumentation of the Raman imaging system, which is usually implemented by a laser scanning Raman microscope with low throughput. The development and increasing availability of a wide-field Raman imaging system^{553,554} should address this problem and allow for faster *in vivo* Raman imaging over a larger field of view without the need to perform raster scan.

4.3.3. Carbon Nanomaterials for Transient Absorption Imaging

Imaging. All previous imaging modalities described in this section acquire images by collecting emitted photons from different carbon nanomaterials, although the mechanism of generating the emitted photons and the wavelength of the emitted photons may vary. In this section we will touch upon a different approach of optical imaging with carbon nanomaterials based on the absorption of incoming photons.

Transient absorption microscopy is an emerging imaging tool allowing for label-free imaging of endogenous biomolecules such as melanin and hemoglobin in cells and biological tissues.^{555,556} In this imaging method, a temporally modulated pump laser is used to perturb the electronic states and the distribution of electrons in these states for a certain molecule or material, while a probe laser is simultaneously used to interrogate the perturbed electronic states by detecting the change in optical absorption of the probe laser as a response to the pump laser. Taking the arc-discharge SWCNTs as an example, when a pump laser at 707 nm and a probe laser at 885 nm are used, since the pump laser wavelength matches the E_{11} transition of metallic SWCNTs (600–800 nm) while the probe laser wavelength matches the E_{22} transition of semiconducting SWCNTs (850–1100 nm),⁴⁷⁶ this pump–probe combination results in reduced absorption of the probe field (in-phase modulation) for semiconducting SWCNTs owing to the stimulated emission, and enhanced absorption of the probe field (antiphase modulation) for metallic SWCNTs due to the broadening of the metallic E_{11} transition and the off-resonance probe wavelength (Figure 30a).⁵⁵⁷ The phase of the transient absorption signal in the probe field can thus be used as imaging contrast to form images that discriminate different electronic types of SWCNTs by performing 2D raster scan of a field of view, where semiconducting SWCNTs appear with positive contrast and metallic SWCNTs appear with negative contrast (Figure 30b–d).

With this powerful tool of imaging both semiconducting SWCNTs and metallic SWCNTs with microscopic spatial resolution, Cheng et al. have shown that cellular uptake and intracellular trafficking of DNA-functionalized SWCNTs can be imaged with transient absorption microscopy (Figure 30e,f).³¹⁵ When the SWCNTs are administered into the mouse via tail vein injection, the circulation of individual SWCNTs can be monitored by intravital transient absorption microscopy with high temporal resolution. Liver tissue slices from the mouse injected with SWCNTs reveal accumulation of SWCNTs mainly in the Kupffer cells, which are labeled with ED-1 antibody (Figure 30g,h). One important advantage of transient absorption microscopy for liver tissue imaging is the negligible interference from tissue autofluorescence, which is a long-lasting, nontrivial problem for conventional fluorescence imaging of liver tissue with immunohistochemical staining.⁵⁵⁸ The transient absorption microscope images shown in Figure 30g,h reveal little to no

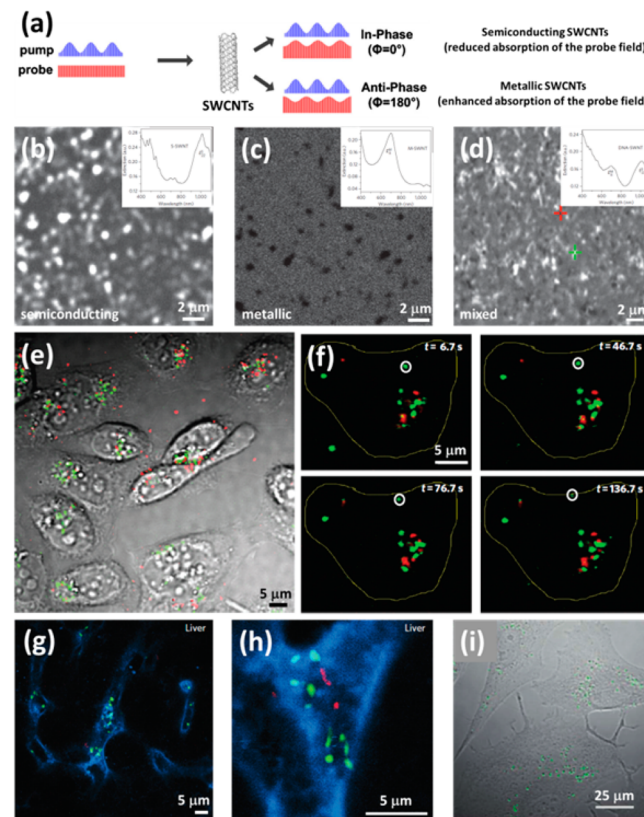


Figure 30. Transient absorption microscopy imaging using carbon nanomaterials. (a) Schematic showing the temporally modulated profiles of the pump and probe lasers, which interact with semiconducting and metallic SWCNTs differently, resulting in in-phase and antiphase modulation of the probe field that can be detected and used as a contrast for forming images. Reprinted with permission from ref 557. Copyright 2010 American Physical Society. (b–d) Transient absorption images of semiconducting SWCNTs (b), metallic SWCNTs (c), and DNA-wrapped SWCNTs containing both electronic types (d). (e) Typical transient absorption microscopy image of CHO cells with internalized DNA-SWCNTs, where the semiconducting SWCNTs with in-phase probe response are color-coded in green and the metallic SWCNTs with antiphase probe response are color-coded in red. (f) Time-lapse transient absorption microscopy images showing the process of a semiconducting SWCNT (green dot in white circle) being transported back to the cell membrane over time. (g) Transient absorption microscopy image of liver tissue from a mouse injected with SWCNTs, showing extremely low autofluorescence background that enables easy detection of individual metallic (red) and semiconducting (green) SWCNTs inside the Kupffer cells (blue). (h) Zoomed-in transient absorption microscopy image of the same liver slice. (b–h) Reprinted with permission from ref 315. Copyright 2012 Nature Publishing Group. (i) Overlaid image of bright-field optical imaging and transient absorption microscopic imaging of NIH-3T3 fibroblasts with internalized nonfluorescent nanodiamonds. The locations of the nanodiamonds are shown as green dots in the image. Reprinted with permission from ref 559. Copyright 2013 Royal Society of Chemistry.

background from autofluorescence, owing to the selection of pump/probe wavelengths that specifically match the transition energy of the SWCNT contrast agents and avoid excitation and stimulated emission of the endogenous, autofluorescent species in the tissue.³¹⁵

One of the most prominent strengths of transient absorption microscopy, as discussed in the beginning of this section, is the capability of imaging nonfluorescent molecules and materials, or samples without photon emission. Therefore, it provides a useful

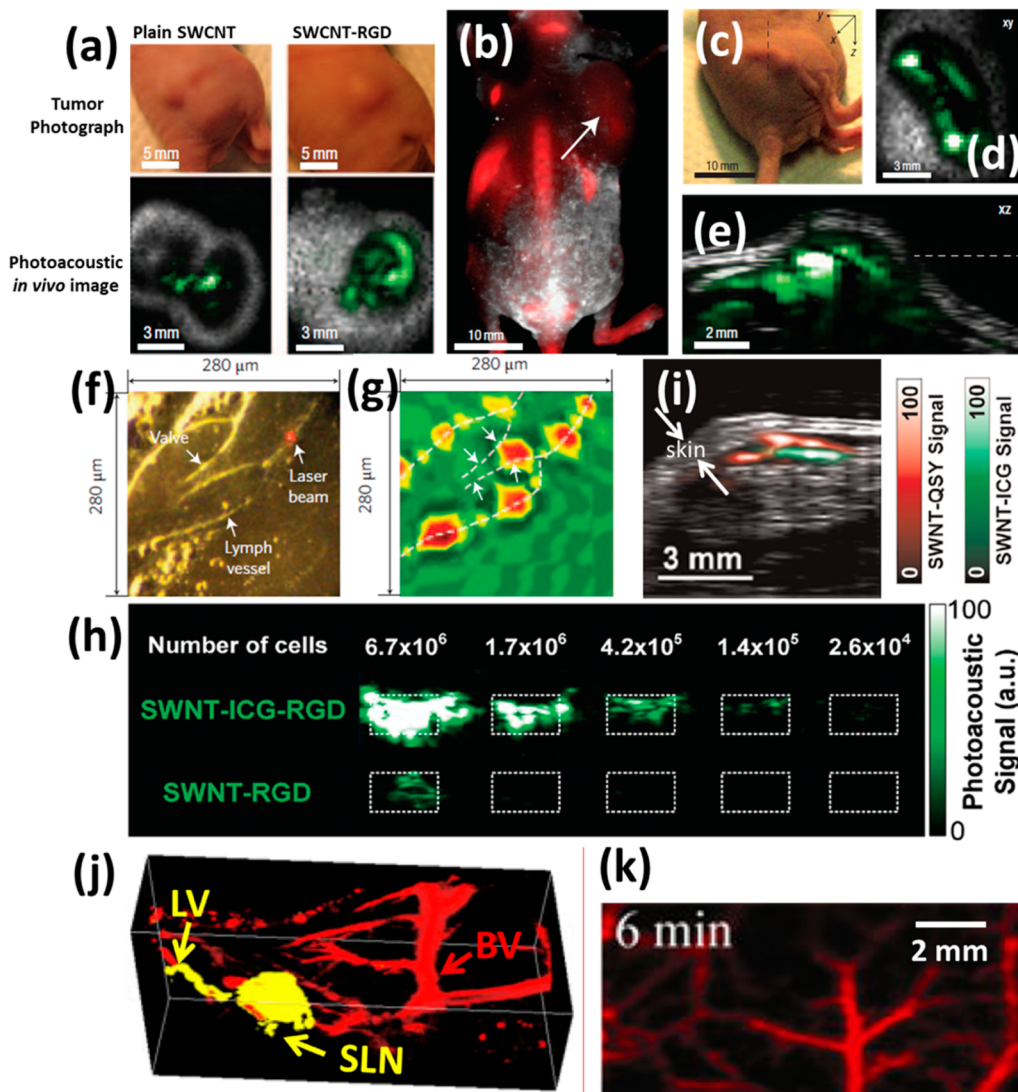


Figure 31. In vivo photoacoustic imaging with carbon nanomaterials. (a) In vivo photoacoustic imaging of U87MG tumors in live tumor-bearing mice injected with plain SWCNT (left column) and SWCNT-RGD (right column). The top row shows the white-light digital photographs of the tumor region in the tumor-bearing mice, while the bottom row shows corresponding photoacoustic images (green) overlaid on top of ultrasound images (gray). (b) Wide-field fluorescence image of a U87MG tumor-bearing mouse injected with RGD-conjugated quantum dots. Due to the short fluorescence wavelength associated with severe photon scattering, the tumor is shown with blurry and diffuse fluorescence signals indicated by the white arrow. (c–e) Photoacoustic imaging of the U87MG tumor (with a digital photograph in (c)), showing sharper feature resolution in the *xy* plane (d) and deeper penetration depth over 2 mm inside the tumor (e). (a–e) Reprinted with permission from ref 12. Copyright 2008 Nature Publishing Group. (f) Fragment of mouse mesentery imaged through optical microscope. The bright yellow lines correspond to the lymphatic vessel walls. (g) Photoacoustic image of the same mouse mesentery fragment, showing the distribution of lymphatic vessel endothelial hyaluronan receptor LYVE-1, probed by golden carbon nanotubes conjugated with the anti-LYVE-1 antibody. The photoacoustic signal from golden carbon nanotubes is displayed from green, yellow to red to show the increasing intensities. (f, g) Reprinted with permission from ref 567. Copyright 2009 Nature Publishing Group. (h) Comparison of photoacoustic images between SWCNT-ICG conjugate (top row) and plain SWCNT (bottom row). The images were taken as vertical slices through an agarose phantom which contains U87MG cancer cells stained with the RGD conjugates of both versions of SWCNTs. Reprinted from ref 568. Copyright 2010 American Chemical Society. (i) Multiplexed two-color in vivo photoacoustic imaging of SWCNT-QSY (with absorption maximum at 710 nm, red) and SWCNT-ICG (with absorption maximum at 780 nm, green), which are subcutaneously injected into a live mouse. Reprinted from ref 571. Copyright 2012 American Chemical Society. (j) A 3D photoacoustic image showing the sentinel lymph node (SLN) and a lymphatic vessel (LV) surrounded by blood vessels (BVs). The contrast of SLN and LV is enhanced by intradermally injected carbon dots, while the BVs are imaged with the endogenous contrast offered by hemoglobin. (k) A 2D photoacoustic image of the femoral blood vasculature at 6 min after intravenous injection of carbon dots. (j, k) Reprinted with permission from ref 581. Copyright 2013 Springer.

tool of imaging nonfluorescent and low-fluorescent carbon nanomaterials such as fullerenes, pristine graphene, and raw nanodiamonds without N–V centers. For example, Huang et al. have applied this imaging technique for N–V center free, nonphotoluminescent, raw nanodiamonds in cells, and the cell internalization dynamics can be probed by using a pseudo-3D

transient absorption microscopy forming images at two focal planes simultaneously (Figure 30i).⁵⁵⁹ Although there has not been any report on using transient absorption microscopy for biomedical imaging based on the fullerene nanoparticles with low fluorescence quantum yields, or pristine, unoxidized graphene sheets without photoluminescent edge states, several works have

already shown the proof of concept that these materials can be imaged by transient absorption microscopy.^{560,561} One possible application along this direction could be *in situ* imaging of graphene-based tissue reinforcing and scaffolding materials^{23,562} to reveal the local morphological changes and interactions with the surrounding biochemical environment of these tissue implants without additional dye labeling.

4.4. Carbon Nanomaterials for Nonoptical Imaging Modalities

Aside from the large variety of optical imaging capabilities offered by carbon nanomaterials, other nonoptical imaging modalities can also be realized by employing these materials either as contrast agents by themselves or as nanocarriers for contrast agents. In this section we will focus on the applications of carbon nanomaterials for nonoptical imaging modalities, including photoacoustic imaging, X-ray CT, magnetic resonance imaging (MRI), and nuclear medicine imaging. Owing to the high optical density in the visible and NIR windows,⁹⁵ carbon nanotubes and graphene can act as contrast agents for photoacoustic imaging. Nanodiamonds can generate MRI contrast due to the existence of N–V centers that impart the magnetic properties to nanodiamonds.⁵⁶³ Moreover, all these carbonaceous nanomaterials can load different exogenous contrast agents for X-ray CT, MRI, positron emission tomography (PET) and single photon emission computed tomography (SPECT), affording multimodality imaging capabilities.

4.4.1. Carbon Nanomaterials for Photoacoustic, Thermoaoustic, and Photothermal Imaging. As a hybrid imaging modality, photoacoustic imaging exploits the photoacoustic effect, in which optical photons are absorbed and converted to heat, leading to emission of acoustic waves as a result of the transient thermoelastic expansion of the locally heated biological tissue. The photoacoustic waves are wide-band ultrasonic waves that can be detected by a high-frequency focused ultrasonic transducer to form images.^{564,565} Photoacoustic imaging can be applied as an *in vivo* label-free imaging modality due to the strong absorption of photons by hemoglobin in the blood, allowing for functional, high resolution imaging of saturated O₂ in the blood and cerebrovascular imaging through intact scalp and skull.^{564,566} On the other hand, the photoacoustic signal can be significantly enhanced by the use of exogenous contrast agent. An ideal contrast material for photoacoustic imaging should have high photon absorbance and sufficient conversion efficiency from light to heat (that is, low likelihood of converting photons to radiative emission and low quantum efficiency of photoluminescence). In this sense, graphitic carbon nanomaterials, including carbon nanotubes and graphenes, are perfect candidates for photoacoustic imaging because not only are they good light absorbers throughout the entire visible and NIR windows, but they also have relatively low fluorescence quantum yields^{87,278,401} indicating greater efficiencies of converting incoming photons to heat.

SWCNTs are the first and the most widely used carbon nanomaterial applied for *in vivo* photoacoustic imaging.^{12,552} The strong optical absorbance of SWCNTs at 690 nm leads to efficient generation of acoustic signals when excited by a 690 nm laser, which are found to increase proportionally to the concentration of SWCNTs. Another advantage of using the 690 nm laser to excite the photoacoustic signal of SWCNTs is that the ratio of SWCNT to hemoglobin acoustic signal is higher at 690 nm than at other wavelengths, minimizing the interference from the photon absorption and acoustic conversion of

hemoglobin molecules.¹² With a photoacoustic excitation light at 690 nm, the Stanford groups reported using a PEGylated SWCNT bioconjugate functionalized with RGD peptide (SWCNT–PEG–RGD) for specific *in vivo* targeting and photoacoustic imaging of α_vβ₃ integrin positive U87MG tumors in live mice, in side-by-side comparison with *in vivo* photoacoustic imaging in the same tumor model using plain SWCNTs without RGD conjugation (Figure 31a). This result suggests that photoacoustic imaging can be employed as a molecular imaging modality by functionalizing the appropriate contrast agents with molecular targeting moieties. In addition, the performance of photoacoustic imaging has been evaluated by comparing to regular fluorescence imaging method with quantum dots (Figure 31b), and photoacoustic imaging with SWCNTs exhibits a much deeper tissue penetration and crisper image resolution due to much lower scattering of acoustic waves, despite scattering associated with the optical excitation light (Figure 31c–e).¹²

Since the first report on *in vivo* photoacoustic molecular imaging using SWCNTs, there have been a few other works aimed at improving the sensitivity of imaging by increasing the absorbance of SWCNTs in the NIR region.⁵⁶⁷ Zharov et al. coated SWCNTs with a thin layer of gold shell (named “golden carbon nanotubes”), which enhances the absorbance of SWCNTs by almost 100 times in the NIR region. This enhancement in photon absorption leads to a much higher photoacoustic signal generated by the golden carbon nanotubes, allowing for targeted lymphatic vessel imaging (Figure 31f,g) under an extremely low laser fluence level on the order of merely millijoules per square centimeter.⁵⁶⁷ Through the π–π stacking interactions, indocyanine green (ICG) molecules with strong optical absorption at 780 nm have been successfully attached to the backbone of SWCNTs, significantly enhancing the photoacoustic signals.^{568,569} Compared to an earlier formulation of photoacoustic contrast agent by using SWCNTs only,¹² the SWCNT–ICG conjugate shows a much lower detection limit of cancer cells down to 1.4×10^5 cells, ~20 times lower than the plain SWCNT without any ICG attachment (Figure 31h).⁵⁶⁸

To afford multiplexed photoacoustic imaging of different biomarkers and anatomical structures for *in vivo* study, photoacoustic contrast agents can be made to have their optical absorption maxima at different wavelengths, resulting in “multicolor” probes that allow for multiplexed targeting and photoacoustic imaging. A pioneering work along this direction was achieved by Zharov et al. in 2009, in which they added the magnetic nanoparticles with strong photoacoustic response at 639 nm to their previously reported golden carbon nanotubes with maximum photoacoustic signal at 900 nm, making a two-color photoacoustic imaging system.⁵⁷⁰ Circulating tumor cells (CTCs) can be labeled with urokinase plasminogen activator conjugated magnetic nanoparticles, folate conjugated golden carbon nanotubes, or both, allowing for identification of different biomarkers and subtypes of CTCs based on the multiplexed probes. When the labeled CTCs are illuminated by consecutive laser pulses at wavelengths of 639 and 900 nm with a 10 ms delay, CTCs with different surface receptors will have temporally different photoacoustic responses that help one discriminate one cell phenotype from another.⁵⁷⁰ More recently, a five-color multiplexed photoacoustic imaging modality has been realized, where the multiple “colors” are created by attaching small optical dyes with different absorption maxima to SWCNTs. A proof-of-concept study is carried out by subcutaneously injecting SWCNT–ICG and SWCNT–QSY in a live mouse, where the SWCNT–QSY gives the maximum photoacoustic signal at 710

nm and SWCNT–ICG at 780 nm. The photoacoustic signals from the dual color contrast agents can be spectrally separated with little crosstalk, boding well for multiplexed *in vivo* molecular imaging in the future (Figure 31i).⁵⁷¹

Besides photoacoustic imaging, it is worth mentioning two other related imaging modalities, thermoacoustic imaging and photothermal imaging, where SWCNTs have been employed as contrast agents. Thermoacoustic imaging differs from photoacoustic imaging in the input energy source, that is, how heat is generated. In photoacoustic imaging, optical photons are absorbed and converted into heat by the light absorber, which causes thermoelastic expansion of the surrounding matrix and generates acoustic signals. Thermoacoustic imaging employs microwave pulses as the input energy source, which can be absorbed by microwave absorbers and turned into heat and acoustic waves. Wang et al. found SWCNTs are good microwave absorbers and can generate thermoacoustic signals after receiving energy from a 3.0-GHz pulsed microwave source, making them potential contrast agent for thermoacoustic imaging.⁵⁷² Photothermal imaging distinguishes itself from photoacoustic imaging in the signal output, or how the light-induced temperature increase is detected. Photoacoustic imaging detects the rise in temperature by collecting acoustic waves as a result of lattice expansion, while photothermal imaging detects the temperature change by employing the so-called thermal lens effect. The thermal lens effect dictates that heat changes the refractive index of the medium as a function of temperature, in which the probing laser light travels and defocuses, and therefore becomes detectable.^{573,574} Therefore, unlike photoacoustic imaging where only one laser is used as input and an ultrasound transducer is used to collect the output signal, photothermal imaging requires the use of two lasers: one as the heating laser and the other as the probing laser. Zharov et al. have shown that golden carbon nanotubes can be used for *in vivo* photothermal imaging to reach similar image quality as photoacoustic imaging.^{567,575}

Other carbon nanomaterials, such as graphene, carbon dots, and nanodiamonds, have also been reported as photoacoustic contrast agents for *in vivo* imaging. For graphene-based nanomaterials, rGO with less destroyed π -conjugated aromatic structures is more favorable for photoacoustic imaging than GO, owing to a higher degree of photon absorption in the NIR region.¹⁵⁷ Liu et al. reported an rGO-based conjugate consisting of strongly NIR light absorbing rGO, iron oxide nanoparticles (IONPs) for multimodal MRI imaging, and PEG chains to increase blood circulation time after intravenous administration. A 4T1 tumor model is used to show the passive accumulation of the rGO–IONP–PEG conjugate in the tumor, evidenced by the detected photoacoustic signals attributed to the existence of rGO.¹⁶⁰ Cai et al. report in a similar manner that nano-rGO synthesized by protein-assisted reduction and surface functionalization shows a much higher photoacoustic signal than the GO precursor under the same laser power, allowing them to use nano-rGO as photoacoustic contrast agent for *in vivo* tumor imaging.⁵⁷⁶ Instead of chemically reducing GO to rGO,⁵⁷⁷ He et al. have reported the direct production of graphene nanosheets with largely retained π -conjugated aromatic structures and showed the potential of using the as-synthesized graphene nanosheets as photoacoustic contrast agent under both 700 and 800 nm red to near-infrared illuminations.¹⁵⁶ In addition to graphene nanosheets, oxidized graphene nanoribbons have also been reported as potential photoacoustic contrast agents.⁵⁷⁸ It is also noteworthy that, in a way similar to SWCNTs, the low

optical absorption of GO can be enhanced with the attachment of ICG, and the GO–ICG conjugate has been used for *in vitro* photoacoustic imaging of colonies formed by HeLa cells.⁵⁷⁹

Aside from graphene and its derivatives, fullerene derivatives also exhibit strong contrast suitable for photoacoustic imaging. Krishna et al. studied how surface groups and coating molecules affect the photoacoustic contrast and found polyhydroxy fullerenes (PHFs) encapsulated in chitosan have the highest photoacoustic contrast.⁵⁸⁰ With intratumoral injection of the chitosan-coated PHF nanoparticles, the tumor body becomes apparently visible in an *in vivo* photoacoustic imaging experiment and can also get ablated by the photothermal effect that we will look into in much more detail later in this review paper. Pan et al. report the synthesis of carbon dots from honey with a strong photoacoustic signal, which allows them to perform 3D photoacoustic imaging of a sentinel lymph node surrounded by many blood vessels by injecting the carbon dots intradermally (Figure 31j). Owing to the high photoacoustic response of the carbon dots, real-time photoacoustic imaging of the circulating carbon dots in femoral blood vessels (Figure 31k) has been made possible to reveal the clearance of the intravenously administered carbon dots over a period of 30 min.^{216,581} Nanodiamonds have also been reported as photoacoustic contrast agents by either conjugating them with gold nanoparticles or engineering the defect centers to afford high absorbance and thus strong photoacoustic signal to NIR illumination.^{582,583}

Photoacoustic imaging, being a hybrid imaging modality, takes advantages of both optical photons and ultrasonic waves to achieve optimum imaging penetration and spatial resolution.⁵⁸⁴ Compared to the all-optical fluorescence imaging in the visible and NIR-I windows with carbon nanomaterials, contrast-enhanced photoacoustic imaging offers deeper tissue penetration that allows for vertical slice imaging as shown in Figure 31e,i, and higher image clarity due to significantly reduced scattering of acoustic waves. Compared to ultrasound imaging where only acoustic waves are employed, photoacoustic imaging gains higher spatial resolution owing to the use of tightly focused optical photons as the excitation source. The development of exogenous contrast agents based on various carbon nanomaterials greatly expands the application of photoacoustic imaging from functional imaging of blood oxygen saturation to multiplexed molecular imaging with high sensitivity and specificity.^{12,552} Therefore, it is foreseeable that the development of more efficient exogenous contrast agents based on the advancement of nanotechnology is likely to offer more opportunities to photoacoustic imaging with deeper penetration depth, higher sensitivity, and greater multiplicity.

4.4.2. Carbon Nanomaterials for X-ray Computed Tomography (CT), Magnetic Resonance Imaging (MRI), and Radionuclide Imaging with Loaded Contrast Agents. CT, MRI, PET, and SPECT are widely used imaging modalities for both fundamental scientific research and clinical diagnosis. Unfortunately, most of the aforementioned carbon nanomaterials do not have the intrinsic properties suitable for these imaging modalities unless loaded with specific contrast agents. For example, a good CT contrast agent requires a high density of heavy atoms with high X-ray absorption cross sections to generate contrast in the form of a shadow to the X-ray illumination. Iodine-containing vesicles or micelles, gold nanoparticles, and lanthanide nanoparticles are the most common contrast agents for X-ray CT imaging owing to the existence of heavy atoms in their chemical compositions.⁵⁸⁵ MRI contrast agents have the effect of shortening the T_1 or T_2 relaxation time.

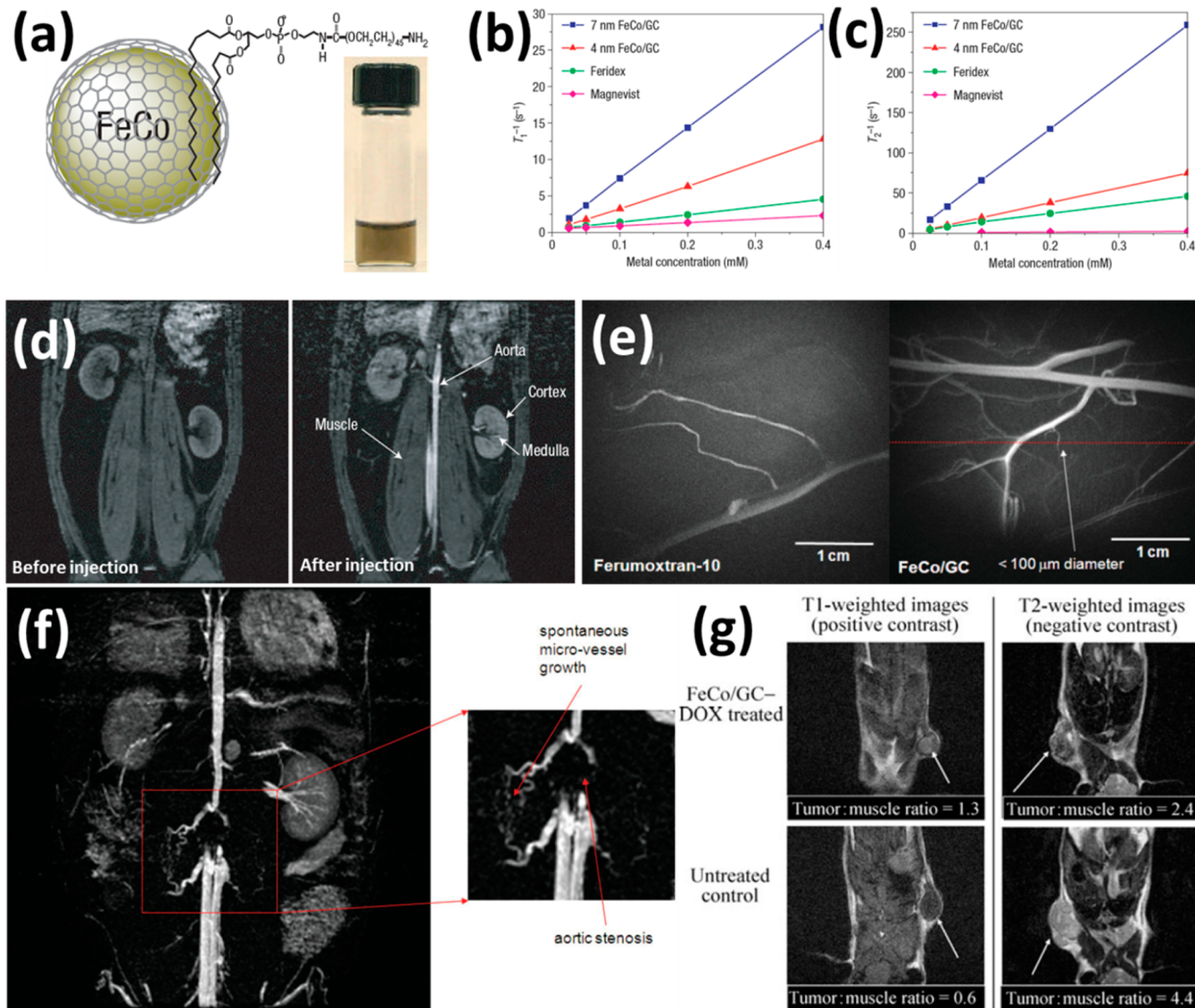


Figure 32. In vivo MRI imaging with FeCo/single-graphitic-shell nanocrystals. (a) Schematic drawing of the FeCo/single-graphitic-shell nanocrystal showing the encapsulation of a FeCo nanoparticle inside a single layer of graphene and the adsorption of phospholipid-PEG on the graphitic surface to increase the water solubility. The inset shows a solution of the FeCo/single-graphitic-shell nanocrystals after being heated up to 80 °C for 1 h, indicating good stability of the suspension. (b) T_1^{-1} plotted as a function of metal concentration for different MRI contrast agents: 7 nm FeCo/graphitic carbon (FeCo/GC), 4 nm FeCo/GC, Feridex, and Magnevist. The slope of each plot represents the T_1 relaxivity of that specific material, and 7 nm FeCo/GC has the highest T_1 relaxivity of $70 \text{ mM}^{-1} \cdot \text{s}^{-1}$. (c) T_2^{-1} plotted as a function of metal concentration for different MRI contrast agents, where the slope of each plot represents the T_2 relaxivity of that specific material. The 7 nm FeCo/GC has the highest T_2 relaxivity of $644 \text{ mM}^{-1} \cdot \text{s}^{-1}$. (d) T_1 -weighted MRI images of a rabbit before (left) and after (right) intravenous injection of the FeCo/single-graphitic-shell nanocrystals. (a–d) Reprinted with permission from ref 292. Copyright 2006 Nature Publishing Group. (e) High resolution MRI images of rabbit upper hind limb vasculature, enhanced by the commercial contrast agent Ferumoxtran-10 (left) and FeCo/GC (right). A small microvessel intersected by the red dashed line in the FeCo/GC enhanced image has a $<100 \mu\text{m}$ diameter (indicated by the white arrow). (f) FeCo/GC contrast enhanced MRI images of microvessels around the aortic stenosis, where the zoomed-in view on the right indicates spontaneous angiogenesis as a response to the induced aortic stenosis. (e, f) Reprinted with permission from ref 601. Copyright 2009 John Wiley & Sons. (g) T_1 -weighted (left column) and T_2 -weighted (right column) MRI images of 4T1 tumor-bearing mice with injection of FeCo/GC (top row) and without any treatment (bottom row). Reprinted with permission from ref 293. Copyright 2011 Springer.

The most widely used MRI contrast agent for T_1 relaxation shortening is the paramagnetic Gd^{3+} -containing chelate molecules, while that for T_2 relaxation shortening is the superparamagnetic iron oxide nanoparticles.⁵⁸⁶ Molecules containing radioactive isotopes are widely used as nuclear medicine contrast agents, such as ^{18}F and ^{64}Cu for PET imaging, as well as $^{99\text{m}}\text{Tc}$ for SPECT imaging.⁵⁸⁷

To afford CT imaging, the X-ray absorption cross section of carbon nanomaterials needs to be significantly increased since

carbon atoms do not provide enough X-ray attenuation for CT imaging. Nevertheless, SWCNTs intrinsically have field electron emission property and can be used as an X-ray source for CT imaging, as Zhou et al. have demonstrated in a myriad of applications ranging from 2D mammography,⁸⁴ to breast tomosynthesis,⁵⁸⁸ to 3D tomography⁵⁸⁹ and to radiotherapy of brain tumors.⁵⁹⁰ Carbon nanomaterials, including SWCNTs and GO, can also be enhanced with high X-ray contrast nanomaterials to afford sufficient contrast for CT imaging. Wilson et al.

report a new X-ray contrast agent design based on a nanocapsule structure of ultrashort SWCNTs incorporating one single I₂ molecule.⁵⁹¹ The same group also reports on the synthesis of ultrashort SWCNT-based nanocarriers encapsulating bismuth-containing nanoparticles to enhance the X-ray contrast owing to the larger atomic number and higher electron density of bismuth than iodine.⁵⁹² Gold nanoparticles with strong X-ray attenuation can be loaded onto graphene oxide to endow GO with X-ray contrast, showing clear identification and localization of the injected nanocomposite in a live mouse by 3D CT imaging.⁵⁹³

MRI scanning has been performed to track the *in vivo* biodistribution of CNTs, by either taking advantage of the metal impurities as residual catalysts at the ends of the CNTs,^{594,595} or using CNTs as nanocarriers to load MRI contrast agents.⁵⁹⁶ The HiPco process is a typical method for producing SWCNTs with diameters of 0.7–1.2 nm, in which SWCNTs are grown via chemical vapor deposition of carbon monoxide (CO) under high pressure with Fe(CO)₅ as the catalyst precursor.⁵⁹⁴ SWCNTs grown in this method have iron oxide nanoparticles attached to one end of the nanotube, allowing people to use the nanocomposite for MRI imaging owing to the superparamagnetic Fe₂O₃ nanoparticles that strongly shorten the T₂ relaxation time. Strano et al. applied a magnetic field gradient to extract the Fe₂O₃-enriched SWCNTs and used the magnetically separated SWCNTs for MRI imaging of murine macrophage cells loaded with the Fe₂O₃-enriched SWCNTs. Although an in-plane imaging resolution of 30 μm × 30 μm is not sufficient for visualization of each individual cell, cell clusters can be imaged in the T₂-weighted MRI image.⁵⁹⁴ As a step forward, SWCNTs with iron impurities along the length of the nanotube have been used for *in vivo* lung imaging in rats to study the effect of nanotube deposition in the pulmonary system after direct exposure to the SWCNTs.⁵⁹⁵ In *in vivo* MRI imaging is made possible in this work by T₂ mapping and detection of the instilled Fe₂O₃-containing SWCNTs in the lung tissue, while the airway and alveolar spaces become visible in the T₂ map as well by inhalation of the contrast agent of ³He hyperpolarized gas.

Superparamagnetic magnetite nanoparticles composed of Fe₃O₄ can be loaded into oxidized carbon nanohorns, which are a carbon nanostructure similar to carbon nanotubes, for *in vivo* MRI imaging.⁵⁹⁷ SWCNTs can also be tagged with exogenous contrast agent such as the Gd³⁺ chelates to reduce the T₁ relaxation time. Scherman et al. synthesized an amphiphilic chelator molecule from stearic acid, with the hydrophobic moiety of the 18-carbon lipid chain noncovalently adsorbing to the surface of the nanotube, and the highly polar, hydrophilic moiety of chelator head binding to Gd³⁺ ions and offering water solubility as well.⁵⁹⁶ In a similar manner Gazeau et al. reported MWCNTs functionalized with the chelating ligand diethylenetriaminepentaaceticdianhydride (DTPA) can efficiently chelate Gd³⁺ ions in an aqueous solution.⁵⁹⁸ Gd³⁺ chelates are widely used as positive contrast agents reducing T₁ relaxation time in MRI imaging while also having the ability to enhance the negative contrast by reducing the T₂ relaxation time. The SWCNTs with amphiphilic Gd³⁺ chelates have shown substantially darkened contrast in the T₂-weighted MRI image after intramuscular injection in a live mouse,⁵⁹⁶ while the MWCNTs covalently functionalized with Gd³⁺ chelates can be used to track the biodistribution of the intravenously administered MWCNTs via T₁-weighted MRI imaging.⁵⁹⁸ Click chemistry has been utilized to tag MWCNTs with iron oxide nanoparticles for MRI imaging of single cells with enhanced T₂ contrast.⁵⁹⁹ Besides these ordinary MRI contrast

agents, it is worth noting that certain chemical species, such as nitroxide radicals, can afford excellent proton relaxation enhancement for both longitudinal (T₁) and transverse (T₂) relaxations when encapsulated inside ultrashort SWCNTs. The relaxation shortening effect is owing to the presence of a single unpaired electron in the nitroxide radicals, and it is found that when the nitroxide radicals are encapsulated in the SWCNTs both T₁ and T₂ relaxivities are significantly enhanced and on par with those of clinical MRI contrast agents, as reported by Wilson et al.⁶⁰⁰

Graphene, on the other hand, can also be conjugated with magnetic nanoparticles for MRI imaging applications. Our group was the first to report the synthesis of water-soluble and biocompatible FeCo/single-graphitic-shell nanocrystals by chemical vapor deposition of methane on the FeCo nanoalloy followed by suspension in phospholipid–PEG.²⁹² The outer shell of the nanocrystal, which is made of a single layer of graphene, can be noncovalently functionalized by phospholipid–PEG to impart water solubility (Figure 32a). The hybrid nanocrystals exhibit unusually high relaxivities for both T₁- and T₂-weighted MRI imaging, suggesting them as better positive contrast agents than the conventional Gd³⁺-containing T₁ contrast agent such as Magnevist (Figure 32b) and also better negative contrast agents than conventional iron oxide containing T₂ contrast agent such as Feridex (Figure 32c).²⁹² In an *in vivo* animal MRI imaging experiment, an aqueous solution of the PEGylated FeCo/single-graphitic-shell nanocrystals is injected intravenously into a rabbit, and T₁-weighted MRI images are taken to show the positive contrast enhanced by the injected nanocrystals. Compared to the MRI image of the same animal before injection, the MRI image after injection clearly reveals the major vessels and the highly vascularized organs including the aorta, the kidney medulla and kidney cortex, owing to the circulating FeCo/single-graphitic-shell nanocrystals in the blood pool (Figure 32d).

In a follow-up work, we and others have used a slightly modified structure of FeCo/single-graphitic-shell nanocrystals with branched PEG coating for MRI-assisted visualization of microvasculature under a higher magnification.⁶⁰¹ The benefit of branched PEG over linear PEG used in the previous study included increased blood circulation time and delayed RES uptake, both of which favor the visualization of small microvessels owing to the longer retention of the contrast agents in the blood pool. We have shown that, with the FeCo/graphene/branched PEG nanocrystals as the contrast agent, the microvasculature in the posterior side of the upper hind limb of a healthy rabbit can be clearly visualized by high resolution MRI with down to <100 μm feature size for the smallest discernible vessel, showing greater contrast and imaging sensitivity than imaging with ferumoxtran-10, a commercial T₂ contrast agent (Figure 32e). Owing to the high sensitivity and long circulation half-life of FeCo/graphene/branched PEG nanocrystals, angiogenic microvessels with submillimeter diameters can be visualized around the aortic stenosis and femoral arterial stenosis in a rabbit by contrast-enhanced MRI imaging (Figure 32f).⁶⁰¹ In another work conducted by our group and the McConnell group, the FeCo/graphene nanoparticles have been applied for the visualization of carotid arterial ligation, as indicated by the T₂* signal loss of the ligated carotid artery as a function of time post surgery.⁶⁰²

Besides *in vivo* MRI imaging using the FeCo/graphene nanocrystals as the contrast agent for blood vessels, we have also used the FeCo/graphene nanocrystals for tumor imaging based

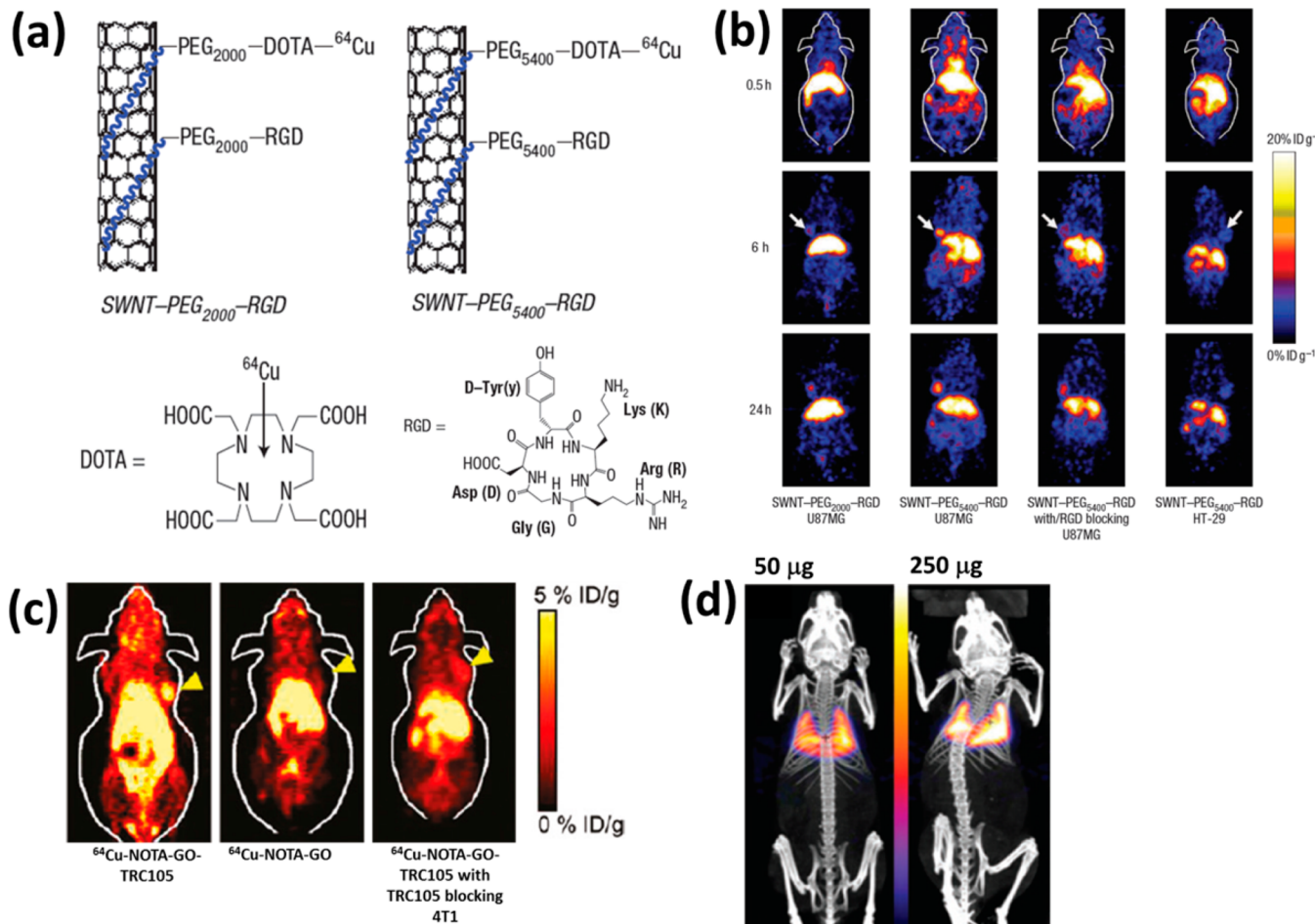


Figure 33. In vivo PET and SPECT imaging with carbon nanomaterials. (a) Schematic drawings of SWCNTs functionalized with PEGs of different molecular weights ($MW = 2000$ and 5400 Da). The PEGs are terminated with amine groups that allow for further conjugation with DOTA-chelated ^{64}Cu for PET imaging, and with RGD for selective targeting of $\alpha_1\beta_3$ integrins. (b) In vivo PET images of mice injected with different formulations of SWCNTs. The first column shows the images after injection of RGD-conjugated SWCNTs with 2000-Da PEG, the second column shows the images after injection of RGD-conjugated SWCNTs with 5400-Da PEG, the third column shows the images after injection of both RGD-conjugated SWCNTs and a blocking dose of free RGD, and the fourth column shows the images after injection in mice with $\alpha_1\beta_3$ integrin negative HT-29 tumor. The images are taken at 0.5 h (first row), 6 h (second row), and 24 h (third row) post injection of SWCNTs. (a, b) Reprinted with permission from ref 291. Copyright 2007 Nature Publishing Group. (c) In vivo PET images of 4T1 tumor-bearing mice injected with ^{64}Cu -labeled GO at 0.5 h post injection. Left, a 4T1 mouse injected with ^{64}Cu -NOTA-GO-TRC105 bioconjugate; middle, a 4T1 mouse injected with ^{64}Cu -NOTA-GO without TRC105; right, a 4T1 mouse injected with ^{64}Cu -NOTA-GO-TRC105 after injection of a blocking dose of TRC105. The yellow triangle indicates the location of the tumor in each image. Reprinted from ref 613. Copyright 2012 American Chemical Society. (d) In vivo SPECT/CT images of mice immediately after intravenous injection of glycosylated Na^{125}I @SWCNTs with doses of $50\ \mu\text{g}$ (left) and $250\ \mu\text{g}$ (right), showing specific accumulation of the γ -ray emitting Na^{125}I @SWCNTs in the lungs. Reprinted with permission from ref 614. Copyright 2010 Nature Publishing Group.

on nonspecific accumulation of the injected FeCo/graphene nanocrystals driven by the EPR effect. Utilizing the high T_1 and T_2 relaxivities of FeCo/graphene, we have acquired both T_1 - and T_2 -weighted MRI images with the same contrast agent, allowing for tumor contrast enhancement and clear identification of the tumor tissue (Figure 32g).²⁹³ With a different formulation of reduced graphene oxide loaded with iron oxide nanoparticles, Liu et al. have imaged the 4T1 tumor on live mice with T_2 -weighted MRI imaging to monitor tumor growth or recession and evaluate the efficacy of photothermal therapy.¹⁶⁰ Graphene nanoribbons conjugated to aquated Gd^{3+} ions have also been proposed as an MRI contrast agent with relaxivities outperforming the Gd^{3+} -based contrast agents currently used in clinics.⁶⁰³

Being a much smaller graphitic cage than in the FeCo/graphene nanocrystals, fullerenes have also been employed as an encapsulating agent to load MRI-active atoms. Bolskar et al. have synthesized a core/shell nanocomplex structure of $\text{Gd}@\text{C}_{60}$ for

T_1 -weighted MRI images.⁶⁰⁴ Owing to the well-functionalized methanofullerene cage with abundant $-\text{COOH}$ functional groups that increase the water solubility of the nanocomplex, the $\text{Gd}@\text{C}_{60}[\text{C}(\text{COOH})_2]_{10}$ is well solubilized and highly stable in biological environment, evidenced by strong T_1 -weighted MRI signals in the kidneys after tail vein injection and gradual clearance from the bladder. A series of gadofullerenes with different surface functionalizations and cage sizes,⁶⁰⁵ as well as lanthanoid endohedral metallofullerenes, have been reported as efficient MRI contrast agents.⁶⁰⁶ More recently, a gadofullerene-**GO** nanohybrid is reported to have higher T_1 relaxivity and better MRI contrast than traditional gadofullerenes, opening up possibilities of novel MRI contrast agents comprised of hybrid carbon nanomaterials.⁶⁰⁷

Using the same strategy of loading MRI contrast agents, nanodiamonds can gain T_1 -weighted MRI imaging contrast by conjugation with gadolinium and iron species through the rich

surface chemistry of nanodiamonds (see section 3.2 for more information).^{608,609} Meade et al. have shown a 10-fold increased T_1 relaxivity of Gd(III)–nanodiamond conjugate compared to the free Gd(III) complex.⁶⁰⁸ It is worth noting that nanodiamonds can be imparted with ferromagnetism via nitrogen (¹⁵N) and carbon (¹²C) ion implantations,^{610,611} providing possibilities of enhanced contrast for MRI imaging without the need to load any additional MRI contrast agents. Moreover, the unique magneto-optical spin detection based on the N–V centers in nanodiamonds could be employed for MRI imaging with extremely high spatial resolution, offering noninvasive optical access to subtle magnetic changes inside a living cell.^{563,612}

Although ¹⁸F is the most common positron-emitting isotope used in fluorodeoxyglucose (FDG) and fluorothymidine (FLT) for PET imaging of tissue metabolic activities, the relatively short half-life of ¹⁸F (~2 h) makes it less suitable for tagging the SWCNT or other carbon nanomaterials through bioconjugation reactions. As an alternative, ⁶⁴Cu with a much longer half-life of ~12.7 h and easy conjugation to chelating agents such as DOTA (1,4,7,10-tetraazacyclododecane-1,4,7,10-tetraacetic acid) has received much more interest for labeling carbon nanomaterials with radioactive isotopes. Our group is among the first to investigate the biodistribution of SWCNTs in live mice based on PET imaging.²⁹¹ HiPco SWCNTs noncovalently functionalized and solubilized with amine-terminated phospholipid PEG are used to further conjugate with DOTA to chelate the positron emitting radionuclide ⁶⁴Cu ions and the $\alpha_v\beta_3$ integrin targeting RGD peptide (Figure 33a). After intravenous injection of the SWCNT bioconjugates into the U87MG tumor-bearing mice, an increasing accumulation of the RGD-conjugated SWCNTs can be visualized in PET images and is shown as a progressively higher signal in the tumor over a period of 24 h (Figure 33b). A dependence of tumor uptake on the molecular weight of PEG has been found, suggesting a higher tumor uptake using SWCNTs with 5400-Da PEG than those with 2000-Da PEG. Negative control experiments using plain SWCNTs without RGD, with blocked $\alpha_v\beta_3$ integrin in the U87MG tumor, and with $\alpha_v\beta_3$ integrin negative HT-29 tumor have suggested that the accumulation of SWCNTs in the U87MG tumor found in PET images is due to specific targeting of SWCNTs to the $\alpha_v\beta_3$ integrin receptors of RGD peptide that are overexpressed on the membrane of U87MG cancer cells, allowing for molecular PET imaging with SWCNTs. PET imaging also helps reveal the *in vivo* biodistribution of the intravenously administered SWCNTs mainly in the reticuloendothelial system (RES) including the liver and spleen without sacrificing the animal and harvesting the organs.

Besides ⁶⁴Cu, a different positron emitting radioisotope, yttrium-86 (⁸⁶Y), has been incorporated into the carbon nanotube bioconjugate in a similar way through the chelating reaction between the DOTA chelator and the chloride salt of ⁸⁶Y.⁶¹⁵ Similar to our findings by ⁶⁴Cu radiolabeling, the ⁸⁶Y-labeled SWCNTs are primarily found in kidneys, liver and spleen at 3–24 h post intravenous injection, suggesting the clearance pathway of SWCNTs as an interplay of both renal and biliary excretions. Although the PET signal in the kidneys is found to decrease significantly from 3 to 24 h post injection indicating fast renal clearance, the signals in both liver and spleen do not show any appreciable change over time, suggesting a much longer tissue retention time of the injected SWCNTs in these organs.⁶¹⁵

Positron emitting isotopes have also been tagged on nanosized GO and rGO to track the biodistribution and specific tumor targeting of intravenously administered rGO nanoparticles. Cai

and Liu et al. report the synthesis of a GO bioconjugate comprised of a PEGylated rGO sheet, targeting moieties of TRC105 antibody that specifically binds to cancer angiogenesis biomarker CD105, and 1,4,7-triazacyclononane-1,4,7-triacetic acid (NOTA) that chelates the radioisotope ⁶⁴Cu. The ⁶⁴Cu–NOTA–GO–TRC105 conjugate shows highly specific targeting effect and accumulation in the CD105 positive 4T1 tumor, as contrasted with two negative control experiments where either ⁶⁴Cu–NOTA–GO without TRC105 is injected, or CD105 receptors in 4T1 tumor are blocked with injection of free TRC105 (Figure 33c).^{613,616}

Although the use of radioisotope-tagged SWCNTs for radioactivity tracing of intravenously administered SWCNTs in different organs based on γ emission can be dated back to 2006,⁶¹⁷ small animal SPECT imaging using carbon nanomaterials labeled with γ ray emitting radioactive isotopes such as ^{99m}Tc, ¹¹¹In, and ¹²⁵I was not realized until more recently.^{340,618} Al-Jamal et al. report radiolabeling of MWCNTs with the γ ray emitting radioisotope ^{99m}Tc through a functionalized bisphosphonate as a cross-linker between ^{99m}Tc and the iron oxide nanoparticles that have been decorated on the sidewalls of oxidized MWCNTs beforehand.⁶¹⁹ SPECT images overlaid on top of the anatomical CT images of the bones clearly reveal the organ distribution of the intravenously injected ^{99m}Tc-MWCNTs mainly in the lungs, liver, and spleen. SPECT/CT imaging has also been applied to track the biodistribution and excretion of ¹¹¹In-labeled MWCNTs through DTPA chelation.^{618,620} For CNTs, the payload can not only be chelated via surface-bound ligands on the chemically modified outer sidewalls, but can also be encapsulated in the internal space of the empty nanotube. To this end, Davis et al. have synthesized SWCNTs filled with Na¹²⁵I inside the nanotube cavity for SPECT/CT imaging and glycosylated on the outer surface to improve solubility and biocompatibility.⁶¹⁴ The Na¹²⁵I@SWCNT after glycosylation can be used as a high density radioprobe with molecular targeting capability that allows it to specifically bind to lung-localized proteins and lung tissues, as evidenced by SPECT/CT overlaid images taken immediately after intravenous administration (Figure 33d). Vallis et al. report radiolabeling of nanographene oxide with ¹¹¹In through π – π stacking of the chelator molecules on the nanographene sheet, and conjugation of the ¹¹¹In-labeled nanographene oxide with anti-HER2 antibody to selectively target HER2 positive tumors *in vivo*. SPECT imaging is used to locate both the xenograft and spontaneous HER2 positive tumors, resulting in a higher tumor-to-background ratio than the radiolabeled antibody alone without any nanographene carrier.⁶²¹

Since these *in vivo* imaging modalities all have their own pros and cons, multimodality imaging by combining two or more imaging modalities together can be realized by using a single imaging nanoplateform based on carbon nanomaterials. For example, Liu et al. have reported that protamine-functionalized SWCNTs with residual Fe/Co catalyst nanoparticles can afford triple-modal *in vivo* imaging and tracking of labeled stem cells based on Raman imaging, photoacoustic imaging, and MRI. Here the Raman and photoacoustic signals are both from the SWCNTs while the MRI signal comes from the metallic nanoparticles.⁵⁵² The same group has also reported triple-modal *in vivo* fluorescence, MRI, and photoacoustic imaging for a xenograft tumor model using a Cy5-labeled nanobioconjugate comprised of reduced graphene oxide and iron oxide nanoparticles.¹⁶⁰ Al-Jamal et al. report the growth of superparamagnetic iron oxide nanoparticles (SPIONs) preferentially

from the oxidized surface groups on the MWCNT sidewalls, endowing the MWCNTs with T_2 -weighted MRI contrast, and subsequent radiolabeling with ^{99m}Tc through a bisphosphonate cross-linker, imparting the MWCNTs with SPECT contrast as well. In vivo dual-modal MRI and SPECT imaging has been realized by using the SWCNT–SPION–bisphosphonate– ^{99m}Tc conjugate.⁶¹⁹ Our group and others have used Cy5-conjugated FeCo/graphene nanoparticles for dual-modal in vivo fluorescence and MRI imaging.⁶⁰² Wilson et al. have loaded the ultrashort SWCNTs with both Gd^{3+} and $^{64}\text{Cu}^{2+}$ for dual-modal MRI and PET imaging.⁶²² Therefore, the ultimate goal here is to find a suitable nanocarrier with the capacity to carry a large payload of contrast agents of various imaging modalities, allowing for multifunctional in vivo imaging based on a single but highly integrated nanoplatform. Such a goal can be easily achieved with graphitic nanomaterials owing to the high surface area as well as intrinsic fluorescence (both visible and NIR fluorescence), Raman, and photoacoustic properties. With chelated PET and SPECT contrast agents, surface-bound superparamagnetic nanoparticles, and gold nanoparticles, it is possible to make carbon nanotube or graphene based multimodal imaging contrast agents for up to seven different in vivo imaging modalities including fluorescence imaging, Raman imaging, photoacoustic imaging, CT, MRI, PET, and SPECT.

5. CARBON NANOMATERIALS FOR NANOMEDICINAL THERAPY

The emergence of carbon nanomaterials has enabled new possibilities and approaches to simultaneously detecting and treating a multitude of diseases, the most prominent of all being cancer. While nanomaterials may be applied to treating a wide variety of ailments and in innovated uses such as vaccine vectors and the delivery of therapeutics to the immune system, cancer is one of the most deadly diseases facing humanity and current treatment methodologies suffer from many deficits such as the inability to completely destroy all cancerous cells as well as the severe toxic side effects of both chemotherapy and radiotherapy.^{623,624} A great deal of the research into the therapeutic applications of carbon nanomaterials focuses on the targeted delivery of anticancer drugs and the selective destruction of cancerous bodies.⁶²⁵

Carbon nanomaterials have many useful electrical and optical properties, yet their size, which ranges from a few nanometers up to a few hundred nanometers, is perfectly tuned for use in both *in vitro* and *in vivo* biological settings as their size is comparable to that of biological macromolecules such as proteins, enzymes, and DNA plasmids.⁸ Furthermore, these materials demonstrate facile transport across the cell membrane, presumably through endocytosis.^{96,449} The ability to easily cross the cell membrane allows fullerenes, carbon nanotubes, graphene, and nanodiamonds to act as transport vehicles for both small molecule based drugs and biopharmaceuticals, making many exciting and innovative approaches to both drug delivery and gene therapy possible.⁶²⁶ The size of carbon nanomaterials offers additional benefits as morbid regions such as tumors show increased fenestration to and retention of nanomaterials due to the EPR effect. The EPR effect occurs through abnormally leaky and tortuous blood vasculature in conjunction with the poor lymphatic drainage commonly associated with tumors which allows nanomaterials to selectively accumulate within cancerous tissue at much higher concentrations than in the surrounding healthy tissue.^{94,470,471} Taking advantage of this selective tumor uptake, carbon nanomaterials can be applied to the selective

destruction of cancerous bodies through photothermal therapy (PTT) by utilizing their high absorbance of NIR light to ablate the tumor or by activating photosensitizing agents piggybacking on the nanomaterial which produce singlet oxygen (SO) or reactive oxygen species (ROS) that in turn kill the surrounding cancer cells.

5.1. Carbon Nanomaterials for Drug Delivery

While a variety of drug delivery systems have been made available to researchers and medical practitioners,^{627,628} carbon nanomaterials offer a promising and efficient alternative for transporting therapeutic molecules. Drug delivery strives to maximize bioavailability at a specific location in the body at the requisite time.^{94,629} The overall dosage of a drug as well as the associated adverse side effects can both be simultaneously reduced through the utilization of carbon nanomaterials as drug delivery vehicles with specificity to targeted locations *in vivo*.⁶²⁵ The utilization of carbon nanomaterials can help get a drug to a specific location within the body, and given the predisposition for nanomaterials to accumulate within tumors, the payload drug molecules can be specifically delivered into the cancerous tissue while leaving the normal tissue unaffected by the drug. Through both covalent and noncovalent methods, the ultrahigh surface area of carbon nanomaterials such as graphene, carbon nanotubes, and nanohorns can be highly decorated with drugs including the anticancer drugs doxorubicin, cisplatin, and methotrexate,^{623,630–633} as well as anti-inflammatory drugs such as dexamethasone.⁶³⁴ These nanomaterials can also serve to highly increase the water solubility of hydrophobic small molecule drugs and facilitate their release in the often acidic conditions found within tumors.⁶³⁵ Interestingly, the nanomaterial–drug complex can significantly increase the drug's efficacy and produce orders of magnitude increases in overall cytotoxicity. In addition to small molecule drugs, carbon nanomaterials can serve as scaffolding to help shuttle peptides, proteins, and other biologics into cells via endocytosis.⁸

Out of all carbon nanomaterials, carbon nanotubes are most commonly used due to their unique spectroscopic properties, and because they can be easily functionalized either covalently or noncovalently and decorated with bioactive peptides, small molecule drugs, proteins, and nucleic acids for gene delivery. After attaching anticancer, antiviral, or antibacterial drugs to the carbon nanotube, the efficacy of the drug must be preserved after crossing the cell membrane or the drug must be anchored to the nanotube through a cleavable bond that promotes the drug's release once inside the cell.⁹⁴ With proper surface functionalizations, carbon nanotubes display low levels of cytotoxicity and can easily be transported across the cell membrane, both of which are key factors for a drug delivery vehicle. Carbon nanotubes are most commonly researched and applied to drug delivery, yet graphene, graphene nanosheets, and carbon nanohorns have also been utilized effectively for drug delivery applications.⁸

Prior to utilizing carbon nanotubes for drug delivery, functionalization either covalently or noncovalently is necessary, as described with sufficient details in section 3. Appropriate surface functionalization is the key to generating sufficient anchoring sites to load and immobilize the cargo molecules on the CNTs, and imparting stability and cell penetration capability to the CNTs. Both covalently and noncovalently functionalized CNTs favor PEGylation to improve stability in physiological buffers,^{291,636} in the meantime allowing for easy functionalization of carbon nanotubes with terminal functional groups on the PEG chains.^{289,291} Functionalized CNTs provide two possible

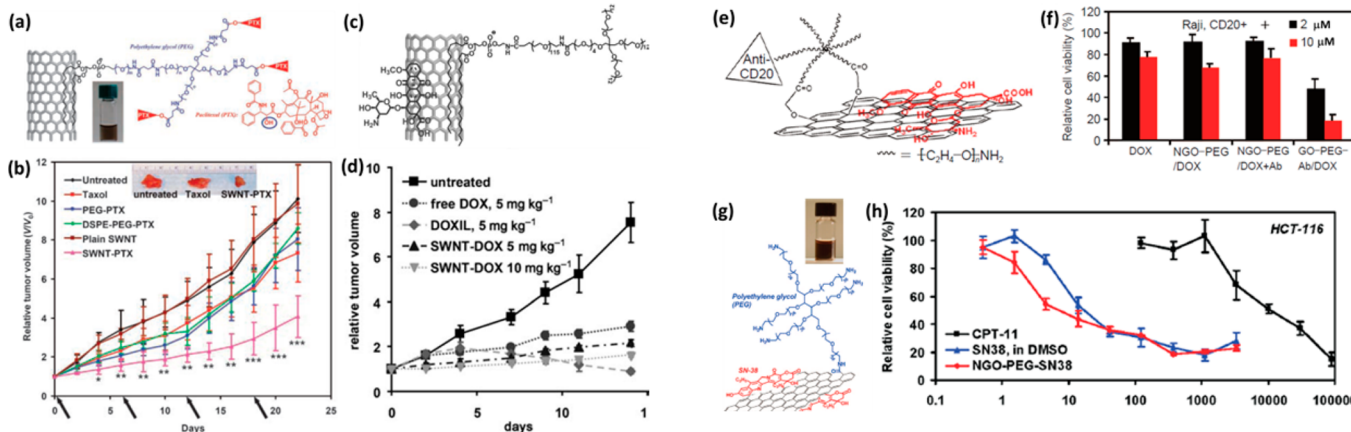


Figure 34. Carbon nanomaterials for drug delivery. (a) Schematic showing the covalent conjugation of PTX molecules to the SWCNT with branched PEGylation. The covalent conjugation is realized through esterification between the hydroxyl group of PTX and succinic anhydride, the latter of which forms amide bonds with the terminal amine groups on the branched PEG chains. The lower left inset shows a photograph of the SWCNT–PTX conjugate in physiologic buffer, and the lower right inset shows the chemical structure of the PTX molecule, highlighting the hydroxyl group in the blue circle. (b) Plots of relative tumor volume (tumor volume on a given day/tumor volume on day 0 when treatment began) in a murine model of 4T1 breast cancer for different treatment groups including untreated (black), Taxol (red), PEG–PTX (blue), phospholipid–PEG–PTX (green), plain SWCNTs without PTX (dark red), and SWCNT–PTX (pink). The top inset shows the resected tumor mass from untreated, Taxol-treated, and SWCNT–PTX-treated mice at the end of the treatment. The arrows indicate the days when treatment via intravenous injection is given. (a, b) Reprinted with permission from ref 94. Copyright 2008 American Association for Cancer Research. (c) Schematic showing the noncovalent loading of a DOX molecule on the SWCNT through π – π interaction between the aromatic rings of DOX and the delocalized π electrons on the nanotube backbone. (d) Plots of relative tumor volume in a murine model of Raji cancer for different treatment groups including untreated (squares), free DOX (circles), DOXIL (diamonds), SWCNT–DOX at 5 mg/kg (up triangles), and 10 mg/kg body weight (down triangles). (c, d) Reprinted with permission from ref 18. Copyright 2009 John Wiley & Sons. (e) Schematic showing the noncovalent loading of a DOX molecule (red) on nanoGO through π – π interaction between the aromatic rings of DOX and the delocalized π electrons in nanoGO. The nanoGO is covalently functionalized with PEG and Rituxan, which is the anti-CD20 antibody. (f) Bar chart showing the in vitro toxicity of free DOX, mixture of DOX and nanoGO–PEG, mixture of DOX, Rituxan, and nanoGO–PEG, and DOX-loaded nanoGO–PEG–Rituxan at a DOX concentration of 2 μ M (black bars) and 10 μ M (red bars) on CD20-positive Raji cells. (e, f) Reprinted with permission from ref 29. Copyright 2008 Springer. (g) Schematic showing the noncovalent loading of an SN38 molecule (red) on nanoGO through π – π interaction between the aromatic rings of SN38 and the delocalized π electrons in nanoGO. The inset shows a photograph of the nanoGO–PEG–SN38 solution. (h) In vitro toxicity of CPT-11 (SN38 prodrug, black), SN38 in DMSO (blue) and nanoGO–PEG–SN38 (red). (g, h) Reprinted from ref 21. Copyright 2008 American Chemical Society.

locations where the exogenous drugs, biologics, or targeting molecules can be loaded: for molecules with functional groups, they can be easily conjugated to the terminal functional groups on the CNTs or the PEG chains; on the other hand, for hydrophobic molecules without any available functional groups such as doxorubicin and SN38, they can adsorb to the similarly hydrophobic backbone of CNTs through π – π stacking or hydrophobic interaction between the drug molecules and the CNTs.

CNT-based drug delivery vehicles can be designed so that the drug payload is only released after the nanotube is within the cell. In a collaboration between our group and the Lippard group, PL–PEG functionalized SWCNTs were used as a platform to improve the internalization process of an inert platinum(IV) complex, a prodrug compound developed by the Lippard group, into cancer cells.⁴³⁹ The platinum(IV) complex was tethered onto the end of the PEG chain through an amide bond. After the SWCNT is taken up by the cell through endocytosis, the SWCNTs become engulfed in endosomes where a drop in environmental pH causes the release of the platinum(II) core complex which kills the cancerous cells. Due to the selective release of platinum(II) in the cell, the cytotoxicity of the platinum(IV)–SWCNT complex increased by over 100-fold when compared to platinum(IV) alone. This effect was only demonstrated in vitro, but as SWCNTs tend to aggregate at high concentrations in tumors, this strategy has the potential to be utilized after intravenous injection.

A further study by our group demonstrated successful drug delivery of paclitaxel (PTX), a commonly used anticancer drug, with carbon nanotubes in vivo.⁹⁴ The PTX molecule has an activatable hydroxyl group that can be covalently linked to the amine terminal groups of PEG chains through succinic anhydride (Figure 34a), rendering the PTX molecule soluble in aqueous biological environment. Due to the passive uptake of carbon nanotubes by cancerous tissue by the EPR effect, the SWCNT–PTX conjugate demonstrated a 10-fold increase in PTX uptake within xenograft murine tumor models compared with Taxol, which is the clinical drug formulation of PTX. It is noteworthy that the ester bond through which the PTX molecule is anchored to the surface of SWCNT is cleavable, leading to controlled release of the drug molecules inside the tumor tissue and successful suppression of the tumor growth in a murine model of 4T1 breast cancer (Figure 34b). After accumulation of SWCNT–PTX conjugates in the tumor at a much higher concentration than the surrounding tissue, cellular internalization of the SWCNT–PTX complex promoted PTX release due to the lower pH in the local tumor environment. The SWCNTs accumulated within the RES system during clearance from circulation as has been demonstrated in previous studies,^{291,637} yet PTX was found to be excreted rapidly due to cleavage of the ester bond, indicating that residual PTX was rapidly removed, much more quickly than the carbon nanotubes, and did not cause an increase in toxicity due to long-term retention in the organs of the RES.⁹⁴ This model can be applied to a variety of water-insoluble drugs to boost their tumor

accumulation abilities. It was proposed that the use of targeting ligands for the selective targeting of particular cell surface receptors would further contribute to the efficacy of this method.

In addition to attaching anticancer drugs covalently through the terminal functional groups on the PL-PEG chains, many anticancer drugs can be loaded onto carbon nanotubes through supramolecular chemistry by loading aromatic drug molecules through $\pi-\pi$ stacking on the carbon nanotube surface (Figure 34c). Doxorubicin (DOX) is a commonly used drug in chemotherapy and can be loaded in extremely high ratios on carbon nanotubes of up to 4 g of doxorubicin for every 1 g of SWCNTs.¹⁹ In addition to the weight of the PL-PEG coating, the SWCNT-DOX complex contained ~50–60 wt % doxorubicin, in stark contrast to the ~8–10 wt % found in conventional liposomes used to solubilize the drug in its commercial formulation. The SWCNT-DOX conjugate demonstrated excellent stability in buffer and serum, yet in acidic conditions as found in liposomes, in endosomes, and within tumor microenvironments, DOX demonstrated rapid release from the carbon nanotube surface, both of which are desirable properties for *in vivo* drug carriers. In this case, while the anticancer drug was loaded onto the carbon nanotube surface, the terminal functional groups on the PL-PEG chains were functionalized with an RGD peptide to facilitate the selective targeting of cancerous cells in an *in vitro* setting. DOX-loaded SWCNTs have also demonstrated significantly enhanced *in vivo* therapeutic efficacy with greatly mitigated toxicity to treated mice in comparison to other formulations of DOX such as the free DOX and DOXIL, which is liposome-solubilized DOX (Figure 34d).¹⁸ In these *in vitro* and *in vivo* studies, carbon nanotubes were used; yet a variety of different carbon nanomaterials have shown similar drug loading behaviors. Supramolecular loading through $\pi-\pi$ stacking is not unique to SWCNTs, as MWCNTs, carbon nanohorns, and nanographene oxide (Figure 34e–h) all exhibit similar drug loading behaviors as well as variable drug release as a function of pH.^{21,29,638,639}

In addition to small molecule anticancer drugs, biological therapeutics can be successfully attached to carbon nanotubes for translocation across the cell membrane. Unlike small molecules, these larger biomacromolecules rarely cross cell membranes unaided. SWCNTs have been used as scaffolds for introducing these bioactive peptides to the immune system, and carbon nanotubes have been proposed as novel vaccine delivery tools.⁶⁴⁰ Proteins such as the epidermal growth factor receptor (EGFR) inhibitor are routinely attached to carbon nanotubes for the targeted delivery of drug payloads to enhance the efficacy of chemotherapy.⁶⁴¹

5.2. Carbon Nanomaterials for Gene Delivery

In a similar fashion to drug delivery, carbon nanomaterials, in particular carbon nanotubes and graphene, are frequently researched and applied to gene delivery applications. A tremendous amount of interest has been given to the treatment of various diseases by introducing nucleic acids which can repair, replace, regulate, and add or delete a certain genetic target responsible for a particular disease given the advent of our understanding of genetic processes and molecular biology.⁶²⁶ While gene therapy holds the promise of introducing new disease treatment strategies, the development of nontoxic, biocompatible, and nonviral vectors for gene therapy is desired for its use in human patients. While both viral and nonviral gene therapy vectors exist, the application of viral vectors in a clinical setting are hindered given immunogenicity concerns, their limited

genetic payload, and the poor targeting of particular cell populations. Nanovectors such as carbon nanotubes offer a promising alternative as well as a plethora of additional benefits including the facile access into a cell, a significant boost in the solubility and biocompatibility of nucleic acids, and, very importantly, increased protection for the loaded nucleic acids from cleavage and degradation.¹⁷¹

Carbon nanomaterials can be covalently or noncovalently functionalized to contain positive charges to bind and deliver the negatively charged DNA and small interfering RNA (siRNA).^{173,288,438,642,643} One benefit of using carbon nanomaterials for gene therapy is their low intracellular toxicity even at very high concentrations, which is in contrast to commercial gene transfection agents. While overall transfection rates are on par with or superior to commercial gene transfection agents such as lipofectamine 2000, new approaches using carbon nanomaterial based transporters for gene delivery have significantly decreased the required dosage and dramatically increased transfection success rate. Finally, new carbon based transfection agents such as carbon dots^{644,645} and nanodiamonds^{271,274} show promise as novel gene therapy agents as well.

The first report of using carbon nanotubes for gene delivery involved covalently functionalized carbon nanotubes (both single-walled and multiwalled) that produced amine terminated functional groups via the 1,3-dipolar cycloaddition of azomethine ylides.⁶⁴² The positive charge induced by the amine groups on the carbon nanotube surface allowed the electrostatic loading of plasmid DNA through their negatively charged phosphate groups. To demonstrate delivery into the nucleus as well as successful gene transfection, marker gene expression (β -galactosidase) in CHO cells was analyzed after exposure to carbon nanotubes decorated with the plasmid DNA encoding the gene. Interestingly, the ratio of charges between the nanotube surface and the DNA phosphate groups was found to determine the level of gene expression, with the ideal charge ratio between 2:1 and 6:1.

The delivery of short siRNA into live cells was pioneered by our group by attaching siRNA to cleavable bonds on the phospholipid-PEG coating of single-walled carbon nanotubes.²⁸⁸ siRNA plays many roles within a cell, yet the most notable is the RNA interference pathway which interferes with gene expression through the binding of complement sequences. As the development of cancer depends on multiple gene pathways, introducing siRNA to silence these genes may be an effective form of therapy. The intracellular transport as well as delivery of siRNA is critical to the siRNA potency, and through this method the highly efficient silencing of the lamin A/C gene was achieved when compared to commercial transfection agents (Figure 35a,b). By incorporating a disulfide bond, the genetic payload could be cleaved enzymatically once inside lysosomal or endosomal compartments to deliver siRNA directly into the cytosol. In contrast with siRNA attached to the carbon nanotube with a cleavable disulfide bond, siRNA covalently linked to the nanotube showed internalization but no nuclear translocation as well as diminished silencing capabilities. A 2-fold increase in the efficiency of transfection was observed when compared to a commercial lipofectamine transfection agent, yet, as opposed to what was observed with the commercial agent, no carbon nanotube cytotoxicity was noted. Furthermore, the SWCNT transfection vehicle showed additional advantages as it was capable of transfection in human T cells and primary cells, in contrast with conventional nonviral cationic liposome-based

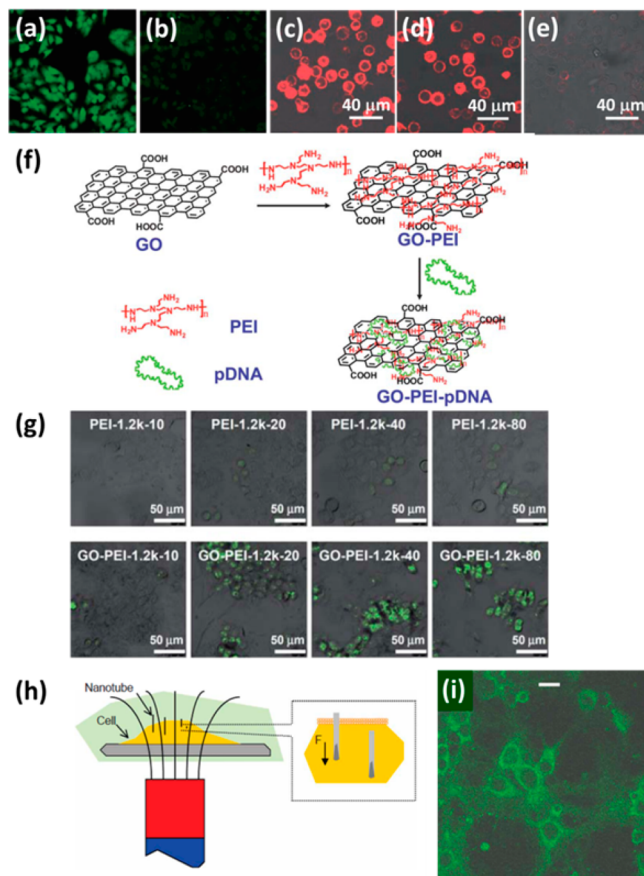


Figure 35. Carbon nanomaterials for gene delivery. (a, b) Fluorescence confocal microscopic images of untreated HeLa cancer cells (a) and HeLa cells treated with SWCNT-siRNA (b) to silence the expression of lamin proteins, which are stained with antilaminin and fluorescence-labeled secondary antibody for confocal imaging. (a, b) Reprinted from ref 288. Copyright 2005 American Chemical Society. (c–e) Fluorescence confocal microscopic images of untreated human T cells (c), human T cells treated with lipofectamine 2000-siRNA (d), and human T cells treated with SWCNT-siRNA (e) to silence the CXCR4 receptors, which are stained with fluorescent PE-anti-CXCR4. (c–e) Reprinted with permission from ref 438. Copyright 2007 John Wiley & Sons. (f) Schematic showing the synthesis of plasmid DNA (pDNA) loaded GO through PEI assisted layer-by-layer assembly. (g) Fluorescence confocal microscopic images of HeLa cells transfected by EGFP-pDNA-loaded PEI (1.2 kDa, top row) and EGFP-pDNA-loaded GO-PEI (1.2 kDa, bottom row) at different nitrogen-to-phosphate ratios (N/P ratios) of 10, 20, 40, and 80 (columns, left to right). (f, g) Reprinted with permission from ref 173. Copyright 2011 Royal Society of Chemistry. (h) Schematic drawing showing “nanotube spearing” by applying magnetic field to nickel-embedded CNTs. (i) Microscopic image of mouse cortical neurons transfected with EGFP via “nanotube spearing”. (h, i) Reprinted with permission from ref 647. Copyright 2005 Nature Publishing Group.

transfection agents for which transfection in these cell lines was not possible (Figure 35c–e).⁴³⁸

Graphene, specifically different forms of graphene oxide, shows promise as a new transfection agent with comparable performance to carbon nanotubes.^{172,643,646} Graphene oxide displays a plethora of carboxylic acid groups that can easily be functionalized with common cationic transfection polymers such as polyethylenimine (PEI) which loads DNA very efficiently, through layer-by-layer assembly.¹⁷³ PEI alone has a high transfection efficiency due to high levels of cellular uptake and

endosomal escape, yet the associated cytotoxicity of PEI severely limits its use as an effective gene transfection agent. However, after conjugation to GO and nanoGO, Liu et al. observed diminished PEI cytotoxicity as evidenced by significantly higher cellular viability for the GO-PEI conjugates while simultaneously maintaining the high transfection levels of commercial cationic transfection agents (Figure 35f,g).^{172,173} The high optical absorbance of GO in the NIR region has been employed to synergistically increase the delivery efficiency of siRNA under NIR laser irradiation and the subsequent photothermal effect, allowing for photocontrollable gene delivery.¹⁷²

Carbon dots, one of the newer members of the carbon nanomaterial family, can have diameters lower than 10 nm that facilitate a high level of cellular uptake. Owing to the similar structures to GO, carbon dots manufactured in a one-step microwave synthesis were utilized in a similar manner in conjunction with PEI, which not only acted as a surface passivation agent to enhance the fluorescence of carbon dots, but also played an important role in electrostatically loading DNA on the surface of carbon dots.⁶⁴⁵ Furthermore, nanodiamonds have also been intensively studied as a nanocarrier of nucleic acids. Ho et al. reported PEI functionalized nanodiamonds with high transfection efficiency of plasmid DNA and without the high toxicity inherent to the free PEI molecules, similar to GO-based gene delivery vehicles.²⁷¹ The same group has also reported on siRNA delivery with PEI functionalized nanodiamonds with enhanced efficacy.²⁷⁴ Treussart and Bertrand et al. have compared the siRNA delivery efficacy using different cationic polymers such as PEI and poly(allylamine hydrochloride) (PAH) as the electrostatic “glue” to bind siRNA on the nanodiamonds. They concluded that the PAH-coated nanodiamonds have a higher affinity to siRNA; however, PAH-coated nanodiamonds are much slower in releasing the loaded siRNA and thus have a lower transfection efficacy than the PEI-coated counterparts.²⁷⁵ The intrinsic fluorescence of carbon dots and nanodiamonds (see section 4.1 for more detailed information) makes these two carbon nanomaterials particularly useful as multifunctional gene delivery vectors that allow for real-time tracking of their locations inside live cells through microscopic fluorescence imaging.

New strategies for increasing the efficiency of the delivery of exogenous DNA into cells using carbon nanotubes are poised to have significant boosts in the efficacy of gene therapy. An innovative approach involves utilizing ferromagnetic nickel embedded nanotubes coated with a DNA plasmid that are driven into cells through a variable magnetic field.⁶⁴⁷ This new approach, termed “nanotube spearing”, takes advantage of the ferromagnetic nickel catalyst particles that are enclosed in the tips of carbon nanotubes after their growth using a plasma-enhanced CVD method. The residual nickel catalyst particles allow nanotubes to respond to external magnetic agitation. By tuning the magnetic fields surrounding cells, these carbon nanotubes carrying a genetic payload can be used to “spear” the cells and deliver their contents directly into the nucleus (Figure 35h). Carbon nanotubes and graphene oxide are naturally taken up through endosomal or lysosomal pathways, and unfortunately many plasmids are hydrolyzed and thus destroyed prior to releasing their genetic payload. Utilizing nanotube spearing, DNA can be directly delivered to the cell nucleus, contributing to the significant boost in efficiency as observed in this transfection method for DNA plasmids containing the sequence of enhanced green fluorescent protein (EGFP) (Figure 35i). Using carbon nanotubes alone requires concentrations of ~1–5 μ M, yet

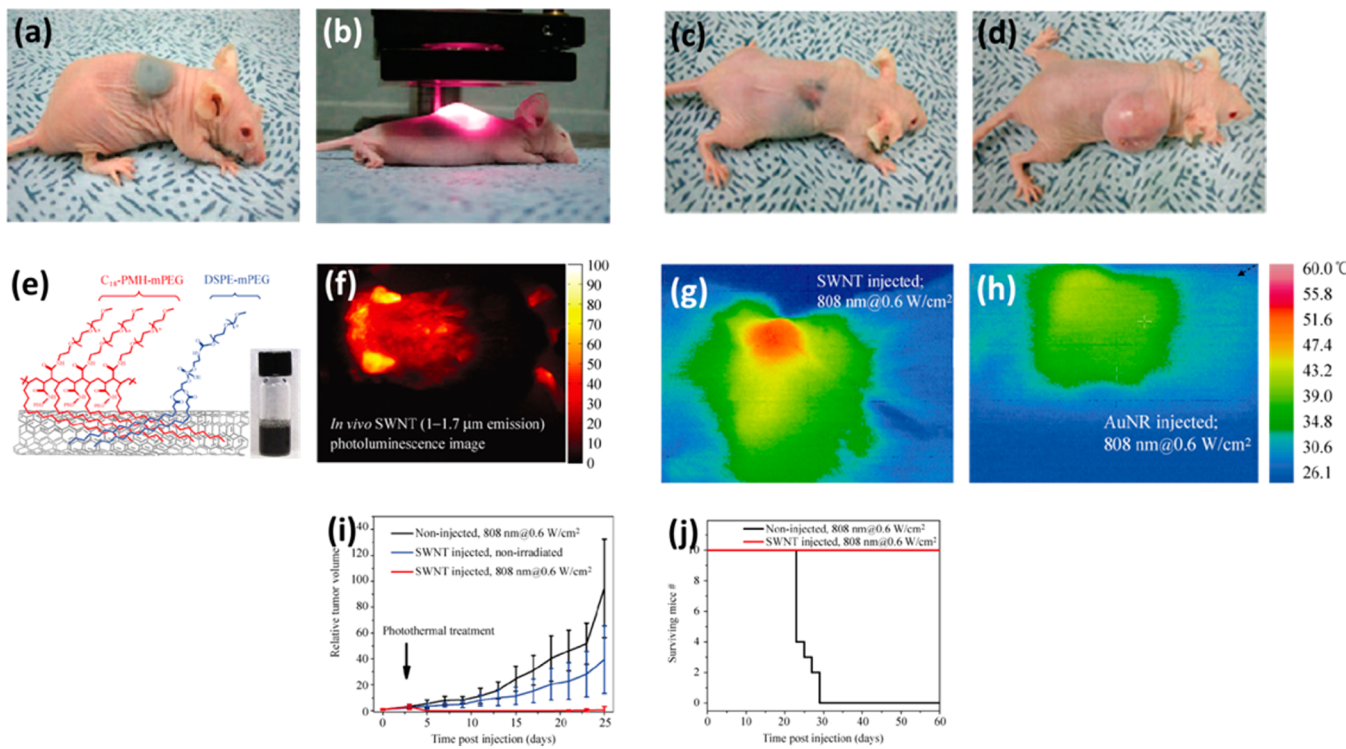


Figure 36. Photothermal therapy with unseparated SWCNTs. (a) Photograph of a KB tumor-bearing mouse intratumorally injected with PEGylated SWCNTs. (b) Photograph of the same mouse under 808 nm NIR irradiation with a power density of 76 W/cm^2 . (c) Photograph of a KB tumor-bearing mouse on day 20 after receiving the treatment involving both SWCNT injection and NIR irradiation. (d) Photograph of a KB tumor-bearing mouse on day 20 after the injection of SWCNTs only. (a–d) Reprinted from ref 654. Copyright 2009 American Chemical Society. (e) Schematic showing the mixed noncovalent coating of PL-PEG and C18-PMH-PEG on the SWCNTs that leads to high tumor uptake and efficient photothermal ablation of the tumor. (f) NIR-II fluorescence image of a 4T1 tumor-bearing mouse at 48 h after intravenous injection of the PEGylated SWCNTs shown in (e). (g) Thermal image of a tumor-bearing mouse intravenously injected with SWCNTs at a dose of 3.6 mg/kg and irradiated with 808 nm NIR light at 0.6 W/cm^2 power density for 4.5 min. (h) Thermal image of a tumor-bearing mouse intravenously injected with gold nanorods at a dose of 35 mg/kg and irradiated with 808 nm NIR light at 0.6 W/cm^2 power density for 4.5 min. (i) Plots of relative 4T1 tumor volume for different treatment groups including untreated (black), SWCNT injected but nonirradiated (blue), and SWCNT injected and irradiated (red). (j) Survival plots of the control group (noninjected with SWCNTs but irradiated with 808 nm laser at 0.6 W/cm^2) and the treated group (both injected with SWCNTs and irradiated under the same condition) up to 60 days after the treatment. (e–h) Reprinted with permission from ref 13. Copyright 2010 Springer.

through nanotube spearing facilitated by the external magnetic field, a low concentration of merely $\sim 100 \text{ fM}$ is required, thus increasing the molecular shuttling efficiency by 10^7 -fold.⁶⁴⁷

5.3. Carbon Nanomaterials for Photothermal Therapy

Carbon nanomaterials such as CNTs and graphene selectively accumulate in tumors through the EPR effect as well as demonstrate extremely high levels of intrinsic absorbance in the biological transparency windows located within the near-infrared ($750\text{--}1700 \text{ nm}$).^{13,32,95,157} Additionally, the strong fluorescence of carbon nanomaterials with emission wavelengths ranging from visible to NIR-II window allows for simultaneous imaging and treatment.^{16,298,397} The combination of these properties makes these materials extremely attractive agents for photothermal therapy (PTT), which involves the selective heating of cancerous tissues with these nanomaterials trapped inside to temperatures at which photocoagulation and cell death occur, resulting in reduced size of the tumor or even complete elimination of the tumor.^{624,648–651} Compared to other nanomaterials including gold nanorods and nanospheres used for photothermal therapy,⁶⁵² the benefits of using carbon nanomaterials come twofold: first, with the proper surface modification to prevent detection from the immune system, carbon nanotubes and graphene can circulate in vivo with half-lives approaching days, which significantly increases the

probability that the intravenously administered carbon nanomaterials will become trapped in a tumor, yielding ultrahigh levels of tumor uptake which have surpassed $30\% \text{ ID/g}$.^{34,298} Second, carbon nanotubes and graphene confer an additional benefit as their strong optical absorbance in the NIR region is ideal given NIR light's superior tissue penetration ability compared to the visible region.^{29,157} Carbon nanotubes have demonstrably outperformed other nanomaterial-based PTT agents such as gold nanoparticles/nanorods¹³ while carbon nanohorns, graphene oxide, and reduced graphene oxide photosensitizers are promising new avenues of carbon-based photothermal therapy as well.^{157,653}

Single-walled carbon nanotubes were the first carbon nanomaterial used for photothermal therapy.^{13,95} To deliver SWCNTs into the tumor body, intratumoral injection⁶⁵⁴ and intravenous injection^{13,298} have both been demonstrated, while the intravenous injection provides a more practical means of in vivo administration especially in the cases of orthotopic and metastatic tumor models. In 2009, Choi et al. reported photothermal ablation of human epidermoid mouth carcinoma KB tumor in mouse intratumorally injected with PEGylated SWCNTs using 808 nm NIR irradiation (Figure 36a,b).⁶⁵⁴ A significantly reduced tumor volume was found for the treated mice, compared to the control, untreated group of mice receiving the same intratumoral injection of PEGylated SWCNTs but

without NIR irradiation (Figure 36c,d). In 2010, our group reported the use of SWCNTs noncovalently functionalized with PL-PEG and C18-PMH-PEG (Figure 36e) to achieve a high passive tumor uptake of ~8% ID/g (injected dose/gram of tissue) based on the EPR effect.¹³ The PEGylated SWCNTs were intravenously injected into mice with xenograft tumors, and very clear images of the tumor were observed by exploiting the intrinsic NIR-II fluorescence of the SWCNTs at 48 h post injection (Figure 36f). Being able to simultaneously detect and then treat cancerous bodies is a strong benefit of SWCNTs as their unique optical properties in the NIR windows allow for both applications.^{13,298} Briefly exciting the carbon nanotubes at a lower laser power density (0.15 W/cm^2) produces crisp and clear fluorescence images of the xenograft tumors on an InGaAs detector and a higher power density (0.6 W/cm^2) causes subsequent ablation. During ablation, only 3.6 mg/kg was required to successfully ablate a tumor at a power density of 0.6 W/cm^2 , yet using gold nanorods, another commonly researched nanomaterial for PTT, ~35 mg/kg at a higher laser power of 2 W/cm^2 was necessary for the tumors to reach $\sim 52^\circ\text{C}$ for successful ablation (Figure 36g,h). It has been found that all tumor-bearing mice receiving both SWCNT injection and NIR irradiation survived without any tumor regrowth, in contrast to the control, untreated group of tumor-bearing mice that exhibited large tumor sizes of $>0.5 \text{ cm}^3$ and were considered “nonsurvival” after 25 days (Figure 36i,j). This was the first work to image tumors in the NIR-II window with SWCNTs and the first systemic injection of these nanomaterials for PTT. While ~8% ID/g was reported using a 50% PL-PEG/50% C18-PMH-PEG mixture, further tuning of the polymer coating produced a greatly extended circulation time and subsequently ultrahigh tumor uptake.²⁹⁸ It is foreseeable that if the above study had been done with an optimized surfactant coating, a much lower dose of intravenously injected carbon nanotubes would have been required.

Advancements in carbon nanotube sorting have had a tremendous impact on the electronic applications of these materials, yet the same benefits garnered by isolating carbon nanotubes of a particular chirality or electronic type can be had in the biological realm. By density gradient ultracentrifugation (DGU) of the surfactant dispersed mixture of carbon nanotubes with different chiralities, the isolation of a particular chirality, (6,5) SWCNTs, was achieved at a purity of ~80%.³⁴ After separation with ionic surfactants in the density gradient, a surfactant exchange procedure was implemented to remove the ionic surfactants and replace them with the PL-PEG polymers necessary for *in vivo* use.³⁰ (6,5) carbon nanotubes have an E_{11} electronic transition at $\sim 991 \text{ nm}$ which is in resonance with an 980 nm excitation laser. By removing all of the other nanotube species that have no absorbance at the wavelength used for heating, an ultralow dose of single-chirality (6,5) nanotubes of 0.254 mg/kg was intravenously injected for successful tumor ablation at a low irradiation power density (0.6 W/cm^2) using 980 nm laser irradiation, reaching a local temperature of the tumor tissue of $>50^\circ\text{C}$ (Figure 37a). In striking contrast, the unseparated HiPco SWCNTs at the same injection dose and the PBS control led to a much lower rise in temperature after the same course of NIR irradiation (Figure 37b-d).³⁴ Using only ~4 μg of SWCNTs for successful tumor detection and treatment per mouse, this was by far the lowest dose out of any other class of nanomaterials used for simultaneous imaging and photothermal therapy in murine models of tumor.

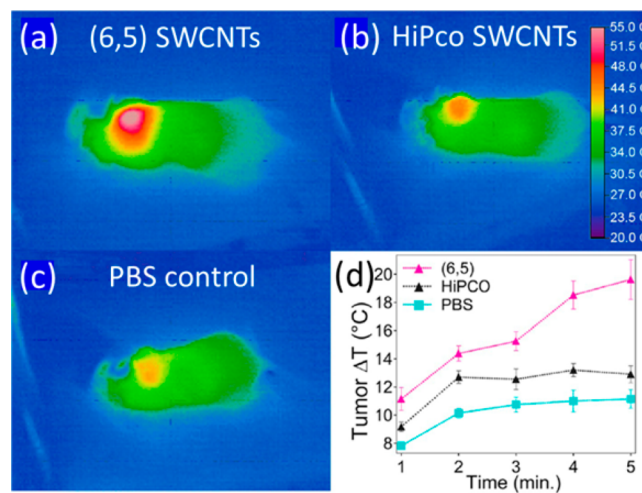


Figure 37. Photothermal therapy with chirality-separated, (6,5) SWCNTs. (a–c) Thermal images of 4T1 tumor-bearing mice at 48 h after intravenous injection of C18-PMH-PEG functionalized (6,5) SWCNTs (a), HiPco SWCNTs (b), and PBS control (c), after 5 min of continuous 980 nm irradiation at a power density of 0.6 W/cm^2 . (d) Plots showing the average tumor temperature rise as a function of irradiation time for the three groups of mice treated with (6,5) SWCNTs (red), HiPco SWCNTs (black), and PBS control (blue). Reprinted from ref 34. Copyright 2013 American Chemical Society.

Besides SWCNTs, graphene oxide has also been successfully applied for photothermal therapy owing to its strong absorbance in the NIR window.³² In a pioneering study by Liu et al., the nanographene sheets (NGS) were PEGylated and then injected into mice for use as a 2D photosensitizer for PTT.³² Amine terminated six-arm branched PEG was conjugated to NGS through amide formation, producing a highly water-soluble and stable conjugate with functional groups available for further decoration with small molecule fluorescent dyes or biomolecules for molecular imaging (Figure 38a). The PEGylated NGS demonstrated very high amounts of tumor uptake which may surpass the EPR uptake levels of carbon nanotubes. This was demonstrated by observing the tumor fluorescence from Cy7 conjugated to the NGS (Figure 38b). Owing to the high uptake inside the tumor, as well as the strong optical absorbance in the NIR, PEGylated NGS allowed for efficient ablation of the tumor mass under an 808 nm laser irradiation at a power density of 2 W/cm^2 (Figure 38c–e). An extensive histology examination post treatment revealed no signs of toxicity. While the injected dose and power density ($20 \text{ mg/kg}; 2 \text{ W/cm}^2$) are currently higher than those required for successful PTT with carbon nanotubes, the high tumor uptake of the NGS has spurred further research into this novel PTT agent.³²

In order to reduce the requisite dosage and laser power density for photothermal therapy with nanographene sheets, the NGS can be reduced to restore a portion of their aromatic, conjugated character, as reported by our group in 2011.¹⁵⁷ After synthesizing graphene oxide with the Hummers method, six-arm branched PEG was covalently conjugated to the GO’s carboxyl functional groups. The NGS were then reduced by adding hydrazine monohydrate to the solution which produced a visible color change from yellow to black, indicating a significant increase of absorbance in the visible to NIR window. It was shown previously that a similar reduction produced a ~30% drop in oxygen content and a significant boost in electrical conductivity.⁶⁵⁵ Similarly, the partial restoration of the aromatic

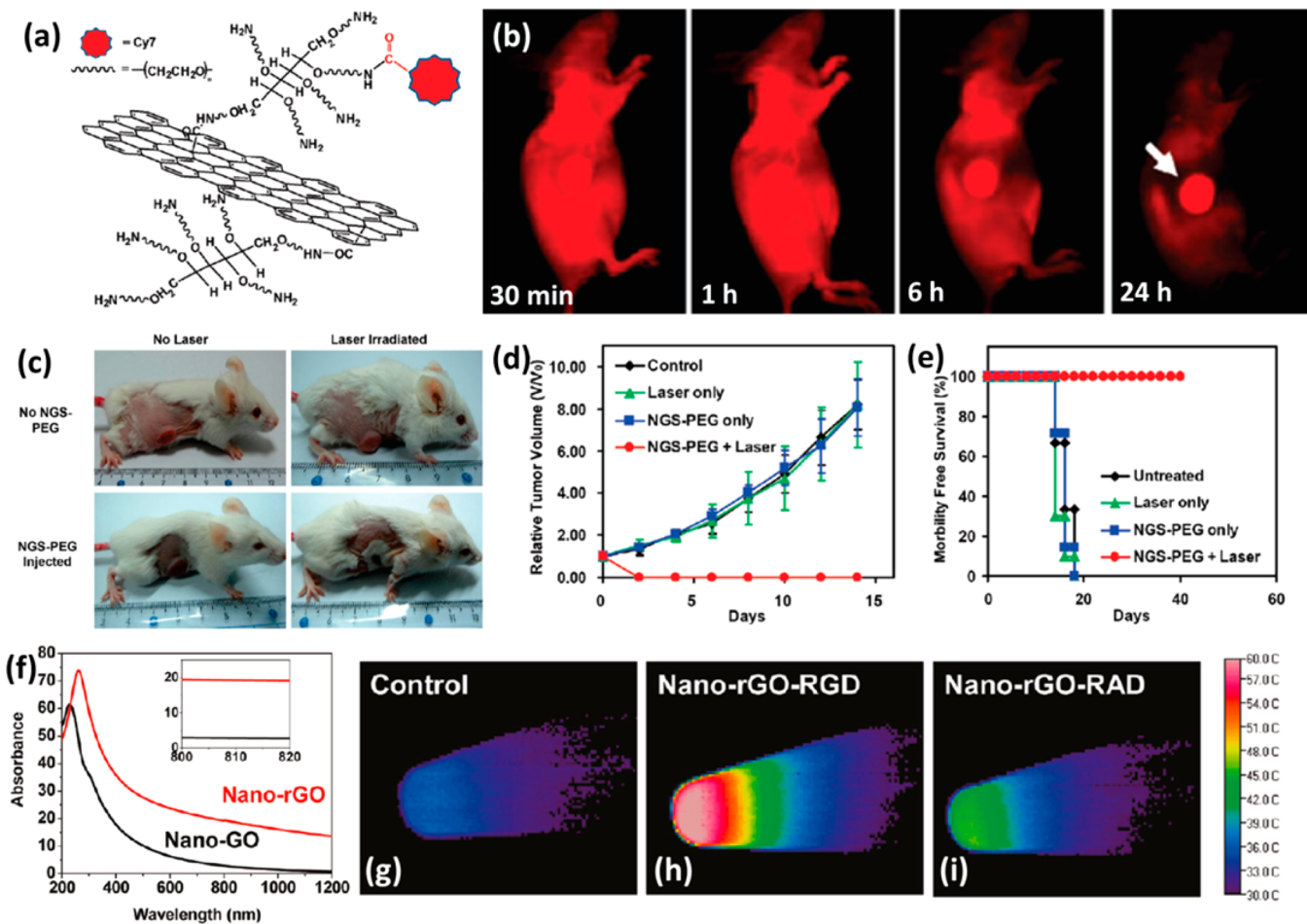


Figure 38. Photothermal therapy with graphene. (a) Schematic drawing of the nanographene sheet covalently functionalized with six-arm branched PEG through the formation of amide bond, allowing for labeling of Cy7 for fluorescence imaging. (b) In vivo fluorescence images of U87MG tumor-bearing mice at different time points up to 24 h after injection of NGS-PEG-Cy7, showing high accumulation of NGS-PEG-Cy7 in the tumor. (c) Photographs of tumor-bearing mice after receiving different treatments as indicated. The mouse injected with NGS and irradiated with 808 nm laser shows complete tumor destruction by photothermal therapy. (d) Plots of relative tumor volume for different treatment groups including untreated control (black), laser irradiation only (green), injection of NGS only (blue), and both NGS injection and laser irradiation (red). (e) Survival plots of different treatment groups including untreated control (black), laser irradiation only (green), injection of NGS only (blue), and both NGS injection and laser irradiation (red) up to 40 days after the treatment. (a–e) Reprinted from ref 32. Copyright 2010 American Chemical Society. (f) Increase in optical absorbance of nanoGO when nanoGO is reduced to nano-rGO via hydrazine treatment. (g–i) Thermal images of U87MG cancer cell pellets, which were not treated (g), treated with RGD-conjugated rGO (h) and treated with RAD-conjugated rGO (i). All cell pellets are illuminated with an 808 nm laser for 8 min. The RAD peptide is a nonfunctional analogue of RGD made of arginine-alanine-aspartic acid and used as a negative control. (f–i) Reprinted from ref 157. Copyright 2011 American Chemical Society.

character of graphene resulted in a 7-fold increase in the NIR absorbance at 808 nm, which was the laser wavelength used for heating in PTT (Figure 38f). Although no in vivo treatment experiments were performed with the reduced NGS, the in vitro heating indicated a significant improvement in heat generation when irradiated, which allowed for targeted ablation of U87MG cancer cells using rGO conjugated with an RGD peptide (Figure 38g–i).

An innovative approach to photothermal therapy used to treat not only the primary tumor but also tumor metastases located in the sentinel lymph nodes involves the direct injection of carbon nanotubes into the primary tumor and the spread of the carbon nanotubes through the lymphatic system to the secondary tumors.⁴⁸⁰ After an injection partially into the healthy tissue surrounding the tumor and the tumor itself, nanotubes can spontaneously migrate to the tumor metastasis located in a sentinel lymph node possibly through circulation and drainage of the lymphatic vasculature. By irradiating the entire area

composed of the primary tumor as well as the metastatic tumor in the lymph node, the complete survival of the mouse was ensured even though metastasis had occurred. As metastatic spread is responsible for more than 90% of cancer deaths, the use of nanotubes to destroy both the primary and secondary tumors as well as image both tumors in the NIR-II window is of significant interest. Irradiation and the subsequent photothermal heating of both tumors resulted in a significantly prolonged mouse survival compared to mice treated with only the ablation of the primary tumor.⁴⁸⁰ Additionally, fatal pulmonary metastasis was observed in all treatment groups despite PTT and surgery of the primary tumor, except when both the primary and secondary tumors were irradiated and completely eradicated.⁴⁸⁰

5.4. Carbon Nanomaterials for Photodynamic Therapy

Photodynamic therapy (PDT) relies on the generation of singlet oxygen (SO) or reactive oxygen species (ROS) which are generated from photosensitizing molecules to kill cancer cells or

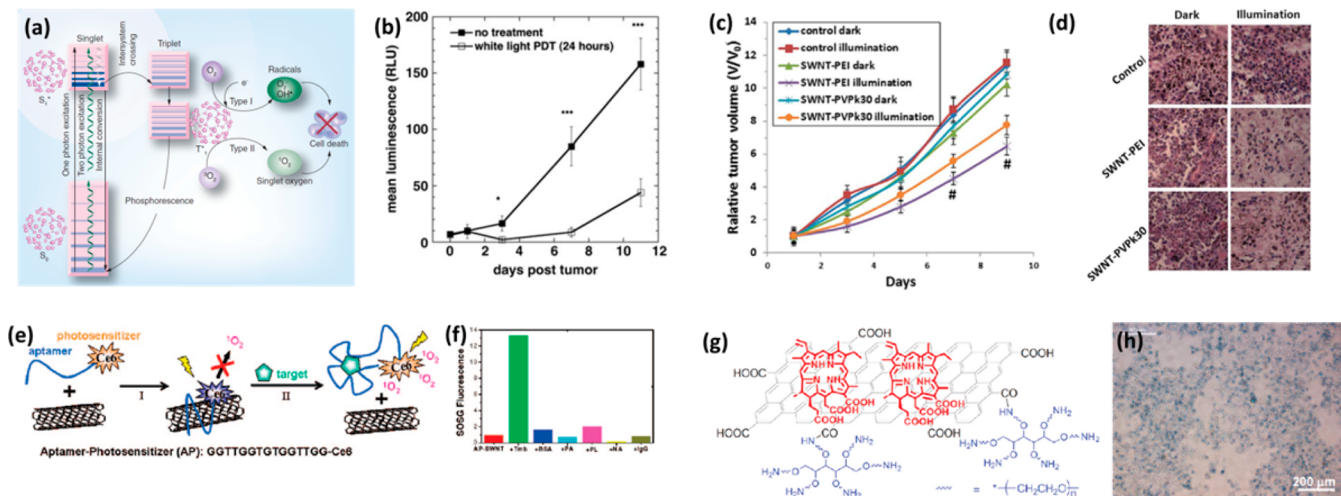


Figure 39. Photodynamic therapy with carbon nanomaterials. (a) Jablonski diagram showing the generation of reactive oxygen species via photoexcitation of fullerene. Reprinted with permission from ref 60. Copyright 2011 Future Medicine. (b) Mean bioluminescence measured from CT26-Luc tumors in control, untreated group and the group receiving intraperitoneal injection of fullerene and white-light PDT. Reprinted with permission from ref 659. Copyright 2011 Elsevier. (c) Plots of relative tumor volume in groups of mice receiving different treatments, including the “control dark” group without injection of SWCNTs or illumination (blue), the “control illumination” group without injection of SWCNTs but with illumination (red), the “PEI dark” group with injection of PEI-functionalized SWCNTs but without illumination (green), the “PEI illumination” group with both injection of PEI-functionalized SWCNTs and illumination (purple), the “PVP dark” group with injection of PVP-functionalized SWCNTs but without illumination (cyan), and the “PVP illumination” group with both injection of PVP-functionalized SWCNTs and illumination (orange), where the PEI illumination group exhibits the slowest tumor growth indicating the highest efficacy of tumor treatment based on SWCNT-enabled PDT. (d) Representative images of H&E stained tumor slices from the six different treatment groups in (c). (c, d) Reprinted with permission from ref 661. Copyright 2014 Royal Society of Chemistry. (e) Schematic showing how the singlet oxygen generation of SWCNT-aptamer-photosensitizer complex can be regulated by the target molecule. (f) Bar chart showing the fluorescence of singlet oxygen sensor green (SOSG), which is the indicator of singlet oxygen concentration, upon the addition of different proteins including thrombin (Tmb), bovine serum albumin (BSA), protein A (PA), protein L (PL), NeutrAvidin (NA), and immunoglobulin G (IgG). One can see that the SWCNT-aptamer-photosensitizer complex only generates detectable singlet oxygen when thrombin is present. (e, f) Reprinted from ref 663. Copyright 2008 American Chemical Society. (g) Schematic showing the GO-PEG-Ce6 conjugate based on supramolecular π - π stacking between GO and Ce6. (h) Typical Trypan Blue stained microscopic cell image showing the KB cells incubated with the GO-PEG-Ce6 conjugate and with 660 nm laser irradiation. (g, h) Reprinted from ref 175. Copyright 2011 American Chemical Society.

bacteria.^{656–658} There are three main components to PDT: a light source used to generate ROS, a photosensitizing molecule, and molecular oxygen in tissues naturally occurring in a triplet state. The photosensitizing molecule can be excited after the absorption of light and undergo an intersystem crossing in order to produce singlet oxygen, which is highly cytotoxic and destroys any organic tissue it encounters. Similar to PTT, after the localization of a photosensitizing agent within a tumor, the cancerous body is exposed to light of a particular wavelength which, in the presence of oxygen, generates cytotoxic SO and/or ROS that kill cells and subsequently cause tissue death. An abundance of photosensitizing molecules exist, and the majority contain porphyrin structures. While overall less research has been conducted on carbon nanomaterials for PDT, the synergistic effects of combining carbon nanotubes, graphene, and carbon dots with photosensitizers significantly boost the efficacy of treatment. In a similar fashion to drug loading applications of carbon nanomaterials, photosensitizers can be noncovalently loaded onto the aromatic surface of carbon nanomaterials coated in biocompatible polymers through π - π stacking for activation after laser excitation.

Fullerenes such as C₆₀ and C₇₀ have been found as photosensitizers with a high efficiency of generating reactive oxygen species,⁵⁹ allowing for efficient photodynamic therapy using fullerenes without the need to load additional photosensitizing molecules. Ground state, singlet fullerene can be photoexcited to a short-lived triplet state, which transfers its energy to molecular oxygen in its triplet state, resulting in a series

of reactive oxygen species including singlet oxygen and oxygen radicals (Figure 39a). Hamblin et al. reported photodynamic therapy using N-methylpyrrolidinium-fullerene for the treatment of colon adenocarcinoma by intraperitoneal injection of the functionalized fullerene into the abdomen of the tumor-bearing mice, and found significantly slowed tumor growth compared to the control group (Figure 39b).⁶⁵⁹ Besides photodynamic treatment of tumor, the same group also reported the use of functionalized C₆₀ fullerene as a broad-spectrum antimicrobial photosensitizer, which cures fatal wound infections under white-light illumination in a mouse model.⁶⁶⁰ The unique property of fullerenes in the efficient conversion from photons to reactive oxygen species has made fullerene derivatives competitive photosensitizers for PDT applications in vivo animal and even preclinical settings.⁶⁰

Carbon nanotubes can either act as photosensitizers themselves^{89,661} or load exogenous photosensitizers for PDT.⁶⁶² Imahori et al. found semiconducting SWCNTs can generate reactive oxygen species more efficiently than metallic SWCNTs, opening up the possibility of using chemically separated, pure semiconducting SWCNTs as photosensitizers for PDT.⁸⁹ A more recent study by Zhang et al. has demonstrated that photodynamic effects of SWCNTs highly depend on a modification method of the nanotubes, and effective in vivo tumor destruction has been realized based on PDT using PEI and PVP (polyvinylpyrrolidone) functionalized SWCNTs (Figure 39c,d).⁶⁶¹ SWCNTs can also be used as nanocarriers to deliver photosensitizers to target tissue such as the tumor, owing to the

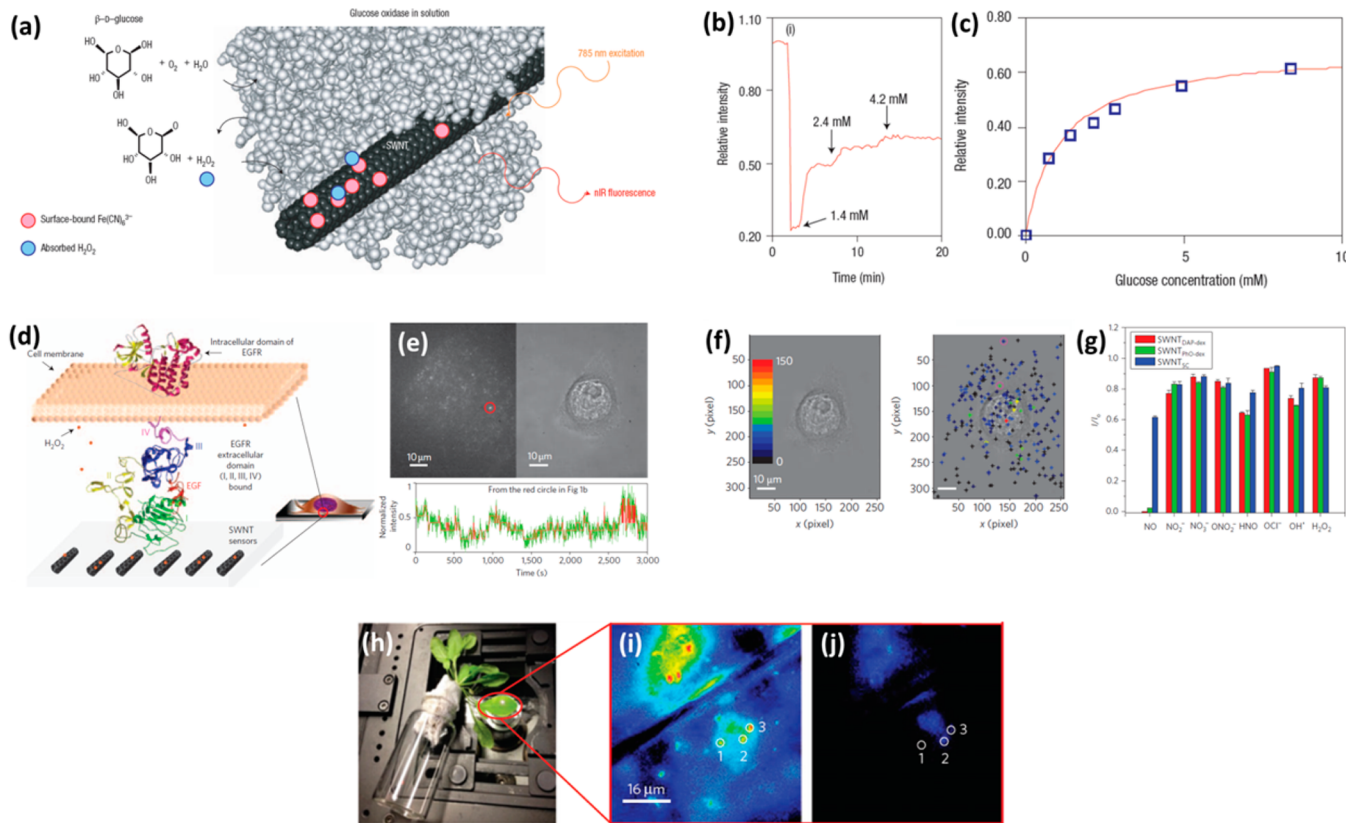


Figure 40. In vitro detection of glucose, ROS, and RNS using SWCNT-based optical sensors. (a) Schematic showing the glucose oxidase wrapped SWCNT with surface-bound $\text{Fe}(\text{CN})_6^{3-}$. In the presence of glucose, the quenched fluorescence of SWCNT recovers due to the production of H_2O_2 , which reduces $\text{Fe}(\text{CN})_6^{3-}$ to nonquenching, $\text{Fe}(\text{CN})_6^{4-}$. (b) Relative fluorescence intensity of the SWCNT sensor shown in (a), exhibiting responses to $\text{Fe}(\text{CN})_6^{3-}$ (initial drop), and addition of glucose at different concentrations (stepwise recovery of fluorescence). (c) Calibration curve showing relative SWCNT fluorescence intensity versus glucose concentration. (a–c) Reprinted with permission from ref 664. Copyright 2005 Nature Publishing Group. (d) Schematic showing the transmembrane structure of EGFR, which releases H_2O_2 (small red dots) upon binding to an EGF molecule. The SWCNT sensors are embedded in a thin film, which is placed underneath the cells and responds to H_2O_2 releasing events with quenching in fluorescence. (e) NIR-II fluorescence image (top left) and its corresponding phase contrast image (top right) of an A431 cell cultured on the SWCNT sensor film. The stepwise fluorescence quenching and dequenching behavior is shown in the bottom panel over time for the bright spot in red circle of the NIR-II image. (f) Phase contrast image (left) and its overlaid image with spatial mapping revealing the number of quenching events within 3000 s recording time (right). For each SWCNT sensor spot (shown as a cross), its number of quenching events is color-coded from red (150) to black (0). (d–f) Reprinted with permission from ref 490. Copyright 2010 Nature Publishing Group. (g) Normalized fluorescence intensity (current intensity I divided by initial intensity I_0) of SWCNTs coated with DAP-dex, phenoxy dextran (PhO-dex), and sodium cholate (SC) in response to different ROS and RNS. Reprinted with permission from ref 481. Copyright 2009 Nature Publishing Group. (h) Photograph of the NO sensing setup *in vivo* in leaves of *Arabidopsis thaliana*. (i) NIR-II fluorescence microscopic image of the leaf shown in the red circle of h. (j) NIR-II fluorescence microscopic image of the leaf in the same region in (i), after exposing the leaf to a solution of NO. (h–j) Reprinted with permission from ref 672. Copyright 2014 Nature Publishing Group.

high accumulation of SWCNTs inside tumor tissue based on the EPR effect. Lee et al. reported the synthesis of PEGylated SWCNTs loaded with a common photosensitizing drug, Chlorin e6 (Ce6), for PDT-based tumor treatment in mice.⁶⁶² It has also been reported by Tan et al. that the nanotube–photosensitizer complex can act as a “smart” PDT agent with molecular specificity. In this study, SWCNTs were used to quench singlet oxygen generation of the photosensitizer molecules, until the photosensitizer molecules were released from the backbone of SWCNTs in the presence of a specific molecular target (Figure 39e).⁶⁶³ Carbon nanotubes are known to strongly quench fluorescence of nearby molecular fluorophores and it was proposed that photosensitizing molecules could be quenched in a similar fashion when in close proximity to the carbon nanotube surface. After conjugating an aptamer that recognized thrombin to the photosensitizer, Ce6, carbon nanotubes, and the aptamer-conjugated photosensitizer were mixed, leading to extremely high quenching of 98%. After the introduction of

thrombin, a large increase in singlet oxygen generation was observed, indicating that the thrombin-recognizing aptamer–photosensitizer conjugate disassociated from the carbon nanotube and allowed recovery of photodynamic efficiency of Ce6 (Figure 39f). This approach has many significant benefits, namely that the generation of the cytotoxic reactive oxygen species is only produced after exposure to a particular target, resulting in a “smart” PDT agent that can be specifically turned on or off via selective molecular recognition and may have enhanced efficacy with mitigated toxicity to normal tissue.⁶⁶³

By taking advantage of the ultrahigh loading of molecules through $\pi-\pi$ stacking, nanoGO has been used to deliver photosensitizers *in vitro* at high concentrations.¹⁷⁵ The same photosensitizer molecule as used in previous studies involving SWCNTs, Ce6 was used and loaded onto the PEGylated and well-dispersed nanoGO sheets through the supramolecular $\pi-\pi$ stacking (Figure 39g). The GO–PEG–Ce6 conjugate demonstrated excellent serum stability and elevated cytotoxicity after

irradiation. While the production of singlet oxygen species was slightly diminished by the presence of the quenching graphene surface (10–15% of free Ce6) in a similar fashion as reported in the previous study with carbon nanotubes,⁶⁶³ many more surface defects are found in graphene oxide, which appears to be much less efficient at absorbing energy than carbon nanotubes. To this end, photodynamic therapy was still readily feasible utilizing nanoGO, evidenced by the large population of dead cells after incubation with GO–PEG–Ce6 conjugate and laser irradiation at 660 nm (Figure 39h). Interestingly, it was found that a slight increase in ambient temperature using another laser of 808 nm that did not activate Ce6 was capable of increasing intracellular uptake of the GO–PEG–Ce6 conjugate by ~2-fold. The higher uptake of GO–PEG–Ce6 contributed to a further boost in the overall cytotoxicity of the nanomaterial–photosensitizer complex. One can envision a pretreatment step involving heating the tumor after an intravenous injection of the GO–PEG–Ce6 complex to improve the accumulation of the photosensitizer within the tumor body, and then switching to the wavelength that produces the cytotoxic effects of Ce6.¹⁷⁵ Another study by Cui et al. involved the use of folic acid conjugated graphene oxide loaded with Ce6 photosensitizers for targeted PDT in incubated cancer cells with remarkable photodynamic efficacy, owing to effective delivery and accumulation of the Ce6 molecules inside the tumor cells with the graphene oxide nanocarriers.¹⁷⁴

5.5. Carbon Nanomaterials for In Vitro Sensing and Diagnostics

The rich optical properties of carbon nanomaterials, such as their traditional fluorescence emission in the visible and NIR windows, fingerprints in resonant Raman scattering spectra, and unique NIR-II fluorescence emission, have also been utilized for detection of characteristic biomarkers in an in vitro setting. Besides their intriguing optical properties, CNT- and graphene-based field-effect transistors (FETs) have been widely applied as biosensors as well.

The emission intensity and energy of the intrinsic NIR-II fluorescence of an SWCNT have been found to be sensitive to its dielectric environment, which can be modulated by the adsorption of different molecules or slight conformation changes of molecules that adsorb on the nanotube backbone. This finding has thus become the foundation of a toolbox of SWCNT-based biosensors for detection of glucose,^{664,665} nitric oxide,⁴⁸¹ nitroaromatics,⁶⁶⁶ hydrogen peroxide,⁴⁹⁰ avidin,⁴⁵¹ genotoxins,⁶⁶⁷ neurotransmitters,⁶⁶⁸ and even DNA conformational polymorphism.⁶⁶⁹ Pioneered by Doorn, Strano, and Weisman, the SWCNT-based biosensors take advantage of Fermi level shift due to surface adsorption events of certain molecules, leading to fluorescence quenching and/or peak shift in the NIR-II window.^{278,451,664} For example, the ferricyanide anion, Fe(CN)₆³⁻, irreversibly adsorbs on the surface of the SWCNT backbone, withdrawing electrons from the SWCNT and causing the Fermi level of the SWCNT to shift into its valence band. Stepwise quenching of the NIR-II fluorescence of SWCNTs has been found in the presence of ferricyanide anions at different concentrations, while the fluorescence intensity can be partially recovered upon addition of hydrogen peroxide (H₂O₂) due to reduction of ferricyanide. This phenomenon has been employed for sensitive detection of glucose, which generates H₂O₂ as a coproduct of the reaction between glucose and glucose oxidase (Figure 40a). Glucose-oxidase-wrapped SWCNTs with surface-bound Fe(CN)₆³⁻ exhibit positively correlated recovery of fluorescence with the addition of glucose (Figure 40b), and the

response function between fluorescence intensity and glucose concentration (Figure 40c) reveals a detection limit of 34.7 μM, which is well below the blood glucose levels for normal persons (up to 6 mM before meal) and diabetic patients (up to 8 mM before meal).⁶⁶⁴ In the follow-up work by the Strano group, other quenching molecules such as boronic acid have been screened for selective detection of glucose and certain pentoses with a turn-on fluorescence response.^{665,670}

Hydrogen peroxide, when acting on its own, also behaves as an electron-withdrawing agent that induces charge transfer from the valence band of SWCNT to the high reduction potential of H₂O₂ and suppresses the NIR-II fluorescence emission of SWCNTs.⁶⁷¹ Unlike other electron-withdrawing agents such as singlet oxygen (¹O₂) and genotoxins that cause red shift of nanotube band gap emission peaks, H₂O₂ has effect only on the emission peak intensity and thus allows for unambiguous fingerprinting of H₂O₂ from other analyte molecules.⁶⁶⁷ An SWCNT array that selectively measures the short-lived H₂O₂ based on the distinct quenching and dequenching rate constants from other ROS and reactive nitrogen species (RNS) has been demonstrated for real-time quantitative mapping of H₂O₂ efflux in epidermoid carcinoma A431 cells from their abundant EGFRs during the EGFR signaling pathway (Figure 40d–f).⁴⁹⁰

Besides H₂O₂, other ROS species such as •OH radical and singlet oxygen ¹O₂ also have an effect on the band gap fluorescence of SWCNTs. For example, when d(GT)₁₅ oligonucleotide wrapped SWCNTs are exposed to •OH radicals, the photoluminescence of (7,5) chirality is quenched more than the (6,5) chirality, while the emission peaks of both chiralities show no red shift; on the other hand, when SWCNTs with the same formulation are exposed to singlet oxygen ¹O₂, a profound red shift in emission wavelength can be found for the (6,5) chirality but not for (7,5). The distinct spectral responses of DNA-wrapped SWCNTs originate from the reactions between the DNA wrapping agent and ROS molecules, and have laid the foundation for multimodal optical sensing of different ROS species.⁶⁶⁷

Nitric oxide (NO) is an important messenger molecule for biological signaling, and SWCNTs can be noncovalently modified with 3,4-diaminophenyl dextran (DAP-dex) to afford high sensitivity and specificity toward detection of the NO molecule. Similar to Fe(CN)₆³⁻ and H₂O₂, NO molecule quenches the intrinsic band gap fluorescence of SWCNTs via an electron transfer mechanism from the nanotube valence band to the lowest unoccupied molecular orbital (LUMO) of the NO radical.⁴⁹¹ The fluorescence quenching, which has been found reversible, shows high selectivity toward NO alone among a number of ROS and RNS (Figure 40g).⁴⁸¹ A further improved version of SWCNT-based NO sensing assay has been developed by the same group using DNA oligonucleotides and PEG functionalized SWCNTs to afford in vivo stability and sensitivity for in situ detection and molecular imaging of NO molecules in live mouse liver in the NIR-II window (see section 4.2.3).³⁵ Besides sensing NO molecules in mammalian cells and live animals, SWCNTs have also been applied for detection of NO molecules in live plant leaves based on the changes in the intrinsic NIR-II fluorescence intensity (Figure 40h–j).⁶⁷²

More complex bioactive molecules, such as DNA and chemotherapeutic alkylating agents, can also be detected with high sensitivity. The Strano group has demonstrated that DNA conformational polymorphism, which involves the transition from the native, right-handed B conformation to the left-handed Z conformation as a result of cation adsorption and charge

screening (Figure 41a), can be optically detected by tracking the band gap emission peak energy of SWCNTs, among which the

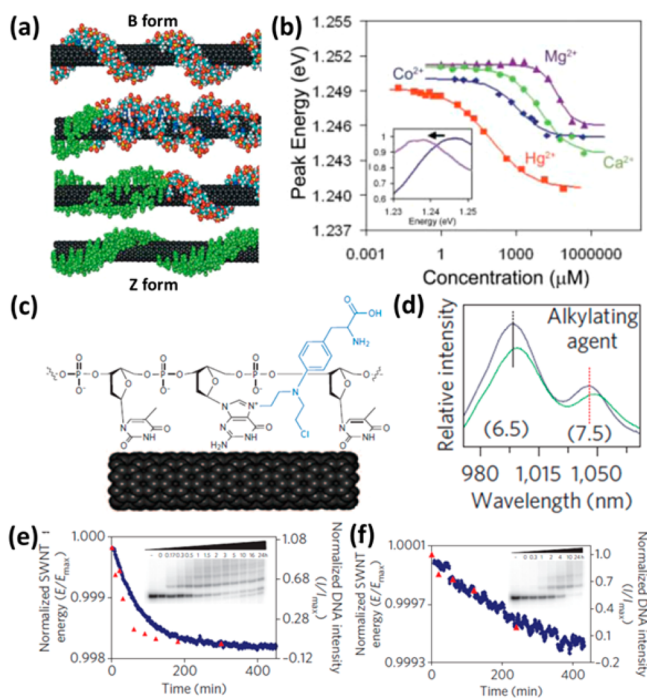


Figure 41. In vitro sensing of DNA conformational changes and genotoxins based on interaction between SWCNT and DNA wrapping agents. (a) Schematic showing the DNA conformational changes from the natural B form to the Z form as a response to cations. (b) Plots showing the shift of emission peak energy of (6,5) chirality upon addition of different divalent metal cations at different concentrations. The inset shows the red shift of (6,5) emission peak upon addition of Hg^{2+} . (a, b) Reprinted with permission from ref 669. Copyright 2006 American Association for the Advancement of Science. (c) Scheme showing the reaction between the G-rich DNA oligonucleotide wrapped SWCNTs (black) with melphalan (blue), which alkylates the guanine base at its N7 position. (d) Emission spectra of SWCNTs showing the intensity decrease and emission peak red shift of both (6,5) and (7,5) chiralities after alkylation with mechlorethamine (black, before; green, after). (e, f) Plots showing the shift of normalized band gap emission energy of (6,5) chirality (blue diamonds) and the kinetic change of unreacted oligonucleotide band intensity (red triangles), the latter of which is derived from polyacrylamide gel electrophoresis (PAGE) as shown in the insets, for two guanine-alkylating agents, melphalan (e) and cisplatin (f). (c–f) Reprinted with permission from ref 667. Copyright 2009 Nature Publishing Group.

(6,5) chirality exhibits the greatest sensitivity (Figure 41b).⁶⁶⁹ The red shift in emission peak energy is a result of the change in the dielectric environment of SWCNTs, and thus can be utilized for sensitive detection of DNA hybridization, which involves complementary binding of an additional DNA chain to the original ssDNA coating on the SWCNT surface, leading to a decrease in the effective dielectric constant of the SWCNT local environment.⁶⁷³ The same concept has been used for detection of a variety of chemotherapeutic alkylating agents, which react with guanine in G-rich DNA oligonucleotides at the N7 position of guanine and causes red shift of DNA-functionalized SWCNTs through local dielectric modulation (Figure 41c–f).⁶⁶⁷

More recently, corona phase molecular recognition has been introduced to the SWCNT-based molecular sensing system, where synthetic heteropolymers with various hydrophobic and

hydrophilic regions are used to coat the surface of SWCNTs and act as “artificial antibodies” for specific recognition of small molecules, which can bind to the synthetic heteropolymers, induce dielectric changes in the corona phase of the SWCNTs, and modulate the spectral properties of the band gap NIR-II fluorescence of SWCNTs.^{666,668,674–676} This new sensing paradigm has allowed for specific detection of a handful of bioactive molecules, including riboflavin, L-thyroxine, estradiol, dopamine, and epinephrine, without relying on the naturally existing recognizing molecules such as peptide motifs, antibodies, and aptamers.^{668,674} This molecular sensing system may also provide a unique platform allowing for thermodynamic and kinetic study of nanoparticle–polymer–biomolecule interaction beyond its biosensing applications.

Although all aforementioned examples employ fluorescence quenching or emission energy red shift of SWCNTs or both to sense and detect different molecular species, the intrinsic NIR-II fluorescence and Raman signature of SWCNTs without intensity or energy modulation have also been widely used for immunoassay in protein microarrays. Yudasaka et al. conjugate the NIR-II fluorescent SWCNTs to IgG for immunoassay and immunoprecipitation of protein G, a bacteria-expressed protein that specifically binds to immunoglobulin. By detecting the NIR-II fluorescence emission of SWCNTs, this immunoassay is able to detect analyte molecules such as protein G with a detection limit of ~ 600 pM, which is owing to the low fluorescence quantum yield of SWCNTs and can be further improved with fluorescence enhancement techniques.⁶⁷⁷ Taking advantage of the characteristic G-band and the large cross section of resonant Raman scattering of SWCNTs, our group has utilized SWCNTs as multicolor Raman labels for protein microarrays with high sensitivity and multiplexity. In our experiments, SWCNTs are noncovalently functionalized with phospholipid–PEG surfactants with amine terminal groups that impart the SWCNT Raman tags with both sufficient immunity to NSB and the ability to further conjugate with an antibody (see section 3.1 for details on noncovalent surface functionalization of SWCNTs). A sandwich assay layout is implemented on gold-coated glass substrate, which not only provides anchoring sites for analyte immobilization but also offers SERS effect to boost the Raman signals (Figure 42a). Both high specificity and sensitivity have been achieved with the SWCNT Raman tags (Figure 42b–d), while multiplexed detection of mouse and human IgGs is demonstrated using SWCNTs comprised of different carbon isotopes (Figure 42e,f; see section 4.3.2 for more details).⁵⁴⁸ In more recent studies, with better morphological control of the underlying gold substrate, we have further improved the detection limit, dynamic range, and multiplexity using a series of Raman and fluorescence tags based on SWCNTs and other small molecule reporters (Figure 42g,h).^{423,453,455,549,678}

As for other carbon nanomaterials such as graphene and carbon dots, they are usually incorporated in a FRET pair such that the intrinsic fluorescence of the donor molecule can be modulated and responsive to analyte biomolecules. Graphene is usually nonfluorescent or weakly fluorescent, but it is a good light absorber and can be employed as the acceptor in the FRET donor/acceptor pair. On the other hand, carbon dot with strong intrinsic fluorescence emission in the visible window is typically used as the donor fluorophore in the FRET pair. For example, in a QD/GO donor/acceptor pair where the fluorescence emission of QDs is quenched by GO in the absence of DNA analyte, the QD fluorescence can be recovered when hybridization occurs between two complementary DNA chains and increases the

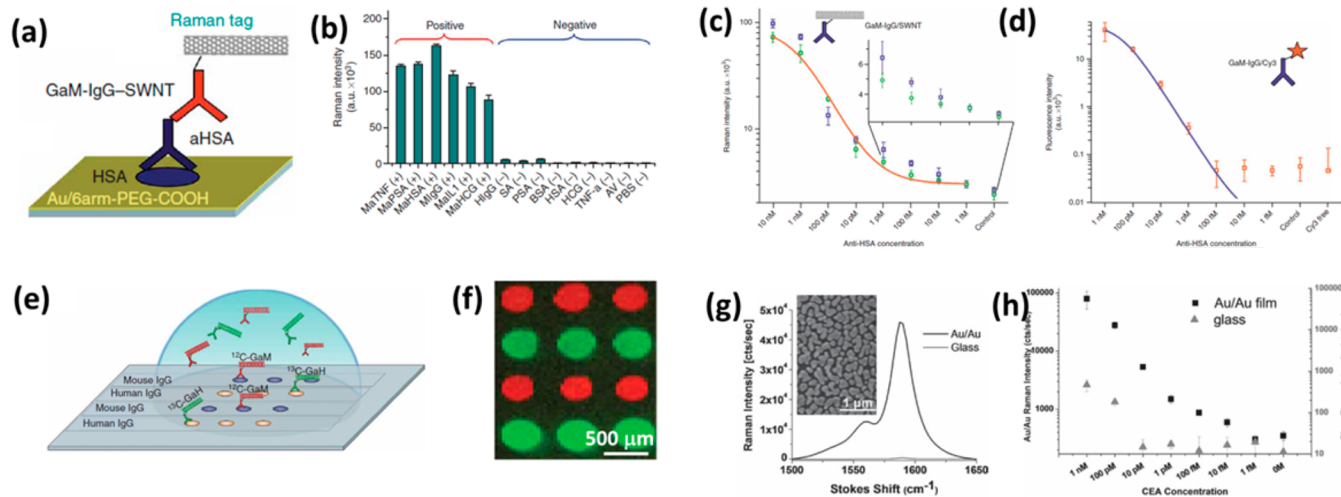


Figure 42. Protein microarray using SWCNTs as multicolor Raman tags on SERS substrates. (a) Schematic showing the sandwich assay scheme of the SWCNT based protein microarray. From bottom to top: Au-coated glass slide with surface modification of branched PEG carboxylic acid (6arm-PEG-COOH) through a self-assembled monolayer (SAM) of cysteamine; human serum albumin (HSA, the capture protein); anti-HSA (aHSA, the analyte antibody); a bioconjugate consisting of SWCNT and goat antimouse IgG (GaM-IgG-SWNT), where the SWCNT acts as the Raman tag. (b) Bar chart showing the detected Raman intensity for positive analytes (mouse IgGs) and negative analytes (non-mouse IgGs and proteins), exhibiting good specificity. (c, d) Calibration curves of Raman-based protein microarray using SWCNTs as Raman tags and fluorescence-based protein microarray using Cy3 as fluorescence tags, showing a much lower detection limit of SWCNT Raman microarray (1 fM (c), where blue and green indicate two separate trials) than fluorescence microarray (100 fM (d)) for the detection of aHSA. (e) Schematic showing the layout of multiplexed detection of mouse and human IgGs based on SWCNTs comprising ^{12}C and ^{13}C isotopes. (f) Representative Raman map of multiplexed detection of mouse and human IgGs, where the G-band of ^{12}C -SWCNTs is color coded in red and that of ^{13}C -SWCNTs is color coded in green. (a–f) Reprinted with permission from ref 548. Copyright 2008 Nature Publishing Group. (g) Resonance Raman spectra of SWCNTs on glass substrate (gray curve) and the Au/Au film (black curve), showing the G-band is enhanced by \sim 200 times on the Au/Au film. The inset shows an SEM image of the Au/Au film. (h) Calibration curves of the Raman G-band intensity of SWCNT Raman tags on the Au/Au film (black squares) and bare glass substrate (gray triangles) versus the concentration of CEA, showing a significantly improved detection limit with the SERS substrate comprised of Au/Au film. (g–h) Reprinted with permission from ref 549. Copyright 2011 John Wiley & Sons.

distance between QD and GO, efficiently suppressing the FRET process and the quenching effect.⁶⁷⁹ In another FRET system where the fluorescent carbon dot acts as the donor fluorophore, its fluorescence can be quenched by Eu $^{3+}$ ions, which are chelated by the rich carboxylate groups at the edges of carbon dots; however, dequenching happens when phosphate anions competitively bind to Eu $^{3+}$ ions and disrupt the FRET pair, releasing the carbon dots from the quenching Eu $^{3+}$ ions and recovering their fluorescence.⁶⁸⁰ Similar strategies have been employed for the detection of Cu $^{2+}$, Hg $^{2+}$, and biothiols in physiological conditions based on fluorescence quenching and dequenching of carbon dots.^{235,681} More interestingly, the fluorescent carbon dot and nonfluorescent rGO can pair up to make a FRET system by themselves: Qu et al. devised and realized a FRET-based sensing system toward the detection of K $^{+}$ ions with a detection limit of \sim 10 μM , where the amine-terminated carbon dots and rGO are connected through 18-crown-6 ether, a cation recognizing ligand with particular affinity for K $^{+}$. In the absence of K $^{+}$ ions, 18-crown-6 ether binds tightly to the amine terminal groups on carbon dots and brings carbon dots close to rGO to cause fluorescence quenching; in the presence of K $^{+}$, 18-crown-6 ether prefers binding to K $^{+}$ over the amine-terminated carbon dots, releasing carbon dots and leading to fluorescence recovery.⁶⁸² This is an interesting example demonstrating the diversity of the family of carbon nanomaterials, from which unlimited possibilities arise to meet various needs for biosensing.

Besides making use of their optical properties, carbon nanotube and graphene have sensitive changes of resistance to gate voltage and can thus act as field effect transistors (FETs) for biosensing applications.^{81,683,684} CNTs and graphene can be

modified with analyte-capturing ligands, and their resistance between the source and drain electrodes will respond to changes in gate voltage, which is modulated by surface adsorption and ligand binding events of analyte molecules. Our lab is among the first to demonstrate that SWCNTs can be used as chemical sensors with sensitive changes in electrical resistance upon exposure to gaseous molecules such as NO₂ and NH₃.⁸⁰ With proper surface modification to prevent NSB, SWCNTs can also act as specific biosensors for the detection of streptavidin (SA),⁶⁸⁵ IgG (Figure 43a,b),²⁸⁴ monoclonal antibodies,²⁸⁴ prostate specific antigen,⁶⁸⁶ and autoantibodies⁶⁸⁷ via conjugation of SWCNTs with different receptors for selective binding to target proteins. Similarly, owing to the ambipolar electric field effect, graphene is naturally suitable as a FET device for detection of surface binding events caused by biomolecules and even bacteria. Berry et al. have shown that the conductance of graphene amine (GA) is sensitive enough to detect the attachment of a single bacterium on its surface (Figure 43c), while a FET device based on GO can be used to detect the absorption of ssDNA and hybridization of double-stranded DNA (dsDNA; Figure 43d).¹³⁹ An aptamer-modified graphene FET has also been demonstrated as a label-free immunosensor for sensitive detection of immunoglobulin E (IgE) protein with detectable changes in drain current with down to 0.29 nM IgE concentration (Figure 43e,f).⁶⁸⁸ Compared to CNT FET devices, the graphene-based FET devices have the benefits of large surface area to interact with the analyte and thus higher sensitivity for the detection of certain biomolecules of interest.⁶⁸⁴

Besides the aforementioned therapeutic application of carbon nanomaterials, carbon nanotubes and graphene have also been

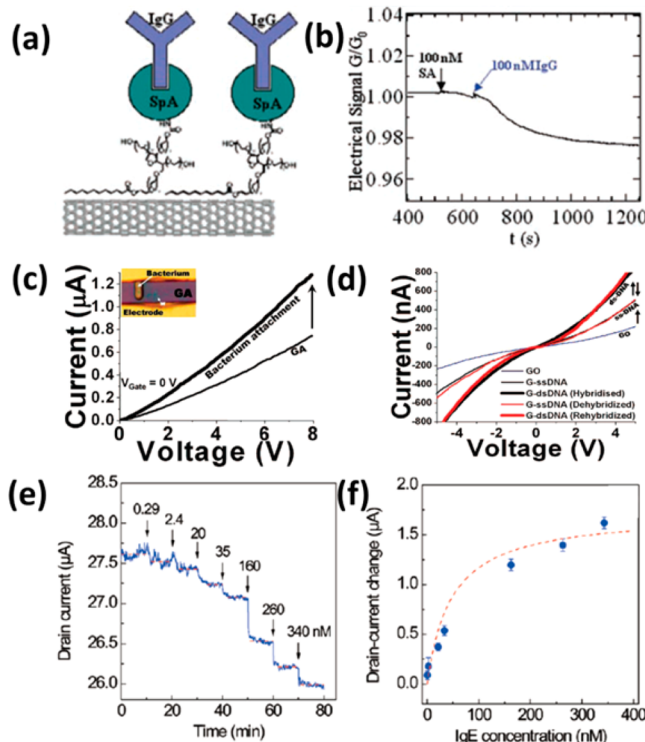


Figure 43. Carbon nanotube and graphene FET devices as specific electronic biosensors. (a) Schematic drawing of a typical SWCNT FET device, in which the SWCNT is surface modified with Tween to prevent NSB and staphylococcal protein A (SpA) to selectively capture IgG proteins. (b) Curve showing the normalized conductance of SWCNT FET device (G/G_0) versus time, where the addition of 100 nM IgG causes detectable changes in conductance due to specific binding to SpA while the addition of 100 nM SA has minimum effect on conductance due to NSB. Reprinted with permission from ref 284. Copyright 2003 National Academy of Sciences. (c) I – V curve of a GA FET device showing increase in conductance upon the attachment of a single bacterium (inset). (d) I – V curves of a GO FET device showing the changes in conductance during the following events: adsorption of ssDNA, hybridization to form dsDNA, dehybridization of the dsDNA, and rehybridization to form dsDNA. Reprinted from ref 139. Copyright 2008 American Chemical Society. (e) Curve showing the change of drain current of an aptamer-modified graphene FET versus time, exhibiting stepwise decrease in drain current upon injection of IgE at progressively increasing concentrations at 10 min intervals. (f) Calibration curve showing the drain current as a function of IgE concentration, which is fit to the Langmuir adsorption isotherm (red dashed line). Reprinted from ref 688. Copyright 2010 American Chemical Society.

used for tissue reinforcement. Carbon nanotubes and intact graphene sheets are some of the strongest materials found in nature and have been successfully utilized as scaffolding and structural support for regeneration during tissue engineering.^{689–693} Regenerative medicine focuses on developing methods which can create new, functional tissue that can repair or replace tissues damaged from injury or disease. Commonly used synthetic polymers such as poly(lactic acid) suffer from insufficient mechanical strength, yet low quantities of additive carbon nanotubes significantly increase the overall mechanical properties of the tissue scaffolding and can often double the Young's modulus and tensile strength.²⁴ As another example, the addition of graphene to chitosan, a common biopolymer used as scaffolding for wound healing, increased the elastic modulus of chitosan by over 200%.⁶⁹⁴ Other than as scaffolding for wound

healing, carbon nanomaterials serve as innovative substrates for the in vitro growth of biological tissue while nanopatterning can produce aligned, directional growth of particular tissue/cell types during tissue and cellular regeneration.^{695–697}

6. PHARMACOKINETICS AND TOXICOLOGY OF CARBON NANOMATERIALS

As for any exogenous molecules or materials to be delivered into living organisms, in vitro cytotoxicity on cells and tissues and in vivo pharmacokinetics and toxicology are always worth full evaluation. For in vitro assessment of cytotoxicity, a few important biochemical indicators, including cell proliferation, apoptosis, necrosis, oxidative stress, and DNA damage, are usually used to give a full account of the biocompatibility of a specific foreign substance to the cell culture.^{500,698} For evaluation of in vivo toxicity, depending on different ways of administration of the foreign molecules or materials, the physiological response may vary to a large extent, resulting in distinct pharmacokinetics, which is the time scale and fate of an externally introduced material including absorption, distribution, interaction, metabolism, retention, and excretion in a living organism.

Another complexity to the in vivo administered nanomaterials is the in vivo toxicology induced by the interactions between the nanomaterials and the living organism, which involves body weight monitoring, the blood chemistry panel, hematology profile, and histological analysis.^{501,698} For carbon nanomaterials, both in vitro and in vivo toxicity highly depend on the shape, size, and surface coating (see section 3 for more information on the surface functionalizations of carbon nanomaterials), which will be discussed in sufficient detail in this section.

6.1. In Vitro Cytotoxicity Study of Carbon Nanomaterials

Being an efficient light sensitizer and singlet oxygen (${}^1\text{O}_2$) producer under exposure to light, fullerene and its derivatives can be highly toxic to living systems in the presence of oxygen molecules, due to the damage to many biologically crucial molecules including DNA, proteins, and lipids through the light-triggered formation of reactive oxygen species such as singlet oxygen and reduced oxygen radicals ($\cdot\text{O}_2^-$, $\cdot\text{OH}$, etc.). This photochemical reaction lays the foundation of photodynamic therapy and antibiotic/antiviral activities of fullerenes;⁵⁹ however, in the meantime it induces nontrivial toxicity concerns to normal cells and tissues as well.

Pristine, unfunctionalized fullerene has been found to have a higher degree of cytotoxicity than the covalently functionalized fullerenes, such as C_{60} fullerenols with different surface coverages of hydroxyl groups and methanofullerenes. The observed cytotoxicity is attributed to light-induced oxidative damage to cell membranes such as peroxidation of lipid bilayers, evidenced by the generation of superoxide anions for water-soluble fullerenes.⁶⁹⁹ However, this ability to cause oxidative damage decreases as the fullerene cage becomes more functionalized and fully derivatized, explaining why the covalently modified fullerenes have less toxic effect to cells than the pristine fullerenes.⁷⁰⁰ In contrast, noncovalently functionalized fullerenes with certain capping agents can be even more toxic due to the formation of a charge-transfer complex between the fullerene core and the solubilizing coating molecules. Such capping agents include polyvinylpyrrolidone, which is known to form a charge-transfer complex with the highest known equilibrium constant so far.⁷⁰¹ The charge-transfer structure enhances the photosensitizing effect that generates more reactive oxygen species upon exposure to ambient light. It has been found that the PVP

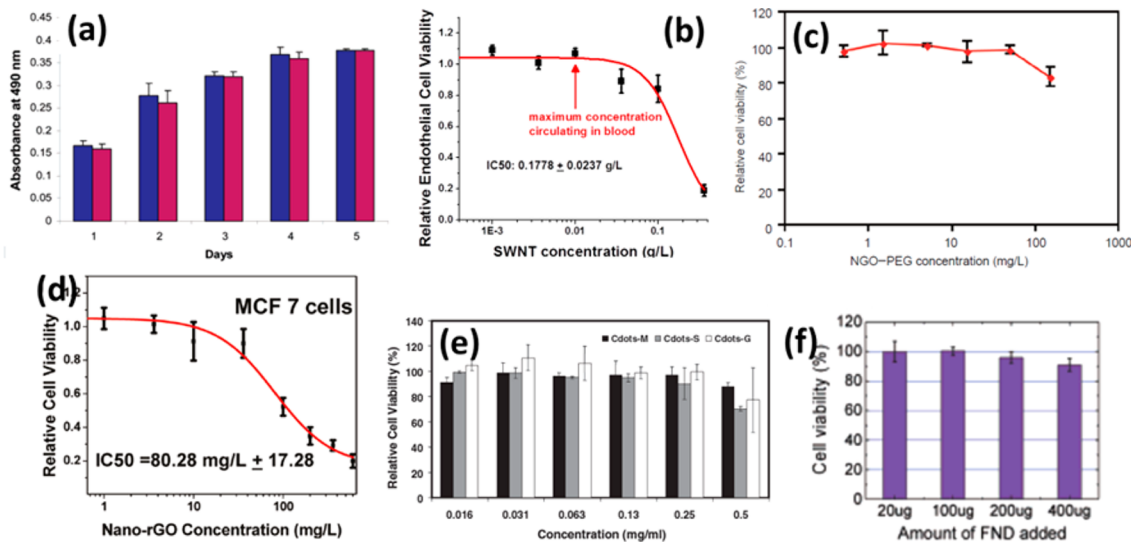


Figure 44. In vitro cytotoxicity of carbon nanomaterials. (a) Cytotoxicity of covalently oxidized and protein-adsorbed SWCNTs studied by cell proliferation MTS assay. The MTS assay was performed for HeLa cells at different time points after the initial incubation with SWCNT–protein bioconjugates at a concentration of 0.025 mg/mL with the duration of the initial incubation of 2–3 h. The blue bars show the formazan absorbance, which is proportional to the number of live cells in the culture, of the control, untreated HeLa cells, while the red bars show the formazan absorbance of the HeLa cells exposed to SWCNT–protein conjugates. Reprinted from ref 316. Copyright 2005 American Chemical Society. (b) Cytotoxicity of SWCNTs noncovalently functionalized with DSPE-mPEG (5 kDa), one type of the PL–PEG surfactants. This curve plots the relative endothelial cell viability as a function of SWCNT incubation concentration, from which the IC₅₀ value is extracted by fitting the original data (black squares) to a sigmoidal function (red curve), revealing an IC₅₀ value of 0.1778 ± 0.0237 g/L. Reprinted with permission from ref 15. Copyright 2012 Nature Publishing Group. (c) Cytotoxicity of nanoGO covalently functionalized with branched PEG (NGO–PEG). Here the relative cell viability against untreated control is plotted as a function of the incubation concentration of NGO–PEG, showing little cytotoxicity to the human B lymphoma Raji cells at a concentration up to 150 mg/L. Reprinted with permission from ref 29. Copyright 2008 Springer. (d) Cytotoxicity of rGO noncovalently functionalized with branched C18-PMH-mPEG. This curve plots the relative viability of human breast cancer MCF-7 cells as a function of the incubation concentration of nano-rGO, revealing an IC₅₀ value of 80.28 ± 17.28 mg/L. Reprinted from ref 157. Copyright 2011 American Chemical Society. (e) Cytotoxicity of bare carbon dots without additional surface functionalization except oxygen-rich groups from the oxidizing synthetic route. The bar chart plots the viability of human kidney embryonic 293T cells incubated with increasing concentrations of MWCNT-derived, SWCNT-derived, and graphene-derived carbon dots (denoted as Cdots-M, Cdots-S, and Cdots-G, respectively). Reprinted with permission from ref 190. Copyright 2012 John Wiley & Sons. (f) Cytotoxicity of raw nanodiamonds after strong oxidative acid treatment. The bar chart shows minimal cytotoxicity of fluorescent nanodiamonds (FNDs) up to an incubation concentration of 400 µg per 1 mL of the cell medium. Reprinted from ref 255. Copyright 2005 American Chemical Society.

solubilized C₆₀ solution has obvious harmful effect to mouse embryos in both in vitro and in vivo settings. A statistically significant inhibitory effect on cell differentiation and proliferation has been revealed for mouse midbrain cell culture incubated in the presence of C₆₀–PVP nanoparticles.⁷⁰²

A similar story exists regarding the cytotoxicity of carbon nanotubes, which highly depends on the method of surface functionalization and properties of surface capping molecules. When SWCNTs and MWCNTs are not functionalized with any surfactants and used as is, they tend to form tight aggregates and bundles in spite of intensive sonication, and cause significant cytotoxicity to alveolar macrophages after incubation for merely 6 h.⁷⁰³ An increasing level of ROS indicating a higher degree of oxidative stress along with the activation of nuclear transcription factor-κB (NF-κB) as a response to harmful cellular stimuli has been found in human keratinocytes, which are treated with pristine SWCNTs dissolved in dimethylformamide (DMF) without any surface functionalization.⁷⁰⁴

The in vitro cytotoxicity can be significantly mitigated by surface functionalization. Our group has shown that when SWCNTs are oxidized on the sidewalls and covalently functionalized with different molecules including fluorescein and poly(ethylene oxide) (PEO) linked biotin, they exhibit very little toxicity to HL60 cells, evidenced by no appreciable cell death. This finding suggests oxidized SWCNTs with surface

carboxyl groups are nontoxic by themselves.³³⁷ In a follow-up work, we have found that oxidized SWCNTs with proteins nonspecifically adsorbed on the nanotube sidewalls (i.e., the SWCNT–protein bioconjugates) do not show any inhibition to the proliferation of the treated HeLa cells up to 5 days after the initial cell exposure to the SWCNT–protein conjugates, as evidenced in the CellTiter 96 MTS assay results that exhibit little deviation of the formazan absorbance in the treated group compared to that in the control, untreated group (Figure 44a).³¹⁶ Besides these two examples of covalently oxidized and functionalized SWCNTs, Weisman et al. have shown that SWCNTs noncovalently functionalized with Pluronic surfactant, which is a nonionic surfactant, do not cause appreciable cytotoxicity by showing similar cell confluence, adhesion, and morphology to the control group cultured in the absence of SWCNTs.⁴³¹ Besides the Pluronic surfactant, we have shown that SWCNTs noncovalently wrapped with DNA do not lead to any adverse effect on cell proliferation and adhesion either.⁹⁵ A more quantitative in vitro toxicity study has suggested a very high half-maximal inhibitory concentration (IC₅₀) of 0.1778 g/L for DSPE-mPEG (5 kDa) coated SWCNTs on human dermal microvascular endothelial cells, derived from a sigmoidal fitting to the plotted cell viability curve at increasing SWCNT incubation concentrations (Figure 44b).¹⁵ SWCNTs noncovalently wrapped with a branched PEG polymer, C18-PMH-

mPEG, are also found as nontoxic at a high incubation concentration, and an IC₅₀ value of 0.136 g/L on 4T1 murine breast cancer cells has been determined for this specific formulation of PEGylated SWCNTs.²⁹⁸

The cytotoxicity of graphene and its derivatives is also highly dependent on surface functionalization, in that the pristine and reduced GO with fewer surface functional groups tend to be more toxic than GO, as suggested by a number of in-depth studies.^{705,706} The observed cytotoxicity of pristine graphene is believed to be the result of two signaling pathways: the mitogen-activated protein kinase (MAPK) pathway and the transforming growth factor beta (TGF- β) pathway. These two signaling pathways both lead to the up-regulation of pro-apoptotic proteins and initiate the apoptosis process that results in cell death under oxidative stress.⁷⁰⁷ In striking contrast, it has been reported that functionalized graphenes, including GO and GO modified with many different hydrophilic macromolecules, can significantly reduce the cytotoxicity. It has been suggested in a *Nature Chemistry* review paper in 2010 that GO should have distinct advantages in reduced toxicity over CNTs, owing to the excellent aqueous solubility without the need to use surfactant to debundle and disperse in water, as well as the lack of metal catalyst impurities that are usually present in CNTs and could be the cause of oxidative stress related to CNTs.¹²⁴ These arguments have been validated in a series of studies showing little or no cytotoxic effect of plain and modified GO at relatively high concentrations. For example, the as-oxidized plain GO without further conjugation to the surface groups does not exhibit any statistically significant reduction of A549 cell viability until an incubation concentration of 50 mg/L is reached.⁷⁰⁸ We have reported that the PEGylated nanoGO shows little cytotoxicity up to a cell incubation concentration of >100 mg/L, in which branched PEG chains are covalently linked to the -COOH groups in GO (Figure 44c).^{21,29} Reduced GO with a decreased number of available functional groups can be noncovalently PEGylated with the branched C18-PMH-mPEG through hydrophobic interaction, and a low cytotoxicity has been found with an IC₅₀ value of 80–90 mg/L to different cancer cell lines (Figure 44d).¹⁵⁷ Besides our group's PEGylation methodology to reduce cytotoxicity, a number of other strategies of surface functionalization have been used by others to reduce the cytotoxicity of GO. Proteins, including the unpurified fetal bovine serum (FBS) proteins and bovine serum albumin (BSA, which is the major component in FBS),³¹⁹ have been used to coat the surface of GO via nonspecific binding, and the cytotoxicity of GO–protein complex is found to be dependent on the protein concentration, where a higher concentration of proteins results in mitigated cytotoxicity of GO.⁷⁰⁹ Other surface passivating molecules and polymers, including chitosan,⁷⁰⁵ dextran,⁷¹⁰ and peptide,⁷¹¹ have been used to coat GO through either electrostatic interaction or covalent bonding between GO and protein. Reduced hemolytic activities and cell toxicity after surface coating suggest a biocompatible protective layer on the GO sheet to reduce toxic effect on the exposed cells.

Carbon dots, on the other hand, can be nontoxic even without any additional surface modification by capping agents. Liu et al. have found that the as-made, bare carbon dots from different carbon precursors do not exhibit any appreciable cytotoxicity to the human kidney embryonic 293T cells until the incubation concentration reaches as high as 0.5 mg/mL (Figure 44e).¹⁹⁰ This result of low toxicity to cells has been confirmed by another independent study on the same 293T cell line but using carbon dots synthesized from a different electrooxidation approach.¹⁸⁷ A

similar level of inhibitory concentration on a different cell line, human hepatocellular carcinoma HepG2 cells, has been found by Ray et al., with unaffected cell proliferation and viability until the incubation concentration of bare carbon dots is increased to >0.5 mg/mL.²¹⁸ In contrast to bare, unfunctionalized pristine graphene that induces considerable cytotoxicity by triggering pro-apoptotic signaling pathways, the bare carbon dots cause much lower toxicity to cells possibly due to the significantly smaller size, higher degree of oxidation, and greater water solubility. Interestingly, when carbon dots are surface-passivated with H₂N–PEG–NH₂, the cytotoxic effect becomes even greater than with the bare carbon dots, evidenced by a lower incubation concentration of 0.2 mg/mL that starts causing appreciable cell death, as reported by Sun et al.³⁸² The authors have attributed the observed cytotoxicity of PEG(1.5 kDa)-amine functionalized carbon dots to the surface passivating agent PEG(1.5 kDa)-amine, which has been found to have a greater cytotoxicity effect by itself.³⁸² These studies have suggested carbon dots as nontoxic, biocompatible, and eco-friendly alternatives to semiconductor quantum dots for a variety of fluorescence imaging applications.⁴

Nanodiamonds have been proposed to have a lower chance of inducing cellular oxidative stress than has been found with other carbon nanomaterials.⁶⁰⁸ Chang et al. have found minimum loss of cell viability up to a nanodiamond incubation concentration of 0.4 mg/mL (Figure 44f), and have proposed that the chemical inertness and lack of toxic impurities are the two main reasons for the observed low cytotoxicity of fluorescent nanodiamonds.²⁵⁵ A more systematic cytotoxicity study of nanodiamonds with diameters of 2–10 nm carried out by Dai et al. has revealed nanodiamonds are nontoxic to many cell types including neuroblastoma cells, macrophages, keratinocytes, and rat pheochromocytoma PC-12 cells.⁷¹² For both raw nanodiamonds and carboxyl group functionalized nanodiamonds, the mitochondrial functions of the tested cells after exposure to nanodiamonds have been evaluated by the MTT assay to reveal negligible damage to the mitochondria, while the amount of ROS inside the tested cells is not significantly increased upon addition of nanodiamonds into the cell culture medium. It is also found that neuroblastoma cells can grow on nanodiamond-COOH coated collagen substrate without appreciable morphological changes in comparison to bare collagen substrate. All these results have indicated the lack of cytotoxicity and high biocompatibility of nanodiamonds for cell fluorescent labeling and cell culture.⁷¹²

6.2. In Vivo Pharmacokinetics and Toxicology of Carbon Nanomaterials

Similar to in vitro cytotoxicity of fullerenes, the in vivo toxicology studies have also revealed the dependency on surface functionalization and coating. Oberdörster has found that uncoated, pristine fullerenes can cause severe oxidative damage and depletion of total glutathione (GSH) in vivo in an aquatic species, which are evidenced by the observation of an appreciable increase in lipid peroxidation of the fish brain. Due to the high hydrophobicity of the pristine C₆₀ nanoparticles, they tend to localize inside the hydrophobic, lipid-rich regions of the brain and cause oxyradical-induced lipid and protein damage to the brain.⁷¹³ In a series of studies that seem contradictory to the other findings of high toxicity associated with pristine fullerenes, not only does C₆₀ fullerene lack any acute or subacute toxicity in vivo, but it also can be used as a powerful antioxidant and liver-protective agent owing to the high electron affinity (about 2.7–2.8 eV) of fullerenes that makes them good radical scavengers for

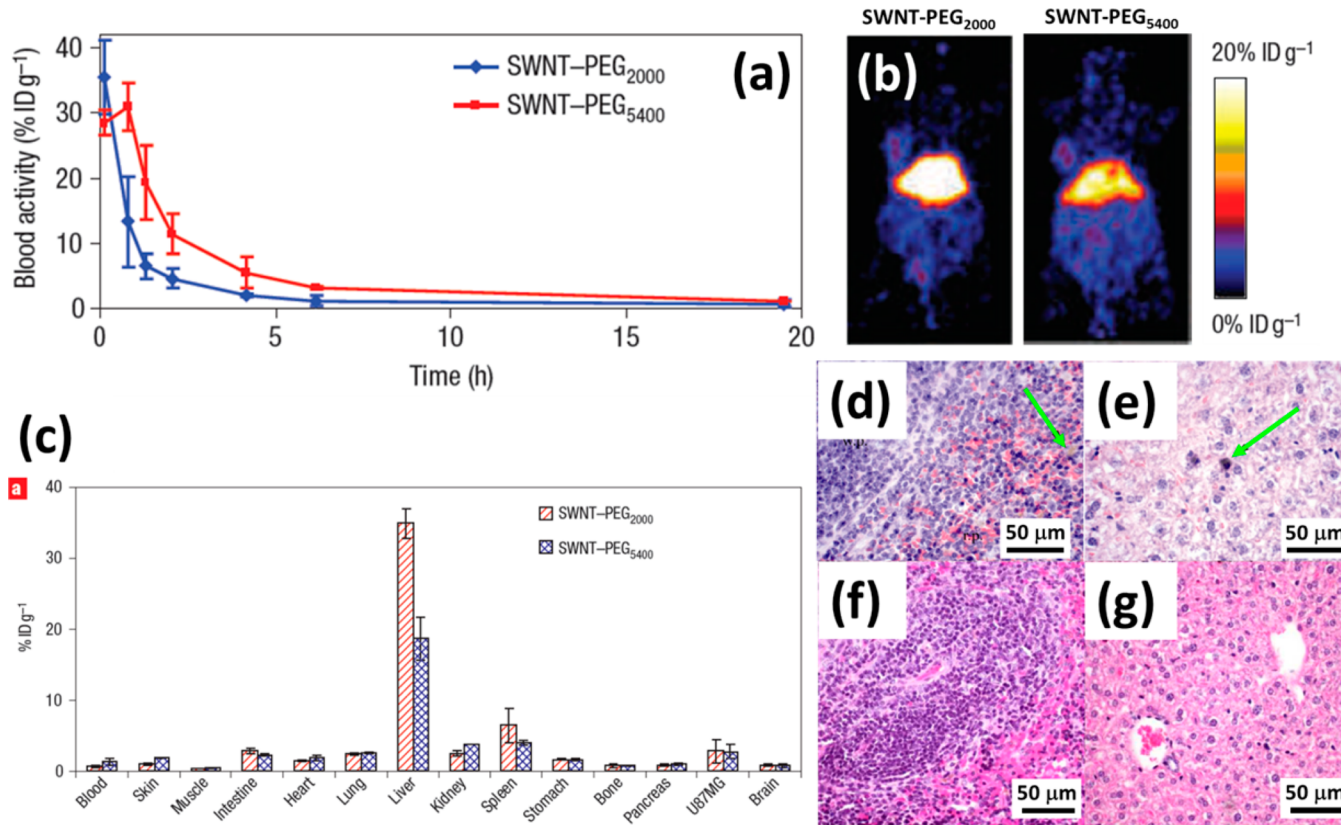


Figure 45. In vivo pharmacokinetics and toxicology of SWCNTs. (a) Determination of blood circulation half-lives of 2000-Da (blue curve) and 5400-Da (red curve) PEGylated SWCNTs by measuring the radio-decay corrected blood activity of ⁶⁴Cu as a function of time post injection of SWCNTs. Half-lives of ~0.5 and ~2 h have been found for the 2000- and 5400-Da PEGylated SWCNTs, respectively. (b) MicroPET images of two mice injected with 2000-Da (left) and 5400-Da (right) PEGylated SWCNTs at 24 h post injection, showing a higher accumulation of the injected SWCNTs in the liver with a smaller PEG. (c) Biodistribution of 2000-Da (red bars) and 5400-Da (blue bars) PEGylated SWCNTs in different organs at 24 h post injection, revealing a significantly higher RES uptake in liver and spleen for the SWCNTs noncovalently functionalized with smaller PEG. (a–c) Reprinted with permission from ref 291. Copyright 2007 Nature Publishing Group. (d, e) Histological microscopic images of hematoxylin and eosin (H&E) stained spleen (d) and liver (e) slices from a mouse injected with unseparated SWCNTs coated with a mixture of 1 MDa C18-PMH-mPEG and 5 kDa PL-PEG surfactant at a 1:1 weight ratio, where the green arrows indicate the presence of residual SWCNTs appearing as gray-brown granular intracytoplasmic pigment. The injected dose is 3.6 mg of SWCNTs/kg of body weight. (d, e) Reprinted with permission from ref 13. Copyright 2010 Springer. (f, g) Histological microscopic images of H&E stained spleen (f) and liver (g) slices from a mouse injected with single chirality (6,5) SWCNTs coated with 90 kDa C18-PMH-mPEG, where there are no residual SWCNTs observed. The injected dose is 0.254 mg of SWCNTs/kg of body weight. (f, g) Reprinted from ref 34. Copyright 2013 American Chemical Society.

protecting organs from radical damage.⁷¹⁴ It has been suggested that the main clearance pathway of in vivo administered pristine C₆₀ is through the biliary pathway due to the large size of the C₆₀ aggregates (30–100 nm)⁷¹³ beyond the renal cutoff size, while the unique radical scavenging property of C₆₀ also helps protect the liver from free radical induced damages.^{715,716} To explain the contrasting reports on the in vivo toxicity of pristine fullerenes, it has been suggested that it is the organic solvent, tetrahydrofuran (THF), which is used as a transition solvent to bring the hydrophobic C₆₀ nanoparticles into aqueous environment, that has caused the observed toxic effect as a result of the formation of THF–C₆₀ nanocomplex.⁷¹⁷ However, it is worth bearing in mind that the photodynamic effect of fullerenes, in particular pristine fullerenes, could be a main cause of tissue and organ damages when they are administered in vivo.

In contrast to pristine fullerenes that form aqueous suspensions as large aggregates, covalently functionalized fullerenes significantly increase the water solubility by introducing hydrophilic groups to the surface of the cage. It has been reported that a dendro[60]fullerene with many carboxyl groups on the fullerene surface can impart high water solubility to the

fullerene nanoparticles,⁴⁹ resulting in rapid urinary excretion from the body through the kidneys as opposed to biliary clearance pathway found for pristine or mildly functionalized C₆₀ fullerenes.⁷¹⁸ This has suggested that, owing to the exceptionally small size of fullerene nanoparticles, they can be ideal nanocapsules for loading various cargo molecules if well functionalized and solubilized as individual nanoparticles in biological medium.

The in vivo pharmacokinetics and toxicology studies for carbon nanotubes can be dated back to a series of pioneering works done by our group and the Sambhir group at Stanford University.^{291,636,637} We have used the radioactive isotope ⁶⁴Cu to label SWCNTs for microPET imaging and radioactivity measurement, and found that, for SWCNTs noncovalently functionalized with PL-PEG, the blood circulation time and biodistribution are both dependent on the molecular weight of PEG chains coating on the surface of the SWCNTs.²⁹¹ PEG chains with two different molecular weights, 2000 and 5400 Da, are tested for this study, and the smaller molecular weight usually results in a shorter blood circulation half-life and a higher RES uptake in the liver and spleen (Figure 45a–c). Shorter blood

circulation and higher RES uptake are usually indicators of faster opsonization and recognition of the foreign materials in the plasma by phagocytes. Therefore, the PEG functionalization with a smaller molecular weight is insufficient to prevent NSB of proteins to SWCNTs, while the 5400-Da PEGylated SWCNTs have high enough hydrophilicity and resistance to protein NSB and opsonization *in vivo*, resulting in better “stealth nanoparticles” that delay the provocation of the immune response.

Due to the short decay half-life of 12.7 h for ^{64}Cu , the isotope labeling followed by γ -counting for the determination of the SWCNT concentrations in tissues is not suitable for long-term biodistribution study to find out the fate of intravenously injected SWCNTs. Owing to the intrinsic and characteristic Raman G-band signal of SWCNTs at 1590 cm^{-1} , we were able to measure the blood circulation, biodistribution, excretion, and long-term fate of SWCNTs with linear and branched PEG functionalizations with different molecular weights.⁶³⁷ It has been found that SWCNTs functionalized by branched, 7 kDa PEG afford the longest blood circulation of up to 1 day, and in the meantime have the lowest uptake in the RES system, suggesting the best surface passivation that efficiently prevents opsonization and RES clearance. Moreover, a higher degree of PEGylation of SWCNTs achieved by using the branched, 7 kDa PEG also affords faster clearance of intravenously administered SWCNTs from the mouse body, and near-complete clearance is observed by Raman-based histology of liver tissue slices at 3 months post injection. This finding contrasts strongly with the biodistribution study for pristine, unfunctionalized SWCNTs, which are found to remain at the same retention level in liver and spleen over time.⁷¹⁹ Raman spectroscopy also allows for excretion study of the injected SWCNTs, which are found in intestine, feces, kidney, and bladder, indicating a mixed clearance pathway of SWCNTs from mice via both biliary and renal excretion.⁶³⁷ Although a nontrivial Raman signal has been unambiguously measured in kidney and bladder (presumably in urine too), compared to the measured Raman signal in intestine and feces, one can find that the majority of the injected PEGylated SWCNTs are excreted through the biliary pathway, which explains the long time (>3 months) required for nearly complete clearance from the body. This is a major shortcoming of SWCNTs for *in vivo* biomedical applications, and we will come back to this issue in section 7.

A systematic *in vivo* toxicology study on PEG-functionalized SWCNTs has been carried out to evaluate both acute and chronic toxicity of SWCNTs after injection into the bloodstream.⁶³⁶ Two formulations of SWCNTs, noncovalently PEGylated SWCNTs (PEG molecular weight = 2 kDa) and oxidized, covalently PEGylated SWCNTs (PEG molecular weight = 10 kDa), are included in this study. Interestingly, blood chemistry panel reveals all relevant parameters within normal ranges for the control group and two treated groups with noncovalent and covalent PEGylation, and there has been no statistically significant difference between the groups by the time of sacrifice. The lack of *in vivo* toxicity for PEGylated SWCNTs contrasts strongly with MWCNTs without proper surface functionalization, with the latter showing asbestos-like pathogenicity to peritoneal macrophages and diaphragm by evoking inflammatory responses after intraperitoneal injection of the long MWCNTs.⁷²⁰ The striking difference of *in vivo* toxicity once again suggests the importance of having biocompatible and “masking” coating on the surface of carbon nanomaterials to minimize any adverse effect.^{721,722} Despite the failure to observe any *in vivo* toxicity for properly functionalized SWCNTs,

histological imaging and Raman microscopic mapping both demonstrate the persistent retention inside the liver and spleen tissue for both formulations of the SWCNTs over a long period of 4 months, suggesting suboptimal surface passivation possibly due to smaller PEG molecular weight and the oxidized nanotube sidewalls.⁶³⁶

More recently, our group has developed a new noncovalent surface functionalization method for SWCNTs with a branched PEG polymer, poly(maleic anhydride-*alt*-1-octadecene)-methoxy poly(ethylene glycol) [C18-PMH-mPEG]. We have found that such a branched PEG polymer with a total molecular weight of ~ 1 MDa (each PEG branch is 5 kDa) can noncovalently coat SWCNTs to afford an exceptionally long blood circulation half-life of 18.9 h,²⁹⁷ significantly longer than that of linear PL-PEG coated SWCNTs (~ 5 h) with the same molecular weight for each linear PEG chain.⁶³⁷ This much longer blood circulation half-life is attributed to a denser packing of PEG chains when they are polymerized into one giant capping molecule as opposed to many smaller PL-PEG molecules.²⁹⁷ Despite the long circulation half-life indicating a better “masking” effect that avoids rapid attack at the SWCNTs by the immune system, and the unusually high tumor uptake of 23% ID/g via the EPR effect, the C18-PMH-mPEG surfactant by itself can lead to even higher skin uptake of ~ 30 % ID/g, which is problematic because of the increased background signal that lowers the signal-to-noise ratio (SNR) for imaging and reduced specificity for photothermal therapy.⁷²³ Our group has come up with a few solutions to tackle this problem. The 1 MDa C18-PMH-mPEG surfactant can be mixed with 5 kDa PL-PEG surfactant at a 1:1 weight ratio to reduce the skin uptake to less than 2% ID/g while keeping sufficient tumor uptake of 8% ID/g.¹³ Another attempt has been made to reduce the total molecular weight of C18-PMH-mPEG to ~ 90 kDa with only 18 PEG chains in one molecule, resulting in a low skin uptake of ~ 6 % ID/g while maintaining an extremely long blood circulation half-life of ~ 31 h and an unprecedented high tumor uptake of 30% ID/g.²⁹⁸ These studies have suggested the power of molecular engineering of the noncovalent capping agents to achieve desired *in vivo* pharmacokinetics.

Besides its long circulation time in the bloodstream, the C18-PMH-mPEG coated SWCNTs have shown minimum toxicity to mice injected with these materials. All blood panel parameters for the injected mice match well with those of control animals, both of which fall within the reported normal range for healthy mice.¹³ Although residual SWCNTs can be visualized without any lesions or damages in histological photomicrographs of liver and spleen slices from the injected mice (Figure 4Sd,e),¹³ the retention in RES organs has been found as highly dependent on the injected dose. In a later study we have found that the chirality-separated SWCNTs with 90 kDa C18-PMH-mPEG coating can afford a much lower dose of injection to achieve the same photothermal efficacy without visible residual nanotube bundles in any organ based on the histological analysis (Figure 4Sf,g).³⁴

To better understand the interactions between functionalized SWCNTs and the living organism, it is important to study the pathophysiological processes, in particular the complement recognition and activation pathways that lead to the potential *in vivo* toxicity of administered SWCNTs. To this end, Moghimi et al. have focused on the activation of the complement system by three different formulations of SWCNTs, including human serum albumin (HSA) coated SWCNTs, linear PL-PEG coated SWCNTs, and branched C18-PMH-mPEG coated SWCNTs.²⁹⁹ They have found that the HSA-coated SWCNTs activate the

complement system via C1q-mediated classical and the alternative pathways, which are different from the lectin pathways triggered by both PEGylated versions of SWCNTs. Moreover, it has been found that the linear and branched PEGylated SWCNTs trigger the lectin pathways via different recognitions, in that the PL-PEG coated SWCNTs trigger the lectin pathway through both mannan-binding lectin and L-ficolin recognition, while the C18-PMH-mPEG coated SWCNTs achieve so by L-ficolin recognition only. This difference makes C18-PMH-mPEG a unique capping agent for nanomaterials with innate immunocompatibility, in that the complement activation by C18-PMH-mPEG does not generate any anaphylatoxin or complement C3 and C5 convertases.²⁹⁹ Based on the conclusions of this study, we believe the noncovalent coating of C18-PMH-mPEG should be the best surface functionalization approach for in vivo applications of carbon nanomaterials.

Radiolabeling is the most widely used method to study the in vivo behavior of graphene and its derivatives, since the characteristic Raman G-band utilized for the quantitation of SWCNTs is usually much less pronounced in GO due to the high degree of oxidation that diminishes the resonant Raman features.⁷²⁴ By labeling the GO nanoparticles with radioactive isotopes, different independent groups have found a high lung accumulation as well as RES uptake of bare GO following intravenous administration, which does not have any surface functionalization except the endogenous oxygen-containing groups from the oxidation process.^{725,726} The high accumulation of injected GO in the lungs may have resulted from the so-called "pulmonary first-pass effect", which usually accounts for the trapping of intravenously delivered stem cells in the pulmonary microvasculature during blood circulation and could explain the similar observation for GO nanoparticles with similar sizes.⁷²⁷ By reducing the size of GO and achieving better surface functionalization with covalently conjugated branched PEG molecules, Liu et al. have shown the lung uptake of nanoGO becomes much less appreciable while the RES uptake of the nanoGO in liver and spleen is still quite prominent, based on radioactive ¹²⁵I labeling. Interestingly, a two-compartment model has been found for the blood circulation curve of PEGylated nanoGO, possibly suggesting the size inhomogeneity that results in different clearance profiles from the blood circulation.⁷²⁸ The size inhomogeneity is confirmed by AFM measurement revealing a broad size distribution of 10–30 nm, and consistent with the body excretion profiles showing the existence of PEGylated nanoGO in both urine and feces, suggesting a mixed biliary and urinary clearance pathway. The smaller portion of the nanoGO is more likely to be filtrated through the kidneys with fast clearance from the body, while the larger nanoGO is found as brown-black clumps in liver histology with a much longer retention.^{159,728} The size variability of GO with potential fast renal clearance is an obvious advantage of graphene derivatives, which is not possible for SWCNTs since they will lose almost all their useful traits when becoming so small.⁴¹⁰

Both short-term and long-term (up to 3 months) toxicology studies on mice injected with PEGylated and dextran-conjugated graphene oxide have revealed the lack of any in vivo toxicity of the functionalized graphenes, as evidenced by the normal blood biochemistry, hematological examination, and histological analysis.^{710,728} These findings strongly contrast the observed blood thrombogenicity, pulmonary edema, and granuloma formation in live animal studies for intravenously injected bare GO without surface coating.^{725,726,729} This striking difference in in vivo toxicity shows a strong dependence on surface

functionalization,^{159,730,731} and highlights the importance of coating the carbon nanomaterials with efficient surface passivating agents such as PEG to minimize interaction with the immune system and reduce the adverse effects on the living organisms.

More recently, Liu et al. have reported their findings on the enzyme induced oxidation and biodegradation of GO by horseradish peroxidase (HRP).⁷³¹ They have found that when the bare GO sample is mixed with an oxidant, H₂O₂, and a catalyst, HRP, the characteristic color of GO gradually disappears over a course of 4 days, while the transmission electron microscopy (TEM) images confirm the significantly reduced sizes of GO due to degradation. However, the PEGylated GO via EDC chemistry shows resistance to the HRP-catalyzed degradation, possibly due to the shielding effect of PEG on the GO sheets. Therefore, an alternative approach of PEGylation via the cleavable disulfide bond is used on the surface functionalization of GO, which shows both excellent biocompatibility and biodegradability. These findings have opened up the possibility of breaking down the relatively large carbon nanomaterials into smaller fragments that can be more readily metabolized and excreted, and thus bode well for clinical uses with more favorable pharmacokinetics.⁷³¹

The exceptionally low cytotoxicity of carbon dots, as discussed in section 6.1, is consistent with the high compatibility and minimum adverse effect for in vivo administered carbon dots. No indicator of in vivo toxicity, such as abnormal food intake, body weight loss, clinical disorders or biochemical abnormalities of the serum, has been found in mice injected with up to 40 mg of carbon dots/kg of body weight.³⁸² The excretion of intravenously administered carbon dots has been found as through both urine and feces, while the urinary clearance constitutes the majority of the total excretion. In stark contrast to CNTs and GO that are usually metabolized via the biliary pathway and cleared out from the body with fecal excretion, the urinary excretion of carbon dots is highly desired and owes to the much smaller size that allows carbon dots to pass the glomerulus. Due to the fast renal clearance, histological imaging and analysis of sliced mouse organs reveal relatively minor accumulations of the injected carbon dots in the RES system without any histopathological abnormality or lesion to the major organs.^{190,382} The ultrasmall size, fast renal clearance, and low medium lethal dose (LD₅₀) of carbon dots all point to their potential uses in the clinic owing to similar performance, toxicology, and pharmacokinetics to small molecule fluorophores.³⁸²

Fluorescent nanodiamonds have also been reported to have negligible in vivo toxicity to different animal models. *C. elegans* has been used as a model organism to test the in vivo toxicity of nanodiamonds in invertebrates.²⁶⁷ Microinjection of bioconjugated nanodiamonds coated with dextran and BSA has not affected the growth, development, lifespan, or progeny production of *C. elegans*, consistent with the ROS measurement that has revealed no increase of ROS level in the nanodiamond-treated group compared to the control group. Stress response assay based on tracking the location of GFP-labeled transcription factor DAF-16 inside the nucleus versus the cytoplasm has not only confirmed the lack of the stress response of *C. elegans* to nanodiamonds, but has also verified that the function of stress response genes in *C. elegans* is not compromised by the nanodiamond treatment.²⁶⁷ For in vivo toxicology studies in larger animals such as mice and rats, the potential adverse effects of nanodiamonds have been evaluated with different administration approaches. Intratracheal instillation is a standard

method for evaluation of respiratory toxicity of nanodiamonds, which can easily spread into air and become harmful to the respiratory system when breathed in. Intratracheally administered nanodiamonds are found in lungs and blood circulation within a few hours after intratracheal instillation, while the concentration has been found to decrease monotonically over time indicating body clearance. The tissue retention of instilled nanodiamonds is mainly found in the lungs and the RES system including liver, spleen, and bones as a result of transportation across the air–blood barrier. The long retention time of the nonbiodegradable nanodiamonds in the lungs has contributed to the elevated toxic effect to the lung tissue, as indicated by the observed lung tissue thickening, abnormal biochemistry of bronchoalveolar lavage fluid, and lung inflammatory responses.⁷³² Nonetheless, it has been reported that orally, subcutaneously, and intraperitoneally administered nanodiamonds do not induce appreciable immune or inflammatory responses in mice.^{269,733–735} Histopathological analysis of different organs collected from rats after receiving intraperitoneal administration of BSA-functionalized nanodiamonds indicates minimum *in vivo* toxicity up to an injection dose of 75 mg/kg body weight.²⁶⁹ As a conclusion, nanodiamonds can be highly nontoxic to live animals except taken up by the respiratory system, while the size of the nanodiamond particles plays an important role in determining the fate of the *in vivo* administered nanodiamonds.

7. CONCLUSIONS AND OUTLOOK

In this review, we have covered the recent progress in the biomedical imaging and therapeutic applications of carbon nanomaterials, which constitute a new class of materials with exciting chemical, optical, and mechanical properties. Although all made of the same chemical element, these nanomaterials with different allotropic forms of carbon exhibit distinct properties and behaviors depending on how the carbon atoms are bonded to form the larger structures on the nanoscale, and on the size of the nanostructures. With a library of well-established surface functionalization and passivation methodologies, it is now possible to make water-soluble and biocompatible carbon nanomaterials with minimum *in vitro* and *in vivo* toxicity, and to use these nanostructures for a myriad of biomedical imaging and therapeutic applications.

For biomedical imaging, we have covered a broad range of optical and nonoptical imaging applications using carbon nanomaterials, with a focus on NIR-II fluorescence imaging with SWCNTs. The NIR-II fluorescence emission of SWCNTs under excitation in the visible and NIR-I windows is unique to SWCNTs, and has not been found with any other materials or molecules until more recently.^{392,394,396} Although all other carbon nanomaterials than SWCNTs only have fluorescence emission in the conventional spectral regions, the resistance to photobleaching makes them more durable fluorescent labels than organic fluorophores for long-term *in vitro* and *in vivo* imaging and tracking experiments, despite their lower fluorescence quantum yields than regular fluorophores such as quantum dots and organic dyes.^{736–738} Besides fluorescence imaging, graphitic carbon nanomaterials such as CNTs and graphene also have Raman signatures that support resonant Raman spectroscopy and imaging, and their extremely large Raman scattering cross sections owing to resonant Raman scattering process make them equally promising Raman probes as SERS nanoparticles for *in vitro* and *in vivo* biomedical imaging.^{540,739,740} All carbon nanomaterials with optical absorbance at certain wavelengths

should theoretically be imaged with transient absorption microscopy and photoacoustic imaging, while their large surface area also allows for loading other imaging contrast agents for X-ray CT, MRI, PET, and SPECT imaging modalities.

Carbon nanomaterials are also promising agents for a variety of therapeutic applications. The large surface area that allows carbon nanomaterials to load imaging contrast agents also affords the capability of delivering drug molecules and nucleic acids into targeted cells and tissues for chemotherapy and gene therapy. The strong optical absorption of carbon nanomaterials allows for photothermal and photodynamic therapies that harness the absorbed photons for selective destruction of malign microorganisms and tumors. The superior mechanical properties of carbon nanomaterials, in particular CNTs and graphenes with extended sp² carbon networks in one and two dimensions, enable them to be used as artificial implant scaffolds for tissue engineering purposes. With sensitive changes of their intrinsic physical properties to external environmental variations or stimuli, carbon nanomaterials have also been employed as biosensors with high specificities and low detection limits.

With the many new avenues and opportunities offered by the unique properties of carbon nanomaterials, we envisage the future of carbon nanomaterials with an optimistic outlook. Studies at the frontier where carbon-based nanotechnology intersects biology and medicine have already proved the usefulness of a variety of carbon nanomaterials, in particular some very unusual properties and capabilities that are almost impossible to achieve with other materials. NIR-II fluorescence imaging with unprecedented penetration depth for *in vivo* imaging is a good example of an emerging field with ever-growing interest that has been ignited by the study on carbon nanotubes,^{14,15,30,417} and in the past years we have also witnessed a sprouting of noncarbon NIR-II active materials aimed at higher sensitivity, lower toxicity, and deeper penetration NIR-II imaging applications.^{392–396,502} The high loading capacity of carbon nanomaterials, in particular graphene and its derivatives with both sides exposed and available for the payload molecules/nanoparticles, can be seen as a synergistic effect of both large surface area and the rich π-electrons, which are not always present for other noncarbon nanomaterials.^{21,29,741} Given the many promising features of carbon nanomaterials, it is worth addressing some of the remaining questions in this concluding section:

1. What are the future directions of carbon nanomaterial based biomedical imaging and therapy (section 7.1)?
2. What are the main hurdles we need to overcome before one can really apply carbon nanomaterials for clinical applications (section 7.2)?
3. What insights can we gain from the studies on carbon-nanomaterial-based imaging and therapy, and how do they inspire new research in the fields of chemistry and biology (section 7.3)?

7.1. What Are the Future Directions of Carbon Nanomaterial Based Biomedical Imaging and Therapy?

One of the focuses of this review article is the NIR-II fluorescence imaging with SWCNTs. As discussed in great depth in section 4, NIR-II fluorescence imaging displays its benefits mainly in *in vivo* live animal imaging, owing to the reduced scattering of photons and thus deeper penetration depths.^{14–16} This unique and useful capability complements traditional fluorescence imaging methods that usually lack sufficient depth for *in vivo* imaging with high resolution. For a long time fluorescence imaging has suffered

from limits on resolution and penetration, where the resolution limit results from diffraction of photons while the penetration limit derives from diffusion of photons. Recent advances in super-resolution microscopy have allowed researchers to overcome the diffraction limit;^{380,381,742,743} however, super-resolution microscopy has only been applicable for *in vitro* cell imaging, while it remains difficult for microscopy to visualize deep features in general. Although a number of techniques have been developed to aid an improved penetration depth through a thick slab of tissue including multiphoton fluorescence imaging,^{510,511} tissue clearing,^{744,745} light sheet illumination,^{746,747} and adaptive optics,^{748,749} it still remains highly challenging to probe micrometer and submicrometer features with a depth of penetration of a few millimeters to centimeters in a living organism. SWCNTs with NIR-II fluorescence in the 1.0–1.7 μm wavelength region represent the fluorophores with longest emission wavelengths ever used for imaging so far, and could potentially be a game changer of *in vivo* high resolution microscopy with unprecedented penetration depths. To this end, we are pointing out three possible directions for NIR-II fluorescence imaging with SWCNTs.

First, SWCNTs can be engineered to have even longer fluorescence emission wavelength to afford even deeper *in vivo* fluorescence imaging. So far the longest emission wavelengths of SWCNTs used for *in vivo* imaging are in the 1.3–1.4 μm region,¹⁶ which has allowed for through-scalp and through-skull brain vascular imaging with >2 mm penetration depth and <10 μm imaging resolution. The comparison between fluorescence images taken in different NIR windows (Figures 20 and 25) has clearly revealed the important role that fluorescence emission wavelength plays in imaging penetration depth and sharpness.¹⁶ The inversely proportional relationship between photon wavelength and scattering predicts further reduced scattering and even deeper tissue penetration with fluorescence wavelengths longer than 1.4 μm , while we have also shown in section 4.2.1 that by changing the diameter of SWCNTs through different synthesis methods it is possible to tune their fluorescence in a broad range up to ~1.9 μm (Figure 10). However, mass production, purification, and biological stabilization of large diameter SWCNTs with extremely long fluorescence wavelength, as well as the limited accessibility to imaging devices with sufficient responsivity in such a range, have both limited the use of these SWCNTs for imaging applications. Therefore, much effort is needed to synthesize or separate certain chiralities of SWCNTs with a single, long-wavelength “color” in the NIR-II region or even beyond, and it is anticipated that such nanotube materials may achieve >5 mm penetration depth with sub-10 μm resolution for noninvasive imaging of the brain and the heart without craniotomy or open heart surgery in experimental animals.

Second, increasing the brightness of SWCNTs can be a key to greater penetration depth and faster imaging rate of *in vivo* NIR-II fluorescence imaging. NIR-II fluorescence imaging has suffered from low fluorescence quantum yields of SWCNTs due to both endogenous nonradiative dark excitons and many external quenchers.^{278,408} This problem becomes even worse when it goes to longer wavelengths, which could be a major barrier preventing the aforementioned SWCNTs with up to 1.9 μm emission wavelengths from imaging uses. It has been pointed out in a recent review paper that the achievable signal-to-noise ratio is a major issue unavoidable for all existing imaging techniques,⁷⁵⁰ and an NIR-II fluorescent agent with 100–10000 times higher brightness is likely to afford more than simply

improved signal-to-noise ratio. For example, the penetration depth is likely to be improved since photon absorption as it travels in tissue is one of the reasons accounting for poor imaging depth. Moreover, dynamic imaging with greater spatiotemporal resolution becomes possible with such “magic” fluorophores as demonstrated in a recent work by our group.³⁹⁶ To improve the apparent fluorescence quantum yield of SWCNTs, plasmonic enhancement with metal nanoparticles adsorbed on SWCNTs^{419,427} and certain surface functionalizations^{404,420} that prevent quenching should provide viable solutions for *in vivo* NIR-II imaging with SWCNT fluorescent reporters.

Third, deep tissue NIR-II super-resolution microscopy can be of great importance and use with on/off tunable SWCNTs and/or novel instrumental designs. Both photoactivatable localization microscopy (PALM) and stochastic optical reconstruction microscopy (STORM) require fluorophores that can be turned on and off under certain laser illuminations. Although the NIR-II fluorescence of SWCNTs has never been reported to have photoswitchable property, it is possible to utilize the SWCNT–quencher pair that has been widely used for molecular sensing and imaging^{451,665} to modulate the emission intensity of SWCNTs under optical stimuli. On the mechanism of the photoswitchable cyanine dyes, it has been found that Cy5 can be turned off into its dark state by a red laser, which forms an adduct of Cy5 and diminishes its absorption.⁴⁵² The quencher molecule usually is also a light absorber, and tuning the absorption of the quencher molecule in an SWCNT–quencher complex should in principle turn on and off the fluorescence of SWCNTs as well (Figure 46). Besides PALM and STORM, we believe SWCNTs,

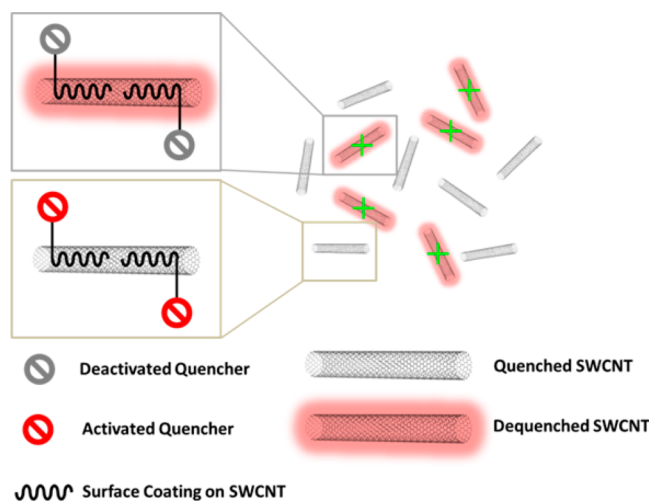


Figure 46. Proposed photoswitchable NIR-II fluorophore based on SWCNT–quencher pair. This schematic drawing shows that, by stochastically turning on and off the quencher molecules adsorbed on the SWCNTs, which can be realized by changing its absorption property in a similar way to Cy5 under red laser illumination,⁴⁵² the SWCNT fluorescence in the NIR-II window can be photoswitchable, opening up the possibility of performing NIR-II STORM imaging.

owing to their nonphotobleachable, ultrastable photoluminescence, are suitable fluorophores for stimulated emission depletion (STED) microscopy and structured illumination microscopy (SIM),⁷⁵¹ which are other methods to realize super-resolution microscopy without the need for photoswitchable fluorophores. Therefore, applying an excitation beam with its wavelength matching the E_{22} band gap of SWCNT and a depletion beam matching the E_{11} band, super-

resolution STED microscopy with SWCNTs in the NIR-II window can be realized. In addition, applying a sinusoidal structured illumination pattern with high spatial frequency to the sample results in Moiré fringes, which have coarser features for the traditional diffraction-limited microscope to observe more easily than both the structured illumination pattern and the sample features. Nonetheless, the Moiré fringes contain higher spatial frequency components of the sample that can be extracted by removing the known structured illumination pattern via inverse Fourier transform back to the real space.⁷⁵² Since SIM simply relies on instrumental implementation and does not place any constraints on fluorophores, it should be readily applicable for NIR-II fluorescence imaging using SWCNTs, especially given the superior photostability of SWCNT photoluminescence that would allow for prolonged structured illumination of the same sample with different orientations. NIR-II fluorescence imaging with SWCNTs can add an important function to all these super-resolution microscopy methods by extending the scope of the third dimension along the depth, and may thus enable deep tissue super-resolution imaging in live animals with minimum invasiveness. This potential capability is likely to make a profound impact on understanding the basic functions of tagged biomarkers on a molecular level in the context of a living object, where dynamic characteristics can be revealed inside naturally functioning tissues and organs.

Of course, the proposed further directions are not limited to SWCNTs or carbon nanomaterials, and any materials with longer emission wavelengths, higher NIR-II fluorescence quantum yields, and viability for super-resolution NIR-II fluorescence imaging should be pursued.

7.2. What Are the Main Hurdles We Need To Overcome before One Can Really Apply Carbon Nanomaterials for Clinical Applications?

As for any exogenous substances, the *in vivo* pharmacokinetics and toxicology have to be well characterized and documented before any clinical applications, and it is strictly required to prove minimum toxicity and benign pharmacokinetic properties of any foreign substance to be administered into the body no matter how promising and useful it is. For carbon nanomaterials, although we have seen in section 6 that their *in vivo* acute or chronic toxicity can be mitigated by proper surface functionalization such as PEGylation, the unfavorable large sizes of most carbon nanomaterials, in particular SWCNTs and GO, raise toxicity concerns for use in the human body due to the slow biliary clearance and long retention time in RES organs such as liver and spleen.

The incompatibility between nanomaterials in general and potential clinical applications comes from the relatively large sizes of nanomaterials, which are on the order between 1 nm and 1 μm , and the small glomerular filtration size in the kidney, which is approximately 5 nm.³⁸⁵ Electron microscopy images at the glomerular filtration barrier of mouse injected with CNTs through the tail vein reveal that only perfectly individualized nanotubes with longitudinal dimension aligned perpendicularly to the endothelial fenestration can pass through the kidney filtration barrier and get excreted via the urine.⁷⁵³ This finding implies the difficulty of rapid clearance of filamentous carbon nanotubes with their lengths greatly exceeding the renal filtration cutoff size after intravenous administration. Therefore, for any nanomaterials with any dimension larger than 5 nm, it is unlike for them to be efficiently transported across the endothelium and excreted via the renal clearance pathway.⁷⁵⁴ As a result, for those

larger nanoparticles that do not biodegrade and decompose into smaller, biologically useful components, the only metabolic pathway for them is to enter the liver and become part of the bile and later the feces. However, this biliary excretion process is very slow and highly inefficient, and increases the chance of having the intravenously administered nanoparticles trapped inside the liver and spleen, raising long-term toxicity concerns. Furthermore, the PEG coating that is intended to reduce the immune response and prevent first-pass capture by the RES system may also increase the hydrodynamic size and slow down the clearance process in an unexpected way. Therefore, a main caveat of applying carbon nanomaterials for preclinical and even clinical applications is the unfavorable excretion pathway (primarily biliary), slow body clearance, long retention time and long-term health concern with the residual materials left inside the body, in comparison to small molecule counterparts with faster and more complete clearance from the body.

Therefore, to overcome this challenge, one needs to make the carbon nanomaterials with further reduced sizes or with biodegradability before they can be considered for clinical trials. This can be realized with efforts on the following aspects: First, for graphene and its derivatives, it is desired to shrink the size to below ~ 5 nm. Carbon dot, in this sense, can afford favorable renal clearance owing to its compact size while retaining the fluorescence imaging and drug loading abilities.³⁸³ Second, it will have far-reaching implications to impart biodegradability to the carbon graphitic nanomaterials, as demonstrated by Kagan et al. for SWCNTs and by Liu et al. for GO.^{731,755–757} This strategy is likely to have a profound impact on SWCNTs, which need to retain the long lengths to afford strong enough NIR-II fluorescence emission for imaging purposes. With future development on biodegradable carbon nanomaterials, SWCNTs and graphenes can still be administered with their original large sizes and desirable optical properties into the body, and they are eventually biodegraded and decomposed into smaller, metabolizable substances inside the *in vivo* environment. Last but not least, other materials and molecules with similar NIR-II fluorescence properties to SWCNTs but more favorable pharmacokinetics should be pursued now that the proof of concept of deep tissue NIR-II fluorescence imaging has been demonstrated with SWCNTs. To this end our group has developed a library of NIR-II fluorophores other than SWCNTs, including Ag_2S quantum dots,^{392,500,501} conjugated polymers,³⁹⁶ small molecule–surfactant complexes,³⁹³ and water-soluble small molecule NIR-II dyes. Many of these alternative NIR-II fluorophores have significantly smaller hydrodynamic diameters than SWCNTs and are likely to make a greater impact on clinical NIR-II fluorescence imaging in the future.

Besides the suboptimal pharmacokinetic behavior and excretion profiles, there exist other obstacles to overcome for different carbon nanomaterials depending on their potential uses in the clinic. Taking SWCNTs as an example, although the SWCNT-based NIR-II fluorescence imaging has shown significant advantages over previous *in vivo* imaging with shorter wavelength fluorescence in the visible and NIR-I windows, in order to make it clinically useful one still needs to make the penetration of NIR-II fluorescence even deeper and suitable for larger objects such as the human body, where the imaging depth with current NIR-II fluorescence technique will still be confined near the surface. Due to the trade-off between penetration depth and imaging resolution, although the deepest penetration depth at sub-10 μm resolution is only 2–3 mm with existing NIR-II fluorophores,¹⁶ centimeter depths have been achieved with

submillimeter spatial resolution.³⁶ In order to make NIR-II fluorescence imaging applicable for vascular and brain imaging in large animals or humans, it is necessary to further improve the NIR-II fluorophores and imaging technique to afford sufficient spatial resolution (ideally sub-10 μm or even approaching the diffraction limit of ~1 μm) at centimeter depths. A variety of established deep tissue imaging techniques, such as adaptive optics,^{748,749,758–760} multiphoton fluorescence imaging,^{511,761} and selective plane illumination microscopy,⁷⁴⁶ can be combined with the opportunity offered by long-wavelength NIR-II photons to achieve an unprecedented depth of imaging that is unattainable with each individual method on its own. The limited availability of the InGaAs-based NIR-II photodetectors and cameras is another major limiting factor for wide applications of NIR-II fluorescence imaging, in unfortunate comparison with silicon-based detectors and cameras that are much more commonly used for the detection of traditional, short-wavelength fluorescence photons.³⁹⁷ Nonetheless, it is likely that the recent progress in NIR-II fluorescence imaging will advance the development of more sensitive and more affordable NIR-II cameras for various biomedical imaging purposes.

7.3. What Insights Can We Gain from the Studies on Carbon-Nanomaterial-Based Imaging and Therapy, and How Do They Inspire New Research in the Fields of Chemistry and Biology?

The studies on carbon-based nanomaterials, in particular carbon nanotubes, have uncovered a class of new strategies for probing and manipulating the biological systems with unprecedented sensitivity and precision, while the many concepts emerging from the studies of carbon-nanomaterial-based imaging and therapy are likely to have far-reaching impacts on the fundamental research in chemistry and biology as well.

We will take the NIR-II fluorescence of SWCNTs as an example. Fluorescence imaging has been used to probe structural and functional information in living organism for decades. However, due to the limitation of regular fluorophores, traditionally fluorescence imaging is only performed in the visible and NIR-I windows, with wavelengths ranging from 400 to 1000 nm. SWCNT is the first material that expands our spectrum for fluorescence imaging to a new, unexplored region beyond 1000 nm and demonstrates the benefits of this new region, and the *in vivo* deep-tissue fluorescence imaging with the intrinsic band gap fluorescence of SWCNTs ushers in a whole new field of research in NIR-II fluorescence imaging, with many other nanomaterials and even organic molecules with similar fluorescence wavelengths added to the toolbox of NIR-II fluorophores.^{392–394,396} NIR-II fluorescence imaging has received growing interest recently,^{88,498,499} primarily owing to the reduced photon scattering and negligible tissue autofluorescence in this long-wavelength window that lead to greater contrast-to-background ratio and deeper tissue penetration. This new field opened up by biomedical research of carbon nanotubes may also bring great opportunities to other popular research in chemistry and biology.

First, genetically encoded fluorescent proteins (FPs) with emission wavelengths in the NIR-II window will have practical advantages for *in vivo* imaging, given that none of the current NIR-II fluorophores is able to specifically label a certain type of cells or indicate the expression of a specific gene. A substantial amount of effort has been made by biochemists, hoping to make red-shifted FPs for deep-tissue *in vivo* imaging.^{762–765} However, to the best of our knowledge there has been no successful report

on the development of a fluorescent protein that fluoresces in the NIR-II window thus far. With the many benefits of NIR-II fluorescence imaging demonstrated by SWCNTs, it is foreseeable that the NIR-II fluorescent proteins will allow researchers to track FP-labeled stem cells and circulating tumor cells *in vivo*,^{766,767} and study the expression of specific genes marked by FPs in live animals⁷⁶⁸ with improved penetration depth and better image contrast and clarity.

Second, NIR-II light-gated ion channels and voltage-sensitive NIR-II fluorescence reporters should enable deep-tissue, all-optical electrophysiology in the brains of live experimental animals.⁷⁶⁹ The recent progress in optogenetics has revolutionized traditional electrophysiology by cell-type specific stimulation of light-gated ion channels. A large library of excitatory and inhibitory optogenetic tools has been developed with different peak activation wavelengths, which are all located in the visible window and greatly limit their *in vivo* applications owing to the necessity of using fiber optics to deliver the stimulating light into the brain.^{492,493} Paired with optical stimulation offered by optogenetics, voltage imaging with voltage-sensitive fluorescent reporters allows for temporal recording of neuronal action potentials without the need for using a patch electrode.^{770–773} However, a similar problem of photon scattering exists here, preventing the researchers from recording neuron firing deep inside the brain in an all-optical way. Light-gated ion channels with response to NIR-II light and voltage-sensitive fluorophores with NIR-II emission should facilitate the current all-optical electrophysiology technique by enabling noninvasive stimulation and recording in a live mouse brain. Possible implementations involve development of NIR-II fluorescent proteins, engineering of opsin structures to afford absorbance and response to NIR-II light, and even using SWCNTs as artificial ion channels as demonstrated recently.⁷⁷⁴

Third, the deep penetration depth of NIR-II fluorescence can be combined with tissue clearing techniques to further the depth of fluorescence imaging in a thick, fixed tissue sample. Recent years have witnessed a number of tissue clearing techniques for microscopic molecular interrogation of *ex vivo* brain sample and even the entire mouse body after tissue fixation.^{744,745,775} However, no clearing agent can perfectly remove all light scatterers in the biological tissue, and labeling structures and molecules of interest with NIR-II dyes before clearing treatment should improve the imaging depth and the available tissue thickness furthermore by minimizing the amount of photon scattering.

As a concluding remark, in this review paper we have provided a comprehensive coverage of recent progress in biological imaging and nanomedicinal therapy using a variety of carbon nanomaterials. Despite the lingering concerns on the *in vivo* behavior of these materials, salient advantages abound for a paradigm shift in medicine catalyzed by the use of multifunctional carbon nanomaterials. For the five categories of carbon nanomaterials reviewed in this paper including fullerene, carbon nanotube, graphene, carbon dot, and nanodiamond, each one of them has its own intriguing properties that are uniquely rooted in its specific chemical structure and nanoscopic size. It is these unique physical and chemical properties of various carbon nanomaterials that make them suitable for certain imaging and therapeutic applications, urging us to establish closer interdisciplinary connections between nanotechnology, biology, and medicine in order to develop more powerful and useful tools for biologists and clinicians. With a particular emphasis given to carbon nanotubes, we have shown in this review paper great

promises of the NIR-II fluorescence imaging technique for noninvasive, deep-tissue interrogation of anatomical structures and molecular compositions in living organisms. The unusually long emission wavelengths of SWCNTs and other new NIR-II active materials hold the key to uncovering the long-hidden secrets behind the scattering biological tissue using an all-optical imaging method. With innumerable exciting opportunities existing down the road, we envisage more interesting biomedical applications of carbon nanomaterials or even new carbon nanostructures bursting onto the scene, toward the development of more environmentally friendly and human friendly products and techniques in the future.

AUTHOR INFORMATION

Corresponding Author

*E-mail: hdai@stanford.edu.

Present Address

[†]G.H.: Department of Chemistry and Chemical Biology, Harvard University, Cambridge, MA, USA.

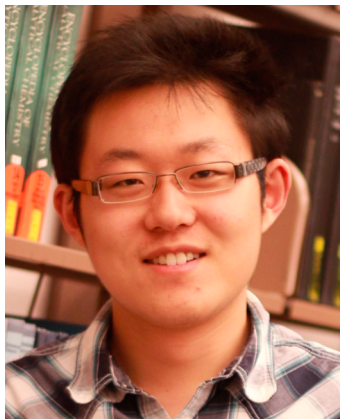
Author Contributions

The manuscript was written through contributions of all authors. All authors have given approval to the final version of the manuscript.

Notes

The authors declare no competing financial interest.

Biographies



Guosong Hong received his bachelor's degree in chemistry from Peking University in China in 2008 (advisor Prof. Limin Qi). He obtained his Ph.D. degree in chemistry from Stanford University in 2014 under the supervision of Prof. Hongjie Dai. He is currently a postdoctoral fellow in the lab of Prof. Charles M. Lieber at Harvard University. His research interests are (1) advancement of fluorescence imaging in the second near-infrared window with new fluorophores and optical setups, for the understanding of physiological and biochemical processes in live animals, and (2) establishment of nanobio interface with closely intertwined flexible materials and biological tissue for functional interrogation of and interaction with intact living organisms.



Shuo Diao received her bachelor's degree in chemistry from Peking University in China in 2011. She is currently a Ph.D. student under the supervision of Prof. Hongjie Dai in the Department of Chemistry at Stanford University in the United States. Her research interests include development of novel near-infrared fluorescence imaging techniques and their applications in biology and medicine.



Alexander Lee Antaris received his B.S. in electrical engineering from Northwestern University in 2009. After working on carbon nanotube separations with biocompatible block copolymers under the direction of Prof. Mark Hersam at Northwestern for a year, he began pursuing his Ph.D. in 2011 in materials science and engineering at Stanford University under the guidance of Prof. Hongjie Dai. His current research focus is fluorescent biomedical imaging with nanomaterials and organic dyes in the second near-infrared window.



Hongjie Dai is the J. G. Jackson and C. J. Wood Professor of Chemistry at Stanford University. His research interfaces with chemistry, physics, materials science, and biological and medical sciences. Thus far, his group has made advances to the basic science of carbon nanotubes and

graphene and potential applications in the areas of nanoelectronics, nanobiotechnology, nanomedicine, energy storage, and catalysis. He has published more than 200 journal papers that have been cited over 100 000 times. He is a fellow of the American Academy of Arts and Sciences. He is also an editor-in-chief of the journal *Nano Research*.

ACKNOWLEDGMENTS

This study was supported by grants from the National Cancer Institute of the U.S. National Institutes of Health (5R01CA135109-02).

ABBREVIATIONS

ALN	axillary lymph node	IgG	immunoglobulin G
BLN	brachial lymph node	IONP	iron oxide nanoparticle
BSA	bovine serum albumin	LBM	layer breathing mode
Ce6	chlorin e6	LD50	medium lethal dose
CEA	carcinoembryonic antigen	LUMO	lowest unoccupied molecular orbital
CHO	Chinese hamster ovary	MAPK	mitogen-activated protein kinase
cmc	critical micelle concentration	MCAO	middle cerebral arterial occlusion
CNR	contrast-to-noise ratio	MSD	mean squared displacement
CNT	carbon nanotube	MW	molecular weight
CT	computed tomography	MWCNT	multiwalled carbon nanotube
CTC	circulating tumor cell	MRI	magnetic resonance imaging
CVD	chemical vapor deposition	NA	NeutrAvidin
DAP	3,4-diaminophenyl	NF- κ B	nuclear transcription factor- κ B
DGU	density gradient ultracentrifugation	NGO	nanosized graphene oxide
DIC	differential interference contrast	NGS	nanographene sheet
DMF	dimethylformamide	NIR	near-infrared (defined as 750–1700 nm)
DOS	density of state	NIR-I	first near-infrared (defined as 750–1000 nm)
DOTA	1,4,7,10-tetraazacyclododecane-1,4,7,10-tetraacetic acid	NIR-II	second near-infrared (defined as 1000–1700 nm)
DOX	doxorubicin	NOTA	1,4,7-triazacyclononane-1,4,7-triacetic acid
dsDNA	double-stranded DNA	NSB	nonspecific binding
DTPA	diethylenetriaminepentaaceticdianhydride	N-V	nitrogen–vacancy
DTT	dithiothreitol	PAGE	polyacrylamide gel electrophoresis
EAC	Ehrlich ascites carcinoma	PAH	poly(allylamine hydrochloride)
EDC	1-ethyl-3-(dimethylamino)propyl carbodiimide	PALM	photoactivated localization microscopy
EGFP	enhanced green fluorescent protein	PBS	phosphate buffered saline
EGFR	epidermal growth factor receptor	PCA	principal component analysis
EPR	enhanced permeability and retention	pDNA	plasmid DNA
FBS	fetal bovine serum	PDT	photodynamic therapy
FDG	fluorodeoxyglucose	PEI	polyethylenimine
FET	field-effect transistor	PEG	polyethylene glycol
FITC	fluorescein isothiocyanate	PEO	poly(ethylene oxide)
FLIM	fluorescence lifetime microscopy	PET	positron emission tomography
FLT	fluorothymidine	PHF	polyhydroxy fullerene
FND	fluorescent nanodiamond	PL	phospholipid
FP	fluorescent protein	PLE	photoluminescence versus excitation
FRET	Förster resonance energy transfer	PTT	photothermal therapy
GO	graphene oxide	PTX	paclitaxel
GSH	glutathione	PVP	polyvinylpyrrolidone
H&E	hematoxylin and eosin	QD	quantum dot
HiPco	high-pressure carbon monoxide	RBC	red blood cell
hMSC	human mesenchymal stem cell	RBM	radial breathing mode
HOMO	highest occupied molecular orbital	RES	reticuloendothelial system
HRP	horseradish peroxidase	RGD	arginine-glycine-aspartic acid
HRTEM	high resolution transmission electron microscopy	rGO	reduced graphene oxide
HSA	human serum albumin	RNS	reactive nitrogen species
IC50	half-maximal inhibitory concentration	ROS	reactive oxygen species
ICG	indocyanine green	SA	streptavidin
ID/g	injected dose per gram	SAM	self-assembled monolayer
IgE	immunoglobulin E	SBP	SPARC binding peptide
		SBR	signal-to-background ratio
		SC	sodium cholate
		SDBS	sodium dodecylbenzenesulfonate
		SDS	sodium dodecyl sulfate
		SEM	scanning electron microscopy
		SERS	surface-enhanced Raman scattering
		SIM	structured illumination microscopy
		siRNA	small interfering RNA
		SLN	sentinel lymph node
		SNR	signal-to-noise ratio
		SO	singlet oxygen
		SOSG	singlet oxygen sensor green
		SpA	staphylococcal protein A
		SPARC	secreted protein, acidic and rich in cysteines

SPECT	single photon emission computed tomography
SPION	superparamagnetic iron oxide nanoparticle
SPR	surface plasmon resonance
SPT	single particle tracking
ssDNA	single-stranded DNA
STED	stimulated emission depletion
STORM	stochastic optical reconstruction microscopy
SWCNT	single-walled carbon nanotube
TEG	tetraethylene glycol
TEM	transmission electron microscopy
TGF	time-gated fluorescence
TGF- β	transforming growth factor beta
THF	tetrahydrofuran
UV	ultraviolet
ZPL	zero-phonon line

REFERENCES

- (1) Smalley, R. E.; Kroto, H.; Heath, J. C60: Buckminsterfullerene. *Nature* **1985**, *318*, 162–163.
- (2) Iijima, S. Helical Microtubules of Graphitic Carbon. *Nature* **1991**, *354*, 56–58.
- (3) Novoselov, K. S.; Geim, A. K.; Morozov, S. V.; Jiang, D.; Zhang, Y.; Dubonos, S. V.; Grigorieva, I. V.; Firsov, A. A. Electric field effect in atomically thin carbon films. *Science* **2004**, *306*, 666–669.
- (4) Baker, S. N.; Baker, G. A. Luminescent Carbon Nanodots: Emergent Nanolights. *Angew. Chem., Int. Ed.* **2010**, *49*, 6726–6744.
- (5) Mochalin, V. N.; Shenderova, O.; Ho, D.; Gogotsi, Y. The properties and applications of nanodiamonds. *Nat. Nanotechnol.* **2012**, *7*, 11–23.
- (6) Fitzgibbons, T. C.; Guthrie, M.; Xu, E. S.; Crespi, V. H.; Davidowski, S. K.; Cody, G. D.; Alem, N.; Badding, J. V. Benzene-derived carbon nanothreads. *Nat. Mater.* **2015**, *14*, 43–47.
- (7) Liu, Z.; Tabakman, S.; Welsher, K.; Dai, H. J. Carbon Nanotubes in Biology and Medicine: In vitro and in vivo Detection, Imaging and Drug Delivery. *Nano Res.* **2009**, *2*, 85–120.
- (8) Liu, Z.; Robinson, J. T.; Tabakman, S. M.; Yang, K.; Dai, H. J. Carbon materials for drug delivery & cancer therapy. *Mater. Today* **2011**, *14*, 316–323.
- (9) Liang, Y.; Li, Y.; Wang, H.; Dai, H. Strongly coupled inorganic/nanocarbon hybrid materials for advanced electrocatalysis. *J. Am. Chem. Soc.* **2013**, *135*, 2013–2036.
- (10) Wang, H. L.; Dai, H. J. Strongly coupled inorganic-nano-carbon hybrid materials for energy storage. *Chem. Soc. Rev.* **2013**, *42*, 3088–3113.
- (11) Ruggiero, A.; Villa, C. H.; Bander, E.; Rey, D. A.; Bergkvist, M.; Batt, C. A.; Manova-Todorova, K.; Deen, W. M.; Scheinberg, D. A.; McDevitt, M. R. Paradoxical glomerular filtration of carbon nanotubes. *Proc. Natl. Acad. Sci. U.S.A.* **2010**, *107*, 12369–12374.
- (12) De La Zerda, A.; Zavaleta, C.; Keren, S.; Vaithilingam, S.; Bodapati, S.; Liu, Z.; Levi, J.; Smith, B. R.; Ma, T. J.; Oralkan, O.; Cheng, Z.; Chen, X. Y.; Dai, H. J.; Khuri-Yakub, B. T.; Gambhir, S. S. Carbon nanotubes as photoacoustic molecular imaging agents in living mice. *Nat. Nanotechnol.* **2008**, *3*, 557–562.
- (13) Robinson, J. T.; Welsher, K.; Tabakman, S. M.; Sherlock, S. P.; Wang, H. L.; Luong, R.; Dai, H. J. High Performance In Vivo Near-IR (> 1 μ m) Imaging and Photothermal Cancer Therapy with Carbon Nanotubes. *Nano Res.* **2010**, *3*, 779–793.
- (14) Welsher, K.; Sherlock, S. P.; Dai, H. J. Deep-tissue anatomical imaging of mice using carbon nanotube fluorophores in the second near-infrared window. *Proc. Natl. Acad. Sci. U.S.A.* **2011**, *108*, 8943–8948.
- (15) Hong, G. S.; Lee, J. C.; Robinson, J. T.; Raaz, U.; Xie, L. M.; Huang, N. F.; Cooke, J. P.; Dai, H. J. Multifunctional in vivo vascular imaging using near-infrared II fluorescence. *Nat. Med.* **2012**, *18*, 1841–1846.
- (16) Hong, G.; Diao, S.; Chang, J.; Antaris, A. L.; Chen, C.; Zhang, B.; Zhao, S.; Atochin, D. N.; Huang, P. L.; Andreasson, K. I.; Kuo, C. J.; Dai, H. Through-skull fluorescence imaging of the brain in a new near-infrared window. *Nat. Photonics* **2014**, *8*, 723–730.
- (17) Wu, T. J.; Tzeng, Y. K.; Chang, W. W.; Cheng, C. A.; Kuo, Y.; Chien, C. H.; Chang, H. C.; Yu, J. Tracking the engraftment and regenerative capabilities of transplanted lung stem cells using fluorescent nanodiamonds. *Nat. Nanotechnol.* **2013**, *8*, 682–689.
- (18) Liu, Z.; Fan, A. C.; Rakha, K.; Sherlock, S.; Goodwin, A.; Chen, X. Y.; Yang, Q. W.; Felsher, D. W.; Dai, H. J. Supramolecular Stacking of Doxorubicin on Carbon Nanotubes for In Vivo Cancer Therapy. *Angew. Chem., Int. Ed.* **2009**, *48*, 7668–7672.
- (19) Liu, Z.; Sun, X. M.; Nakayama-Ratchford, N.; Dai, H. J. Supramolecular chemistry on water-soluble carbon nanotubes for drug loading and delivery. *ACS Nano* **2007**, *1*, 50–56.
- (20) Sherlock, S. P.; Tabakman, S. M.; Xie, L. M.; Dai, H. J. Photothermally Enhanced Drug Delivery by Ultrasmall Multifunctional FeCo/Graphitic Shell Nanocrystals. *ACS Nano* **2011**, *5*, 1505–1512.
- (21) Liu, Z.; Robinson, J. T.; Sun, X. M.; Dai, H. J. PEGylated nanographene oxide for delivery of water-insoluble cancer drugs. *J. Am. Chem. Soc.* **2008**, *130*, 10876–10877.
- (22) Shin, S. R.; Bae, H.; Cha, J. M.; Mun, J. Y.; Chen, Y. C.; Tekin, H.; Shin, H.; Farshchi, S.; Dokmeci, M. R.; Tang, S.; Khademhosseini, A. Carbon Nanotube Reinforced Hybrid Micogels as Scaffold Materials for Cell Encapsulation. *ACS Nano* **2012**, *6*, 362–372.
- (23) Zhao, B.; Hu, H.; Mandal, S. K.; Haddon, R. C. A bone mimic based on the self-assembly of hydroxyapatite on chemically functionalized single-walled carbon nanotubes. *Chem. Mater.* **2005**, *17*, 3235–3241.
- (24) Correa-Duarte, M. A.; Wagner, N.; Rojas-Chapana, J.; Morszeck, C.; Thie, M.; Giersig, M. Fabrication and biocompatibility of carbon nanotube-based 3D networks as scaffolds for cell seeding and growth. *Nano Lett.* **2004**, *4*, 2233–2236.
- (25) Li, N.; Zhang, Q.; Gao, S.; Song, Q.; Huang, R.; Wang, L.; Liu, L. W.; Dai, J. W.; Tang, M. L.; Cheng, G. S. Three-dimensional graphene foam as a biocompatible and conductive scaffold for neural stem cells. *Sci. Rep.* **2013**, *3*, 1604.
- (26) Nayak, T. R.; Andersen, H.; Makam, V. S.; Khaw, C.; Bae, S.; Xu, X. F.; Ee, P. L. R.; Ahn, J. H.; Hong, B. H.; Pastorin, G.; Ozilmez, B. Graphene for Controlled and Accelerated Osteogenic Differentiation of Human Mesenchymal Stem Cells. *ACS Nano* **2011**, *5*, 4670–4678.
- (27) Bachilo, S. M.; Strano, M. S.; Kittrell, C.; Hauge, R. H.; Smalley, R. E.; Weisman, R. B. Structure-assigned optical spectra of single-walled carbon nanotubes. *Science* **2002**, *298*, 2361–2366.
- (28) Sun, Y. P.; Zhou, B.; Lin, Y.; Wang, W.; Fernando, K. A. S.; Pathak, P.; Meziani, M. J.; Harruff, B. A.; Wang, X.; Wang, H. F.; Luo, P. J. G.; Yang, H.; Kose, M. E.; Chen, B. L.; Veca, L. M.; Xie, S. Y. Quantum-sized carbon dots for bright and colorful photoluminescence. *J. Am. Chem. Soc.* **2006**, *128*, 7756–7757.
- (29) Sun, X. M.; Liu, Z.; Welsher, K.; Robinson, J. T.; Goodwin, A.; Zaric, S.; Dai, H. J. Nano-Graphene Oxide for Cellular Imaging and Drug Delivery. *Nano Res.* **2008**, *1*, 203–212.
- (30) Welsher, K.; Liu, Z.; Sherlock, S. P.; Robinson, J. T.; Chen, Z.; Daranciang, D.; Dai, H. J. A route to brightly fluorescent carbon nanotubes for near-infrared imaging in mice. *Nat. Nanotechnol.* **2009**, *4*, 773–780.
- (31) Yang, S. T.; Cao, L.; Luo, P. G. J.; Lu, F. S.; Wang, X.; Wang, H. F.; Meziani, M. J.; Liu, Y. F.; Qi, G.; Sun, Y. P. Carbon Dots for Optical Imaging in Vivo. *J. Am. Chem. Soc.* **2009**, *131*, 11308–11309.
- (32) Yang, K.; Zhang, S. A.; Zhang, G. X.; Sun, X. M.; Lee, S. T.; Liu, Z. A. Graphene in Mice: Ultrahigh In Vivo Tumor Uptake and Efficient Photothermal Therapy. *Nano Lett.* **2010**, *10*, 3318–3323.
- (33) Diao, S.; Hong, G. S.; Robinson, J. T.; Jiao, L. Y.; Antaris, A. L.; Wu, J. Z.; Choi, C. L.; Dai, H. J. Chirality Enriched (12,1) and (11,3) Single-Walled Carbon Nanotubes for Biological Imaging. *J. Am. Chem. Soc.* **2012**, *134*, 16971–16974.
- (34) Antaris, A. L.; Robinson, J. T.; Yaghi, O. K.; Hong, G. S.; Diao, S.; Luong, R.; Dai, H. J. Ultra-Low Doses of Chirality Sorted (6,5) Carbon Nanotubes for Simultaneous Tumor Imaging and Photothermal Therapy. *ACS Nano* **2013**, *7*, 3644–3652.

- (35) Iverson, N. M.; Barone, P. W.; Shandell, M.; Trudel, L. J.; Sen, S.; Sen, F.; Ivanov, V.; Atolia, E.; Farias, E.; McNicholas, T. P.; Reuel, N.; Parry, N. M. A.; Wogan, G. N.; Strano, M. S. In vivo biosensing via tissue-localizable near-infrared-fluorescent single-walled carbon nanotubes. *Nat. Nanotechnol.* **2013**, *8*, 873–880.
- (36) Ghosh, D.; Bagley, A. F.; Na, Y. J.; Birrer, M. J.; Bhatia, S. N.; Belcher, A. M. Deep, noninvasive imaging and surgical guidance of submillimeter tumors using targeted M13-stabilized single-walled carbon nanotubes. *Proc. Natl. Acad. Sci. U.S.A.* **2014**, *111*, 13948–13953.
- (37) Diederich, F.; Thilgen, C. Covalent fullerene chemistry. *Science* **1996**, *271*, 317–323.
- (38) Diederich, F.; Gomez-Lopez, M. Supramolecular fullerene chemistry. *Chem. Soc. Rev.* **1999**, *28*, 263–277.
- (39) Thompson, B. C.; Frechet, J. M. J. Organic photovoltaics—Polymer-fullerene composite solar cells. *Angew. Chem., Int. Ed.* **2008**, *47*, 58–77.
- (40) Ramuz, M. P.; Vosgueritchian, M.; Wei, P.; Wang, C. G.; Gao, Y. L.; Wu, Y. P.; Chen, Y. S.; Bao, Z. N. Evaluation of Solution-Processable Carbon-Based Electrodes for All-Carbon Solar Cells. *ACS Nano* **2012**, *6*, 10384–10395.
- (41) Lanzelotto, C.; Favero, G.; Antonelli, M. L.; Tortolini, C.; Cannistraro, S.; Coppapi, E.; Mazzei, F. Nanostructured enzymatic biosensor based on fullerene and gold nanoparticles: Preparation, characterization and analytical applications. *Biosens. Bioelectron.* **2014**, *55*, 430–437.
- (42) Bakry, R.; Vallant, R. M.; Najam-Ul-Haq, M.; Rainer, M.; Szabo, Z.; Huck, C. W.; Bonn, G. K. Medicinal applications of fullerenes. *Int. J. Nanomed.* **2007**, *2*, 639–649.
- (43) Ueno, H.; Nakamura, Y.; Ikuma, N.; Kokubo, K.; Oshima, T. Synthesis of a lithium-encapsulated fullerol and the effect of the internal lithium cation on its aggregation behavior. *Nano Res.* **2012**, *5*, 558–564.
- (44) Ren, J.; Meng, S.; Kaxiras, E. Theoretical investigation of the C-60/copper phthalocyanine organic photovoltaic heterojunction. *Nano Res.* **2012**, *5*, 248–257.
- (45) Cha, C. Y.; Shin, S. R.; Annabi, N.; Dokmeci, M. R.; Khademhosseini, A. Carbon-Based Nanomaterials: Multifunctional Materials for Biomedical Engineering. *ACS Nano* **2013**, *7*, 2891–2897.
- (46) Kratschmer, W.; Lamb, L. D.; Fostiropoulos, K.; Huffman, D. R. Solid C-60—a New Form of Carbon. *Nature* **1990**, *347*, 354–358.
- (47) Scott, L. T.; Boorum, M. M.; McMahon, B. J.; Hagen, S.; Mack, J.; Blank, J.; Wegner, H.; de Meijere, A. A rational chemical synthesis of C-60. *Science* **2002**, *295*, 1500–1503.
- (48) Bianco, A.; Maggini, M.; Scorrano, G.; Toniolo, C.; Marconi, G.; Villani, C.; Prato, M. Synthesis, chiroptical properties, and configurational assignment of fulleroproline derivatives and peptides. *J. Am. Chem. Soc.* **1996**, *118*, 4072–4080.
- (49) Brettreich, M.; Hirsch, A. A highly water-soluble dendro[60]-fullerene. *Tetrahedron Lett.* **1998**, *39*, 2731–2734.
- (50) Andersson, T.; Nilsson, K.; Sundahl, M.; Westman, G.; Wennerstrom, O. C-60 Embedded in Gamma-Cyclodextrin—a Water-Soluble Fullerene. *J. Chem. Soc., Chem. Commun.* **1992**, 604–606.
- (51) Torres, V. M.; Posa, M.; Srdjenovic, B.; Simplicio, A. L. Solubilization of fullerene C-60 in micellar solutions of different solubilizers. *Colloids Surf., B* **2011**, *82*, 46–53.
- (52) Ashcroft, J. M.; Tsypbalski, D. A.; Hartman, K. B.; Zakharian, T. Y.; Marks, J. W.; Weisman, R. B.; Rosenblum, M. G.; Wilson, L. J. Fullerene (C-60) immunoconjugates: interaction of water-soluble C-60 derivatives with the murine anti-gp240 melanoma antibody. *Chem. Commun.* **2006**, 3004–3006.
- (53) Ghiassi, K. B.; Olmstead, M. M.; Balch, A. L. Gadolinium-containing endohedral fullerenes: structures and function as magnetic resonance imaging (MRI) agents. *Dalton Trans.* **2014**, *43*, 7346–7358.
- (54) Karam, L. R.; Mitch, M. G.; Coursey, B. M. Encapsulation of Tc-99m within fullerenes: A novel radionuclidic carrier. *Appl. Radiat. Isot.* **1997**, *48*, 771–776.
- (55) Boutorine, A. S.; Tokuyama, H.; Takasugi, M.; Isobe, H.; Nakamura, E.; Helene, C. Fullerene-Oligonucleotide Conjugates—Photoinduced Sequence-Specific DNA Cleavage. *Angew. Chem., Int. Ed.* **1994**, *33*, 2462–2465.
- (56) Isobe, H.; Nakanishi, W.; Tomita, N.; Jinno, S.; Okayama, H.; Nakamura, E. Nonviral gene delivery by tetraamino fullerene. *Mol. Pharmaceutics* **2006**, *3*, 124–134.
- (57) Nakamura, E.; Isobe, H. Functionalized fullerenes in water. The first 10 years of their chemistry, biology, and nanoscience. *Acc. Chem. Res.* **2003**, *36*, 807–815.
- (58) Zakharian, T. Y.; Seryshev, A.; Sitharaman, B.; Gilbert, B. E.; Knight, V.; Wilson, L. J. A fullerene-paclitaxel chemotherapeutic: Synthesis, characterization, and study of biological activity in tissue culture. *J. Am. Chem. Soc.* **2005**, *127*, 12508–12509.
- (59) Yamakoshi, Y.; Umezawa, N.; Ryu, A.; Arakane, K.; Miyata, N.; Goda, Y.; Masumizu, T.; Nagano, T. Active oxygen species generated from photoexcited fullerene (C_{60}) as potential medicines: $O_2^{-\bullet}$ versus 1O_2 . *J. Am. Chem. Soc.* **2003**, *125*, 12803–12809.
- (60) Sharma, S. K.; Chiang, L. Y.; Hamblin, M. R. Photodynamic therapy with fullerenes in vivo: reality or a dream? *Nanomedicine* **2011**, *6*, 1813–1825.
- (61) Jeong, J.; Jung, J.; Choi, M.; Kim, J. W.; Chung, S. J.; Lim, S.; Lee, H.; Chung, B. H. Color-Tunable Photoluminescent Fullerene Nanoparticles. *Adv. Mater.* **2012**, *24*, 1999–2003.
- (62) Levi, N.; Hantgan, R. R.; Lively, M. O.; Carroll, D. L.; Prasad, G. L. C₆₀-fullerenes: detection of intracellular photoluminescence and lack of cytotoxic effects. *J. Nanobiotechnol.* **2006**, *4*, 14.
- (63) Jeong, J.; Cho, M.; Lim, Y. T.; Song, N. W.; Chung, B. H. Synthesis and Characterization of a Photoluminescent Nanoparticle Based on Fullerene-Silica Hybridization. *Angew. Chem., Int. Ed.* **2009**, *48*, 5296–5299.
- (64) Lin, S.; Jones, D. X.; Mount, A. S.; Ke, P. C. Fluorescence of Water-Soluble Fullerenes in Biological Systems. *NSTI—Nanotech*; CRC Press: Boca Raton, FL, 2007; Vol. 4, pp 238–241.
- (65) Friedman, S. H.; Decamp, D. L.; Sijbesma, R. P.; Srdanov, G.; Wudl, F.; Kenyon, G. L. Inhibition of the HIV-1 Protease by Fullerene Derivatives—Model-Building Studies and Experimental-Verification. *J. Am. Chem. Soc.* **1993**, *115*, 6506–6509.
- (66) Sijbesma, R.; Srdanov, G.; Wudl, F.; Castoro, J. A.; Wilkins, C.; Friedman, S. H.; Decamp, D. L.; Kenyon, G. L. Synthesis of a Fullerene Derivative for the Inhibition of HIV Enzymes. *J. Am. Chem. Soc.* **1993**, *115*, 6510–6512.
- (67) Liang, X. J.; Meng, H.; Wang, Y. Z.; He, H. Y.; Meng, J.; Lu, J.; Wang, P. C.; Zhao, Y. L.; Gao, X. Y.; Sun, B. Y.; Chen, C. Y.; Xing, G. M.; Shen, D. W.; Gottesman, M. M.; Wu, Y.; Yin, J. J.; Jia, L. Metallofullerene nanoparticles circumvent tumor resistance to cisplatin by reactivating endocytosis. *Proc. Natl. Acad. Sci. U.S.A.* **2010**, *107*, 7449–7454.
- (68) Yang, D.; Zhao, Y. L.; Guo, H.; Li, Y. N.; Tewary, P.; Xing, G. M.; Hou, W.; Oppenheim, J. J.; Zhang, N. [Gd@C-82(OH)(22)](n) Nanoparticles Induce Dendritic Cell Maturation and Activate Th1 Immune Responses. *ACS Nano* **2010**, *4*, 1178–1186.
- (69) Radushkevich, L.; Lukyanovich, V. O strukture ugleroda, obrazujucegoja pri termiceskom razlozenii okisi ugleroda na zelenom kontakte. *Zh. Fiz. Chim.* **1952**, *26*, 88–95.
- (70) Iijima, S.; Ichihashi, T. Single-Shell Carbon Nanotubes of 1-Nm Diameter. *Nature* **1993**, *363*, 603–605.
- (71) Bethune, D. S.; Kiang, C. H.; Devries, M. S.; Gorman, G.; Savoy, R.; Vazquez, J.; Beyers, R. Cobalt-Catalyzed Growth of Carbon Nanotubes with Single-Atomic-Layerwalls. *Nature* **1993**, *363*, 605–607.
- (72) Monthioux, M.; Kuznetsov, V. L. Who should be given the credit for the discovery of carbon nanotubes? *Carbon* **2006**, *44*, 1621–1623.
- (73) Bernholc, J.; Brenner, D.; Nardelli, M. B.; Meunier, V.; Roland, C. Mechanical and electrical properties of nanotubes. *Annu. Rev. Mater. Res.* **2002**, *32*, 347–375.
- (74) Dresselhaus, M. S.; Dresselhaus, G.; Eklund, P. C. *Science of Fullerenes and Carbon Nanotubes*; Academic Press: San Diego, 1996.
- (75) Wilder, J. W. G.; Venema, L. C.; Rinzler, A. G.; Smalley, R. E.; Dekker, C. Electronic structure of atomically resolved carbon nanotubes. *Nature* **1998**, *391*, 59–62.

- (76) Odom, T. W.; Huang, J. L.; Kim, P.; Lieber, C. M. Atomic structure and electronic properties of single-walled carbon nanotubes. *Nature* **1998**, *391*, 62–64.
- (77) Tans, S. J.; Verschueren, A. R. M.; Dekker, C. Room-temperature transistor based on a single carbon nanotube. *Nature* **1998**, *393*, 49–52.
- (78) Martel, R.; Schmidt, T.; Shea, H. R.; Hertel, T.; Avouris, P. Single- and multi-wall carbon nanotube field-effect transistors. *Appl. Phys. Lett.* **1998**, *73*, 2447–2449.
- (79) Baughman, R. H.; Zakhidov, A. A.; de Heer, W. A. Carbon nanotubes—the route toward applications. *Science* **2002**, *297*, 787–792.
- (80) Kong, J.; Franklin, N. R.; Zhou, C. W.; Chapline, M. G.; Peng, S.; Cho, K. J.; Dai, H. J. Nanotube molecular wires as chemical sensors. *Science* **2000**, *287*, 622–625.
- (81) Balasubramanian, K.; Kern, K. 25th Anniversary Article: Label-Free Electrical Biodetection Using Carbon Nanostructures. *Adv. Mater.* **2014**, *26*, 1154–1175.
- (82) Gao, B.; Yue, G. Z.; Qiu, Q.; Cheng, Y.; Shimoda, H.; Fleming, L.; Zhou, O. Fabrication and electron field emission properties of carbon nanotube films by electrophoretic deposition. *Adv. Mater.* **2001**, *13*, 1770–1773.
- (83) Yue, G. Z.; Qiu, Q.; Gao, B.; Cheng, Y.; Zhang, J.; Shimoda, H.; Chang, S.; Lu, J. P.; Zhou, O. Generation of continuous and pulsed diagnostic imaging x-ray radiation using a carbon-nanotube-based field-emission cathode. *Appl. Phys. Lett.* **2002**, *81*, 355–357.
- (84) Tucker, A. W.; Calliste, J.; Gidcumb, E. M.; Wu, J.; Kuzmiak, C. M.; Hyun, N.; Zeng, D. L.; Lu, J. P.; Zhou, O.; Lee, Y. Z. Comparison of a Stationary Digital Breast Tomosynthesis System to Magnified 2D Mammography Using Breast Tissue Specimens. *Acad. Radiol.* **2014**, *21*, 1547–1552.
- (85) Hadsell, M.; Cao, G. H.; Zhang, J.; Burk, L.; Schreiber, T.; Schreiber, E.; Chang, S.; Lu, J. P.; Zhou, O. Pilot study for compact microbeam radiation therapy using a carbon nanotube field emission micro-CT scanner. *Med. Phys.* **2014**, *41*, 061710.
- (86) Zhang, L.; Yuan, H.; Inscue, C.; Chtcheprov, P.; Hadsell, M.; Lee, Y.; Lu, J. P.; Chang, S.; Zhou, O. Nanotube x-ray for cancer therapy: a compact microbeam radiation therapy system for brain tumor treatment. *Expert Rev. Anticancer Ther.* **2014**, *14*, 1411–1418.
- (87) O’Connell, M. J.; Bachilo, S. M.; Huffman, C. B.; Moore, V. C.; Strano, M. S.; Haroz, E. H.; Rialon, K. L.; Boul, P. J.; Noon, W. H.; Kittrell, C.; Ma, J. P.; Hauge, R. H.; Weisman, R. B.; Smalley, R. E. Band gap fluorescence from individual single-walled carbon nanotubes. *Science* **2002**, *297*, 593–596.
- (88) Smith, A. M.; Mancini, M. C.; Nie, S. M. BIOIMAGING Second window for in vivo imaging. *Nat. Nanotechnol.* **2009**, *4*, 710–711.
- (89) Murakami, T.; Nakatsuji, H.; Inada, M.; Matoba, Y.; Umeyama, T.; Tsujimoto, M.; Isoda, S.; Hashida, M.; Imahori, H. Photodynamic and Photothermal Effects of Semiconducting and Metallic-Enriched Single-Walled Carbon Nanotubes. *J. Am. Chem. Soc.* **2012**, *134*, 17862–17865.
- (90) Wong, E. W.; Sheehan, P. E.; Lieber, C. M. Nanobeam mechanics: Elasticity, strength, and toughness of nanorods and nanotubes. *Science* **1997**, *277*, 1971–1975.
- (91) Iijima, S.; Brabec, C.; Maiti, A.; Bernholc, J. Structural flexibility of carbon nanotubes. *J. Chem. Phys.* **1996**, *104*, 2089–2092.
- (92) Wei, H. M.; Wei, Y.; Wu, Y.; Liu, L.; Fan, S. S.; Jiang, K. L. High-strength composite yarns derived from oxygen plasma modified super-aligned carbon nanotube arrays. *Nano Res.* **2013**, *6*, 208–215.
- (93) Shi, X. F.; Sitharaman, B.; Pham, Q. P.; Liang, F.; Wu, K.; Billups, W. E.; Wilson, L. J.; Mikos, A. G. Fabrication of porous ultra-short single-walled carbon nanotube nanocomposite scaffolds for bone tissue engineering. *Biomaterials* **2007**, *28*, 4078–4090.
- (94) Liu, Z.; Chen, K.; Davis, C.; Sherlock, S.; Cao, Q. Z.; Chen, X. Y.; Dai, H. J. Drug delivery with carbon nanotubes for in vivo cancer treatment. *Cancer Res.* **2008**, *68*, 6652–6660.
- (95) Kam, N. W. S.; O’Connell, M.; Wisdom, J. A.; Dai, H. J. Carbon nanotubes as multifunctional biological transporters and near-infrared agents for selective cancer cell destruction. *Proc. Natl. Acad. Sci. U.S.A.* **2005**, *102*, 11600–11605.
- (96) Kam, N. W. S.; Liu, Z. A.; Dai, H. J. Carbon nanotubes as intracellular transporters for proteins and DNA: An investigation of the uptake mechanism and pathway. *Angew. Chem., Int. Ed.* **2006**, *45*, 577–581.
- (97) Lotya, M.; Hernandez, Y.; King, P. J.; Smith, R. J.; Nicolosi, V.; Karlsson, L. S.; Blighe, F. M.; De, S.; Wang, Z. M.; McGovern, I. T.; Duesberg, G. S.; Coleman, J. N. Liquid Phase Production of Graphene by Exfoliation of Graphite in Surfactant/Water Solutions. *J. Am. Chem. Soc.* **2009**, *131*, 3611–3620.
- (98) Park, S.; Ruoff, R. S. Chemical methods for the production of graphenes. *Nat. Nanotechnol.* **2009**, *4*, 217–224.
- (99) Zhang, D. D.; Fu, L.; Liao, L.; Liu, N.; Dai, B. Y.; Zhang, C. X. Preparation, characterization, and application of electrochemically functional graphene nanocomposites by one-step liquid-phase exfoliation of natural flake graphite with methylene blue. *Nano Res.* **2012**, *5*, 875–887.
- (100) Del Rio-Castillo, A. E.; Merino, C.; Diez-Barra, E.; Vazquez, E. Selective suspension of single layer graphene mechanochemically exfoliated from carbon nanofibres. *Nano Res.* **2014**, *7*, 963–972.
- (101) Qu, K. G.; Wu, L.; Ren, J. S.; Qu, X. G. Enzyme-directed pH-responsive exfoliation and dispersion of graphene and its decoration by gold nanoparticles for use as a hybrid catalyst. *Nano Res.* **2013**, *6*, 693–702.
- (102) Jiao, L. Y.; Zhang, L.; Wang, X. R.; Diankov, G.; Dai, H. J. Narrow graphene nanoribbons from carbon nanotubes. *Nature* **2009**, *458*, 877–880.
- (103) Kosynkin, D. V.; Higginbotham, A. L.; Sinitskii, A.; Lomeda, J. R.; Dimiev, A.; Price, B. K.; Tour, J. M. Longitudinal unzipping of carbon nanotubes to form graphene nanoribbons. *Nature* **2009**, *458*, 872–876.
- (104) Jiao, L. Y.; Xie, L. M.; Dai, H. J. Densely aligned graphene nanoribbons at similar to 35 nm pitch. *Nano Res.* **2012**, *5*, 292–296.
- (105) Jiao, L. Y.; Wang, X. R.; Diankov, G.; Wang, H. L.; Dai, H. J. Facile synthesis of high-quality graphene nanoribbons. *Nat. Nanotechnol.* **2010**, *5*, 321–325.
- (106) Kim, K. S.; Zhao, Y.; Jang, H.; Lee, S. Y.; Kim, J. M.; Kim, K. S.; Ahn, J. H.; Kim, P.; Choi, J. Y.; Hong, B. H. Large-scale pattern growth of graphene films for stretchable transparent electrodes. *Nature* **2009**, *457*, 706–710.
- (107) Ma, D. L.; Zhang, Y. F.; Liu, M. X.; Ji, Q. Q.; Gao, T.; Zhang, Y.; Liu, Z. F. Clean transfer of graphene on Pt foils mediated by a carbon monoxide intercalation process. *Nano Res.* **2013**, *6*, 671–678.
- (108) Li, X. S.; Cai, W. W.; An, J. H.; Kim, S.; Nah, J.; Yang, D. X.; Piner, R.; Velamakanni, A.; Jung, I.; Tutuc, E.; Banerjee, S. K.; Colombo, L.; Ruoff, R. S. Large-Area Synthesis of High-Quality and Uniform Graphene Films on Copper Foils. *Science* **2009**, *324*, 1312–1314.
- (109) Zhang, L. C.; Shi, Z. W.; Liu, D. H.; Yang, R.; Shi, D. X.; Zhang, G. Y. Vapour-phase graphene epitaxy at low temperatures. *Nano Res.* **2012**, *5*, 258–264.
- (110) Sun, Z. Z.; Yan, Z.; Yao, J.; Beitler, E.; Zhu, Y.; Tour, J. M. Growth of graphene from solid carbon sources. *Nature* **2010**, *468*, 549–552.
- (111) Chaika, A. N.; Molodtsova, O. V.; Zakharov, A. A.; Marchenko, D.; Sanchez-Barriga, J.; Varykhalov, A.; Shvets, I. V.; Aristov, V. Y. Continuous wafer-scale graphene on cubic-SiC(001). *Nano Res.* **2013**, *6*, 562–570.
- (112) Zhang, Y. F.; Gao, T.; Xie, S. B.; Dai, B. Y.; Fu, L.; Gao, Y. B.; Chen, Y. B.; Liu, M. X.; Liu, Z. F. Different growth behaviors of ambient pressure chemical vapor deposition graphene on Ni(111) and Ni films: A scanning tunneling microscopy study. *Nano Res.* **2012**, *5*, 402–411.
- (113) Reina, A.; Jia, X. T.; Ho, J.; Nezich, D.; Son, H. B.; Bulovic, V.; Dresselhaus, M. S.; Kong, J. Large Area, Few-Layer Graphene Films on Arbitrary Substrates by Chemical Vapor Deposition. *Nano Lett.* **2009**, *9*, 30–35.
- (114) Cai, J. M.; Ruffieux, P.; Jaafar, R.; Bieri, M.; Braun, T.; Blankenburg, S.; Muoth, M.; Seitsonen, A. P.; Saleh, M.; Feng, X. L.; Mullen, K.; Fasel, R. Atomically precise bottom-up fabrication of graphene nanoribbons. *Nature* **2010**, *466*, 470–473.
- (115) Cai, J.; Pignedoli, C. A.; Talirz, L.; Ruffieux, P.; Sode, H.; Liang, L.; Meunier, V.; Berger, R.; Li, R.; Feng, X.; Mullen, K.; Fasel, R.

- Graphene nanoribbon heterojunctions. *Nat. Nanotechnol.* **2014**, *9*, 896–900.
- (116) Nakada, K.; Fujita, M.; Dresselhaus, G.; Dresselhaus, M. S. Edge state in graphene ribbons: Nanometer size effect and edge shape dependence. *Phys. Rev. B* **1996**, *54*, 17954–17961.
- (117) Geim, A. K. Graphene: Status and Prospects. *Science* **2009**, *324*, 1530–1534.
- (118) Bolotin, K. I.; Sikes, K. J.; Jiang, Z.; Klima, M.; Fudenberg, G.; Hone, J.; Kim, P.; Stormer, H. L. Ultrahigh electron mobility in suspended graphene. *Solid State Commun.* **2008**, *146*, 351–355.
- (119) Du, X.; Skachko, I.; Barker, A.; Andrei, E. Y. Approaching ballistic transport in suspended graphene. *Nat. Nanotechnol.* **2008**, *3*, 491–495.
- (120) Pop, E.; Varshney, V.; Roy, A. K. Thermal properties of graphene: Fundamentals and applications. *MRS Bull.* **2012**, *37*, 1273–1281.
- (121) Novoselov, K. S.; Jiang, Z.; Zhang, Y.; Morozov, S. V.; Stormer, H. L.; Zeitler, U.; Maan, J. C.; Boebinger, G. S.; Kim, P.; Geim, A. K. Room-temperature quantum hall effect in graphene. *Science* **2007**, *315*, 1379–1379.
- (122) Westervelt, R. M. Applied physics—Graphene nanoelectronics. *Science* **2008**, *320*, 324–325.
- (123) Wang, H. L.; Holt, C. M. B.; Li, Z.; Tan, X. H.; Amirkhiz, B. S.; Xu, Z. W.; Olsen, B. C.; Stephenson, T.; Mitlin, D. Graphene-nickel cobaltite nanocomposite asymmetrical supercapacitor with commercial level mass loading. *Nano Res.* **2012**, *5*, 605–617.
- (124) Loh, K. P.; Bao, Q. L.; Eda, G.; Chhowalla, M. Graphene oxide as a chemically tunable platform for optical applications. *Nat. Chem.* **2010**, *2*, 1015–1024.
- (125) Xu, Y. X.; Huang, X. Q.; Lin, Z. Y.; Zhong, X.; Huang, Y.; Duan, X. F. One-step strategy to graphene/Ni(OH)₂ composite hydrogels as advanced three-dimensional supercapacitor electrode materials. *Nano Res.* **2013**, *6*, 65–76.
- (126) Long, X.; Li, J. K.; Xiao, S.; Yan, K. Y.; Wang, Z. L.; Chen, H. N.; Yang, S. H. A Strongly Coupled Graphene and FeNi Double Hydroxide Hybrid as an Excellent Electrocatalyst for the Oxygen Evolution Reaction. *Angew. Chem., Int. Ed.* **2014**, *53*, 7584–7588.
- (127) de Abajo, F. J. G. Graphene Nanophotonics. *Science* **2013**, *339*, 917–918.
- (128) Shi, Z. W.; Lu, H. L.; Zhang, L. C.; Yang, R.; Wang, Y.; Liu, D. H.; Guo, H. M.; Shi, D. X.; Gao, H. J.; Wang, E. G.; Zhang, G. Y. Studies of graphene-based nanoelectromechanical switches. *Nano Res.* **2012**, *5*, 82–87.
- (129) Sun, H.; Xu, G. L.; Xu, Y. F.; Sun, S. G.; Zhang, X. F.; Qiu, Y. C.; Yang, S. H. A composite material of uniformly dispersed sulfur on reduced graphene oxide: Aqueous one-pot synthesis, characterization and excellent performance as the cathode in rechargeable lithium-sulfur batteries. *Nano Res.* **2012**, *5*, 726–738.
- (130) Pembroke, E.; Ruan, G. D.; Sinitkii, A.; Corley, D. A.; Yan, Z.; Sun, Z. Z.; Tour, J. M. Effect of anchor and functional groups in functionalized graphene devices. *Nano Res.* **2013**, *6*, 138–148.
- (131) Son, D. I.; Kwon, B. W.; Yang, J. D.; Park, D. H.; Seo, W. S.; Lee, H.; Yi, Y.; Lee, C. L.; Choi, W. K. Charge separation and ultraviolet photovoltaic conversion of ZnO quantum dots conjugated with graphene nanoshells. *Nano Res.* **2012**, *5*, 747–761.
- (132) Lherbier, A.; Roche, S.; Restrepo, O. A.; Niquet, Y. M.; Delcorte, A.; Charlier, J. C. Highly defective graphene: A key prototype of two-dimensional Anderson insulators. *Nano Res.* **2013**, *6*, 326–334.
- (133) Yang, K.; Feng, L. Z.; Shi, X. Z.; Liu, Z. Nano-graphene in biomedicine: theranostic applications. *Chem. Soc. Rev.* **2013**, *42*, 530–547.
- (134) Mao, H. Y.; Laurent, S.; Chen, W.; Akhavan, O.; Imani, M.; Ashkarran, A. A.; Mahmoudi, M. Graphene: Promises, Facts, Opportunities, and Challenges in Nanomedicine. *Chem. Rev.* **2013**, *113*, 3407–3424.
- (135) Bitounis, D.; Ali-Boucetta, H.; Hong, B. H.; Min, D. H.; Kostarelos, K. Prospects and Challenges of Graphene in Biomedical Applications. *Adv. Mater.* **2013**, *25*, 2258–2268.
- (136) Feng, L. Y.; Wu, L.; Qu, X. G. New Horizons for Diagnostics and Therapeutic Applications of Graphene and Graphene Oxide. *Adv. Mater.* **2013**, *25*, 168–186.
- (137) Huang, Y. X.; Dong, X. C.; Shi, Y. M.; Li, C. M.; Li, L. J.; Chen, P. Nanoelectronic biosensors based on CVD grown graphene. *Nanoscale* **2010**, *2*, 1485–1488.
- (138) Kwak, Y. H.; Choi, D. S.; Kim, Y. N.; Kim, H.; Yoon, D. H.; Ahn, S. S.; Yang, J. W.; Yang, W. S.; Seo, S. Flexible glucose sensor using CVD-grown graphene-based field effect transistor. *Biosens. Bioelectron.* **2012**, *37*, 82–87.
- (139) Mohanty, N.; Berry, V. Graphene-Based Single-Bacterium Resolution Biodevice and DNA Transistor: Interfacing Graphene Derivatives with Nanoscale and Microscale Biocomponents. *Nano Lett.* **2008**, *8*, 4469–4476.
- (140) Saltzgaber, G.; Wojcik, P.; Sharf, T.; Leyden, M. R.; Wardini, J. L.; Heist, C. A.; Adenuga, A. A.; Remcho, V. T.; Minot, E. D. Scalable graphene field-effect sensors for specific protein detection. *Nanotechnology* **2013**, *24*, No. 355502.
- (141) Zhou, M.; Zhai, Y. M.; Dong, S. J. Electrochemical Sensing and Biosensing Platform Based on Chemically Reduced Graphene Oxide. *Anal. Chem.* **2009**, *81*, 5603–5613.
- (142) Kybert, N. J.; Han, G. H.; Lerner, M. B.; Dattoli, E. N.; Esfandiar, A.; Johnson, A. T. C. Scalable arrays of chemical vapor sensors based on DNA-decorated graphene. *Nano Res.* **2014**, *7*, 95–103.
- (143) Wang, B.; Liddell, K. L.; Wang, J. J.; Koger, B.; Keating, C. D.; Zhu, J. Oxide-on-graphene field effect bio-ready sensors. *Nano Res.* **2014**, *7*, 1263–1270.
- (144) Cagliani, A.; Mackenzie, D. M. A.; Tschanmer, L. K.; Pizzocchero, F.; Almdal, K.; Boggild, P. Large-area nanopatterned graphene for ultrasensitive gas sensing. *Nano Res.* **2014**, *7*, 743–754.
- (145) Shang, N. G.; Papakonstantinou, P.; McMullan, M.; Chu, M.; Stamboulis, A.; Potenza, A.; Dhesi, S. S.; Marchetto, H. Catalyst-Free Efficient Growth, Orientation and Biosensing Properties of Multilayer Graphene Nanoflake Films with Sharp Edge Planes. *Adv. Funct. Mater.* **2008**, *18*, 3506–3514.
- (146) Shan, C. S.; Yang, H. F.; Song, J. F.; Han, D. X.; Ivaska, A.; Niu, L. Direct Electrochemistry of Glucose Oxidase and Biosensing for Glucose Based on Graphene. *Anal. Chem.* **2009**, *81*, 2378–2382.
- (147) Dey, R. S.; Raj, C. R. Development of an Amperometric Cholesterol Biosensor Based on Graphene-Pt Nanoparticle Hybrid Material. *J. Phys. Chem. C* **2010**, *114*, 21427–21433.
- (148) Ling, X.; Xie, L. M.; Fang, Y.; Xu, H.; Zhang, H. L.; Kong, J.; Dresselhaus, M. S.; Zhang, J.; Liu, Z. F. Can Graphene be used as a Substrate for Raman Enhancement? *Nano Lett.* **2010**, *10*, 553–561.
- (149) Qiu, C. Y.; Zhou, H. Q.; Yang, H. C.; Chen, M. J.; Guo, Y. J.; Sun, L. F. Investigation of n-Layer Graphenes as Substrates for Raman Enhancement of Crystal Violet. *J. Phys. Chem. C* **2011**, *115*, 10019–10025.
- (150) Yu, X. X.; Cai, H. B.; Zhang, W. H.; Li, X. J.; Pan, N.; Luo, Y.; Wang, X. P.; Hou, J. G. Tuning Chemical Enhancement of SERS by Controlling the Chemical Reduction of Graphene Oxide Nanosheets. *ACS Nano* **2011**, *5*, 952–958.
- (151) Xu, W. G.; Ling, X.; Xiao, J. Q.; Dresselhaus, M. S.; Kong, J.; Xu, H. X.; Liu, Z. F.; Zhang, J. Surface enhanced Raman spectroscopy on a flat graphene surface. *Proc. Natl. Acad. Sci. U.S.A.* **2012**, *109*, 9281–9286.
- (152) He, S. J.; Liu, K. K.; Su, S.; Yan, J.; Mao, X. H.; Wang, D. F.; He, Y.; Li, L. J.; Song, S. P.; Fan, C. H. Graphene-Based High-Efficiency Surface-Enhanced Raman Scattering-Active Platform for Sensitive and Multiplex DNA Detection. *Anal. Chem.* **2012**, *84*, 4622–4627.
- (153) Deng, S. B.; Xu, W. G.; Wang, J. Y.; Ling, X.; Wu, J. X.; Xie, L. M.; Kong, J.; Dresselhaus, M. S.; Zhang, J. Direct measurement of the Raman enhancement factor of rhodamine 6G on graphene under resonant excitation. *Nano Res.* **2014**, *7*, 1271–1279.
- (154) Shang, J. Z.; Ma, L.; Li, J. W.; Ai, W.; Yu, T.; Gurzadyan, G. G. The Origin of Fluorescence from Graphene Oxide. *Sci. Rep.* **2012**, *2*, 792.
- (155) Qian, J.; Wang, D.; Cai, F. H.; Xi, W.; Peng, L.; Zhu, Z. F.; He, H.; Hu, M. L.; He, S. L. Observation of Multiphoton-Induced Fluorescence

- from Graphene Oxide Nanoparticles and Applications in In Vivo Functional Bioimaging. *Angew. Chem., Int. Ed.* **2012**, *51*, 10570–10575.
- (156) Patel, M. A.; Yang, H.; Chiu, P. L.; Mastrogiovanni, D. D. T.; Flach, C. R.; Savaram, K.; Gomez, L.; Hemnarine, A.; Mendelsohn, R.; Garfunkel, E.; Jiang, H. B.; He, H. X. Direct Production of Graphene Nanosheets for Near Infrared Photoacoustic Imaging. *ACS Nano* **2013**, *7*, 8147–8157.
- (157) Robinson, J. T.; Tabakman, S. M.; Liang, Y. Y.; Wang, H. L.; Casalongue, H. S.; Vinh, D.; Dai, H. J. Ultrasmall Reduced Graphene Oxide with High Near-Infrared Absorbance for Photothermal Therapy. *J. Am. Chem. Soc.* **2011**, *133*, 6825–6831.
- (158) Romero-Aburto, R.; Narayanan, T. N.; Nagaoka, Y.; Hasumura, T.; Mitcham, T. M.; Fukuda, T.; Cox, P. J.; Bouchard, R. R.; Maekawa, T.; Kumar, D. S.; Torti, S. V.; Mani, S. A.; Ajayan, P. M. Fluorinated Graphene Oxide; a New Multimodal Material for Biological Applications. *Adv. Mater.* **2013**, *25*, 5632–5637.
- (159) Yang, K.; Wan, J. M.; Zhang, S.; Tian, B.; Zhang, Y. J.; Liu, Z. The influence of surface chemistry and size of nanoscale graphene oxide on photothermal therapy of cancer using ultra-low laser power. *Biomaterials* **2012**, *33*, 2206–2214.
- (160) Yang, K.; Hu, L. L.; Ma, X. X.; Ye, S. Q.; Cheng, L.; Shi, X. Z.; Li, C. H.; Li, Y. G.; Liu, Z. Multimodal Imaging Guided Photothermal Therapy using Functionalized Graphene Nanosheets Anchored with Magnetic Nanoparticles. *Adv. Mater.* **2012**, *24*, 1868–1872.
- (161) Hu, S. H.; Chen, Y. W.; Hung, W. T.; Chen, I. W.; Chen, S. Y. Quantum-Dot-Tagged Reduced Graphene Oxide Nanocomposites for Bright Fluorescence Bioimaging and Photothermal Therapy Monitored In Situ. *Adv. Mater.* **2012**, *24*, 1748–1754.
- (162) Ma, X. X.; Tao, H. Q.; Yang, K.; Feng, L. Z.; Cheng, L.; Shi, X. Z.; Li, Y. G.; Guo, L.; Liu, Z. A functionalized graphene oxide–iron oxide nanocomposite for magnetically targeted drug delivery, photothermal therapy, and magnetic resonance imaging. *Nano Res.* **2012**, *5*, 199–212.
- (163) Li, M.; Yang, X. J.; Ren, J. S.; Qu, K. G.; Qu, X. G. Using Graphene Oxide High Near-Infrared Absorbance for Photothermal Treatment of Alzheimer's Disease. *Adv. Mater.* **2012**, *24*, 1722–1728.
- (164) Yang, H. W.; Hua, M. Y.; Hwang, T. L.; Lin, K. J.; Huang, C. Y.; Tsai, R. Y.; Ma, C. C. M.; Hsu, P. H.; Wey, S. P.; Hsu, P. W.; Chen, P. Y.; Huang, Y. C.; Lu, Y. J.; Yen, T. C.; Feng, L. Y.; Lin, C. W.; Liu, H. L.; Wei, K. C. Non-Invasive Synergistic Treatment of Brain Tumors by Targeted Chemotherapeutic Delivery and Amplified Focused Ultrasound-Hyperthermia Using Magnetic Nanographene Oxide. *Adv. Mater.* **2013**, *25*, 3605–3611.
- (165) Feng, L. Z.; Li, K. Y.; Shi, X. Z.; Gao, M.; Liu, J.; Liu, Z. Smart pH-Responsive Nanocarriers Based on Nano-Graphene Oxide for Combined Chemo- and Photothermal Therapy Overcoming Drug Resistance. *Adv. Healthcare Mater.* **2014**, *3*, 1261–1271.
- (166) Wang, F.; Liu, B. W.; Ip, A. C. F.; Liu, J. W. Orthogonal Adsorption Onto Nano-Graphene Oxide Using Different Intermolecular Forces for Multiplexed Delivery. *Adv. Mater.* **2013**, *25*, 4087–4092.
- (167) Zhang, L. M.; Xia, J. G.; Zhao, Q. H.; Liu, L. W.; Zhang, Z. J. Functional Graphene Oxide as a Nanocarrier for Controlled Loading and Targeted Delivery of Mixed Anticancer Drugs. *Small* **2010**, *6*, 537–544.
- (168) Yang, X. Y.; Zhang, X. Y.; Liu, Z. F.; Ma, Y. F.; Huang, Y.; Chen, Y. High-Efficiency Loading and Controlled Release of Doxorubicin Hydrochloride on Graphene Oxide. *J. Phys. Chem. C* **2008**, *112*, 17554–17558.
- (169) Liu, K. P.; Zhang, J. J.; Cheng, F. F.; Zheng, T. T.; Wang, C. M.; Zhu, J. J. Green and facile synthesis of highly biocompatible graphene nanosheets and its application for cellular imaging and drug delivery. *J. Mater. Chem.* **2011**, *21*, 12034–12040.
- (170) Wen, H. Y.; Dong, C. Y.; Dong, H. Q.; Shen, A. J.; Xia, W. J.; Cai, X. J.; Song, Y. Y.; Li, X. Q.; Li, Y. Y.; Shi, D. L. Engineered Redox-Responsive PEG Detachment Mechanism in PEGylated Nano-Graphene Oxide for Intracellular Drug Delivery. *Small* **2012**, *8*, 760–769.
- (171) Lu, C. H.; Zhu, C. L.; Li, J.; Liu, J. J.; Chen, X.; Yang, H. H. Using graphene to protect DNA from cleavage during cellular delivery. *Chem. Commun.* **2010**, *46*, 3116–3118.
- (172) Feng, L. Z.; Yang, X. Z.; Shi, X. Z.; Tan, X. F.; Peng, R.; Wang, J.; Liu, Z. Polyethylene Glycol and Polyethylenimine Dual-Functionalized Nano-Graphene Oxide for Photothermally Enhanced Gene Delivery. *Small* **2013**, *9*, 1989–1997.
- (173) Feng, L. Z.; Zhang, S. A.; Liu, Z. A. Graphene based gene transfection. *Nanoscale* **2011**, *3*, 1252–1257.
- (174) Huang, P.; Xu, C.; Lin, J.; Wang, C.; Wang, X. S.; Zhang, C. L.; Zhou, X. J.; Guo, S. W.; Cui, D. X. Folic Acid-conjugated Graphene Oxide loaded with Photosensitizers for Targeting Photodynamic Therapy. *Theranostics* **2011**, *1*, 240–250.
- (175) Tian, B.; Wang, C.; Zhang, S.; Feng, L. Z.; Liu, Z. Photothermally Enhanced Photodynamic Therapy Delivered by Nano-Graphene Oxide. *ACS Nano* **2011**, *5*, 7000–7009.
- (176) Stoberl, U.; Wurstbauer, U.; Wegscheider, W.; Weiss, D.; Eroms, J. Morphology and flexibility of graphene and few-layer graphene on various substrates. *Appl. Phys. Lett.* **2008**, *93*, 051906.
- (177) Lee, C.; Wei, X. D.; Kysar, J. W.; Hone, J. Measurement of the elastic properties and intrinsic strength of monolayer graphene. *Science* **2008**, *321*, 385–388.
- (178) Lanza, M.; Wang, Y.; Gao, T.; Bayerl, A.; Porti, M.; Nafria, M.; Zhou, Y. B.; Jing, G. Y.; Zhang, Y. F.; Liu, Z. F.; Yu, D. P.; Duan, H. L. Electrical and mechanical performance of graphene sheets exposed to oxidative environments. *Nano Res.* **2013**, *6*, 485–495.
- (179) Serrano, M. C.; Patino, J.; Garcia-Rama, C.; Ferrer, M. L.; Fierro, J. L. G.; Tamayo, A.; Collazos-Castro, J. E.; del Monte, F.; Gutierrez, M. C. 3D free-standing porous scaffolds made of graphene oxide as substrates for neural cell growth. *J. Mater. Chem. B* **2014**, *2*, 5698–5706.
- (180) Depan, D.; Girase, B.; Shah, J. S.; Misra, R. D. K. Structure-process-property relationship of the polar graphene oxide-mediated cellular response and stimulated growth of osteoblasts on hybrid chitosan network structure nanocomposite scaffolds. *Acta Biomater.* **2011**, *7*, 3432–3445.
- (181) Kalbacova, M.; Broz, A.; Kong, J.; Kalbac, M. Graphene substrates promote adherence of human osteoblasts and mesenchymal stromal cells. *Carbon* **2010**, *48*, 4323–4329.
- (182) Li, H. T.; Kang, Z. H.; Liu, Y.; Lee, S. T. Carbon nanodots: synthesis, properties and applications. *J. Mater. Chem.* **2012**, *22*, 24230–24253.
- (183) Brodie, B. C. On the atomic weight of graphite. *Philos. Trans. R. Soc. London* **1859**, 249–259.
- (184) Hummers, W. S.; Offeman, R. E. Preparation of Graphitic Oxide. *J. Am. Chem. Soc.* **1958**, *80*, 1339.
- (185) Xu, X. Y.; Ray, R.; Gu, Y. L.; Ploehn, H. J.; Gearheart, L.; Raker, K.; Scrivens, W. A. Electrophoretic analysis and purification of fluorescent single-walled carbon nanotube fragments. *J. Am. Chem. Soc.* **2004**, *126*, 12736–12737.
- (186) Luo, P. J. G.; Yang, F.; Yang, S. T.; Sonkar, S. K.; Yang, L. J.; Broglie, J. J.; Liu, Y.; Sun, Y. P. Carbon-based quantum dots for fluorescence imaging of cells and tissues. *RSC Adv.* **2014**, *4*, 10791–10807.
- (187) Zhao, Q. L.; Zhang, Z. L.; Huang, B. H.; Peng, J.; Zhang, M.; Pang, D. W. Facile preparation of low cytotoxicity fluorescent carbon nanocrystals by electrooxidation of graphite. *Chem. Commun.* **2008**, 5116–5118.
- (188) Lu, J.; Yang, J. X.; Wang, J. Z.; Lim, A. L.; Wang, S.; Loh, K. P. One-Pot Synthesis of Fluorescent Carbon Nanoribbons, Nanoparticles, and Graphene by the Exfoliation of Graphite in Ionic Liquids. *ACS Nano* **2009**, *3*, 2367–2375.
- (189) Zheng, L. Y.; Chi, Y. W.; Dong, Y. Q.; Lin, J. P.; Wang, B. B. Electrochemiluminescence of Water-Soluble Carbon Nanocrystals Released Electrochemically from Graphite. *J. Am. Chem. Soc.* **2009**, *131*, 4564–4565.
- (190) Tao, H. Q.; Yang, K.; Ma, Z.; Wan, J. M.; Zhang, Y. J.; Kang, Z. H.; Liu, Z. In Vivo NIR Fluorescence Imaging, Biodistribution, and Toxicology of Photoluminescent Carbon Dots Produced from Carbon Nanotubes and Graphite. *Small* **2012**, *8*, 281–290.
- (191) Hu, S. L.; Niu, K. Y.; Sun, J.; Yang, J.; Zhao, N. Q.; Du, X. W. One-step synthesis of fluorescent carbon nanoparticles by laser irradiation. *J. Mater. Chem.* **2009**, *19*, 484–488.

- (192) Lu, J.; Yeo, P. S. E.; Gan, C. K.; Wu, P.; Loh, K. P. Transforming C-60 molecules into graphene quantum dots. *Nat. Nanotechnol.* **2011**, *6*, 247–252.
- (193) Zhou, J. G.; Booker, C.; Li, R. Y.; Zhou, X. T.; Sham, T. K.; Sun, X. L.; Ding, Z. F. An electrochemical avenue to blue luminescent nanocrystals from multiwalled carbon nanotubes (MWCNTs). *J. Am. Chem. Soc.* **2007**, *129*, 744–745.
- (194) Bottini, M.; Balasubramanian, C.; Dawson, M. I.; Bergamaschi, A.; Bellucci, S.; Mustelin, T. Isolation and characterization of fluorescent nanoparticles from pristine and oxidized electric arc-produced single-walled carbon nanotubes. *J. Phys. Chem. B* **2006**, *110*, 831–836.
- (195) Pan, D. Y.; Zhang, J. C.; Li, Z.; Wu, M. H. Hydrothermal Route for Cutting Graphene Sheets into Blue-Luminescent Graphene Quantum Dots. *Adv. Mater.* **2010**, *22*, 734–738.
- (196) Ponomarenko, L. A.; Schedin, F.; Katsnelson, M. I.; Yang, R.; Hill, E. W.; Novoselov, K. S.; Geim, A. K. Chaotic dirac billiard in graphene quantum dots. *Science* **2008**, *320*, 356–358.
- (197) Pan, D. Y.; Guo, L.; Zhang, J. C.; Xi, C.; Xue, Q.; Huang, H.; Li, J. H.; Zhang, Z. W.; Yu, W. J.; Chen, Z. W.; Li, Z.; Wu, M. H. Cutting sp(2) clusters in graphene sheets into colloidal graphene quantum dots with strong green fluorescence. *J. Mater. Chem.* **2012**, *22*, 3314–3318.
- (198) Peng, J.; Gao, W.; Gupta, B. K.; Liu, Z.; Romero-Aburto, R.; Ge, L. H.; Song, L.; Alemany, L. B.; Zhan, X. B.; Gao, G. H.; Vithayathil, S. A.; Kaipparettu, B. A.; Marti, A. A.; Hayashi, T.; Zhu, J. J.; Ajayan, P. M. Graphene Quantum Dots Derived from Carbon Fibers. *Nano Lett.* **2012**, *12*, 844–849.
- (199) Bao, L.; Zhang, Z. L.; Tian, Z. Q.; Zhang, L.; Liu, C.; Lin, Y.; Qi, B. P.; Pang, D. W. Electrochemical Tuning of Luminescent Carbon Nanodots: From Preparation to Luminescence Mechanism. *Adv. Mater.* **2011**, *23*, 5801–5806.
- (200) Liu, H. P.; Ye, T.; Mao, C. D. Fluorescent carbon nanoparticles derived from candle soot. *Angew. Chem., Int. Ed.* **2007**, *46*, 6473–6475.
- (201) Liu, C. J.; Zhang, P.; Tian, F.; Li, W. C.; Li, F.; Liu, W. G. One-step synthesis of surface passivated carbon nanodots by microwave assisted pyrolysis for enhanced multicolor photoluminescence and bioimaging. *J. Mater. Chem.* **2011**, *21*, 13163–13167.
- (202) Lee, C. H.; Rajendran, R.; Jeong, M. S.; Ko, H. Y.; Joo, J. Y.; Cho, S.; Chang, Y. W.; Kim, S. Bioimaging of targeting cancers using aptamer-conjugated carbon nanodots. *Chem. Commun.* **2013**, *49*, 6543–6545.
- (203) Wang, X. H.; Qu, K. G.; Xu, B. L.; Ren, J. S.; Qu, X. G. Microwave assisted one-step green synthesis of cell-permeable multicolor photoluminescent carbon dots without surface passivation reagents. *J. Mater. Chem.* **2011**, *21*, 2445–2450.
- (204) Yang, Z. C.; Wang, M.; Yong, A. M.; Wong, S. Y.; Zhang, X. H.; Tan, H.; Chang, A. Y.; Li, X.; Wang, J. Intrinsically fluorescent carbon dots with tunable emission derived from hydrothermal treatment of glucose in the presence of monopotassium phosphate. *Chem. Commun.* **2011**, *47*, 11615–11617.
- (205) Tang, L. B.; Ji, R. B.; Cao, X. K.; Lin, J. Y.; Jiang, H. X.; Li, X. M.; Teng, K. S.; Luk, C. M.; Zeng, S. J.; Hao, J. H.; Lau, S. P. Deep Ultraviolet Photoluminescence of Water-Soluble Self-Passivated Graphene Quantum Dots. *ACS Nano* **2012**, *6*, 5102–5110.
- (206) Bourlinos, A. B.; Stassinopoulos, A.; Anglos, D.; Zboril, R.; Karakassis, M.; Giannelis, E. P. Surface functionalized carbogenic quantum dots. *Small* **2008**, *4*, 455–458.
- (207) Bourlinos, A. B.; Stassinopoulos, A.; Anglos, D.; Zboril, R.; Georgakilas, V.; Giannelis, E. P. Photoluminescent carbogenic dots. *Chem. Mater.* **2008**, *20*, 4539–4541.
- (208) Zong, J.; Zhu, Y. H.; Yang, X. L.; Shen, J. H.; Li, C. Z. Synthesis of photoluminescent carbogenic dots using mesoporous silica spheres as nanoreactors. *Chem. Commun.* **2011**, *47*, 764–766.
- (209) Yan, X.; Cui, X.; Li, L. S. Synthesis of Large, Stable Colloidal Graphene Quantum Dots with Tunable Size. *J. Am. Chem. Soc.* **2010**, *132*, 5944–5945.
- (210) Yan, X.; Cui, X.; Li, B. S.; Li, L. S. Large, Solution-Processable Graphene Quantum Dots as Light Absorbers for Photovoltaics. *Nano Lett.* **2010**, *10*, 1869–1873.
- (211) Liu, R. L.; Wu, D. Q.; Feng, X. L.; Mullen, K. Bottom-Up Fabrication of Photoluminescent Graphene Quantum Dots with Uniform Morphology. *J. Am. Chem. Soc.* **2011**, *133*, 15221–15223.
- (212) Wu, Z. L.; Zhang, P.; Gao, M. X.; Liu, C. F.; Wang, W.; Leng, F.; Huang, C. Z. One-pot hydrothermal synthesis of highly luminescent nitrogen-doped amphoteric carbon dots for bioimaging from Bombyx mori silk—natural proteins. *J. Mater. Chem. B* **2013**, *1*, 2868–2873.
- (213) Sahu, S.; Behera, B.; Maiti, T. K.; Mohapatra, S. Simple one-step synthesis of highly luminescent carbon dots from orange juice: application as excellent bio-imaging agents. *Chem. Commun.* **2012**, *48*, 8835–8837.
- (214) De, B.; Karak, N. A green and facile approach for the synthesis of water soluble fluorescent carbon dots from banana juice. *RSC Adv.* **2013**, *3*, 8286–8290.
- (215) Wu, L.; Luderer, M.; Yang, X.; Swain, C.; Zhang, H.; Nelson, K.; Stacy, A. J.; Shen, B.; Lanza, G. M.; Pan, D. Surface passivation of carbon nanoparticles with branched macromolecules influences near infrared bioimaging. *Theranostics* **2013**, *3*, 677–686.
- (216) Wu, L. N.; Cai, X.; Nelson, K.; Xing, W. X.; Xia, J.; Zhang, R. Y.; Stacy, A. J.; Luderer, M.; Lanza, G. M.; Wang, L. V.; Shen, B. Z.; Pan, D. P. J. A green synthesis of carbon nanoparticles from honey and their use in real-time photoacoustic imaging. *Nano Res.* **2013**, *6*, 312–325.
- (217) Park, S. Y.; Lee, H. U.; Park, E. S.; Lee, S. C.; Lee, J. W.; Jeong, S. W.; Kim, C. H.; Lee, Y. C.; Huh, Y. S.; Lee, J. Photoluminescent Green Carbon Nanodots from Food-Waste-Derived Sources: Large-Scale Synthesis, Properties, and Biomedical Applications. *ACS Appl. Mater. Interfaces* **2014**, *6*, 3365–3370.
- (218) Ray, S. C.; Saha, A.; Jana, N. R.; Sarkar, R. Fluorescent Carbon Nanoparticles: Synthesis, Characterization, and Bioimaging Application. *J. Phys. Chem. C* **2009**, *113*, 18546–18551.
- (219) Tang, L. B.; Ji, R. B.; Li, X. M.; Bai, G. X.; Liu, C. P.; Hao, J. H.; Lin, J. Y.; Jiang, H. X.; Teng, K. S.; Yang, Z. B.; Lau, S. P. Deep Ultraviolet to Near-Infrared Emission and Photoresponse in Layered N-Doped Graphene Quantum Dots. *ACS Nano* **2014**, *8*, 6312–6320.
- (220) Nurunnabi, M.; Khatun, Z.; Reeck, G. R.; Lee, D. Y.; Lee, Y. K. Near infra-red photoluminescent graphene nanoparticles greatly expand their use in noninvasive biomedical imaging. *Chem. Commun.* **2013**, *49*, 5079–5081.
- (221) Alivisatos, A. P.; Gu, W. W.; Larabell, C. Quantum dots as cellular probes. *Annu. Rev. Biomed. Eng.* **2005**, *7*, 55–76.
- (222) Guclu, A. D.; Potasz, P.; Hawrylak, P. Excitonic absorption in gate-controlled graphene quantum dots. *Phys. Rev. B* **2010**, *82*, 155445.
- (223) Zhu, S. J.; Zhang, J. H.; Tang, S. J.; Qiao, C. Y.; Wang, L.; Wang, H. Y.; Liu, X.; Li, B.; Li, Y. F.; Yu, W. L.; Wang, X. F.; Sun, H. C.; Yang, B. Surface Chemistry Routes to Modulate the Photoluminescence of Graphene Quantum Dots: From Fluorescence Mechanism to Up-Conversion Bioimaging Applications. *Adv. Funct. Mater.* **2012**, *22*, 4732–4740.
- (224) Tang, J.; Kong, B.; Wu, H.; Xu, M.; Wang, Y. C.; Wang, Y. L.; Zhao, D. Y.; Zheng, G. F. Carbon Nanodots Featuring Efficient FRET for Real-Time Monitoring of Drug Delivery and Two-Photon Imaging. *Adv. Mater.* **2013**, *25*, 6569–6574.
- (225) Cao, L.; Wang, X.; Meziani, M. J.; Lu, F. S.; Wang, H. F.; Luo, P. J. G.; Lin, Y.; Harruff, B. A.; Veca, L. M.; Murray, D.; Xie, S. Y.; Sun, Y. P. Carbon dots for multiphoton bioimaging. *J. Am. Chem. Soc.* **2007**, *129*, 11318–11319.
- (226) Liu, Q.; Guo, B. D.; Rao, Z. Y.; Zhang, B. H.; Gong, J. R. Strong Two-Photon-Induced Fluorescence from Photostable, Biocompatible Nitrogen-Doped Graphene Quantum Dots for Cellular and Deep-Tissue Imaging. *Nano Lett.* **2013**, *13*, 2436–2441.
- (227) Lawrence, K.; Xia, F.; Arrowsmith, R. L.; Ge, H.; Nelson, G. W.; Foord, J. S.; Felipe-Sotelo, M.; Evans, N. D.; Mitchells, J. M.; Flower, S. E. Hydrothermal Conversion of One-Photon-Fluorescent Poly (4-vinylpyridine) into Two-Photon-Fluorescent Carbon Nanodots. *Langmuir* **2014**, *30*, 11746–11752.
- (228) Stefanakis, D.; Philippidis, A.; Sygellou, L.; Filippidis, G.; Ghanotakis, D.; Anglos, D. Synthesis of fluorescent carbon dots by a microwave heating process: structural characterization and cell imaging applications. *J. Nanopart. Res.* **2014**, *16*, 1–10.

- (229) Kong, B.; Zhu, A. W.; Ding, C. Q.; Zhao, X. M.; Li, B.; Tian, Y. Carbon Dot-Based Inorganic–Organic Nanosystem for Two-Photon Imaging and Biosensing of pH Variation in Living Cells and Tissues. *Adv. Mater.* **2012**, *24*, 5844–5848.
- (230) Salinas-Castillo, A.; Ariza-Avidad, M.; Pritz, C.; Camprubí-Robles, M.; Fernandez, B.; Ruedas-Rama, M. J.; Megia-Fernandez, A.; Lapresta-Fernandez, A.; Santoyo-Gonzalez, F.; Schrott-Fischer, A.; Capitan-Vallvey, L. F. Carbon dots for copper detection with down and upconversion fluorescent properties as excitation sources. *Chem. Commun.* **2013**, *49*, 1103–1105.
- (231) Wang, F.; Xie, Z.; Zhang, H.; Liu, C. Y.; Zhang, Y. G. Highly Luminescent Organosilane-Functionalized Carbon Dots. *Adv. Funct. Mater.* **2011**, *21*, 1027–1031.
- (232) Zhu, S. J.; Zhang, J. H.; Qiao, C. Y.; Tang, S. J.; Li, Y. F.; Yuan, W. J.; Li, B.; Tian, L.; Liu, F.; Hu, R.; Gao, H. N.; Wei, H. T.; Zhang, H.; Sun, H. C.; Yang, B. Strongly green-photoluminescent graphene quantum dots for bioimaging applications. *Chem. Commun.* **2011**, *47*, 6858–6860.
- (233) Chandra, S.; Das, P.; Bag, S.; Laha, D.; Pramanik, P. Synthesis, functionalization and bioimaging applications of highly fluorescent carbon nanoparticles. *Nanoscale* **2011**, *3*, 1533–1540.
- (234) Fang, Y. X.; Guo, S. J.; Li, D.; Zhu, C. Z.; Ren, W.; Dong, S. J.; Wang, E. K. Easy Synthesis and Imaging Applications of Cross-Linked Green Fluorescent Hollow Carbon Nanoparticles. *ACS Nano* **2012**, *6*, 400–409.
- (235) Qu, Q.; Zhu, A. W.; Shao, X. L.; Shi, G. Y.; Tian, Y. Development of a carbon quantum dots-based fluorescent Cu²⁺ probe suitable for living cell imaging. *Chem. Commun.* **2012**, *48*, 5473–5475.
- (236) Hsu, P. C.; Chang, H. T. Synthesis of high-quality carbon nanodots from hydrophilic compounds: role of functional groups. *Chem. Commun.* **2012**, *48*, 3984–3986.
- (237) Song, Y. C.; Shi, W.; Chen, W.; Li, X. H.; Ma, H. M. Fluorescent carbon nanodots conjugated with folic acid for distinguishing folate-receptor-positive cancer cells from normal cells. *J. Mater. Chem.* **2012**, *22*, 12568–12573.
- (238) Zhang, M.; Bai, L. L.; Shang, W. H.; Xie, W. J.; Ma, H.; Fu, Y. Y.; Fang, D. C.; Sun, H.; Fan, L. Z.; Han, M.; Liu, C. M.; Yang, S. H. Facile synthesis of water-soluble, highly fluorescent graphene quantum dots as a robust biological label for stem cells. *J. Mater. Chem.* **2012**, *22*, 7461–7467.
- (239) Chen, B. S.; Li, F. M.; Li, S. X.; Weng, W.; Guo, H. X.; Guo, T.; Zhang, X. Y.; Chen, Y. B.; Huang, T. T.; Hong, X. L.; You, S. Y.; Lin, Y. M.; Zeng, K. H.; Chen, S. Large scale synthesis of photoluminescent carbon nanodots and their application for bioimaging. *Nanoscale* **2013**, *5*, 1967–1971.
- (240) Xu, Y.; Wu, M.; Liu, Y.; Feng, X. Z.; Yin, X. B.; He, X. W.; Zhang, Y. K. Nitrogen-Doped Carbon Dots: A Facile and General Preparation Method, Photoluminescence Investigation, and Imaging Applications. *Chem.—Eur. J.* **2013**, *19*, 2276–2283.
- (241) Chandra, S.; Patra, P.; Pathan, S. H.; Roy, S.; Mitra, S.; Layek, A.; Bhar, R.; Pramanik, P.; Goswami, A. Luminescent S-doped carbon dots: an emergent architecture for multimodal applications. *J. Mater. Chem. B* **2013**, *1*, 2375–2382.
- (242) Qu, K. G.; Wang, J. S.; Ren, J. S.; Qu, X. G. Carbon Dots Prepared by Hydrothermal Treatment of Dopamine as an Effective Fluorescent Sensing Platform for the Label-Free Detection of Iron(III) Ions and Dopamine. *Chem.—Eur. J.* **2013**, *19*, 7243–7249.
- (243) Bhunia, S. K.; Saha, A.; Maity, A. R.; Ray, S. C.; Jana, N. R. Carbon Nanoparticle-based Fluorescent Bioimaging Probes. *Sci. Rep.* **2013**, *3*, 1473.
- (244) Lemenager, G.; De Luca, E.; Sun, Y. P.; Pompa, P. P. Super-resolution fluorescence imaging of biocompatible carbon dots. *Nanoscale* **2014**, *6*, 8617–8623.
- (245) Sun, H. J.; Wu, L.; Gao, N.; Ren, J. S.; Qu, X. G. Improvement of Photoluminescence of Graphene Quantum Dots with a Biocompatible Photochemical Reduction Pathway and Its Bioimaging Application. *ACS Appl. Mater. Interfaces* **2013**, *5*, 1174–1179.
- (246) Hu, C. F.; Liu, Y. L.; Yang, Y. H.; Cui, J. H.; Huang, Z. R.; Wang, Y. L.; Yang, L. F.; Wang, H. B.; Xiao, Y.; Rong, J. H. One-step preparation of nitrogen-doped graphene quantum dots from oxidized debris of graphene oxide. *J. Mater. Chem. B* **2013**, *1*, 39–42.
- (247) Cao, L.; Yang, S. T.; Wang, X.; Luo, P. G.; Liu, J. H.; Sahu, S.; Liu, Y.; Sun, Y. P. Competitive performance of carbon “quantum” dots in optical bioimaging. *Theranostics* **2012**, *2*, 295–301.
- (248) Huang, P.; Lin, J.; Wang, X. S.; Wang, Z.; Zhang, C. L.; He, M.; Wang, K.; Chen, F.; Li, Z. M.; Shen, G. X.; Cui, D. X.; Chen, X. Y. Light-Triggered Theranostics Based on Photosensitizer-Conjugated Carbon Dots for Simultaneous Enhanced-Fluorescence Imaging and Photodynamic Therapy. *Adv. Mater.* **2012**, *24*, 5104–5110.
- (249) Thakur, M.; Pandey, S.; Mewada, A.; Patil, V.; Khade, M.; Goshi, E.; Sharon, M. Antibiotic Conjugated Fluorescent Carbon Dots as a Theranostic Agent for Controlled Drug Release, Bioimaging, and Enhanced Antimicrobial Activity. *J. Drug Delivery* **2014**, *2014*, 282193.
- (250) Wang, L. Q.; Wang, X. Y.; Bhirde, A.; Cao, J. B.; Zeng, Y.; Huang, X. L.; Sun, Y. P.; Liu, G.; Chen, X. Y. Carbon-Dot-Based Two-Photon Visible Nanocarriers for Safe and Highly Efficient Delivery of siRNA and DNA. *Adv. Healthcare Mater.* **2014**, *3*, 1203–1209.
- (251) Karthik, S.; Saha, B.; Ghosh, S. K.; Singh, N. D. P. Photoresponsive quinoline tethered fluorescent carbon dots for regulated anticancer drug delivery. *Chem. Commun.* **2013**, *49*, 10471–10473.
- (252) Markovic, Z. M.; Ristic, B. Z.; Arsikin, K. M.; Klisic, D. G.; Harhaji-Trajkovic, L. M.; Todorovic-Markovic, B. M.; Kepic, D. P.; Kravic-Stevovic, T. K.; Jovanovic, S. P.; Milenkovic, M. M.; Milivojevic, D. D.; Bumbasirevic, V. Z.; Dramicanin, M. D.; Trajkovic, V. S. Graphene quantum dots as autophagy-inducing photodynamic agents. *Biomaterials* **2012**, *33*, 7084–7092.
- (253) Greiner, N. R.; Phillips, D. S.; Johnson, J. D.; Volk, F. Diamonds in Detonation Soot. *Nature* **1988**, *333*, 440–442.
- (254) Fu, C. C.; Lee, H. Y.; Chen, K.; Lim, T. S.; Wu, H. Y.; Lin, P. K.; Wei, P. K.; Tsao, P. H.; Chang, H. C.; Fann, W. Characterization and application of single fluorescent nanodiamonds as cellular biomarkers. *Proc. Natl. Acad. Sci. U.S.A.* **2007**, *104*, 727–732.
- (255) Yu, S. J.; Kang, M. W.; Chang, H. C.; Chen, K. M.; Yu, Y. C. Bright fluorescent nanodiamonds: No photobleaching and low cytotoxicity. *J. Am. Chem. Soc.* **2005**, *127*, 17604–17605.
- (256) Gruber, A.; Drabenstedt, A.; Tietz, C.; Fleury, L.; Wrachtrup, J.; von Borczyskowski, C. Scanning confocal optical microscopy and magnetic resonance on single defect centers. *Science* **1997**, *276*, 2012–2014.
- (257) Han, K. Y.; Willig, K. I.; Rittweger, E.; Jelezko, F.; Eggeling, C.; Hell, S. W. Three-Dimensional Stimulated Emission Depletion Microscopy of Nitrogen-Vacancy Centers in Diamond Using Continuous-Wave Light. *Nano Lett.* **2009**, *9*, 3323–3329.
- (258) Rittweger, E.; Han, K. Y.; Irvine, S. E.; Eggeling, C.; Hell, S. W. STED microscopy reveals crystal colour centres with nanometric resolution. *Nat. Photonics* **2009**, *3*, 144–147.
- (259) Gaebel, T.; Popa, I.; Gruber, A.; Domhan, M.; Jelezko, F.; Wrachtrup, J. Stable single-photon source in the near infrared. *New J. Phys.* **2004**, *6*, 98.
- (260) Kong, X. L.; Huang, L. C. L.; Liau, S. C. V.; Han, C. C.; Chang, H. C. Polylysine-coated diamond nanocrystals for MALDI-TOF mass analysis of DNA oligonucleotides. *Anal. Chem.* **2005**, *77*, 4273–4277.
- (261) Krueger, A.; Liang, Y. J.; Jarre, G.; Stegk, J. Surface functionalisation of detonation diamond suitable for biological applications. *J. Mater. Chem.* **2006**, *16*, 2322–2328.
- (262) Chang, Y. R.; Lee, H. Y.; Chen, K.; Chang, C. C.; Tsai, D. S.; Fu, C. C.; Lim, T. S.; Tzeng, Y. K.; Fang, C. Y.; Han, C. C.; Chang, H. C.; Fann, W. Mass production and dynamic imaging of fluorescent nanodiamonds. *Nat. Nanotechnol.* **2008**, *3*, 284–288.
- (263) Chao, J. I.; Perevedentseva, E.; Chung, P. H.; Liu, K. K.; Cheng, C. Y.; Chang, C. C.; Cheng, C. L. Nanometer-sized diamond particle as a probe for biolabeling. *Biophys. J.* **2007**, *93*, 2199–2208.
- (264) Zhang, X. Q.; Lam, R.; Xu, X. Y.; Chow, E. K.; Kim, H. J.; Ho, D. Multimodal Nanodiamond Drug Delivery Carriers for Selective Targeting, Imaging, and Enhanced Chemotherapeutic Efficacy. *Adv. Mater.* **2011**, *23*, 4770–4775.

- (265) Faklaris, O.; Joshi, V.; Irinopoulou, T.; Tauc, P.; Sennour, M.; Girard, H.; Gesset, C.; Arnault, J. C.; Thorel, A.; Boudou, J. P.; Curmi, P. A.; Treussart, F. Photoluminescent Diamond Nanoparticles for Cell Labeling: Study of the Uptake Mechanism in Mammalian Cells. *ACS Nano* **2009**, *3*, 3955–3962.
- (266) Faklaris, O.; Garrot, D.; Joshi, V.; Druon, F.; Boudou, J. P.; Sauvage, T.; Georges, P.; Curmi, P. A.; Treussart, F. Detection of Single Photoluminescent Diamond Nanoparticles in Cells and Study of the Internalization Pathway. *Small* **2008**, *4*, 2236–2239.
- (267) Mohan, N.; Chen, C. S.; Hsieh, H. H.; Wu, Y. C.; Chang, H. C. In Vivo Imaging and Toxicity Assessments of Fluorescent Nanodiamonds in *Caenorhabditis elegans*. *Nano Lett.* **2010**, *10*, 3692–3699.
- (268) Igarashi, R.; Yoshinari, Y.; Yokota, H.; Sugi, T.; Sugihara, F.; Ikeda, K.; Sumiya, H.; Tsuji, S.; Mori, I.; Tochio, H.; Harada, Y.; Shirakawa, M. Real-Time Background-Free Selective Imaging of Fluorescent Nanodiamonds in Vivo. *Nano Lett.* **2012**, *12*, 5726–5732.
- (269) Vaijayanthimala, V.; Cheng, P. Y.; Yeh, S. H.; Liu, K. K.; Hsiao, C. H.; Chao, J. I.; Chang, H. C. The long-term stability and biocompatibility of fluorescent nanodiamond as an in vivo contrast agent. *Biomaterials* **2012**, *33*, 7794–7802.
- (270) Chow, E. K.; Zhang, X. Q.; Chen, M.; Lam, R.; Robinson, E.; Huang, H. J.; Schaffer, D.; Osawa, E.; Goga, A.; Ho, D. Nanodiamond Therapeutic Delivery Agents Mediate Enhanced Chemoresistant Tumor Treatment. *Sci. Transl. Med.* **2011**, *3*, 73ra21.
- (271) Zhang, X. Q.; Chen, M.; Lam, R.; Xu, X. Y.; Osawa, E.; Ho, D. Polymer-Functionalized Nanodiamond Platforms as Vehicles for Gene Delivery. *ACS Nano* **2009**, *3*, 2609–2616.
- (272) Merkel, T. J.; DeSimone, J. M. Dodging Drug-Resistant Cancer with Diamonds. *Sci. Transl. Med.* **2011**, *3*, 73ps78.
- (273) Smith, A. H.; Robinson, E. M.; Zhang, X. Q.; Chow, E. K.; Lin, Y.; Osawa, E.; Xi, J. Z.; Ho, D. A. Triggered release of therapeutic antibodies from nanodiamond complexes. *Nanoscale* **2011**, *3*, 2844–2848.
- (274) Chen, M.; Zhang, X. Q.; Man, H. B.; Lam, R.; Chow, E. K.; Ho, D. A. Nanodiamond Vectors Functionalized with Polyethylenimine for siRNA Delivery. *J. Phys. Chem. Lett.* **2010**, *1*, 3167–3171.
- (275) Alhaddad, A.; Adam, M. P.; Botsoa, J.; Dantelle, G.; Perruchas, S.; Gacoin, T.; Mansuy, C.; Lavielle, S.; Malvy, C.; Treussart, F.; Bertrand, J. R. Nanodiamond as a Vector for siRNA Delivery to Ewing Sarcoma Cells. *Small* **2011**, *7*, 3087–3095.
- (276) Thalhammer, A.; Edgington, R. J.; Cingolani, L. A.; Schoepfer, R.; Jackman, R. B. The use of nanodiamond monolayer coatings to promote the formation of functional neuronal networks. *Biomaterials* **2010**, *31*, 2097–2104.
- (277) Zhang, Q. W.; Mochalin, V. N.; Neitzel, I.; Knoke, I. Y.; Han, J. J.; Klug, C. A.; Zhou, J. G.; Lelkes, P. I.; Gogotsi, Y. Fluorescent PLLA-nanodiamond composites for bone tissue engineering. *Biomaterials* **2011**, *32*, 87–94.
- (278) Cognet, L.; Tsybouski, D. A.; Rocha, J. D. R.; Doyle, C. D.; Tour, J. M.; Weisman, R. B. Stepwise quenching of exciton fluorescence in carbon nanotubes by single-molecule reactions. *Science* **2007**, *316*, 1465–1468.
- (279) Islam, M. F.; Rojas, E.; Bergey, D. M.; Johnson, A. T.; Yodh, A. G. High weight fraction surfactant solubilization of single-wall carbon nanotubes in water. *Nano Lett.* **2003**, *3*, 269–273.
- (280) Wenseleers, W.; Vlasov, I. I.; Goovaerts, E.; Obraztsova, E. D.; Lobach, A. S.; Bouwen, A. Efficient isolation and solubilization of pristine single-walled nanotubes in bile salt micelles. *Adv. Funct. Mater.* **2004**, *14*, 1105–1112.
- (281) Xiao, Q.; Wang, P. H.; Ji, L. L.; Tan, X. K.; Ouyang, L. L. Dispersion of carbon nanotubes in aqueous solution with cationic surfactant CTAB. *J. Inorg. Mater.* **2007**, *22*, 1122–1126.
- (282) Zafour, A.; Abdelkader, D.; Flahaut, E.; Rebizi, N.; Skender, A. Dispersion of the carbon nanotubes (DWNTC) by the cationic surfactants imidazolinium type. *IOP Conf. Ser.: Mater. Sci. Eng.* **2012**, *28*, 012010.
- (283) Liu, J.; Rinzler, A. G.; Dai, H. J.; Hafner, J. H.; Bradley, R. K.; Boul, P. J.; Lu, A.; Iverson, T.; Shelimov, K.; Huffman, C. B.; Rodriguez-
Macias, F.; Shon, Y. S.; Lee, T. R.; Colbert, D. T.; Smalley, R. E. Fullerene pipes. *Science* **1998**, *280*, 1253–1256.
- (284) Chen, R. J.; Bangsaruntip, S.; Drouvalakis, K. A.; Kam, N. W. S.; Shim, M.; Li, Y. M.; Kim, W.; Utz, P. J.; Dai, H. J. Noncovalent functionalization of carbon nanotubes for highly specific electronic biosensors. *Proc. Natl. Acad. Sci. U.S.A.* **2003**, *100*, 4984–4989.
- (285) Lotya, M.; King, P. J.; Khan, U.; De, S.; Coleman, J. N. High-Concentration, Surfactant-Stabilized Graphene Dispersions. *ACS Nano* **2010**, *4*, 3155–3162.
- (286) Hsieh, A. G.; Punckt, C.; Korkut, S.; Aksay, I. A. Adsorption of Sodium Dodecyl Sulfate on Functionalized Graphene Measured by Conductometric Titration. *J. Phys. Chem. B* **2013**, *117*, 7950–7958.
- (287) Nam, C. W.; Kang, S. J.; Kang, Y. K.; Kwak, M. K. Cell Growth Inhibition and Apoptosis by SDS-solubilized Single-walled Carbon Nanotubes in Normal Rat Kidney Epithelial Cells. *Arch. Pharm. Res.* **2011**, *34*, 661–669.
- (288) Kam, N. W. S.; Liu, Z.; Dai, H. J. Functionalization of carbon nanotubes via cleavable disulfide bonds for efficient intracellular delivery of siRNA and potent gene silencing. *J. Am. Chem. Soc.* **2005**, *127*, 12492–12493.
- (289) Liu, Z.; Tabakman, S. M.; Chen, Z.; Dai, H. J. Preparation of carbon nanotube bioconjugates for biomedical applications. *Nat. Protoc.* **2009**, *4*, 1372–1382.
- (290) Chen, X.; Ramstrom, O.; Yan, M. D. Glyconanomaterials: Emerging applications in biomedical research. *Nano Res.* **2014**, *7*, 1381–1403.
- (291) Liu, Z.; Cai, W. B.; He, L. N.; Nakayama, N.; Chen, K.; Sun, X. M.; Chen, X. Y.; Dai, H. J. In vivo biodistribution and highly efficient tumour targeting of carbon nanotubes in mice. *Nat. Nanotechnol.* **2007**, *2*, 47–52.
- (292) Seo, W. S.; Lee, J. H.; Sun, X. M.; Suzuki, Y.; Mann, D.; Liu, Z.; Terashima, M.; Yang, P. C.; McConnell, M. V.; Nishimura, D. G.; Dai, H. J. FeCo/graphitic-shell nanocrystals as advanced magnetic-resonance-imaging and near-infrared agents. *Nat. Mater.* **2006**, *5*, 971–976.
- (293) Sherlock, S. P.; Dai, H. J. Multifunctional FeCo-graphitic carbon nanocrystals for combined imaging, drug delivery and tumor-specific photothermal therapy in mice. *Nano Res.* **2011**, *4*, 1248–1260.
- (294) Welsher, K.; Liu, Z.; Daranciang, D.; Dai, H. Selective probing and imaging of cells with single walled carbon nanotubes as near-infrared fluorescent molecules. *Nano Lett.* **2008**, *8*, 586–590.
- (295) Kosuge, H.; Sherlock, S. P.; Kitagawa, T.; Dash, R.; Robinson, J. T.; Dai, H. J.; McConnell, M. V. Near Infrared Imaging and Photothermal Ablation of Vascular Inflammation Using Single-Walled Carbon Nanotubes. *J. Am. Heart Assoc.* **2012**, *1*, No. e002568.
- (296) Chang, C. C.; Chen, C. C.; Hung, W. H.; Hsu, I. K.; Pimenta, M. A.; Cronin, S. B. Strain-induced D band observed in carbon nanotubes. *Nano Res.* **2012**, *5*, 854–862.
- (297) Prencipe, G.; Tabakman, S. M.; Welsher, K.; Liu, Z.; Goodwin, A. P.; Zhang, L.; Henry, J.; Dai, H. J. PEG Branched Polymer for Functionalization of Nanomaterials with Ultralong Blood Circulation. *J. Am. Chem. Soc.* **2009**, *131*, 4783–4787.
- (298) Robinson, J. T.; Hong, G. S.; Liang, Y. Y.; Zhang, B.; Yaghi, O. K.; Dai, H. J. In Vivo Fluorescence Imaging in the Second Near-Infrared Window with Long Circulating Carbon Nanotubes Capable of Ultrahigh Tumor Uptake. *J. Am. Chem. Soc.* **2012**, *134*, 10664–10669.
- (299) Andersen, A. J.; Robinson, J. T.; Dai, H. J.; Hunter, A. C.; Andresen, T. L.; Moghimi, S. M. Single-Walled Carbon Nanotube Surface Control of Complement Recognition and Activation. *ACS Nano* **2013**, *7*, 1108–1119.
- (300) Yang, K.; Gong, H.; Shi, X. Z.; Wan, J. M.; Zhang, Y. J.; Liu, Z. In vivo biodistribution and toxicology of functionalized nano-graphene oxide in mice after oral and intraperitoneal administration. *Biomaterials* **2013**, *34*, 2787–2795.
- (301) Chen, R. J.; Zhang, Y. G.; Wang, D. W.; Dai, H. J. Noncovalent sidewall functionalization of single-walled carbon nanotubes for protein immobilization. *J. Am. Chem. Soc.* **2001**, *123*, 3838–3839.
- (302) Ehli, C.; Rahman, G. M. A.; Jux, N.; Balbinot, D.; Guldi, D. M.; Paolucci, F.; Marcaccio, M.; Paolucci, D.; Melle-Franco, M.; Zerbetto,

- F.; Campidelli, S.; Prato, M. Interactions in single wall carbon nanotubes/pyrene/porphyrin nanohybrids. *J. Am. Chem. Soc.* **2006**, *128*, 11222–11231.
- (303) Hirsch, A. Functionalization of single-walled carbon nanotubes. *Angew. Chem., Int. Ed.* **2002**, *41*, 1853–1859.
- (304) Petrov, P.; Stassin, F.; Pagnoulle, C.; Jerome, R. Noncovalent functionalization of multi-walled carbon nanotubes by pyrene containing polymers. *Chem. Commun.* **2003**, 2904–2905.
- (305) Lou, X. D.; Daussin, R.; Cuenot, S.; Duwez, A. S.; Pagnoulle, C.; Detrembleur, C.; Bailly, C.; Jerome, R. Synthesis of pyrene-containing polymers and noncovalent sidewall functionalization of multiwalled carbon nanotubes. *Chem. Mater.* **2004**, *16*, 4005–4011.
- (306) Zheng, M.; Jagota, A.; Semke, E. D.; Diner, B. A.; Mclean, R. S.; Lustig, S. R.; Richardson, R. E.; Tassi, N. G. DNA-assisted dispersion and separation of carbon nanotubes. *Nat. Mater.* **2003**, *2*, 338–342.
- (307) Zheng, M.; Jagota, A.; Strano, M. S.; Santos, A. P.; Barone, P.; Chou, S. G.; Diner, B. A.; Dresselhaus, M. S.; McLean, R. S.; Onoa, G. B.; Samsonidze, G. G.; Semke, E. D.; Usrey, M.; Walls, D. J. Structure-based carbon nanotube sorting by sequence-dependent DNA assembly. *Science* **2003**, *302*, 1545–1548.
- (308) Strano, M. S.; Zheng, M.; Jagota, A.; Onoa, G. B.; Heller, D. A.; Barone, P. W.; Usrey, M. L. Understanding the nature of the DNA-assisted separation of single-walled carbon nanotubes using fluorescence and Raman spectroscopy. *Nano Lett.* **2004**, *4*, 543–550.
- (309) Tu, X. M.; Manohar, S.; Jagota, A.; Zheng, M. DNA sequence motifs for structure-specific recognition and separation of carbon nanotubes. *Nature* **2009**, *460*, 250–253.
- (310) Zheng, M.; Semke, E. D. Enrichment of single chirality carbon nanotubes. *J. Am. Chem. Soc.* **2007**, *129*, 6084–6085.
- (311) Zhang, L.; Tu, X. M.; Welsher, K.; Wang, X. R.; Zheng, M.; Dai, H. J. Optical Characterizations and Electronic Devices of Nearly Pure (10,5) Single-Walled Carbon Nanotubes. *J. Am. Chem. Soc.* **2009**, *131*, 2454–2455.
- (312) Tu, X. M.; Zheng, M. A DNA-Based Approach to the Carbon Nanotube Sorting Problem. *Nano Res.* **2008**, *1*, 185–194.
- (313) Huang, X. Y.; McLean, R. S.; Zheng, M. High-resolution length sorting and purification of DNA-wrapped carbon nanotubes by size-exclusion chromatography. *Anal. Chem.* **2005**, *77*, 6225–6228.
- (314) Dukovic, G.; Balaz, M.; Doak, P.; Berova, N. D.; Zheng, M.; Mclean, R. S.; Brus, L. E. Racemic single-walled carbon nanotubes exhibit circular dichroism when wrapped with DNA. *J. Am. Chem. Soc.* **2006**, *128*, 9004–9005.
- (315) Tong, L.; Liu, Y. X.; Dolash, B. D.; Jung, Y.; Slipchenko, M. N.; Bergstrom, D. E.; Cheng, J. X. Label-free imaging of semiconducting and metallic carbon nanotubes in cells and mice using transient absorption microscopy. *Nat. Nanotechnol.* **2012**, *7*, 56–61.
- (316) Kam, N. W. S.; Dai, H. J. Carbon nanotubes as intracellular protein transporters: Generality and biological functionality. *J. Am. Chem. Soc.* **2005**, *127*, 6021–6026.
- (317) Laaksonen, P.; Kainlauri, M.; Laaksonen, T.; Shchepetov, A.; Jiang, H.; Ahopelto, J.; Linder, M. B. Interfacial Engineering by Proteins: Exfoliation and Functionalization of Graphene by Hydrophobins. *Angew. Chem., Int. Ed.* **2010**, *49*, 4946–4949.
- (318) Liu, J. B.; Fu, S. H.; Yuan, B.; Li, Y. L.; Deng, Z. X. Toward a Universal “Adhesive Nanosheet” for the Assembly of Multiple Nanoparticles Based on a Protein-Induced Reduction/Decoration of Graphene Oxide. *J. Am. Chem. Soc.* **2010**, *132*, 7279–7281.
- (319) Mu, Q. X.; Su, G. X.; Li, L. W.; Gilbertson, B. O.; Yu, L. H.; Zhang, Q.; Sun, Y. P.; Yan, B. Size-Dependent Cell Uptake of Protein-Coated Graphene Oxide Nanosheets. *ACS Appl. Mater. Interfaces* **2012**, *4*, 2259–2266.
- (320) Dang, X. N.; Yi, H. J.; Ham, M. H.; Qi, J. F.; Yun, D. S.; Ladewski, R.; Strano, M. S.; Hammond, P. T.; Belcher, A. M. Virus-templated self-assembled single-walled carbon nanotubes for highly efficient electron collection in photovoltaic devices. *Nat. Nanotechnol.* **2011**, *6*, 377–384.
- (321) Yi, H. J.; Ghosh, D.; Ham, M. H.; Qi, J. F.; Barone, P. W.; Strano, M. S.; Belcher, A. M. M13 Phage-Functionalized Single-Walled Carbon Nanotubes As Nanoprobes for Second Near-Infrared Window Fluorescence Imaging of Targeted Tumors. *Nano Lett.* **2012**, *12*, 1176–1183.
- (322) Bardhan, N. M.; Ghosh, D.; Belcher, A. M. Carbon nanotubes as in vivo bacterial probes. *Nat. Commun.* **2014**, *5*, 4918.
- (323) Oh, D. Y.; Dang, X. N.; Yi, H. J.; Allen, M. A.; Xu, K.; Lee, Y. J.; Belcher, A. M. Graphene Sheets Stabilized on Genetically Engineered M13 Viral Templates as Conducting Frameworks for Hybrid Energy-Storage Materials. *Small* **2012**, *8*, 1006–1011.
- (324) Ghosh, D.; Lee, Y.; Thomas, S.; Kohli, A. G.; Yun, D. S.; Belcher, A. M.; Kelly, K. A. M13-templated magnetic nanoparticles for targeted in vivo imaging of prostate cancer. *Nat. Nanotechnol.* **2012**, *7*, 677–682.
- (325) Ghosh, D.; Kohli, A. G.; Moser, F.; Endy, D.; Belcher, A. M. Refactored M13 Bacteriophage as a Platform for Tumor Cell Imaging and Drug Delivery. *ACS Synth. Biol.* **2012**, *1*, 576–582.
- (326) Yurekli, K.; Mitchell, C. A.; Krishnamoorti, R. Small-angle neutron scattering from surfactant-assisted aqueous dispersions of carbon nanotubes. *J. Am. Chem. Soc.* **2004**, *126*, 9902–9903.
- (327) Hirsch, A.; Brettreich, M. *Fullerenes: Chemistry and Reactions*; John Wiley & Sons: Hoboken, NJ, 2006.
- (328) Maggini, M.; Scorrano, G.; Prato, M. Addition of Azomethine Ylides to C-60—Synthesis, Characterization, and Functionalization of Fullerene Pyrrolidines. *J. Am. Chem. Soc.* **1993**, *115*, 9798–9799.
- (329) Bingel, C. Cyclopropanierung von fullerenen. *Chem. Ber.* **1993**, *126*, 1957–1959.
- (330) Chiang, L. Y.; Bhonsle, J. B.; Wang, L. Y.; Shu, S. F.; Chang, T. M.; Hwu, J. R. Efficient one-flask synthesis of water-soluble [60]-fullerenols. *Tetrahedron* **1996**, *52*, 4963–4972.
- (331) Da Ros, T.; Prato, M. Medicinal chemistry with fullerenes and fullerene derivatives. *Chem. Commun.* **1999**, 663–669.
- (332) Kwag, D. S.; Park, K.; Oh, K. T.; Lee, E. S. Hyaluronated fullerenes with photoluminescent and antitumoral activity. *Chem. Commun.* **2013**, *49*, 282–284.
- (333) Wakai, H.; Momoi, T.; Yamauchi, T.; Tsubokawa, N. A Simple Preparation of C-60-Poly(ethylene glycol) Gel and its Properties. *Polym. J.* **2009**, *41*, 40–45.
- (334) Yang, X.; Ebrahimi, A.; Li, J.; Cui, Q. Fullerene–biomolecule conjugates and their biomedical applications. *Int. J. Nanomed.* **2014**, *9*, 77–92.
- (335) Georgakilas, V.; Kordatos, K.; Prato, M.; Guldi, D. M.; Holzinger, M.; Hirsch, A. Organic functionalization of carbon nanotubes. *J. Am. Chem. Soc.* **2002**, *124*, 760–761.
- (336) Chen, J.; Hamon, M. A.; Hu, H.; Chen, Y. S.; Rao, A. M.; Eklund, P. C.; Haddon, R. C. Solution properties of single-walled carbon nanotubes. *Science* **1998**, *282*, 95–98.
- (337) Kam, N. W. S.; Jessop, T. C.; Wender, P. A.; Dai, H. J. Nanotube molecular transporters: Internalization of carbon nanotube-protein conjugates into mammalian cells. *J. Am. Chem. Soc.* **2004**, *126*, 6850–6851.
- (338) Huang, W. J.; Taylor, S.; Fu, K. F.; Lin, Y.; Zhang, D. H.; Hanks, T. W.; Rao, A. M.; Sun, Y. P. Attaching proteins to carbon nanotubes via diimide-activated amidation. *Nano Lett.* **2002**, *2*, 311–314.
- (339) Cheng, J. P.; Fernando, K. A. S.; Veca, L. M.; Sun, Y. P.; Lamond, A. I.; Lam, Y. W.; Cheng, S. H. Reversible Accumulation of PEGylated Single-Walled Carbon Nanotubes in the Mammalian Nucleus. *ACS Nano* **2008**, *2*, 2085–2094.
- (340) Wu, W.; Li, R. T.; Bian, X. C.; Zhu, Z. S.; Ding, D.; Li, X. L.; Jia, Z. J.; Jiang, X. Q.; Hu, Y. Q. Covalently Combining Carbon Nanotubes with Anticancer Agent: Preparation and Antitumor Activity. *ACS Nano* **2009**, *3*, 2740–2750.
- (341) Piao, Y. M.; Meany, B.; Powell, L. R.; Valley, N.; Kwon, H.; Schatz, G. C.; Wang, Y. H. Brightening of carbon nanotube photoluminescence through the incorporation of sp(3) defects. *Nat. Chem.* **2013**, *5*, 840–845.
- (342) Brozena, A. H.; Leeds, J. D.; Zhang, Y.; Fourkas, J. T.; Wang, Y. H. Controlled Defects in Semiconducting Carbon Nanotubes Promote Efficient Generation and Luminescence of Trions. *ACS Nano* **2014**, *8*, 4239–4247.
- (343) Lonkar, S. P.; Deshmukh, Y. S.; Abdala, A. A. Recent advances in chemical modifications of graphene. *Nano Res.* **2014**, 1–36.

- (344) Bao, H. Q.; Pan, Y. Z.; Ping, Y.; Sahoo, N. G.; Wu, T. F.; Li, L.; Li, J.; Gan, L. H. Chitosan-Functionalized Graphene Oxide as a Nanocarrier for Drug and Gene Delivery. *Small* **2011**, *7*, 1569–1578.
- (345) Si, Y.; Samulski, E. T. Synthesis of water soluble graphene. *Nano Lett.* **2008**, *8*, 1679–1682.
- (346) Jiang, H. Q.; Chen, F.; Lagally, M. G.; Denes, F. S. New Strategy for Synthesis and Functionalization of Carbon Nanoparticles. *Langmuir* **2010**, *26*, 1991–1995.
- (347) Arnault, J. C.; Petit, T.; Girard, H.; Chavanne, A.; Gesset, C.; Sennour, M.; Chaigneau, M. Surface chemical modifications and surface reactivity of nanodiamonds hydrogenated by CVD plasma. *Phys. Chem. Chem. Phys.* **2011**, *13*, 11481–11487.
- (348) Ando, T.; Nakagawa, K.; Nishitani-Gamo, M. New carbon materials: Biological applications of functionalized nanodiamond materials. *Oyo Butsuri* **2001**, *70*, 1447–1451. Reviewed in Krueger, A. New carbon materials: Biological applications of functionalized nanodiamond materials. *Chem.—Eur. J.* **2008**, *14*, 1382–1390.
- (349) Meinhardt, T.; Lang, D.; Dill, H.; Krueger, A. Pushing the Functionality of Diamond Nanoparticles to New Horizons: Orthogonally Functionalized Nanodiamond Using Click Chemistry. *Adv. Funct. Mater.* **2011**, *21*, 494–500.
- (350) Reber, C.; Yee, L.; McKiernan, J.; Zink, J. I.; Williams, R. S.; Tong, W. M.; Ohlberg, D. A. A.; Whetten, R. L.; Diederich, F. Luminescence and Absorption-Spectra of C₆₀ Films. *J. Phys. Chem.* **1991**, *95*, 2127–2129.
- (351) Capozzi, V.; Casamassima, G.; Lorusso, G. F.; Minafra, A.; Piccolo, R.; Trovato, T.; Valentini, A. Optical spectra and photoluminescence of C-60 thin films. *Solid State Commun.* **1996**, *98*, 853–858.
- (352) Capozzi, V.; Santoro, M.; Celentano, G.; Berger, H.; Lorusso, G. F. Growth and photoluminescence spectra of C-60 single crystals. *J. Lumin.* **1998**, *76*–77, 395–398.
- (353) Lin, S. K.; Shiu, L. L.; Chien, K. M.; Luh, T. Y.; Lin, T. I. Fluorescence of Fullerene Derivatives at Room-Temperature. *J. Phys. Chem.* **1995**, *99*, 105–111.
- (354) Tachibana, M.; Nishimura, K.; Kikuchi, K.; Achiba, Y.; Kojima, K. Photoluminescence and structural defects of C-60 single crystals. *J. Lumin.* **1995**, *66*–7, 249–252.
- (355) Jensen, A. W.; Wilson, S. R.; Schuster, D. I. Biological applications of fullerenes. *Bioorg. Med. Chem.* **1996**, *4*, 767–779.
- (356) Dresselhaus, M. S.; Dresselhaus, G. Intercalation compounds of graphite. *Adv. Phys.* **2002**, *51*, 1–186.
- (357) Son, Y. W.; Cohen, M. L.; Louie, S. G. Energy gaps in graphene nanoribbons. *Phys. Rev. Lett.* **2006**, *97*, 216803.
- (358) Han, M. Y.; Ozyilmaz, B.; Zhang, Y. B.; Kim, P. Energy band-gap engineering of graphene nanoribbons. *Phys. Rev. Lett.* **2007**, *98*, 206805.
- (359) Chernov, A. I.; Fedotov, P. V.; Talyzin, A. V.; Lopez, I. S.; Anoshkin, I. V.; Nasibulin, A. G.; Kauppinen, E. I.; Obraztsova, E. D. Optical Properties of Graphene Nanoribbons Encapsulated in Single-Walled Carbon Nanotubes. *ACS Nano* **2013**, *7*, 6346–6353.
- (360) Chien, C. T.; Li, S. S.; Lai, W. J.; Yeh, Y. C.; Chen, H. A.; Chen, I. S.; Chen, L. C.; Chen, K. H.; Nemoto, T.; Isoda, S.; Chen, M. W.; Fujita, T.; Eda, G.; Yamaguchi, H.; Chhowalla, M.; Chen, C. W. Tunable Photoluminescence from Graphene Oxide. *Angew. Chem., Int. Ed.* **2012**, *51*, 6662–6666.
- (361) Eda, G.; Lin, Y. Y.; Mattevi, C.; Yamaguchi, H.; Chen, H. A.; Chen, I. S.; Chen, C. W.; Chhowalla, M. Blue Photoluminescence from Chemically Derived Graphene Oxide. *Adv. Mater.* **2010**, *22*, 505–509.
- (362) Galande, C.; Mohite, A. D.; Naumov, A. V.; Gao, W.; Ci, L. J.; Ajayan, A.; Gao, H.; Srivastava, A.; Weisman, R. B.; Ajayan, P. M. Quasi-Molecular Fluorescence from Graphene Oxide. *Sci. Rep.* **2011**, *1*, 85.
- (363) Luo, Z. T.; Vora, P. M.; Mele, E. J.; Johnson, A. T. C.; Kikkawa, J. M. Photoluminescence and band gap modulation in graphene oxide. *Appl. Phys. Lett.* **2009**, *94*, 111909.
- (364) Gokus, T.; Nair, R. R.; Bonetti, A.; Bohmler, M.; Lombardo, A.; Novoselov, K. S.; Geim, A. K.; Ferrari, A. C.; Hartschuh, A. Making Graphene Luminescent by Oxygen Plasma Treatment. *ACS Nano* **2009**, *3*, 3963–3968.
- (365) Subach, F. V.; Verkhusha, V. V. Chromophore Transformations in Red Fluorescent Proteins. *Chem. Rev.* **2012**, *112*, 4308–4327.
- (366) Li, H. T.; He, X. D.; Kang, Z. H.; Huang, H.; Liu, Y.; Liu, J. L.; Lian, S. Y.; Tsang, C. H. A.; Yang, X. B.; Lee, S. T. Water-Soluble Fluorescent Carbon Quantum Dots and Photocatalyst Design. *Angew. Chem., Int. Ed.* **2010**, *49*, 4430–4434.
- (367) Aharonovich, I.; Greentree, A. D.; Prawer, S. Diamond photonics. *Nat. Photonics* **2011**, *5*, 397–405.
- (368) Mochalin, V. N.; Gogotsi, Y. Wet Chemistry Route to Hydrophobic Blue Fluorescent Nanodiamond. *J. Am. Chem. Soc.* **2009**, *131*, 4594–4595.
- (369) Hui, Y. Y.; Su, L. J.; Chen, O. Y.; Chen, Y. T.; Liu, T. M.; Chang, H. C. Wide-field imaging and flow cytometric analysis of cancer cells in blood by fluorescent nanodiamond labeling and time gating. *Sci. Rep.* **2014**, *4*, 5574.
- (370) Mei, Q. S.; Jiang, C. L.; Guan, G. J.; Zhang, K.; Liu, B. H.; Liu, R. Y.; Zhang, Z. P. Fluorescent graphene oxide logic gates for discrimination of iron (3+) and iron (2+) in living cells by imaging. *Chem. Commun.* **2012**, *48*, 7468–7470.
- (371) Liu, R. L.; Wu, D. Q.; Liu, S. H.; Koynov, K.; Knoll, W.; Li, Q. An Aqueous Route to Multicolor Photoluminescent Carbon Dots Using Silica Spheres as Carriers. *Angew. Chem., Int. Ed.* **2009**, *48*, 4598–4601.
- (372) Zhai, X. Y.; Zhang, P.; Liu, C. J.; Bai, T.; Li, W. C.; Dai, L. M.; Liu, W. G. Highly luminescent carbon nanodots by microwave-assisted pyrolysis. *Chem. Commun.* **2012**, *48*, 7955–7957.
- (373) Cushing, S. K.; Li, M.; Huang, F. Q.; Wu, N. Q. Origin of Strong Excitation Wavelength Dependent Fluorescence of Graphene Oxide. *ACS Nano* **2014**, *8*, 1002–1013.
- (374) Zhu, A. W.; Qu, Q.; Shao, X. L.; Kong, B.; Tian, Y. Carbon-Dot-Based Dual-Emission Nanohybrid Produces a Ratiometric Fluorescent Sensor for In Vivo Imaging of Cellular Copper Ions. *Angew. Chem., Int. Ed.* **2012**, *51*, 7185–7189.
- (375) Zhang, Z. M.; Shi, Y. P.; Pan, Y.; Cheng, X.; Zhang, L. L.; Chen, J. Y.; Li, M. J.; Yi, C. Q. Quinoline derivative-functionalized carbon dots as a fluorescent nanosensor for sensing and intracellular imaging of Zn²⁺. *J. Mater. Chem. B* **2014**, *2*, 5020–5027.
- (376) Zhu, S. J.; Meng, Q. N.; Wang, L.; Zhang, J. H.; Song, Y. B.; Jin, H.; Zhang, K.; Sun, H. C.; Wang, H. Y.; Yang, B. Highly Photoluminescent Carbon Dots for Multicolor Patterning, Sensors, and Bioimaging. *Angew. Chem., Int. Ed.* **2013**, *52*, 3953–3957.
- (377) Hou, X. F.; Zeng, F.; Du, F. K.; Wu, S. Z. Carbon-dot-based fluorescent turn-on sensor for selectively detecting sulfide anions in totally aqueous media and imaging inside live cells. *Nanotechnology* **2013**, *24*, 335502.
- (378) Gao, X.; Ding, C. Q.; Zhu, A. W.; Tian, Y. Carbon-Dot-Based Ratiometric Fluorescent Probe for Imaging and Biosensing of Superoxide Anion in Live Cells. *Anal. Chem.* **2014**, *86*, 7071–7078.
- (379) Li, Q.; Ohulchansky, T. Y.; Liu, R. L.; Koynov, K.; Wu, D. Q.; Best, A.; Kumar, R.; Bonoju, A.; Prasad, P. N. Photoluminescent Carbon Dots as Biocompatible Nanoprobes for Targeting Cancer Cells in Vitro. *J. Phys. Chem. C* **2010**, *114*, 12062–12068.
- (380) Betzig, E.; Patterson, G. H.; Sougrat, R.; Lindwasser, O. W.; Olenych, S.; Bonifacino, J. S.; Davidson, M. W.; Lippincott-Schwartz, J.; Hess, H. F. Imaging intracellular fluorescent proteins at nanometer resolution. *Science* **2006**, *313*, 1642–1645.
- (381) Rust, M. J.; Bates, M.; Zhuang, X. W. Sub-diffraction-limit imaging by stochastic optical reconstruction microscopy (STORM). *Nat. Methods* **2006**, *3*, 793–795.
- (382) Yang, S. T.; Wang, X.; Wang, H. F.; Lu, F. S.; Luo, P. J. G.; Cao, L.; Meziani, M. J.; Liu, J. H.; Liu, Y. F.; Chen, M.; Huang, Y. P.; Sun, Y. P. Carbon Dots as Nontoxic and High-Performance Fluorescence Imaging Agents. *J. Phys. Chem. C* **2009**, *113*, 18110–18114.
- (383) LeCroy, G. E.; Sonkar, S. K.; Yang, F.; Veca, L. M.; Wang, P.; Tackett, K. N.; Yu, J. J.; Vasile, E.; Qian, H. J.; Liu, Y. M.; Luo, P.; Sun, Y. P. Toward Structurally Defined Carbon Dots as Ultracompact Fluorescent Probes. *ACS Nano* **2014**, *8*, 4522–4529.
- (384) Zhang, B. L.; Li, Y. Q.; Fang, C. Y.; Chang, C. C.; Chen, C. S.; Chen, Y. Y.; Chang, H. C. Receptor-Mediated Cellular Uptake of Folate-

- Conjugated Fluorescent Nanodiamonds: A Combined Ensemble and Single-Particle Study. *Small* **2009**, *5*, 2716–2721.
- (385) Choi, H. S.; Liu, W.; Misra, P.; Tanaka, E.; Zimmer, J. P.; Ipe, B. L.; Bawendi, M. G.; Frangioni, J. V. Renal clearance of quantum dots. *Nat. Biotechnol.* **2007**, *25*, 1165–1170.
- (386) Dresselhaus, M. S.; Dresselhaus, G.; Saito, R. Physics of Carbon Nanotubes. *Carbon* **1995**, *33*, 883–891.
- (387) Bronikowski, M. J.; Willis, P. A.; Colbert, D. T.; Smith, K. A.; Smalley, R. E. Gas-phase production of carbon single-walled nanotubes from carbon monoxide via the HiPco process: A parametric study. *J. Vac. Sci. Technol. A* **2001**, *19*, 1800–1805.
- (388) Ma, J.; Wang, J. N.; Wang, X. X. Large-diameter and water-dispersible single-walled carbon nanotubes: synthesis, characterization and applications. *J. Mater. Chem.* **2009**, *19*, 3033–3041.
- (389) Davies, J. H. *The Physics of Low-Dimensional Semiconductors: An Introduction*; Cambridge University Press: Cambridge, U.K., 1998.
- (390) Ma, Y. Z.; Valkunas, L.; Bachilo, S. M.; Fleming, G. R. Exciton binding energy in semiconducting single-walled carbon nanotubes. *J. Phys. Chem. B* **2005**, *109*, 15671–15674.
- (391) Hertel, T.; Perebeinos, V.; Crochet, J.; Arnold, K.; Kappes, M.; Avouris, P. Intersubband decay of 1-D exciton resonances in carbon nanotubes. *Nano Lett.* **2008**, *8*, 87–91.
- (392) Hong, G. S.; Robinson, J. T.; Zhang, Y. J.; Diao, S.; Antaris, A. L.; Wang, Q. B.; Dai, H. J. In Vivo Fluorescence Imaging with Ag₂S Quantum Dots in the Second Near-Infrared Region. *Angew. Chem., Int. Ed.* **2012**, *51*, 9818–9821.
- (393) Tao, Z. M.; Hong, G. S.; Shinji, C.; Chen, C. X.; Diao, S.; Antaris, A. L.; Zhang, B.; Zou, Y. P.; Dai, H. J. Biological Imaging Using Nanoparticles of Small Organic Molecules with Fluorescence Emission at Wavelengths Longer than 1000 nm. *Angew. Chem., Int. Ed.* **2013**, *52*, 13002–13006.
- (394) Naczynski, D. J.; Tan, M. C.; Zevon, M.; Wall, B.; Kohl, J.; Kulesa, A.; Chen, S.; Roth, C. M.; Rimani, R. E.; Moghe, P. V. Rare-earth-doped biological composites as in vivo shortwave infrared reporters. *Nat. Commun.* **2013**, *4*, 2199.
- (395) Dong, B. H.; Li, C. Y.; Chen, G. C.; Zhang, Y. J.; Zhang, Y.; Deng, M. J.; Wang, Q. B. Facile Synthesis of Highly Photoluminescent Ag₂Se Quantum Dots as a New Fluorescent Probe in the Second Near-Infrared Window for in Vivo Imaging. *Chem. Mater.* **2013**, *25*, 2503–2509.
- (396) Hong, G. S.; Zou, Y. P.; Antaris, A. L.; Diao, S.; Wu, D.; Cheng, K.; Zhang, X. D.; Chen, C. X.; Liu, B.; He, Y. H.; Wu, J. Z.; Yuan, J.; Zhang, B.; Tao, Z. M.; Fukunaga, C.; Dai, H. J. Ultrafast fluorescence imaging in vivo with conjugated polymer fluorophores in the second near-infrared window. *Nat. Commun.* **2014**, *5*, 4206.
- (397) Hong, G. S.; Lee, J. C.; Jha, A.; Diao, S.; Nakayama, K. H.; Hou, L. Q.; Doyle, T. C.; Robinson, J. T.; Antaris, A. L.; Dai, H. J.; Cooke, J. P.; Huang, N. F. Near-Infrared II Fluorescence for Imaging Hindlimb Vessel Regeneration With Dynamic Tissue Perfusion Measurement. *Circ.: Cardiovasc. Imaging* **2014**, *7*, 517–525.
- (398) Diao, S.; Blackburn, J. L.; Hong, G.; Antaris, A. L.; Chang, J.; Wu, J. Z.; Zhang, B.; Kuo, C. J.; Dai, H. J. Fluorescence Imaging In Vivo up to 1700 nm. 2015. arXiv:physics.bio-ph/1502.02775. arXiv.org. e-Print archive. <http://arxiv.org/abs/1502.02775>.
- (399) Villa, I.; Vedda, A.; Cantarelli, I. X.; Pedroni, M.; Piccinelli, F.; Bettinelli, M.; Spaghini, A.; Quintanilla, M.; Vetrone, F.; Rocha, U.; Jacinto, C.; Carrasco, E.; Rodríguez, F. S.; Juarranz, Á.; del Rosal, B.; Ortgies, D. H.; Gonzalez, P. H.; Solé, J. G.; Jaque García, D. 1.3 μm emitting SrF₂: Nd³⁺ nanoparticles for high contrast in vivo imaging in the second biological window. *Nano Res.* **2015**, *8*, 649–665.
- (400) Avouris, P.; Freitag, M.; Perebeinos, V. Carbon-nanotube photonics and optoelectronics. *Nat. Photonics* **2008**, *2*, 341–350.
- (401) Crochet, J.; Clemens, M.; Hertel, T. Quantum yield heterogeneities of aqueous single-wall carbon nanotube suspensions. *J. Am. Chem. Soc.* **2007**, *129*, 8058–8059.
- (402) Peng, X. X.; Chen, H. X.; Draney, D. R.; Volcheck, W.; Schutz-Geschwender, A.; Olive, D. M. A nonfluorescent, broad-range quencher dye for Förster resonance energy transfer assays. *Anal. Biochem.* **2009**, *388*, 220–228.
- (403) Stuerzl, N.; Lebedkin, S.; Kappes, M. M. Revisiting the Laser Dye Styryl-13 As a Reference Near-Infrared Fluorophore: Implications for the Photoluminescence Quantum Yields of Semiconducting Single-Walled Carbon Nanotubes. *J. Phys. Chem. A* **2009**, *113*, 10238–10240.
- (404) Ju, S. Y.; Kopcha, W. P.; Papadimitrakopoulos, F. Brightly Fluorescent Single-Walled Carbon Nanotubes via an Oxygen-Excluding Surfactant Organization. *Science* **2009**, *323*, 1319–1323.
- (405) Murphy, J. E.; Beard, M. C.; Norman, A. G.; Ahrenkiel, S. P.; Johnson, J. C.; Yu, P. R.; Micic, O. I.; Ellingson, R. J.; Nozik, A. J. PbTe colloidal nanocrystals: Synthesis, characterization, and multiple exciton generation. *J. Am. Chem. Soc.* **2006**, *128*, 3241–3247.
- (406) Semonin, O. E.; Johnson, J. C.; Luther, J. M.; Midgett, A. G.; Nozik, A. J.; Beard, M. C. Absolute Photoluminescence Quantum Yields of IR-26 Dye, PbS, and PbSe Quantum Dots. *J. Phys. Chem. Lett.* **2010**, *1*, 2445–2450.
- (407) Hatami, S.; Wurth, C.; Kaiser, M.; Leubner, S.; Gabriel, S.; Bahrig, L.; Lesnyak, V.; Pauli, J.; Gaponik, N.; Eychmuller, A.; Resch-Genger, U. Absolute photoluminescence quantum yields of IR26 and IR-emissive Cd_{1-x}Hg_xTe and PbS quantum dots—method- and material-inherent challenges. *Nanoscale* **2015**, *7*, 133–143.
- (408) Perebeinos, V.; Tersoff, J.; Avouris, P. Radiative lifetime of excitons in carbon nanotubes. *Nano Lett.* **2005**, *5*, 2495–2499.
- (409) Tabakman, S. M.; Welsher, K.; Hong, G. S.; Dai, H. J. Optical Properties of Single-Walled Carbon Nanotubes Separated in a Density Gradient: Length, Bundling, and Aromatic Stacking Effects. *J. Phys. Chem. C* **2010**, *114*, 19569–19575.
- (410) Sun, X.; Zaric, S.; Daranciang, D.; Welsher, K.; Lu, Y.; Li, X.; Dai, H. Optical properties of ultrashort semiconducting single-walled carbon nanotube capsules down to sub-10 nm. *J. Am. Chem. Soc.* **2008**, *130*, 6551–6555.
- (411) Lefebvre, J.; Homma, Y.; Finnie, P. Bright band gap photoluminescence from unprocessed single-walled carbon nanotubes. *Phys. Rev. Lett.* **2003**, *90*, 217401.
- (412) Naumov, A. V.; Bachilo, S. M.; Tsyboulski, D. A.; Weisman, R. B. Electric field quenching of carbon nanotube photoluminescence. *Nano Lett.* **2008**, *8*, 1527–1531.
- (413) Dukovic, G.; White, B. E.; Zhou, Z. Y.; Wang, F.; Jockusch, S.; Steigerwald, M. L.; Heinz, T. F.; Friesner, R. A.; Turro, N. J.; Brus, L. E. Reversible surface oxidation and efficient luminescence quenching in semiconductor single-wall carbon nanotubes. *J. Am. Chem. Soc.* **2004**, *126*, 15269–15276.
- (414) Crochet, J. J.; Duque, J. G.; Werner, J. H.; Doorn, S. K. Photoluminescence imaging of electronic-impurity-induced exciton quenching in single-walled carbon nanotubes. *Nat. Nanotechnol.* **2012**, *7*, 126–132.
- (415) Chen, J.; Perebeinos, V.; Freitag, M.; Tsang, J.; Fu, Q.; Liu, J.; Avouris, P. Bright infrared emission from electrically induced excitons in carbon nanotubes. *Science* **2005**, *310*, 1171–1174.
- (416) Huang, N. N.; Wang, H. Q.; Zhao, J. H.; Lui, H.; Korbelik, M.; Zeng, H. S. Single-Wall Carbon Nanotubes Assisted Photothermal Cancer Therapy: Animal Study With a Murine Model of Squamous Cell Carcinoma. *Laser Surg. Med.* **2010**, *42*, 638–648.
- (417) Hong, G. S.; Tabakman, S. M.; Welsher, K.; Wang, H. L.; Wang, X. R.; Dai, H. J. Metal-Enhanced Fluorescence of Carbon Nanotubes. *J. Am. Chem. Soc.* **2010**, *132*, 15920–15923.
- (418) Kim, S. J.; Park, J.; Jeong, Y.; Go, H.; Lee, K.; Hong, S.; Seong, M. J. Metal-particle-induced enhancement of the photoluminescence from biomolecule-functionalized carbon nanotubes. *Nanoscale Res. Lett.* **2014**, *9*, 85.
- (419) Glaeske, M.; Setaro, A. Nanoplasmonic colloidal suspensions for the enhancement of the luminescent emission from single-walled carbon nanotubes. *Nano Res.* **2013**, *6*, 593–601.
- (420) Lee, A. J.; Wang, X. Y.; Carlson, L. J.; Smyder, J. A.; Loesch, B.; Tu, X. M.; Zheng, M.; Krauss, T. D. Bright Fluorescence from Individual Single-Walled Carbon Nanotubes. *Nano Lett.* **2011**, *11*, 1636–1640.
- (421) Xie, L. M.; Liu, C.; Zhang, J.; Zhang, Y. Y.; Jiao, L. Y.; Jiang, L.; Dai, L.; Liu, Z. F. Photoluminescence recovery from single-walled carbon nanotubes on substrates. *J. Am. Chem. Soc.* **2007**, *129*, 12382–12383.

- (422) Strano, M. S.; Huffman, C. B.; Moore, V. C.; O'Connell, M. J.; Haroz, E. H.; Hubbard, J.; Miller, M.; Rialon, K.; Kittrell, C.; Ramesh, S.; Hauge, R. H.; Smalley, R. E. Reversible, band-gap-selective protonation of single-walled carbon nanotubes in solution. *J. Phys. Chem. B* **2003**, *107*, 6979–6985.
- (423) Zhang, B.; Price, J.; Hong, G. S.; Tabakman, S. M.; Wang, H. L.; Jarrell, J. A.; Feng, J.; Utz, P. J.; Dai, H. J. Multiplexed cytokine detection on plasmonic gold substrates with enhanced near-infrared fluorescence. *Nano Res.* **2013**, *6*, 113–120.
- (424) Zhou, C. J.; Wang, S.; Sun, J. L.; Wei, N.; Yang, L. J.; Zhang, Z. Y.; Liao, J. H.; Peng, L. M. Plasmonic enhancement of photocurrent in carbon nanotube by Au nanoparticles. *Appl. Phys. Lett.* **2013**, *102*, 103102.
- (425) Watahiki, R.; Shimada, T.; Zhao, P.; Chiashi, S.; Iwamoto, S.; Arakawa, Y.; Maruyama, S.; Kato, Y. K. Enhancement of carbon nanotube photoluminescence by photonic crystal nanocavities. *Appl. Phys. Lett.* **2012**, *101*, 141124.
- (426) Liu, X. J.; Kuzmany, H.; Ayala, P.; Calvaresi, M.; Zerbetto, F.; Pichler, T. Selective Enhancement of Photoluminescence in Filled Single-Walled Carbon Nanotubes. *Adv. Funct. Mater.* **2012**, *22*, 3202–3208.
- (427) Hong, G. S.; Tabakman, S. M.; Welsher, K.; Chen, Z.; Robinson, J. T.; Wang, H. L.; Zhang, B.; Dai, H. J. Near-Infrared-Fluorescence-Enhanced Molecular Imaging of Live Cells on Gold Substrates. *Angew. Chem., Int. Ed.* **2011**, *50*, 4644–4648.
- (428) Fakhri, N.; Wessel, A. D.; Willms, C.; Pasquali, M.; Klopfenstein, D. R.; MacKintosh, F. C.; Schmidt, C. F. High-resolution mapping of intracellular fluctuations using carbon nanotubes. *Science* **2014**, *344*, 1031–1035.
- (429) Dumortier, H.; Lacotte, S.; Pastorin, G.; Marega, R.; Wu, W.; Bonifazi, D.; Briand, J. P.; Prato, M.; Muller, S.; Bianco, A. Functionalized carbon nanotubes are non-cytotoxic and preserve the functionality of primary immune cells. *Nano Lett.* **2006**, *6*, 1522–1528, Addition & Correction for *Nano Lett.* **2006**, *6*, 1522. 3003.
- (430) Pantarotto, D.; Briand, J. P.; Prato, M.; Bianco, A. Translocation of bioactive peptides across cell membranes by carbon nanotubes. *Chem. Commun.* **2004**, *16*–17.
- (431) Cherukuri, P.; Bachilo, S. M.; Litovsky, S. H.; Weisman, R. B. Near-infrared fluorescence microscopy of single-walled carbon nanotubes in phagocytic cells. *J. Am. Chem. Soc.* **2004**, *126*, 15638–15639.
- (432) Cherukuri, P.; Gannon, C. J.; Leeuw, T. K.; Schmidt, H. K.; Smalley, R. E.; Curley, S. A.; Weisman, R. B. Mammalian pharmacokinetics of carbon nanotubes using intrinsic near-infrared fluorescence. *Proc. Natl. Acad. Sci. U.S.A.* **2006**, *103*, 18882–18886.
- (433) Shim, M.; Kam, N. W. S.; Chen, R. J.; Li, Y. M.; Dai, H. J. Functionalization of carbon nanotubes for biocompatibility and biomolecular recognition. *Nano Lett.* **2002**, *2*, 285–288.
- (434) Hillaireau, H.; Couvreur, P. Nanocarriers' entry into the cell: relevance to drug delivery. *Cell. Mol. Life Sci.* **2009**, *66*, 2873–2896.
- (435) Xie, X.; Xu, A. M.; Angle, M. R.; Tayebi, N.; Verma, P.; Melosh, N. A. Mechanical Model of Vertical Nanowire Cell Penetration. *Nano Lett.* **2013**, *13*, 6002–6008.
- (436) Xu, A. M.; Aalipour, A.; Leal-Ortiz, S.; Mekhdjian, A. H.; Xie, X.; Dunn, A. R.; Garner, C. C.; Melosh, N. A. Quantification of nanowire penetration into living cells. *Nat. Commun.* **2014**, *5*, 3613.
- (437) Fu, T. M.; Duan, X. J.; Jiang, Z.; Dai, X. C.; Xie, P.; Cheng, Z. G.; Lieber, C. M. Sub-10-nm intracellular bioelectronic probes from nanowire-nanotube heterostructures. *Proc. Natl. Acad. Sci. U.S.A.* **2014**, *111*, 1259–1264.
- (438) Liu, Z.; Winters, M.; Holodniy, M.; Dai, H. J. siRNA delivery into human T cells and primary cells with carbon-nanotube transporters. *Angew. Chem., Int. Ed.* **2007**, *46*, 2023–2027.
- (439) Feazell, R. P.; Nakayama-Ratchford, N.; Dai, H.; Lippard, S. J. Soluble single-walled carbon nanotubes as longboat delivery systems for Platinum(IV) anticancer drug design. *J. Am. Chem. Soc.* **2007**, *129*, 8438–8439.
- (440) Liu, Y.; Wu, D. C.; Zhang, W. D.; Jiang, X.; He, C. B.; Chung, T. S.; Goh, S. H.; Leong, K. W. Polyethylenimine-grafted multiwalled carbon nanotubes for secure noncovalent immobilization and efficient delivery of DNA. *Angew. Chem., Int. Ed.* **2005**, *44*, 4782–4785.
- (441) Shi, X. H.; von dem Bussche, A.; Hurt, R. H.; Kane, A. B.; Gao, H. J. Cell entry of one-dimensional nanomaterials occurs by tip recognition and rotation. *Nat. Nanotechnol.* **2011**, *6*, 714–719.
- (442) Shi, X. H.; Kong, Y.; Gao, H. J. Coarse grained molecular dynamics and theoretical studies of carbon nanotubes entering cell membrane. *Acta Mech. Sin.* **2008**, *24*, 161–169.
- (443) Neves, V.; Gerondopoulos, A.; Heister, E.; Tilmaci, C.; Flahaut, E.; Soula, B.; Silva, S. R. P.; McFadden, J.; Coley, H. M. Cellular localization, accumulation and trafficking of double-walled carbon nanotubes in human prostate cancer cells. *Nano Res.* **2012**, *5*, 223–234.
- (444) Lu, Q.; Moore, J. M.; Huang, G.; Mount, A. S.; Rao, A. M.; Larcom, L. L.; Ke, P. C. RNA polymer translocation with single-walled carbon nanotubes. *Nano Lett.* **2004**, *4*, 2473–2477.
- (445) Bianco, A.; Hoebeke, J.; Godefroy, S.; Chaloin, O.; Pantarotto, D.; Briand, J. P.; Muller, S.; Prato, M.; Partidos, C. D. Cationic carbon nanotubes bind to CpG oligodeoxynucleotides and enhance their immunostimulatory properties. *J. Am. Chem. Soc.* **2005**, *127*, 58–59.
- (446) Lopez, C. F.; Nielsen, S. O.; Moore, P. B.; Klein, M. L. Understanding nature's design for a nanosyringe. *Proc. Natl. Acad. Sci. U.S.A.* **2004**, *101*, 4431–4434.
- (447) Jin, H.; Heller, D. A.; Strano, M. S. Single-particle tracking of endocytosis and exocytosis of single-walled carbon nanotubes in NIH-3T3 cells. *Nano Lett.* **2008**, *8*, 1577–1585.
- (448) Jin, H.; Heller, D. A.; Sharma, R.; Strano, M. S. Size-Dependent Cellular Uptake and Expulsion of Single-Walled Carbon Nanotubes: Single Particle Tracking and a Generic Uptake Model for Nanoparticles. *ACS Nano* **2009**, *3*, 149–158.
- (449) Hong, G. S.; Wu, J. Z.; Robinson, J. T.; Wang, H. L.; Zhang, B.; Dai, H. J. Three-dimensional imaging of single nanotube molecule endocytosis on plasmonic substrates. *Nat. Commun.* **2012**, *3*, 700.
- (450) Tsybouski, D. A.; Bachilo, S. M.; Weisman, R. B. Versatile visualization of individual single-walled carbon nanotubes with near-infrared fluorescence microscopy. *Nano Lett.* **2005**, *5*, 975–979.
- (451) Satishkumar, B. C.; Brown, L. O.; Gao, Y.; Wang, C. C.; Wang, H. L.; Doorn, S. K. Reversible fluorescence quenching in carbon nanotubes for biomolecular sensing. *Nat. Nanotechnol.* **2007**, *2*, 560–564.
- (452) Dempsey, G. T.; Bates, M.; Kowtoniuk, W. E.; Liu, D. R.; Tsien, R. Y.; Zhuang, X. W. Photoswitching Mechanism of Cyanine Dyes. *J. Am. Chem. Soc.* **2009**, *131*, 18192–18193.
- (453) Tabakman, S. M.; Lau, L.; Robinson, J. T.; Price, J.; Sherlock, S. P.; Wang, H. L.; Zhang, B.; Chen, Z.; Tangsombatvisit, S.; Jarrell, J. A.; Utz, P. J.; Dai, H. J. Plasmonic substrates for multiplexed protein microarrays with femtomolar sensitivity and broad dynamic range. *Nat. Commun.* **2011**, *2*, 466.
- (454) Zhang, B.; Yang, J.; Zou, Y. P.; Gong, M.; Chen, H.; Hong, G. S.; Antaris, A. L.; Li, X. Y.; Liu, C. L.; Chen, C. X.; Dai, H. J. Plasmonic micro-beads for fluorescence enhanced, multiplexed protein detection with flow cytometry. *Chem. Sci.* **2014**, *5*, 4070–4075.
- (455) Zhang, B.; Kumar, R. B.; Dai, H. J.; Feldman, B. J. A plasmonic chip for biomarker discovery and diagnosis of type 1 diabetes. *Nat. Med.* **2014**, *20*, 948–953.
- (456) Horton, N. G.; Wang, K.; Kobat, D.; Clark, C. G.; Wise, F. W.; Schaffer, C. B.; Xu, C. In vivo three-photon microscopy of subcortical structures within an intact mouse brain. *Nat. Photonics* **2013**, *7*, 205–209.
- (457) Bashkatov, A. N.; Genina, E. A.; Kochubey, V. I.; Tuchin, V. V. Optical properties of human skin, subcutaneous and mucous tissues in the wavelength range from 400 to 2000 nm. *J. Phys. D: Appl. Phys.* **2005**, *38*, 2543–2555.
- (458) Bashkatov, A. N.; Genina, E. A.; Tuchin, V. V. Optical Properties of Skin, Subcutaneous, and Muscle Tissues: A Review. *J. Innovative Opt. Health Sci.* **2011**, *4*, 9–38.
- (459) Bashkatov, A. N.; Genina, E. A.; Kochubey, V. I.; Tuchin, V. V. Optical properties of human cranial bone in the spectral range from 800 to 2000 nm. *Proc. SPIE* **2006**, *6163*, 616310 DOI: 10.1117/12.697305.

- (460) Vanstaveren, H. J.; Moes, C. J. M.; Vanmarle, J.; Prahl, S. A.; Vangemert, M. J. C. Light-Scattering in Intralipid-10-Percent in the Wavelength Range of 400–1100 nm. *Appl. Opt.* **1991**, *30*, 4507–4514.
- (461) Curcio, J. A.; Petty, C. C. The near Infrared Absorption Spectrum of Liquid Water. *J. Opt. Soc. Am.* **1951**, *41*, 302–304.
- (462) Drabkin, D. L. Spectrophotometric Studies. 14. The Crystallographic and Optical Properties of the Hemoglobin of Man in Comparison with Those of Other Species. *J. Biol. Chem.* **1946**, *164*, 703–723.
- (463) Frangioni, J. V. In vivo near-infrared fluorescence imaging. *Curr. Opin. Chem. Biol.* **2003**, *7*, 626–634.
- (464) Inoue, Y.; Izawa, K.; Kiryu, S.; Tojo, A.; Ohtomo, K. Diet and abdominal autofluorescence detected by in vivo fluorescence imaging of living mice. *Mol. Imaging* **2008**, *7*, 21–27.
- (465) Georgakoudi, I.; Jacobson, B. C.; Muller, M. G.; Sheets, E. E.; Badizadegan, K.; Carr-Locke, D. L.; Crum, C. P.; Boone, C. W.; Dasari, R. R.; Van Dam, J.; Feld, M. S. NAD(P)H and collagen as in vivo quantitative fluorescent biomarkers of epithelial precancerous changes. *Cancer Res.* **2002**, *62*, 682–687.
- (466) Sun, M.; Song, P. S.; Moore, T. A. Molecular Luminescence Studies of Flavins. 1. Excited-States of Flavins. *J. Am. Chem. Soc.* **1972**, *94*, 1730–1740.
- (467) Brown, E. B.; Campbell, R. B.; Tsuzuki, Y.; Xu, L.; Carmeliet, P.; Fukumura, D.; Jain, R. K. In vivo measurement of gene expression, angiogenesis and physiological function in tumors using multiphoton laser scanning microscopy. *Nat. Med.* **2001**, *7*, 864–868.
- (468) Leeuw, T. K.; Reith, R. M.; Simonette, R. A.; Harden, M. E.; Cherukuri, P.; Tsybouski, D. A.; Beckingham, K. M.; Weisman, R. B. Single-walled carbon nanotubes in the intact organism: Near-IR imaging and biocompatibility studies in *Drosophila*. *Nano Lett.* **2007**, *7*, 2650–2654.
- (469) Hillman, E. M. C.; Moore, A. All-optical anatomical co-registration for molecular imaging of small animals using dynamic contrast. *Nat. Photonics* **2007**, *1*, 526–530.
- (470) Peer, D.; Karp, J. M.; Hong, S.; Farokhzad, O. C.; Margalit, R.; Langer, R. Nanocarriers as an emerging platform for cancer therapy. *Nat. Nanotechnol.* **2007**, *2*, 751–760.
- (471) Schroeder, A.; Heller, D. A.; Winslow, M. M.; Dahlman, J. E.; Pratt, G. W.; Langer, R.; Jacks, T.; Anderson, D. G. Treating metastatic cancer with nanotechnology. *Nat. Rev. Cancer* **2012**, *12*, 39–50.
- (472) Lim, Y. T.; Kim, S.; Nakayama, A.; Stott, N. E.; Bawendi, M. G.; Frangioni, J. V. Selection of quantum dot wavelengths for biomedical assays and imaging. *Mol. Imaging* **2003**, *2*, 50–64.
- (473) Miyata, Y.; Shiozawa, K.; Asada, Y.; Ohno, Y.; Kitaura, R.; Mizutani, T.; Shinohara, H. Length-Sorted Semiconducting Carbon Nanotubes for High-Mobility Thin Film Transistors. *Nano Res.* **2011**, *4*, 963–970.
- (474) Liu, H. P.; Nishide, D.; Tanaka, T.; Kataura, H. Large-scale single-chirality separation of single-wall carbon nanotubes by simple gel chromatography. *Nat. Commun.* **2011**, *2*, 309.
- (475) Liu, H. P.; Tanaka, T.; Urabe, Y.; Kataura, H. High-Efficiency Single-Chirality Separation of Carbon Nanotubes Using Temperature-Controlled Gel Chromatography. *Nano Lett.* **2013**, *13*, 1996–2003.
- (476) Wu, J.; Xie, L. M.; Hong, G. S.; Lim, H. E.; Thendie, B.; Miyata, Y.; Shinohara, H.; Dai, H. J. Short channel field-effect transistors from highly enriched semiconducting carbon nanotubes. *Nano Res.* **2012**, *5*, 388–394.
- (477) Zhang, J. L.; Gui, H.; Liu, B. L.; Liu, J.; Zhou, C. W. Comparative study of gel-based separated arcdischarge, HiPCO, and CoMoCAT carbon nanotubes for macroelectronic applications. *Nano Res.* **2013**, *6*, 906–920.
- (478) Ghosh, S.; Bachilo, S. M.; Weisman, R. B. Advanced sorting of single-walled carbon nanotubes by nonlinear density-gradient ultracentrifugation. *Nat. Nanotechnol.* **2010**, *5*, 443–450.
- (479) Green, A. A.; Hersam, M. C. Processing and properties of highly enriched double-wall carbon nanotubes. *Nat. Nanotechnol.* **2009**, *4*, 64–70.
- (480) Liang, C.; Diao, S.; Wang, C.; Gong, H.; Liu, T.; Hong, G. S.; Shi, X. Z.; Dai, H. J.; Liu, Z. Tumor Metastasis Inhibition by Imaging-Guided Photothermal Therapy with Single-Walled Carbon Nanotubes. *Adv. Mater.* **2014**, *26*, 5646–5652.
- (481) Kim, J. H.; Heller, D. A.; Jin, H.; Barone, P. W.; Song, C.; Zhang, J.; Trudel, L. J.; Wogan, G. N.; Tannenbaum, S. R.; Strano, M. S. The rational design of nitric oxide selectivity in single-walled carbon nanotube near-infrared fluorescence sensors for biological detection. *Nat. Chem.* **2009**, *1*, 473–481.
- (482) Kitai, T.; Inomoto, T.; Miwa, M.; Shikayama, T. Fluorescence navigation with indocyanine green for detecting sentinel lymph nodes in breast cancer. *Breast Cancer* **2005**, *12*, 211–215.
- (483) Hirche, C.; Murawa, D.; Mohr, Z.; Kneif, S.; Hunerbein, M. ICG fluorescence-guided sentinel node biopsy for axillary nodal staging in breast cancer. *Breast Cancer Res. Treat.* **2010**, *121*, 373–378.
- (484) Kim, C.; Song, K. H.; Gao, F.; Wang, L. H. V. Sentinel Lymph Nodes and Lymphatic Vessels: Noninvasive Dual-Modality in Vivo Mapping by Using Indocyanine Green in Rats—Volumetric Spectroscopic Photoacoustic Imaging and Planar Fluorescence Imaging. *Radiology* **2010**, *255*, 442–450.
- (485) Chi, C. W.; Ye, J. Z.; Ding, H. L.; He, D.; Huang, W. H.; Zhang, G. J.; Tian, J. Use of Indocyanine Green for Detecting the Sentinel Lymph Node in Breast Cancer Patients: From Preclinical Evaluation to Clinical Validation. *PLoS One* **2013**, *8*, e83927.
- (486) Cloyd, J. M.; Wapnir, I. L.; Read, B. M.; Swetter, S.; Greco, R. S. Indocyanine green and fluorescence lymphangiography for sentinel lymph node identification in cutaneous melanoma. *J. Surg. Oncol.* **2014**, *110*, 888–892.
- (487) Guo, W. B.; Zhang, L.; Ji, J.; Gao, W.; Liu, J. T.; Tong, M. Breast cancer sentinel lymph node mapping using near-infrared guided indocyanine green in comparison with blue dye. *Tumor Biol.* **2014**, *35*, 3073–3078.
- (488) Verbeek, F. P.; Troyan, S. L.; Mieog, J. S.; Liefers, G. J.; Moffitt, L. A.; Rosenberg, M.; Hirshfield-Bartek, J.; Gioux, S.; van de Velde, C. J.; Vahrmeijer, A. L.; Frangioni, J. V. Near-infrared fluorescence sentinel lymph node mapping in breast cancer: a multicenter experience. *Breast Cancer Res. Treat.* **2014**, *143*, 333–342.
- (489) Jin, H.; Heller, D. A.; Kim, J. H.; Strano, M. S. Stochastic Analysis of Stepwise Fluorescence Quenching Reactions on Single-Walled Carbon Nanotubes: Single Molecule Sensors. *Nano Lett.* **2008**, *8*, 4299–4304.
- (490) Jin, H.; Heller, D. A.; Kalbacova, M.; Kim, J. H.; Zhang, J. Q.; Boghossian, A. A.; Maheshri, N.; Strano, M. S. Detection of single-molecule H₂O₂ signalling from epidermal growth factor receptor using fluorescent single-walled carbon nanotubes. *Nat. Nanotechnol.* **2010**, *5*, 302–309.
- (491) Zhang, J. Q.; Boghossian, A. A.; Barone, P. W.; Rwei, A.; Kim, J. H.; Lin, D. H.; Heller, D. A.; Hilmer, A. J.; Nair, N.; Reuel, N. F.; Strano, M. S. Single Molecule Detection of Nitric Oxide Enabled by d(AT)(15) DNA Adsorbed to Near Infrared Fluorescent Single-Walled Carbon Nanotubes. *J. Am. Chem. Soc.* **2011**, *133*, 567–581.
- (492) Yizhar, O.; Feno, L. E.; Davidson, T. J.; Mogri, M.; Deisseroth, K. Optogenetics in Neural Systems. *Neuron* **2011**, *71*, 9–34.
- (493) Aravanis, A. M.; Wang, L. P.; Zhang, F.; Meltzer, L. A.; Mogri, M. Z.; Schneider, M. B.; Deisseroth, K. An optical neural interface: in vivo control of rodent motor cortex with integrated fiberoptic and optogenetic technology. *J. Neural Eng.* **2007**, *4*, S143–S156.
- (494) Martirosyan, N. L.; Cavalcanti, D. D.; Eschbacher, J. M.; Delaney, P. M.; Scheck, A. C.; Abdelwahab, M. G.; Nakaji, P.; Spetzler, R. F.; Preul, M. C. Use of in vivo near-infrared laser confocal endomicroscopy with indocyanine green to detect the boundary of infiltrative tumor Laboratory investigation. *J. Neurosurg.* **2011**, *115*, 1131–1138.
- (495) Drew, P. J.; Shih, A. Y.; Driscoll, J. D.; Knutsen, P. M.; Blinder, P.; Davalos, D.; Akassoglou, K.; Tsai, P. S.; Kleinfeld, D. Chronic optical access through a polished and reinforced thinned skull. *Nat. Methods* **2010**, *7*, 981–984.
- (496) Ku, T.; Choi, C. Noninvasive Optical Measurement of Cerebral Blood Flow in Mice Using Molecular Dynamics Analysis of Indocyanine Green. *PLoS One* **2012**, *7*.

- (497) Tsukasaki, Y.; Morimatsu, M.; Nishimura, G.; Sakata, T.; Yasuda, H.; Komatsuzaki, A.; Watanabe, T. M.; Jin, T. Synthesis and optical properties of emission-tunable PbS/CdS core-shell quantum dots for *in vivo* fluorescence imaging in the second near-infrared window. *RSC Adv.* **2014**, *4*, 41164–41171.
- (498) Vogt, N. A windowless peek into the brain. *Nat. Methods* **2014**, *11*, 988.
- (499) Madsen, S. J. Biophotonics: Through-skull brain imaging. *Nat. Photonics* **2014**, *8*, 677–678.
- (500) Zhang, Y.; Hong, G. S.; Zhang, Y. J.; Chen, G. C.; Li, F.; Dai, H. J.; Wang, Q. B. Ag₂S Quantum Dot: A Bright and Biocompatible Fluorescent Nanoprobe in the Second Near-Infrared Window. *ACS Nano* **2012**, *6*, 3695–3702.
- (501) Zhang, Y.; Zhang, Y. J.; Hong, G. S.; He, W.; Zhou, K.; Yang, K.; Li, F.; Chen, G. C.; Liu, Z.; Dai, H. J.; Wang, Q. B. Biodistribution, pharmacokinetics and toxicology of Ag₂S near-infrared quantum dots in mice. *Biomaterials* **2013**, *34*, 3639–3646.
- (502) Chen, G.; Tian, F.; Zhang, Y.; Zhang, Y.; Li, C.; Wang, Q. Tracking of Transplanted Human Mesenchymal Stem Cells in Living Mice using Near-Infrared Ag₂S Quantum Dots. *Adv. Funct. Mater.* **2014**, *24*, 2481–2488.
- (503) Li, C. Y.; Zhang, Y. J.; Wang, M.; Zhang, Y.; Chen, G. C.; Li, L.; Wu, D. M.; Wang, Q. B. In *vivo* real-time visualization of tissue blood flow and angiogenesis using Ag₂S quantum dots in the NIR-II window. *Biomaterials* **2014**, *35*, 393–400.
- (504) Hu, F.; Li, C.; Zhang, Y.; Wang, M.; Wu, D.; Wang, Q. Real-Time In Vivo Visualization of Tumor Therapy by A Near-Infrared-II Ag₂S Quantum Dot-Based Theranostic Nanoplatform. *Nano Res.* **2014**, DOI: 10.1007/s12274-014-0653-2.
- (505) Nakane, Y.; Tsukasaki, Y.; Sakata, T.; Yasuda, H.; Jin, T. Aqueous synthesis of glutathione-coated PbS quantum dots with tunable emission for non-invasive fluorescence imaging in the second near-infrared biological window (1000–1400 nm). *Chem. Commun.* **2013**, *49*, 7584–7586.
- (506) Tsukasaki, Y.; Komatsuzaki, A.; Mori, Y.; Ma, Q.; Yoshioka, Y.; Jin, T. A short-wavelength infrared emitting multimodal probe for non-invasive visualization of phagocyte cell migration in living mice. *Chem. Commun.* **2014**, *50*, 14356–14359.
- (507) Sasaki, A.; Tsukasaki, Y.; Komatsuzaki, A.; Sakata, T.; Yasuda, H.; Jin, T. Recombinant protein (EGFP-Protein G)-coated PbS quantum dots for *in vitro* and *in vivo* dual fluorescence (visible and second-NIR) imaging of breast tumor. *Nanoscale* **2015**, *7*, 5115–5119.
- (508) Rocha, U.; Kumar, K. U.; Jacinto, C.; Villa, I.; Sanz-Rodriguez, F.; de la Cruz, M. D. I.; Juarranz, A.; Carrasco, E.; van Veggel, F. C. J. M.; Boero, E.; Sole, J. G.; Jaque, D. Neodymium-Doped LaF₃ Nanoparticles for Fluorescence Bioimaging in the Second Biological Window. *Small* **2014**, *10*, 1141–1154.
- (509) Naczynski, D. J.; Sun, C.; Türkcan, S.; Jenkins, C.; Koh, A. L.; Ikeda, D.; Pratx, G.; Xing, L. X-ray induced shortwave infrared biomedical imaging using rare-earth nanoprobes. *Nano Lett.* **2015**, *15*, 96–102.
- (510) Denk, W.; Strickler, J. H.; Webb, W. W. 2-Photon Laser Scanning Fluorescence Microscopy. *Science* **1990**, *248*, 73–76.
- (511) Helmchen, F.; Denk, W. Deep tissue two-photon microscopy. *Nat. Methods* **2005**, *2*, 932–940.
- (512) Svoboda, K.; Yasuda, R. Principles of two-photon excitation microscopy and its applications to neuroscience. *Neuron* **2006**, *50*, 823–839.
- (513) Trachtenberg, J. T.; Chen, B. E.; Knott, G. W.; Feng, G. P.; Sanes, J. R.; Welker, E.; Svoboda, K. Long-term *in vivo* imaging of experience-dependent synaptic plasticity in adult cortex. *Nature* **2002**, *420*, 788–794.
- (514) Palczewska, G.; Dong, Z. Q.; Golczak, M.; Hunter, J. J.; Williams, D. R.; Alexander, N. S.; Palczewski, K. Noninvasive two-photon microscopy imaging of mouse retina and retinal pigment epithelium through the pupil of the eye. *Nat. Med.* **2014**, *20*, 785–789.
- (515) Kawakami, R.; Sawada, K.; Sato, A.; Hibi, T.; Kozawa, Y.; Sato, S.; Yokoyama, H.; Nemoto, T. Visualizing hippocampal neurons with *in vivo* two-photon microscopy using a 1030 nm picosecond pulse laser. *Sci. Rep.* **2013**, *3*, 1014.
- (516) Truong, T. V.; Supatto, W.; Koos, D. S.; Choi, J. M.; Fraser, S. E. Deep and fast live imaging with two-photon scanned light-sheet microscopy. *Nat. Methods* **2011**, *8*, 757–760.
- (517) Cheng, W. D.; Wu, D. S.; Li, X. D.; Lan, Y. Z.; Zhang, H.; Chen, D. G.; Gong, Y. J.; Zhang, Y. C.; Li, F. F.; Shen, J.; Kan, Z. G. Design of single-walled carbon nanotubes with a large two-photon absorption cross section. *Phys. Rev. B* **2004**, *70*, 155401.
- (518) Wang, F.; Dukovic, G.; Brus, L. E.; Heinz, T. F. The optical resonances in carbon nanotubes arise from excitons. *Science* **2005**, *308*, 838–841.
- (519) Li, J. L.; Bao, H. C.; Hou, X. L.; Sun, L.; Wang, X. G.; Gu, M. Graphene Oxide Nanoparticles as a Nonbleaching Optical Probe for Two-Photon Luminescence Imaging and Cell Therapy. *Angew. Chem., Int. Ed.* **2012**, *51*, 1830–1834.
- (520) Zhu, A. W.; Ding, C. Q.; Tian, Y. A two-photon ratiometric fluorescence probe for Cupric Ions in Live Cells and Tissues. *Sci. Rep.* **2013**, *3*, 2933.
- (521) Hui, Y. Y.; Zhang, B. L.; Chang, Y. C.; Chang, C. C.; Chang, H. C.; Hsu, J. H.; Chang, K.; Chang, F. H. Two-photon fluorescence correlation spectroscopy of lipid-encapsulated fluorescent nanodiamonds in living cells. *Opt. Express* **2010**, *18*, 5896–5905.
- (522) Morgan, J. L.; Lichtman, J. W. Why not connectomics? *Nat. Methods* **2013**, *10*, 494–500.
- (523) Liang, Y. Q.; Shilagard, T.; Xiao, S. Y.; Snyder, N.; Lau, D.; Cicalese, L.; Weiss, H.; Vargas, G.; Lemon, S. M. Visualizing Hepatitis C Virus Infections in Human Liver by Two-Photon Microscopy. *Gastroenterology* **2009**, *137*, 1448–1458.
- (524) Schmitt, M.; Popp, J. Raman spectroscopy at the beginning of the twenty-first century. *J. Raman Spectrosc.* **2006**, *37*, 20–28.
- (525) Rao, A. M.; Richter, E.; Bandow, S.; Chase, B.; Eklund, P. C.; Williams, K. A.; Fang, S.; Subbaswamy, K. R.; Menon, M.; Thess, A.; Smalley, R. E.; Dresselhaus, G.; Dresselhaus, M. S. Diameter-selective Raman scattering from vibrational modes in carbon nanotubes. *Science* **1997**, *275*, 187–191.
- (526) Xie, L. M.; Wang, H. L.; Jin, C. H.; Wang, X. R.; Jiao, L. Y.; Suenaga, K.; Dai, H. J. Graphene Nanoribbons from Unzipped Carbon Nanotubes: Atomic Structures, Raman Spectroscopy, and Electrical Properties. *J. Am. Chem. Soc.* **2011**, *133*, 10394–10397.
- (527) Kumar, G. S.; Roy, R.; Sen, D.; Ghorai, U. K.; Thapa, R.; Mazumder, N.; Saha, S.; Chattopadhyay, K. K. Amino-functionalized graphene quantum dots: origin of tunable heterogeneous photoluminescence. *Nanoscale* **2014**, *6*, 3384–3391.
- (528) Campos-Delgado, J.; Cancado, L. G.; Achete, C. A.; Jorio, A.; Raskin, J. P. Raman scattering study of the phonon dispersion in twisted bilayer graphene. *Nano Res.* **2013**, *6*, 269–274.
- (529) Yin, X. L.; Li, Y. L.; Ke, F.; Lin, C. F.; Zhao, H. B.; Gan, L.; Luo, Z. T.; Zhao, R. G.; Heinz, T. F.; Hu, Z. H. Evolution of the Raman spectrum of graphene grown on copper upon oxidation of the substrate. *Nano Res.* **2014**, *7*, 1613–1622.
- (530) Jorio, A.; Saito, R.; Hafner, J. H.; Lieber, C. M.; Hunter, M.; McClure, T.; Dresselhaus, G.; Dresselhaus, M. S. Structural (n, m) determination of isolated single-wall carbon nanotubes by resonant Raman scattering. *Phys. Rev. Lett.* **2001**, *86*, 1118–1121.
- (531) Strano, M. S.; Doorn, S. K.; Haroz, E. H.; Kittrell, C.; Hauge, R. H.; Smalley, R. E. Assignment of (n, m) Raman and optical features of metallic single-walled carbon nanotubes. *Nano Lett.* **2003**, *3*, 1091–1096.
- (532) Ferrari, A. C.; Basko, D. M. Raman spectroscopy as a versatile tool for studying the properties of graphene. *Nat. Nanotechnol.* **2013**, *8*, 235–246.
- (533) Liu, Z. A.; Li, X. L.; Tabakman, S. M.; Jiang, K. L.; Fan, S. S.; Dai, H. J. Multiplexed multicolor Raman imaging of live cells with isotopically modified single walled carbon nanotubes. *J. Am. Chem. Soc.* **2008**, *130*, 13540–13541.
- (534) Liu, Z.; Tabakman, S.; Sherlock, S.; Li, X. L.; Chen, Z.; Jiang, K. L.; Fan, S. S.; Dai, H. J. Multiplexed Five-Color Molecular Imaging of

- Cancer Cells and Tumor Tissues with Carbon Nanotube Raman Tags in the Near-Infrared. *Nano Res.* **2010**, *3*, 222–233.
- (535) Heller, D. A.; Baik, S.; Eurell, T. E.; Strano, M. S. Single-walled carbon nanotube spectroscopy in live cells: Towards long-term labels and optical sensors. *Adv. Mater.* **2005**, *17*, 2793–2799.
- (536) Zavaleta, C.; de la Zerda, A.; Liu, Z.; Keren, S.; Cheng, Z.; Schipper, M.; Chen, X.; Dai, H.; Gambhir, S. S. Noninvasive Raman spectroscopy in living mice for evaluation of tumor targeting with carbon nanotubes. *Nano Lett.* **2008**, *8*, 2800–2805.
- (537) Liu, Q. H.; Wei, L.; Wang, J. Y.; Peng, F.; Luo, D.; Cui, R. L.; Niu, Y.; Qin, X. J.; Liu, Y.; Sun, H.; Yang, J.; Li, Y. Cell imaging by graphene oxide based on surface enhanced Raman scattering. *Nanoscale* **2012**, *4*, 7084–7089.
- (538) Zavaleta, C. L.; Smith, B. R.; Walton, I.; Doering, W.; Davis, G.; Shojaei, B.; Natan, M. J.; Gambhir, S. S. Multiplexed imaging of surface enhanced Raman scattering nanotags in living mice using noninvasive Raman spectroscopy. *Proc. Natl. Acad. Sci. U.S.A.* **2009**, *106*, 13511–13516.
- (539) Ling, X. Y.; Yan, R. X.; Lo, S.; Hoang, D. T.; Liu, C.; Fardy, M. A.; Khan, S. B.; Asiri, A. M.; Bawaked, S. M.; Yang, P. D. Alumina-coated Ag nanocrystal monolayers as surface enhanced Raman spectroscopy platforms for the direct spectroscopic detection of water splitting reaction intermediates. *Nano Res.* **2014**, *7*, 132–143.
- (540) Qian, X. M.; Peng, X. H.; Ansari, D. O.; Yin-Goen, Q.; Chen, G. Z.; Shin, D. M.; Yang, L.; Young, A. N.; Wang, M. D.; Nie, S. M. In vivo tumor targeting and spectroscopic detection with surface-enhanced Raman nanoparticle tags. *Nat. Biotechnol.* **2008**, *26*, 83–90.
- (541) Huang, Z. L.; Meng, G. W.; Huang, Q.; Chen, B.; Zhou, F.; Hu, X. Y.; Qian, Y. W.; Tang, H. B.; Han, F. M.; Chu, Z. Q. Polyacrylic acid sodium salt film entrapped Ag-nanocubes as molecule traps for SERS detection. *Nano Res.* **2014**, *7*, 1177–1187.
- (542) Keren, S.; Zavaleta, C.; Cheng, Z.; de la Zerda, A.; Gheysens, O.; Gambhir, S. S. Noninvasive molecular imaging of small living subjects using Raman spectroscopy. *Proc. Natl. Acad. Sci. U.S.A.* **2008**, *105*, 5844–5849.
- (543) Wang, Y. D.; Lu, N.; Wang, W. T.; Liu, L. X.; Feng, L.; Zeng, Z. F.; Li, H. B.; Xu, W. Q.; Wu, Z. J.; Hu, W.; Lu, Y. Q.; Chi, L. F. Highly effective and reproducible surface-enhanced Raman scattering substrates based on Ag pyramidal arrays. *Nano Res.* **2013**, *6*, 159–166.
- (544) Huang, P.; Pandoli, O.; Wang, X. S.; Wang, Z.; Li, Z. M.; Zhang, C. L.; Chen, F.; Lin, J.; Cui, D. X.; Chen, X. Y. Chiral guanosine 5'-monophosphate-capped gold nanoflowers: Controllable synthesis, characterization, surface-enhanced Raman scattering activity, cellular imaging and photothermal therapy. *Nano Res.* **2012**, *5*, 630–639.
- (545) Day, R. N.; Davidson, M. W. The fluorescent protein palette: tools for cellular imaging. *Chem. Soc. Rev.* **2009**, *38*, 2887–2921.
- (546) Nie, S. M.; Emery, S. R. Probing single molecules and single nanoparticles by surface-enhanced Raman scattering. *Science* **1997**, *275*, 1102–1106.
- (547) Talley, C. E.; Jackson, J. B.; Oubre, C.; Grady, N. K.; Hollars, C. W.; Lane, S. M.; Huser, T. R.; Nordlander, P.; Halas, N. J. Surface-enhanced Raman scattering from individual Au nanoparticles and nanoparticle dimer substrates. *Nano Lett.* **2005**, *5*, 1569–1574.
- (548) Chen, Z.; Tabakman, S. M.; Goodwin, A. P.; Kattah, M. G.; Daranciang, D.; Wang, X. R.; Zhang, G. Y.; Li, X. L.; Liu, Z.; Utz, P. J.; Jiang, K. L.; Fan, S. S.; Dai, H. J. Protein microarrays with carbon nanotubes as multicolor Raman labels. *Nat. Biotechnol.* **2008**, *26*, 1285–1292.
- (549) Tabakman, S. M.; Chen, Z.; Casalongue, H. S.; Wang, H. L.; Dai, H. J. A New Approach to Solution-Phase Gold Seeding for SERS Substrates. *Small* **2011**, *7*, 499–505.
- (550) Wang, X. J.; Wang, C.; Cheng, L.; Lee, S. T.; Liu, Z. Noble Metal Coated Single-Walled Carbon Nanotubes for Applications in Surface Enhanced Raman Scattering Imaging and Photothermal Therapy. *J. Am. Chem. Soc.* **2012**, *134*, 7414–7422.
- (551) Liu, Z. M.; Guo, Z. Y.; Zhong, H. Q.; Qin, X. C.; Wan, M. M.; Yang, B. W. Graphene oxide based surface-enhanced Raman scattering probes for cancer cell imaging. *Phys. Chem. Chem. Phys.* **2013**, *15*, 2961–2966.
- (552) Wang, C.; Ma, X. X.; Ye, S. Q.; Cheng, L.; Yang, K.; Guo, L.; Li, C. H.; Li, Y. G.; Liu, Z. Protamine Functionalized Single-Walled Carbon Nanotubes for Stem Cell Labeling and In Vivo Raman/Magnetic Resonance/Photoacoustic Triple-Modal Imaging. *Adv. Funct. Mater.* **2012**, *22*, 2363–2375.
- (553) Yang, S.; Li, B. L.; Akkus, A.; Akkus, O.; Lang, L. S. Wide-field Raman imaging of dental lesions. *Analyst* **2014**, *139*, 3107–3114.
- (554) Havener, R. W.; Ju, S. Y.; Brown, L.; Wang, Z. H.; Wojcik, M.; Ruiz-Vargas, C. S.; Park, J. High-Throughput Graphene Imaging on Arbitrary Substrates with Widefield Raman Spectroscopy. *ACS Nano* **2012**, *6*, 373–380.
- (555) Fu, D.; Ye, T.; Matthews, T. E.; Yurtsever, G.; Warren, W. S. Two-color, two-photon, and excited-state absorption microscopy. *J. Biomed. Opt.* **2007**, *12*, 054004.
- (556) Min, W.; Lu, S. J.; Chong, S. S.; Roy, R.; Holtom, G. R.; Xie, X. S. Imaging chromophores with undetectable fluorescence by stimulated emission microscopy. *Nature* **2009**, *461*, 1105–1109.
- (557) Jung, Y.; Slipchenko, M. N.; Liu, C. H.; Ribbe, A. E.; Zhong, Z. H.; Yang, C.; Cheng, J. X. Fast Detection of the Metallic State of Individual Single-Walled Carbon Nanotubes Using a Transient-Absorption Optical Microscope. *Phys. Rev. Lett.* **2010**, *105*, 217401.
- (558) Krawczynski, K.; Beach, M. J.; Bradley, D. W.; Kuo, G.; di Bisceglie, A. M.; Houghton, M.; Reyes, G. R.; Kim, J. P.; Choo, Q. L.; Alter, M. J. Hepatitis C virus antigen in hepatocytes: immunomorphologic detection and identification. *Gastroenterology* **1992**, *103*, 622–629.
- (559) Chen, T.; Lu, F.; Streets, A. M.; Fei, P.; Quan, J. M.; Huang, Y. Y. Optical imaging of non-fluorescent nanodiamonds in live cells using transient absorption microscopy. *Nanoscale* **2013**, *5*, 4701–4705.
- (560) Grancini, G.; Polli, D.; Fazzi, D.; Cabanillas-Gonzalez, J.; Cerullo, G.; Lanzani, G. Transient Absorption Imaging of P3HT:PCBM Photovoltaic Blend: Evidence For Interfacial Charge Transfer State. *J. Phys. Chem. Lett.* **2011**, *2*, 1099–1105.
- (561) Wang, P.; Slipchenko, M. N.; Mitchell, J.; Yang, C.; Potma, E. O.; Xu, X. F.; Cheng, J. X. Far-field imaging of non-fluorescent species with subdiffraction resolution. *Nat. Photonics* **2013**, *7*, 450–454.
- (562) Ramanathan, T.; Abdala, A. A.; Stankovich, S.; Dikin, D. A.; Herrera-Alonso, M.; Piner, R. D.; Adamson, D. H.; Schniepp, H. C.; Chen, X.; Ruoff, R. S.; Nguyen, S. T.; Aksay, I. A.; Prud'homme, R. K.; Brinson, L. C. Functionalized graphene sheets for polymer nanocomposites. *Nat. Nanotechnol.* **2008**, *3*, 327–331.
- (563) Balasubramanian, G.; Chan, I. Y.; Kolesov, R.; Al-Hmoud, M.; Tisler, J.; Shin, C.; Kim, C.; Wojcik, A.; Hemmer, P. R.; Krueger, A.; Hanke, T.; Leitenstorfer, A.; Bratschitsch, R.; Jelezko, F.; Wrachtrup, J. Nanoscale imaging magnetometry with diamond spins under ambient conditions. *Nature* **2008**, *455*, 648–651.
- (564) Zhang, H. F.; Maslov, K.; Stoica, G.; Wang, L. H. V. Functional photoacoustic microscopy for high-resolution and noninvasive in vivo imaging. *Nat. Biotechnol.* **2006**, *24*, 848–851.
- (565) Wang, L. V. Multiscale photoacoustic microscopy and computed tomography. *Nat. Photonics* **2009**, *3*, 503–509.
- (566) Wang, X. D.; Pang, Y. J.; Ku, G.; Xie, X. Y.; Stoica, G.; Wang, L. H. V. Noninvasive laser-induced photoacoustic tomography for structural and functional in vivo imaging of the brain. *Nat. Biotechnol.* **2003**, *21*, 803–806.
- (567) Kim, J. W.; Galanzha, E. I.; Shashkov, E. V.; Moon, H. M.; Zharov, V. P. Golden carbon nanotubes as multimodal photoacoustic and photothermal high-contrast molecular agents. *Nat. Nanotechnol.* **2009**, *4*, 688–694.
- (568) de la Zerda, A.; Liu, Z. A.; Bodapati, S.; Teed, R.; Vaithilingam, S.; Khuri-Yakub, B. T.; Chen, X. Y.; Dai, H. J.; Gambhir, S. S. Ultrahigh Sensitivity Carbon Nanotube Agents for Photoacoustic Molecular Imaging in Living Mice. *Nano Lett.* **2010**, *10*, 2168–2172.
- (569) Zanganeh, S.; Li, H.; Kumavor, P. D.; Alqasemi, U.; Aguirre, A.; Mohammad, I.; Stanford, C.; Smith, M. B.; Zhu, Q. Photoacoustic imaging enhanced by indocyanine green-conjugated single-wall carbon nanotubes. *J. Biomed. Opt.* **2013**, *18*, 096006.
- (570) Galanzha, E. I.; Shashkov, E. V.; Kelly, T.; Kim, J. W.; Yang, L. L.; Zharov, V. P. In vivo magnetic enrichment and multiplex photoacoustic

- detection of circulating tumour cells. *Nat. Nanotechnol.* **2009**, *4*, 855–860.
- (571) de la Zerda, A.; Bodapati, S.; Teed, R.; May, S. Y.; Tabakman, S. M.; Liu, Z.; Khuri-Yakub, B. T.; Chen, X. Y.; Dai, H. J.; Gambhir, S. S. Family of Enhanced Photoacoustic Imaging Agents for High-Sensitivity and Multiplexing Studies in Living Mice. *ACS Nano* **2012**, *6*, 4694–4701.
- (572) Pramanik, M.; Swierczewska, M.; Green, D.; Sitharaman, B.; Wang, L. V. Single-walled carbon nanotubes as a multimodal-thermoacoustic and photoacoustic-contrast agent. *J. Biomed. Opt.* **2009**, *14*, 034018.
- (573) Shashkov, E. V.; Everts, M.; Galanzha, E. I.; Zharov, V. P. Quantum Dots as Multimodal Photoacoustic and Photothermal Contrast Agents. *Nano Lett.* **2008**, *8*, 3953–3958.
- (574) de la Zerda, A.; Kim, J. W.; Galanzha, E. I.; Gambhir, S. S.; Zharov, V. P. Advanced contrast nanoagents for photoacoustic molecular imaging, cytometry, blood test and photothermal theranostics. *Contrast Media Mol. Imaging* **2011**, *6*, 346–369.
- (575) Khodakovskaya, M. V.; de Silva, K.; Nedosekin, D. A.; Dervishi, E.; Biris, A. S.; Shashkov, E. V.; Galanzha, E. I.; Zharov, V. P. Complex genetic, photothermal, and photoacoustic analysis of nanoparticle-plant interactions. *Proc. Natl. Acad. Sci. U.S.A.* **2011**, *108*, 1028–1033.
- (576) Sheng, Z. H.; Song, L.; Zheng, J. X.; Hu, D. H.; He, M.; Zheng, M. B.; Gao, G. H.; Gong, P.; Zhang, P. F.; Ma, Y. F.; Cai, L. T. Protein-assisted fabrication of nano-reduced graphene oxide for combined in vivo photoacoustic imaging and photothermal therapy. *Biomaterials* **2013**, *34*, 5236–5243.
- (577) Rozada, R.; Paredes, J. I.; Villar-Rodil, S.; Martinez-Alonso, A.; Tascon, J. M. D. Towards full repair of defects in reduced graphene oxide films by two-step graphitization. *Nano Res.* **2013**, *6*, 216–233.
- (578) Lalwani, G.; Cai, X.; Nie, L.; Wang, L. V.; Sitharaman, B. Graphene-based contrast agents for photoacoustic and thermoacoustic tomography. *Photoacoustics* **2013**, *1*, 62–67.
- (579) Wang, Y. W.; Fu, Y. Y.; Peng, Q. L.; Guo, S. S.; Liu, G.; Li, J.; Yang, H. H.; Chen, G. N. Dye-enhanced graphene oxide for photothermal therapy and photoacoustic imaging. *J. Mater. Chem. B* **2013**, *1*, 5762–5767.
- (580) Krishna, V.; Singh, A.; Sharma, P.; Iwakuma, N.; Wang, Q. A.; Zhang, Q. Z.; Knapik, J.; Jiang, H. B.; Grobmyer, S. R.; Koopman, B.; Moudgil, B. Polyhydroxy Fullerenes for Non-Invasive Cancer Imaging and Therapy. *Small* **2010**, *6*, 2236–2241.
- (581) Wu, L.; Cai, X.; Nelson, K.; Xing, W.; Xia, J.; Zhang, R.; Stacy, A. J.; Luderer, M.; Lanza, G. M.; Wang, L. V.; Shen, B.; Pan, D. A Green Synthesis of Carbon Nanoparticle from Honey for Real-Time Photoacoustic Imaging. *Nano Res.* **2013**, *6*, 312–325.
- (582) Zhang, B. L.; Fang, C. Y.; Chang, C. C.; Peterson, R.; Maswadi, S.; Glickman, R. D.; Chang, H. C.; Ye, J. Y. Photoacoustic emission from fluorescent nanodiamonds enhanced with gold nanoparticles. *Biomed. Opt. Express* **2012**, *3*, 1662–1669.
- (583) Zhang, T.; Cui, H. Z.; Fang, C. Y.; Su, L. J.; Ren, S. Q.; Chang, H. C.; Yang, X. M.; Forrest, M. L. Photoacoustic contrast imaging of biological tissues with nanodiamonds fabricated for high near-infrared absorbance. *J. Biomed. Opt.* **2013**, *18*, 026018.
- (584) Wang, L. H. V.; Hu, S. Photoacoustic Tomography: In Vivo Imaging from Organelles to Organs. *Science* **2012**, *335*, 1458–1462.
- (585) Lee, N.; Choi, S. H.; Hyeon, T. Nano-Sized CT Contrast Agents. *Adv. Mater.* **2013**, *25*, 2641–2660.
- (586) Hao, D. P.; Ai, T.; Goerner, F.; Hu, X. M.; Runge, V. M.; Tweedle, M. MRI contrast agents: Basic chemistry and safety. *J. Magn. Reson. Imaging* **2012**, *36*, 1060–1071.
- (587) Sharma, V.; Piwnica-Worms, D. Molecular imaging of gene expression and protein function in vivo with PET and SPECT. *J. Magn. Reson. Imaging* **2002**, *16*, 336–351.
- (588) Qian, X.; Tucker, A.; Gidcumb, E.; Shan, J.; Yang, G.; Calderon-Colon, X.; Sultana, S.; Lu, J. P.; Zhou, O.; Spronk, D.; Sprenger, F.; Zhang, Y. H.; Kennedy, D.; Farbizio, T.; Jing, Z. X. High resolution stationary digital breast tomosynthesis using distributed carbon nanotube x-ray source array. *Med. Phys.* **2012**, *39*, 2090–2099.
- (589) Wait, J. M. S.; Tomita, H.; Burk, L. M.; Lu, J. P.; Zhou, O. Z.; Maeda, N.; Lee, Y. Z. Detection of Aortic Arch Calcification in Apolipoprotein E-Null Mice Using Carbon Nanotube-Based Micro-CT System. *J. Am. Heart Assoc.* **2013**, *2*, e003358.
- (590) Hadsell, M.; Zhang, J.; Laganis, P.; Sprenger, F.; Shan, J.; Zhang, L.; Burk, L.; Yuan, H.; Chang, S.; Lu, J.; Zhou, O. A first generation compact microbeam radiation therapy system based on carbon nanotube X-ray technology. *Appl. Phys. Lett.* **2013**, *103*, 183505.
- (591) Ashcroft, J. M.; Hartman, K. B.; Kissell, K. R.; Mackeyev, Y.; Pheasant, S.; Young, S.; Van der Heide, P. A. W.; Mikos, A. G.; Wilson, L. J. Single-molecule I-2@US-tube nanocapsules: A new X-ray contrast-agent design. *Adv. Mater.* **2007**, *19*, 573–576.
- (592) Rivera, E. J.; Tran, L. A.; Hernandez-Rivera, M.; Yoon, D.; Mikos, A. G.; Rusakova, I. A.; Cheong, B. Y.; Cabreira-Hansen, M. D.; Willerson, J. T.; Perin, E. C.; Wilson, L. J. Bismuth@US-tubes as a potential contrast agent for X-ray imaging applications. *J. Mater. Chem. B* **2013**, *1*, 4792–4800.
- (593) Jin, Y. S.; Wang, J. R.; Ke, H. T.; Wang, S. M.; Dai, Z. F. Graphene oxide modified PLA microcapsules containing gold nanoparticles for ultrasonic/CT bimodal imaging guided photothermal tumor therapy. *Biomaterials* **2013**, *34*, 4794–4802.
- (594) Choi, J. H.; Nguyen, F. T.; Barone, P. W.; Heller, D. A.; Moll, A. E.; Patel, D.; Boppert, S. A.; Strano, M. S. Multimodal biomedical imaging with asymmetric single-walled carbon nanotube/iron oxide nanoparticle complexes. *Nano Lett.* **2007**, *7*, 861–867.
- (595) Al Faraj, A.; Cieslar, K.; Lacroix, G.; Gaillard, S.; Canot-Soulas, E.; Cremillieux, Y. In Vivo Imaging of Carbon Nanotube Biodistribution Using Magnetic Resonance Imaging. *Nano Lett.* **2009**, *9*, 1023–1027.
- (596) Richard, C.; Doan, B. T.; Beloeil, J. C.; Bessodes, M.; Toth, E.; Scherman, D. Noncovalent functionalization of carbon nanotubes with amphiphilic Gd3+ chelates: Toward powerful T-1 and T-2 MRI contrast agents. *Nano Lett.* **2008**, *8*, 232–236.
- (597) Miyawaki, J.; Yudasaka, M.; Imai, H.; Yorimitsu, H.; Isobe, H.; Nakamura, E.; Iijima, S. In vivo magnetic resonance imaging of single-walled carbon nanohorns by labeling with magnetite nanoparticles. *Adv. Mater.* **2006**, *18*, 1010–1014.
- (598) Marangon, I.; Ménard-Moyon, C.; Kolosnjaj-Tabi, J.; Béoutis, M. L.; Lartigue, L.; Alloyeau, D.; Pach, E.; Ballesteros, B.; Autret, G.; Ninjbadgar, T.; Brougham, D. F.; Bianco, A.; Gazeau, F. Covalent Functionalization of Multi-walled Carbon Nanotubes with a Gadolinium Chelate for Efficient T1-Weighted Magnetic Resonance Imaging. *Adv. Funct. Mater.* **2014**, *24*, 7173–7186.
- (599) Lamanna, G.; Garofalo, A.; Popa, G.; Wilhelm, C.; Begin-Colin, S.; Felder-Flesch, D.; Bianco, A.; Gazeau, F.; Menard-Moyon, C. Endowing carbon nanotubes with superparamagnetic properties: applications for cell labeling, MRI cell tracking and magnetic manipulations. *Nanoscale* **2013**, *5*, 4412–4421.
- (600) Rivera, E. J.; Sethi, R.; Qu, F. F.; Krishnamurthy, R.; Muthupillai, R.; Alford, M.; Swanson, M. A.; Eaton, S. S.; Eaton, G. R.; Wilson, L. J. Nitroxide Radicals@US-Tubes: New Spin Labels for Biomedical Applications. *Adv. Funct. Mater.* **2012**, *22*, 3691–3698.
- (601) Lee, J. H.; Sherlock, S. P.; Terashima, M.; Kosuge, H.; Suzuki, Y.; Goodwin, A.; Robinson, J.; Seo, W. S.; Liu, Z.; Luong, R.; McConnell, M. V.; Nishimura, D. G.; Dai, H. J. High-Contrast In Vivo Visualization of Microvessels Using Novel FeCo/GC Magnetic Nanocrystals. *Magn. Reson. Med.* **2009**, *62*, 1497–1509.
- (602) Kosuge, H.; Sherlock, S. P.; Kitagawa, T.; Terashima, M.; Barral, J. K.; Nishimura, D. G.; Dai, H. J.; McConnell, M. V. FeCo/Graphite Nanocrystals for Multi-Modality Imaging of Experimental Vascular Inflammation. *PLoS One* **2011**, *6*, e14523.
- (603) Gizzatov, A.; Keshishian, V.; Guven, A.; Dimiev, A. M.; Qu, F. F.; Muthupillai, R.; Decuzzi, P.; Bryant, R. G.; Tour, J. M.; Wilson, L. J. Enhanced MRI relaxivity of aquated Gd3+ ions by carboxyphenylated water-dispersed graphene nanoribbons. *Nanoscale* **2014**, *6*, 3059–3063.
- (604) Bolkskar, R. D.; Benedetto, A. F.; Husebo, L. O.; Price, R. E.; Jackson, E. F.; Wallace, S.; Wilson, L. J.; Alford, J. M. First soluble M@C-60 derivatives provide enhanced access to metallofullerenes and permit in vivo evaluation of Gd@C-60[C(COOH)(2)](10) as a MRI contrast agent. *J. Am. Chem. Soc.* **2003**, *125*, 5471–5478.

- (605) Bolksar, R. D. Gadofullerene MRI contrast agents. *Nanomedicine* **2008**, *3*, 201–213.
- (606) Kato, H.; Kanazawa, Y.; Okumura, M.; Taninaka, A.; Yokawa, T.; Shinohara, H. Lanthanoid endohedral metallofullerenols for MRI contrast agents. *J. Am. Chem. Soc.* **2003**, *125*, 4391–4397.
- (607) Cui, R.; Li, J.; Huang, H.; Zhang, M.; Guo, X.; Chang, Y.; Li, M.; Dong, J.; Sun, B.; Xing, G. Novel carbon nanohybrids as highly efficient magnetic resonance imaging contrast agents. *Nano Res.* **2014**, DOI: 10.1007/s12274-014-0613-x.
- (608) Manus, L. M.; Mastarone, D. J.; Waters, E. A.; Zhang, X. Q.; Schultz-Sikma, E. A.; MacRenaris, K. W.; Ho, D.; Meade, T. J. Gd(III)-Nanodiamond Conjugates for MRI Contrast Enhancement. *Nano Lett.* **2010**, *10*, 484–489.
- (609) Chang, I. P.; Hwang, K. C.; Chiang, C. S. Preparation of Fluorescent Magnetic Nanodiamonds and Cellular Imaging. *J. Am. Chem. Soc.* **2008**, *130*, 15476–15481.
- (610) Talapatra, S.; Ganeshan, P. G.; Kim, T.; Vajtai, R.; Huang, M.; Shima, M.; Ramanath, G.; Srivastava, D.; Deevi, S. C.; Ajayan, P. M. Irradiation-induced magnetism in carbon nanostructures. *Phys. Rev. Lett.* **2005**, *95*, 097201.
- (611) Lien, Z. Y.; Hsu, T. C.; Liu, K. K.; Liao, W. S.; Hwang, K. C.; Chao, J. I. Cancer cell labeling and tracking using fluorescent and magnetic nanodiamond. *Biomaterials* **2012**, *33*, 6172–6185.
- (612) Knowles, H. S.; Kara, D. M.; Atature, M. Observing bulk diamond spin coherence in high-purity nanodiamonds. *Nat. Mater.* **2014**, *13*, 21–25.
- (613) Hong, H.; Yang, K.; Zhang, Y.; Engle, J. W.; Feng, L. Z.; Yang, Y. A.; Nayak, T. R.; Goel, S.; Bean, J.; Theuer, C. P.; Barnhart, T. E.; Liu, Z.; Cai, W. B. In Vivo Targeting and Imaging of Tumor Vasculature with Radiolabeled, Antibody-Conjugated Nanographene. *ACS Nano* **2012**, *6*, 2361–2370.
- (614) Hong, S. Y.; Tobias, G.; Al-Jamal, K. T.; Ballesteros, B.; Ali-Boucetta, H.; Lozano-Perez, S.; Nellist, P. D.; Sim, R. B.; Finucane, C.; Mather, S. J.; Green, M. L. H.; Kostarelos, K.; Davis, B. G. Filled and glycosylated carbon nanotubes for in vivo radioemitter localization and imaging. *Nat. Mater.* **2010**, *9*, 485–490.
- (615) McDevitt, M. R.; Chattopadhyay, D.; Jaggi, J. S.; Finn, R. D.; Zanzonico, P. B.; Villa, C.; Rey, D.; Mendenhall, J.; Batt, C. A.; Njardarson, J. T.; Scheinberg, D. A. PET Imaging of Soluble Yttrium-86-Labeled Carbon Nanotubes in Mice. *PLoS One* **2007**, *2*, e907.
- (616) Shi, S. X.; Yang, K.; Hong, H.; Valdovinos, H. F.; Nayak, T. R.; Zhang, Y.; Theuer, C. P.; Barnhart, T. E.; Liu, Z.; Cai, W. B. Tumor vasculature targeting and imaging in living mice with reduced graphene oxide. *Biomaterials* **2013**, *34*, 3002–3009.
- (617) Singh, R.; Pantarotto, D.; Lacerda, L.; Pastorin, G.; Klumpp, C.; Prato, M.; Bianco, A.; Kostarelos, K. Tissue biodistribution and blood clearance rates of intravenously administered carbon nanotube radiotracers. *Proc. Natl. Acad. Sci. U.S.A.* **2006**, *103*, 3357–3362.
- (618) Lacerda, L.; Soundararajan, A.; Singh, R.; Pastorin, G.; Al-Jamal, K. T.; Turton, J.; Frederik, P.; Herrero, M. A.; Bao, S. L. A.; Emfietzoglou, D.; Mather, S.; Phillips, W. T.; Prato, M.; Bianco, A.; Goins, B.; Kostarelos, K. Dynamic Imaging of functionalized multi-walled carbon nanotube systemic circulation and urinary excretion. *Adv. Mater.* **2008**, *20*, 225–230.
- (619) Wang, J. T. W.; Cabana, L.; Bourgognon, M.; Kafa, H.; Protti, A.; Venner, K.; Shah, A. M.; Sosabowski, J. K.; Mather, S. J.; Roig, A.; Ke, X. X.; Van Tendeloo, G.; Rosales, R. T. M.; Tobias, G.; Al-Jamal, K. T. Magnetically Decorated Multiwalled Carbon Nanotubes as Dual MRI and SPECT Contrast Agents. *Adv. Funct. Mater.* **2014**, *24*, 1880–1894.
- (620) Al-Jamal, K. T.; Nunes, A.; Methven, L.; Ali-Boucetta, H.; Li, S. P.; Toma, F. M.; Herrero, M. A.; Al-Jamal, W. T.; ten Eikelder, H. M. M.; Foster, J.; Mather, S.; Prato, M.; Bianco, A.; Kostarelos, K. Degree of Chemical Functionalization of Carbon Nanotubes Determines Tissue Distribution and Excretion Profile. *Angew. Chem., Int. Ed.* **2012**, *51*, 6389–6393.
- (621) Cornelissen, B.; Able, S.; Kersemans, V.; Waghorn, P. A.; Myhra, S.; Jurkshat, K.; Crossley, A.; Vallis, K. A. Nanographene oxide-based radioimmunoconstructs for in vivo targeting and SPECT imaging of HER2-positive tumors. *Biomaterials* **2013**, *34*, 1146–1154.
- (622) Cisneros, B. T.; Law, J. J.; Matson, M. L.; Azhdarinia, A.; Sevick-Muraca, E. M.; Wilson, L. J. Stable confinement of positron emission tomography and magnetic resonance agents within carbon nanotubes for bimodal imaging. *Nanomedicine (London, U.K.)* **2014**, *9*, 2499–2509.
- (623) Barreto, J. A.; O’Malley, W.; Kubeil, M.; Graham, B.; Stephan, H.; Spiccia, L. Nanomaterials: Applications in Cancer Imaging and Therapy. *Adv. Mater.* **2011**, *23*, H18–H40.
- (624) Liu, Y.; Yin, J.-J.; Nie, Z. Harnessing the collective properties of nanoparticle ensembles for cancer theranostics. *Nano Res.* **2014**, *7*, 1719–1730.
- (625) Bianco, A.; Kostarelos, K.; Prato, M. Opportunities and challenges of carbon-based nanomaterials for cancer therapy. *Expert Opin. Drug Delivery* **2008**, *5*, 331–342.
- (626) Bates, K.; Kostarelos, K. Carbon nanotubes as vectors for gene therapy: Past achievements, present challenges and future goals. *Adv. Drug Delivery Rev.* **2013**, *65*, 2023–2033.
- (627) Xie, X.; Xu, A. M.; Leal-Ortiz, S.; Cao, Y. H.; Garner, C. C.; Melosh, N. A. Nanostraw-Electroporation System for Highly Efficient Intracellular Delivery and Transfection. *ACS Nano* **2013**, *7*, 4351–4358.
- (628) Ma, D.; Zhang, L. M.; Xie, X.; Liu, T.; Xie, M. Q. Tunable supramolecular hydrogel for in situ encapsulation and sustained release of bioactive lysozyme. *J. Colloid Interface Sci.* **2011**, *359*, 399–406.
- (629) Li, S. S.; He, H.; Jiao, Q. C.; Chuong, P. H. Applications of Carbon Nanotubes in Drug and Gene Delivery. *Prog. Chem.* **2008**, *20*, 1798–1803.
- (630) Ajima, K.; Yudasaka, M.; Murakami, T.; Maigne, A.; Shiba, K.; Iijima, S. Carbon nanohorns as anticancer drug carriers. *Mol. Pharmaceutics* **2005**, *2*, 475–480.
- (631) Zhang, M.; Yudasaka, M. Potential application of nanocarbons as a drug delivery system. *Carbon* **2014**, *69*, 642.
- (632) Ajima, K.; Murakami, T.; Mizoguchi, Y.; Tsuchida, K.; Ichihashi, T.; Iijima, S.; Yudasaka, M. Enhancement of In Vivo Anticancer Effects of Cisplatin by Incorporation Inside Single-Wall Carbon Nanohorns. *ACS Nano* **2008**, *2*, 2057–2064.
- (633) Dhar, S.; Liu, Z.; Thomale, J.; Dai, H. J.; Lippard, S. J. Targeted single-wall carbon nanotube-mediated Pt(IV) prodrug delivery using folate as a homing device. *J. Am. Chem. Soc.* **2008**, *130*, 11467–11476.
- (634) Muralkami, T.; Ajima, K.; Miyawaki, J.; Yudasaka, M.; Iijima, S.; Shiba, K. Drug-loaded carbon nanohorns: Adsorption and release of dexamethasone in vitro. *Mol. Pharmaceutics* **2004**, *1*, 399–405.
- (635) Bianco, A.; Kostarelos, K.; Prato, M. Applications of carbon nanotubes in drug delivery. *Curr. Opin. Chem. Biol.* **2005**, *9*, 674–679.
- (636) Schipper, M. L.; Nakayama-Ratchford, N.; Davis, C. R.; Kam, N. W. S.; Chu, P.; Liu, Z.; Sun, X. M.; Dai, H. J.; Gambhir, S. S. A pilot toxicology study of single-walled carbon nanotubes in a small sample of mice. *Nat. Nanotechnol.* **2008**, *3*, 216–221.
- (637) Liu, Z.; Davis, C.; Cai, W. B.; He, L.; Chen, X. Y.; Dai, H. J. Circulation and long-term fate of functionalized, biocompatible single-walled carbon nanotubes in mice probed by Raman spectroscopy. *Proc. Natl. Acad. Sci. U.S.A.* **2008**, *105*, 1410–1415.
- (638) Ali-Boucetta, H.; Al-Jamal, K. T.; McCarthy, D.; Prato, M.; Bianco, A.; Kostarelos, K. Multiwalled carbon nanotube-doxorubicin supramolecular complexes for cancer therapeutics. *Chem. Commun.* **2008**, 459–461.
- (639) Muralkami, T.; Fan, J.; Yudasaka, M.; Iijima, S.; Shiba, K. Solubilization of single-wall carbon nanohorns using a PEG-doxorubicin conjugate. *Mol. Pharmaceutics* **2006**, *3*, 407–414.
- (640) Pantarotto, D.; Partidos, C. D.; Hoebeke, J.; Brown, F.; Kramer, E.; Briand, J. P.; Muller, S.; Prato, M.; Bianco, A. Immunization with peptide-functionalized carbon nanotubes enhances virus-specific neutralizing antibody responses. *Chem. Biol.* **2003**, *10*, 961–966.
- (641) Bhirde, A. A.; Patel, V.; Gavard, J.; Zhang, G. F.; Sousa, A. A.; Masedunskas, A.; Leapman, R. D.; Weigert, R.; Gutkind, J. S.; Rusling, J. F. Targeted Killing of Cancer Cells in Vivo and in Vitro with EGF-Directed Carbon Nanotube-Based Drug Delivery. *ACS Nano* **2009**, *3*, 307–316.
- (642) Pantarotto, D.; Singh, R.; McCarthy, D.; Erhardt, M.; Briand, J. P.; Prato, M.; Kostarelos, K.; Bianco, A. Functionalized carbon

- nanotubes for plasmid DNA gene delivery. *Angew. Chem., Int. Ed.* **2004**, *43*, 5242–5246.
- (643) Zhou, X.; Laroche, F.; Lamers, G. E. M.; Torracca, V.; Voskamp, P.; Lu, T.; Chu, F. Q.; Spaink, H. P.; Abrahams, J. P.; Liu, Z. F. Ultra-small graphene oxide functionalized with polyethylenimine (PEI) for very efficient gene delivery in cell and zebrafish embryos. *Nano Res.* **2012**, *5*, 703–709.
- (644) Hu, L. M.; Sun, Y.; Li, S. L.; Wang, X. L.; Hu, K. L.; Wang, L. R.; Liang, X. J.; Wu, Y. Multifunctional carbon dots with high quantum yield for imaging and gene delivery. *Carbon* **2014**, *67*, 508–513.
- (645) Liu, C. J.; Zhang, P.; Zhai, X. Y.; Tian, F.; Li, W. C.; Yang, J. H.; Liu, Y.; Wang, H. B.; Wang, W.; Liu, W. G. Nano-carrier for gene delivery and bioimaging based on carbon dots with PEI-passivation enhanced fluorescence. *Biomaterials* **2012**, *33*, 3604–3613.
- (646) Kim, H.; Namgung, R.; Singha, K.; Oh, I. K.; Kim, W. J. Graphene Oxide-Polyethylenimine Nanoconstruct as a Gene Delivery Vector and Bioimaging Tool. *Bioconjugate Chem.* **2011**, *22*, 2558–2567.
- (647) Cai, D.; Mataraza, J. M.; Qin, Z. H.; Huang, Z. P.; Huang, J. Y.; Chiles, T. C.; Carnahan, D.; Kempa, K.; Ren, Z. F. Highly efficient molecular delivery into mammalian cells using carbon nanotube spearing. *Nat. Methods* **2005**, *2*, 449–454.
- (648) Hirsch, L. R.; Stafford, R. J.; Bankson, J. A.; Sershen, S. R.; Rivera, B.; Price, R. E.; Hazle, J. D.; Halas, N. J.; West, J. L. Nanoshell-mediated near-infrared thermal therapy of tumors under magnetic resonance guidance. *Proc. Natl. Acad. Sci. U.S.A.* **2003**, *100*, 13549–13554.
- (649) Huang, X. H.; El-Sayed, I. H.; Qian, W.; El-Sayed, M. A. Cancer cell imaging and photothermal therapy in the near-infrared region by using gold nanorods. *J. Am. Chem. Soc.* **2006**, *128*, 2115–2120.
- (650) Song, X.; Chen, Q.; Liu, Z. Recent advances in the development of organic photothermal nano-agents. *Nano Res.* **2015**, *8*, 340–354.
- (651) Tang, S.; Chen, M.; Zheng, N. Multifunctional ultrasmall Pd nanosheets for enhanced near-infrared photothermal therapy and chemotherapy of cancer. *Nano Res.* **2015**, *8*, 165–174.
- (652) Terentyuk, G.; Panfilova, E.; Khanadeev, V.; Chumakov, D.; Genina, E.; Bashkatov, A.; Tuchin, V.; Bucharskaya, A.; Maslyakova, G.; Khlebtsov, N.; Khlebtsov, B. Gold nanorods with a hematoporphyrin-loaded silica shell for dual-modality photodynamic and photothermal treatment of tumors *in vivo*. *Nano Res.* **2014**, *7*, 325–337.
- (653) Chechetka, S. A.; Pichon, B.; Zhang, M.; Yudasaka, M.; Bégin-Colin, S.; Bianco, A.; Miyako, E. Multifunctional Carbon Nanohorn Complexes for Cancer Treatment. *Chem.—Asian J.* **2015**, *10*, 160–165.
- (654) Moon, H. K.; Lee, S. H.; Choi, H. C. In Vivo Near-Infrared Mediated Tumor Destruction by Photothermal Effect of Carbon Nanotubes. *ACS Nano* **2009**, *3*, 3707–3713.
- (655) Wang, H. L.; Robinson, J. T.; Li, X. L.; Dai, H. J. Solvothermal Reduction of Chemically Exfoliated Graphene Sheets. *J. Am. Chem. Soc.* **2009**, *131*, 9910–9911.
- (656) Wang, S. Z.; Gao, R. M.; Zhou, F. M.; Selke, M. Nanomaterials and singlet oxygen photosensitizers: potential applications in photodynamic therapy. *J. Mater. Chem.* **2004**, *14*, 487–493.
- (657) Ji, S. R.; Liu, C.; Zhang, B.; Yang, F.; Xu, J.; Long, J. A.; Jin, C.; Fu, D. L.; Ni, Q. X.; Yu, X. J. Carbon nanotubes in cancer diagnosis and therapy. *Biochim. Biophys. Acta, Rev. Cancer* **2010**, *1806*, 29–35.
- (658) Bhaumik, J.; Mittal, A. K.; Banerjee, A.; Chisti, Y.; Banerjee, U. C. Applications of phototheranostic nanoagents in photodynamic therapy. *Nano Res.* **2014**, *1*–22.
- (659) Mroz, P.; Xia, Y. M.; Asanuma, D.; Konopko, A.; Zhiyentayev, T.; Huang, Y. Y.; Sharma, S. K.; Dai, T. H.; Khan, U. J.; Wharton, T.; Hamblin, M. R. Intraperitoneal photodynamic therapy mediated by a fullerene in a mouse model of abdominal dissemination of colon adenocarcinoma. *Nanomed.-Nanotechnol.* **2011**, *7*, 965–974.
- (660) Lu, Z. S.; Dai, T. H.; Huang, L. Y.; Kurup, D. B.; Tegos, G. P.; Jahnke, A.; Wharton, T.; Hamblin, M. R. Photodynamic therapy with a cationic functionalized fullerene rescues mice from fatal wound infections. *Nanomedicine* **2010**, *5*, 1525–1533.
- (661) Wang, L.; Shi, J. J.; Liu, R. Y.; Liu, Y.; Zhang, J.; Yu, X. Y.; Gao, J.; Zhang, C. F.; Zhang, Z. Z. Photodynamic effect of functionalized single-walled carbon nanotubes: a potential sensitizer for photodynamic therapy. *Nanoscale* **2014**, *6*, 4642–4651.
- (662) Lee, D. J.; Park, S. Y.; Oh, Y. T.; Oh, N. M.; Oh, K. T.; Youn, Y. S.; Lee, E. S. Preparation of Chlorine e6-Conjugated Single-Wall Carbon Nanotube for Photodynamic Therapy. *Macromol. Res.* **2011**, *19*, 848–852.
- (663) Zhu, Z.; Tang, Z. W.; Phillips, J. A.; Yang, R. H.; Wang, H.; Tan, W. H. Regulation of singlet oxygen generation using single-walled carbon nanotubes. *J. Am. Chem. Soc.* **2008**, *130*, 10856–10857.
- (664) Barone, P. W.; Baik, S.; Heller, D. A.; Strano, M. S. Near-infrared optical sensors based on single-walled carbon nanotubes. *Nat. Mater.* **2005**, *4*, 86–92.
- (665) Yum, K.; Ahn, J. H.; McNicholas, T. P.; Barone, P. W.; Mu, B.; Kim, J. H.; Jain, R. M.; Strano, M. S. Boronic Acid Library for Selective, Reversible Near-Infrared Fluorescence Quenching of Surfactant Suspended Single-Walled Carbon Nanotubes in Response to Glucose. *ACS Nano* **2012**, *6*, 819–830.
- (666) Heller, D. A.; Pratt, G. W.; Zhang, J. Q.; Nair, N.; Hansborough, A. J.; Boghossian, A. A.; Reuel, N. F.; Barone, P. W.; Strano, M. S. Peptide secondary structure modulates single-walled carbon nanotube fluorescence as a chaperone sensor for nitroaromatics. *Proc. Natl. Acad. Sci. U.S.A.* **2011**, *108*, 8544–8549.
- (667) Heller, D. A.; Jin, H.; Martinez, B. M.; Patel, D.; Miller, B. M.; Yeung, T. K.; Jena, P. V.; Hobartner, C.; Ha, T.; Silverman, S. K.; Strano, M. S. Multimodal optical sensing and analyte specificity using single-walled carbon nanotubes. *Nat. Nanotechnol.* **2009**, *4*, 114–120.
- (668) Kruss, S.; Landry, M. P.; Vander Ende, E.; Lima, B. M. A.; Reuel, N. F.; Zhang, J. Q.; Nelson, J.; Mu, B.; Hilmer, A.; Strano, M. S. Neurotransmitter Detection Using Corona Phase Molecular Recognition on Fluorescent Single-Walled Carbon Nanotube Sensors. *J. Am. Chem. Soc.* **2014**, *136*, 713–724.
- (669) Heller, D. A.; Jeng, E. S.; Yeung, T. K.; Martinez, B. M.; Moll, A. E.; Gastala, J. B.; Strano, M. S. Optical detection of DNA conformational polymorphism on single-walled carbon nanotubes. *Science* **2006**, *311*, 508–511.
- (670) Mu, B.; McNicholas, T. P.; Zhang, J. Q.; Hilmer, A. J.; Jin, Z.; Reuel, N. F.; Kim, J. H.; Yum, K.; Strano, M. S. A Structure-Function Relationship for the Optical Modulation of Phenyl Boronic Acid-Grafted, Polyethylene Glycol-Wrapped Single-Walled Carbon Nanotubes. *J. Am. Chem. Soc.* **2012**, *134*, 17620–17627.
- (671) Song, C. H.; Pehrsson, P. E.; Zhao, W. Recoverable solution reaction of HiPco carbon nanotubes with hydrogen peroxide. *J. Phys. Chem. B* **2005**, *109*, 21634–21639.
- (672) Giraldo, J. P.; Landry, M. P.; Faltermeier, S. M.; McNicholas, T. P.; Iverson, N. M.; Boghossian, A. A.; Reuel, N. F.; Hilmer, A. J.; Sen, F.; Brew, J. A.; Strano, M. S. Plant nanobionics approach to augment photosynthesis and biochemical sensing. *Nat. Mater.* **2014**, *13*, 400–408; Corrigendum: Plant nanobionics approach to augment photosynthesis and biochemical sensing. **530**.
- (673) Jeng, E. S.; Moll, A. E.; Roy, A. C.; Gastala, J. B.; Strano, M. S. Detection of DNA hybridization using the near-infrared band-gap fluorescence of single-walled carbon nanotubes. *Nano Lett.* **2006**, *6*, 371–375.
- (674) Zhang, J. Q.; Landry, M. P.; Barone, P. W.; Kim, J. H.; Lin, S. C.; Ulissi, Z. W.; Lin, D. H.; Mu, B.; Boghossian, A. A.; Hilmer, A. J.; Rwei, A.; Hinckley, A. C.; Kruss, S.; Shandell, M. A.; Nair, N.; Blake, S.; Sen, F.; Sen, S.; Croy, R. G.; Li, D. Y.; Yum, K.; Ahn, J. H.; Jin, H.; Heller, D. A.; Essigmann, J. M.; Blankschtein, D.; Strano, M. S. Molecular recognition using corona phase complexes made of synthetic polymers adsorbed on carbon nanotubes. *Nat. Nanotechnol.* **2013**, *8*, 959–968.
- (675) Roxbury, D.; Mittal, J.; Jagota, A. Molecular-Basis of Single-Walled Carbon Nanotube Recognition by Single-Stranded DNA. *Nano Lett.* **2012**, *12*, 1464–1469.
- (676) Ulissi, Z. W.; Zhang, J. Q.; Sresht, V.; Blankschtein, D.; Strano, M. S. 2D Equation-of-State Model for Corona Phase Molecular Recognition on Single-Walled Carbon Nanotube and Graphene Surfaces. *Langmuir* **2015**, *31*, 628–636.
- (677) Izumi, Y.; Okazaki, T.; Ikebara, Y.; Ogura, M.; Fukata, S.; Yudasaka, M. Immunoassay with Single-Walled Carbon Nanotubes as Near-Infrared Fluorescent Labels. *ACS Appl. Mater. Interfaces* **2013**, *5*, 7665–7670.

- (678) Zhang, B.; Jarrell, J. A.; Price, J. V.; Tabakman, S. M.; Li, Y. G.; Gong, M.; Hong, G. S.; Feng, J.; Utz, P. J.; Dai, H. J. An Integrated Peptide-Antigen Microarray on Plasmonic Gold Films for Sensitive Human Antibody Profiling. *PLoS One* **2013**, *8*, e71043.
- (679) Dong, H. F.; Gao, W. C.; Yan, F.; Ji, H. X.; Ju, H. X. Fluorescence Resonance Energy Transfer between Quantum Dots and Graphene Oxide for Sensing Biomolecules. *Anal. Chem.* **2010**, *82*, 5511–5517.
- (680) Zhao, H. X.; Liu, L. Q.; Liu, Z. D.; Wang, Y.; Zhaoa, X. J.; Huang, C. Z. Highly selective detection of phosphate in very complicated matrixes with an off-on fluorescent probe of europium-adjusted carbon dots. *Chem. Commun.* **2011**, *47*, 2604–2606.
- (681) Zhou, L.; Lin, Y. H.; Huang, Z. Z.; Ren, J. S.; Qu, X. G. Carbon nanodots as fluorescence probes for rapid, sensitive, and label-free detection of Hg^{2+} and biothiols in complex matrices. *Chem. Commun.* **2012**, *48*, 1147–1149.
- (682) Wei, W. L.; Xu, C.; Ren, J. S.; Xu, B. L.; Qu, X. G. Sensing metal ions with ion selectivity of a crown ether and fluorescence resonance energy transfer between carbon dots and graphene. *Chem. Commun.* **2012**, *48*, 1284–1286.
- (683) Gao, N.; Zhou, W.; Jiang, X.; Hong, G.; Fu, T.-M.; Lieber, C. M. General strategy for biodetection in high ionic strength solutions using transistor-based nanoelectronic sensors. *Nano Lett.* **2015**, *15*, 2143–2148.
- (684) Zhan, B. B.; Li, C.; Yang, J.; Jenkins, G.; Huang, W.; Dong, X. C. Graphene Field-Effect Transistor and Its Application for Electronic Sensing. *Small* **2014**, *10*, 4042–4065.
- (685) Star, A.; Gabriel, J. C. P.; Bradley, K.; Gruner, G. Electronic detection of specific protein binding using nanotube FET devices. *Nano Lett.* **2003**, *3*, 459–463.
- (686) Li, C.; Curreli, M.; Lin, H.; Lei, B.; Ishikawa, F. N.; Datar, R.; Cote, R. J.; Thompson, M. E.; Zhou, C. W. Complementary detection of prostate-specific antigen using $In(2)O(3)$ nanowires and carbon nanotubes. *J. Am. Chem. Soc.* **2005**, *127*, 12484–12485.
- (687) Drouvalakis, K. A.; Bangsaruntip, S.; Hueber, W.; Kozar, L. G.; Utz, P. J.; Dai, H. J. Peptide-coated nanotube-based biosensor for the detection of disease-specific autoantibodies in human serum. *Biosens. Bioelectron.* **2008**, *23*, 1413–1421.
- (688) Ohno, Y.; Maehashi, K.; Matsumoto, K. Label-Free Biosensors Based on Aptamer-Modified Graphene Field-Effect Transistors. *J. Am. Chem. Soc.* **2010**, *132*, 18012–18013.
- (689) Harrison, B. S.; Atala, A. Carbon nanotube applications for tissue engineering. *Biomaterials* **2007**, *28*, 344–353.
- (690) Zhang, X.; Ozkan, C.; Prasad, S.; Ozkan, M.; Niyogi, S. Functional carbon nanotube substrates for tissue engineering applications. *Mater. Res. Soc. Symp. Proc.* **2005**, *872*, 443–452.
- (691) Boccaccini, A. R.; Gerhardt, L. C. Carbon Nanotube Composite Scaffolds and Coatings for Tissue Engineering Applications. *Key Eng. Mater.* **2010**, *441*, 31–52.
- (692) Misra, S. K.; Ohashi, F.; Valappil, S. P.; Knowles, J. C.; Roy, I.; Silva, S. R. P.; Salih, V.; Boccaccini, A. R. Characterization of carbon nanotube (MWCNT) containing P(3HB)/bioactive glass composites for tissue engineering applications. *Acta Biomater.* **2010**, *6*, 735–742.
- (693) MacDonald, R. A.; Laurenzi, B. F.; Viswanathan, G.; Ajayan, P. M.; Stegemann, J. P. Collagen-carbon nanotube composite materials as scaffolds in tissue engineering. *J. Biomed. Mater. Res., Part A* **2005**, *74A*, 489–496.
- (694) Fan, H. L.; Wang, L. L.; Zhao, K. K.; Li, N.; Shi, Z. J.; Ge, Z. G.; Jin, Z. X. Fabrication, Mechanical Properties, and Biocompatibility of Graphene-Reinforced Chitosan Composites. *Biomacromolecules* **2010**, *11*, 2345–2351.
- (695) Mattson, M. P.; Haddon, R. C.; Rao, A. M. Molecular functionalization of carbon nanotubes and use as substrates for neuronal growth. *J. Mol. Neurosci.* **2000**, *14*, 175–182.
- (696) Hu, H.; Ni, Y. C.; Montana, V.; Haddon, R. C.; Parpura, V. Chemically functionalized carbon nanotubes as substrates for neuronal growth. *Nano Lett.* **2004**, *4*, 507–511.
- (697) Fan, L.; Feng, C.; Zhao, W. M.; Qian, L.; Wang, Y. Q.; Li, Y. D. Directional Neurite Outgrowth on Superaligned Carbon Nanotube Yarn Patterned Substrate. *Nano Lett.* **2012**, *12*, 3668–3673.
- (698) Nel, A.; Xia, T.; Meng, H.; Wang, X.; Lin, S. J.; Ji, Z. X.; Zhang, H. Y. Nanomaterial Toxicity Testing in the 21st Century: Use of a Predictive Toxicological Approach and High-Throughput Screening. *Acc. Chem. Res.* **2013**, *46*, 607–621.
- (699) Sayes, C. M.; Gobin, A. M.; Ausman, K. D.; Mendez, J.; West, J. L.; Colvin, V. L. Nano-C-60 cytotoxicity is due to lipid peroxidation. *Biomaterials* **2005**, *26*, 7587–7595.
- (700) Sayes, C. M.; Fortner, J. D.; Guo, W.; Lyon, D.; Boyd, A. M.; Ausman, K. D.; Tao, Y. J.; Sitharaman, B.; Wilson, L. J.; Hughes, J. B.; West, J. L.; Colvin, V. L. The differential cytotoxicity of water-soluble fullerenes. *Nano Lett.* **2004**, *4*, 1881–1887.
- (701) Ungurenasu, C.; Airinei, A. Highly stable C-60/poly(vinylpyrrolidone) charge-transfer complexes afford new predictions for biological applications of underivatized fullerenes. *J. Med. Chem.* **2000**, *43*, 3186–3188.
- (702) Tsuchiya, T.; Oguri, I.; Yamakoshi, Y. N.; Miyata, N. Novel harmful effects of [60]fullerene on mouse embryos in vitro and in vivo. *FEBS Lett.* **1996**, *393*, 139–145.
- (703) Jia, G.; Wang, H. F.; Yan, L.; Wang, X.; Pei, R. J.; Yan, T.; Zhao, Y. L.; Guo, X. B. Cytotoxicity of carbon nanomaterials: Single-wall nanotube, multi-wall nanotube, and fullerene. *Environ. Sci. Technol.* **2005**, *39*, 1378–1383.
- (704) Manna, S. K.; Sarkar, S.; Barr, J.; Wise, K.; Barrera, E. V.; Jejelowo, O.; Rice-Ficht, A. C.; Ramesh, G. T. Single-walled carbon nanotube induces oxidative stress and activates nuclear transcription factor-kappa B in human keratinocytes. *Nano Lett.* **2005**, *5*, 1676–1684.
- (705) Liao, K. H.; Lin, Y. S.; Macosko, C. W.; Haynes, C. L. Cytotoxicity of Graphene Oxide and Graphene in Human Erythrocytes and Skin Fibroblasts. *ACS Appl. Mater. Interfaces* **2011**, *3*, 2607–2615.
- (706) Zhang, Y. B.; Ali, S. F.; Dervishi, E.; Xu, Y.; Li, Z. R.; Casciano, D.; Biris, A. S. Cytotoxicity Effects of Graphene and Single-Wall Carbon Nanotubes in Neural Phaeochromocytoma-Derived PC12 Cells. *ACS Nano* **2010**, *4*, 3181–3186.
- (707) Li, Y.; Liu, Y.; Fu, Y. J.; Wei, T. T.; Le Guyader, L.; Gao, G.; Liu, R. S.; Chang, Y. Z.; Chen, C. Y. The triggering of apoptosis in macrophages by pristine graphene through the MAPK and TGF-beta signaling pathways. *Biomaterials* **2012**, *33*, 402–411.
- (708) Chang, Y. L.; Yang, S. T.; Liu, J. H.; Dong, E.; Wang, Y. W.; Cao, A. N.; Liu, Y. F.; Wang, H. F. In vitro toxicity evaluation of graphene oxide on A549 cells. *Toxicol. Lett.* **2011**, *200*, 201–210.
- (709) Hu, W. B.; Peng, C.; Lv, M.; Li, X. M.; Zhang, Y. J.; Chen, N.; Fan, C. H.; Huang, Q. Protein Corona-Mediated Mitigation of Cytotoxicity of Graphene Oxide. *ACS Nano* **2011**, *5*, 3693–3700.
- (710) Zhang, S. A.; Yang, K.; Feng, L. Z.; Liu, Z. In vitro and in vivo behaviors of dextran functionalized graphene. *Carbon* **2011**, *49*, 4040–4049.
- (711) Bhunia, S. K.; Jana, N. R. Peptide-Functionalized Colloidal Graphene via Interdigitated Bilayer Coating and Fluorescence Turn-on Detection of Enzyme. *ACS Appl. Mater. Interfaces* **2011**, *3*, 3335–3341.
- (712) Schrand, A. M.; Huang, H. J.; Carlson, C.; Schlager, J. J.; Osawa, E.; Hussain, S. M.; Dai, L. M. Are diamond nanoparticles cytotoxic? *J. Phys. Chem. B* **2007**, *111*, 2–7.
- (713) Oberdörster, E. Manufactured nanomaterials (Fullerenes, C-60) induce oxidative stress in the brain of juvenile largemouth bass. *Environ. Health Perspect.* **2004**, *112*, 1058–1062.
- (714) Zeynalov, E. B.; Allen, N. S.; Salmanova, N. I. Radical scavenging efficiency of different fullerenes C-60-C-70 and fullerene soot. *Polym. Degrad. Stab.* **2009**, *94*, 1183–1189.
- (715) Gharbi, N.; Pressac, M.; Hadchouel, M.; Szwarc, H.; Wilson, S. R.; Moussa, F. [60]Fullerene is a powerful antioxidant in vivo with no acute or subacute toxicity. *Nano Lett.* **2005**, *5*, 2578–2585.
- (716) Moussa, F.; Roux, S.; Pressac, M.; Genin, E.; Hadchouel, M.; Trivin, F.; Rassat, A.; Ceolin, R.; Szwarc, H. In vivo reaction between [60]fullerene and vitamin A in mouse liver. *New J. Chem.* **1998**, *22*, 989–992.
- (717) Kolosnjaj, J.; Smarc, H.; Moussa, F. Toxicity studies of fullerenes and derivatives. *Adv. Exp. Med. Biol.* **2007**, *620*, 168–180.

- (718) Moussa, F.; Gharbi, N.; Pressac, M.; Tomberli, V.; Da Ros, T.; Trivin, F.; Céolin, R.; Hirsch, A. In vivo acute toxicity of two C60 derivatives. *Electrochim. Soc. Proc.* **2000**, *240–243*.
- (719) Yang, S. T.; Guo, W.; Lin, Y.; Deng, X. Y.; Wang, H. F.; Sun, H. F.; Liu, Y. F.; Wang, X.; Wang, W.; Chen, M.; Huang, Y. P.; Sun, Y. P. Biodistribution of pristine single-walled carbon nanotubes in vivo. *J. Phys. Chem. C* **2007**, *111*, 17761–17764.
- (720) Poland, C. A.; Duffin, R.; Kinloch, I.; Maynard, A.; Wallace, W. A. H.; Seaton, A.; Stone, V.; Brown, S.; MacNee, W.; Donaldson, K. Carbon nanotubes introduced into the abdominal cavity of mice show asbestos-like pathogenicity in a pilot study. *Nat. Nanotechnol.* **2008**, *3*, 423–428.
- (721) Kolosnjaj-Tabi, J.; Hartman, K. B.; Boudjemaa, S.; Ananta, J. S.; Morgant, G.; Szwarc, H.; Wilson, L. J.; Moussa, F. In Vivo Behavior of Large Doses of Ultrashort and Full-Length Single-Walled Carbon Nanotubes after Oral and Intraperitoneal Administration to Swiss Mice. *ACS Nano* **2010**, *4*, 1481–1492.
- (722) Gong, H.; Peng, R.; Liu, Z. Carbon nanotubes for biomedical imaging: The recent advances. *Adv. Drug Delivery Rev.* **2013**, *65*, 1951–1963.
- (723) Liu, X. W.; Tao, H. Q.; Yang, K.; Zhang, S. A.; Lee, S. T.; Liu, Z. A. Optimization of surface chemistry on single-walled carbon nanotubes for in vivo photothermal ablation of tumors. *Biomaterials* **2011**, *32*, 144–151.
- (724) Yang, K.; Li, Y. J.; Tan, X. F.; Peng, R.; Liu, Z. Behavior and Toxicity of Graphene and Its Functionalized Derivatives in Biological Systems. *Small* **2013**, *9*, 1492–1503.
- (725) Zhang, X. Y.; Yin, J. L.; Peng, C.; Hu, W. Q.; Zhu, Z. Y.; Li, W. X.; Fan, C. H.; Huang, Q. Distribution and biocompatibility studies of graphene oxide in mice after intravenous administration. *Carbon* **2011**, *49*, 986–995.
- (726) Wang, K.; Ruan, J.; Song, H.; Zhang, J. L.; Wo, Y.; Guo, S. W.; Cui, D. X. Biocompatibility of Graphene Oxide. *Nanoscale Res. Lett.* **2011**, *6*, 8.
- (727) Fischer, U. M.; Harting, M. T.; Jimenez, F.; Monzon-Posadas, W. O.; Xue, H. S.; Savitz, S. I.; Laine, G. A.; Cox, C. S. Pulmonary Passage is a Major Obstacle for Intravenous Stem Cell Delivery: The Pulmonary First-Pass Effect. *Stem Cells Dev.* **2009**, *18*, 683–691.
- (728) Yang, K.; Wan, J. M.; Zhang, S. A.; Zhang, Y. J.; Lee, S. T.; Liu, Z. A. In Vivo Pharmacokinetics, Long-Term Biodistribution, and Toxicology of PEGylated Graphene in Mice. *ACS Nano* **2011**, *5*, 516–522.
- (729) Singh, S. K.; Singh, M. K.; Nayak, M. K.; Kumari, S.; Shrivastava, S.; Gracio, J. J. A.; Dash, D. Thrombus Inducing Property of Atomically Thin Graphene Oxide Sheets. *ACS Nano* **2011**, *5*, 4987–4996.
- (730) Singh, S. K.; Singh, M. K.; Kulkarni, P. P.; Sonkar, V. K.; Gracio, J. J. A.; Dash, D. Amine-Modified Graphene. Thrombo-Protective Safer Alternative to Graphene Oxide for Biomedical Applications. *ACS Nano* **2012**, *6*, 2731–2740.
- (731) Li, Y. J.; Feng, L. Z.; Shi, X. Z.; Wang, X. J.; Yang, Y. L.; Yang, K.; Liu, T.; Yang, G. B.; Liu, Z. Surface Coating-Dependent Cytotoxicity and Degradation of Graphene Derivatives: Towards the Design of Non-Toxic, Degradable Nano-Graphene. *Small* **2014**, *10*, 1544–1554.
- (732) Zhang, X. Y.; Yin, J. L.; Kang, C.; Li, J.; Zhu, Y.; Li, W. X.; Huang, Q.; Zhu, Z. Y. Biodistribution and toxicity of nanodiamonds in mice after intratracheal instillation. *Toxicol. Lett.* **2010**, *198*, 237–243.
- (733) Schrand, A. M.; Hens, S. A. C.; Shenderova, O. A. Nanodiamond Particles: Properties and Perspectives for Bioapplications. *Crit. Rev. Solid State* **2009**, *34*, 18–74.
- (734) Puzyr, A. P.; Baron, A. V.; Purtov, K. V.; Bortnikov, E. V.; Skobelev, N. N.; Moginaya, O. A.; Bondar, V. S. Nanodiamonds with novel properties: A biological study. *Diamond Relat. Mater.* **2007**, *16*, 2124–2128.
- (735) Zhu, Y.; Li, J.; Li, W. X.; Zhang, Y.; Yang, X. F.; Chen, N.; Sun, Y. H.; Zhao, Y.; Fan, C. H.; Huang, Q. The Biocompatibility of Nanodiamonds and Their Application in Drug Delivery Systems. *Theranostics* **2012**, *2*, 302–312.
- (736) Reiss, P.; Bleuse, J.; Pron, A. Highly luminescent CdSe/ZnSe core/shell nanocrystals of low size dispersion. *Nano Lett.* **2002**, *2*, 781–784.
- (737) Michalet, X.; Pinaud, F. F.; Bentolila, L. A.; Tsay, J. M.; Doose, S.; Li, J. J.; Sundaresan, G.; Wu, A. M.; Gambhir, S. S.; Weiss, S. Quantum dots for live cells, in vivo imaging, and diagnostics. *Science* **2005**, *307*, 538–544.
- (738) Wang, C. Y.; Yeh, Y. S.; Li, E. Y.; Liu, Y. H.; Peng, S. M.; Liu, S. T.; Chou, P. T. A new class of laser dyes, 2-oxa-bicyclo[3.3.0]octa-4,8-diene-3,6-diones with unity fluorescence yield. *Chem. Commun.* **2006**, 2693–2695.
- (739) Harmsen, S.; Huang, R. M.; Wall, M. A.; Karabeber, H.; Samii, J. M.; Spalvieri, M.; White, J. R.; Monette, S.; O'Connor, R.; Pitter, K. L.; Sastra, S. A.; Saborowski, M.; Holland, E. C.; Singer, S.; Olive, K. P.; Lowe, S. W.; Blasberg, R. G.; Kircher, M. F. Surface-enhanced resonance Raman scattering nanostars for high-precision cancer imaging. *Sci. Transl. Med.* **2015**, *7*, 271ra277.
- (740) Kircher, M. F.; de la Zerda, A.; Jokerst, J. V.; Zavaleta, C. L.; Kempen, P. J.; Mittra, E.; Pitter, K.; Huang, R. M.; Campos, C.; Habte, F.; Sinclair, R.; Brennan, C. W.; Mellinghoff, I. K.; Holland, E. C.; Gambhir, S. S. A brain tumor molecular imaging strategy using a new triple-modality MRI-photoacoustic-Raman nanoparticle. *Nat. Med.* **2012**, *18*, 829–834.
- (741) Novoselov, K. S.; Fal'ko, V. I.; Colombo, L.; Gellert, P. R.; Schwab, M. G.; Kim, K. A roadmap for graphene. *Nature* **2012**, *490*, 192–200.
- (742) Hell, S. W.; Wichmann, J. Breaking the Diffraction Resolution Limit by Stimulated-Emission: Stimulated-Emission-Depletion Fluorescence Microscopy. *Opt. Lett.* **1994**, *19*, 780–782.
- (743) Klar, T. A.; Hell, S. W. Subdiffraction resolution in far-field fluorescence microscopy. *Opt. Lett.* **1999**, *24*, 954–956.
- (744) Chung, K.; Wallace, J.; Kim, S. Y.; Kalyanasundaram, S.; Andelman, A. S.; Davidson, T. J.; Mirzabekov, J. J.; Zalocusky, K. A.; Mattis, J.; Denisin, A. K.; Pak, S.; Bernstein, H.; Ramakrishnan, C.; Grosenick, L.; Gradinaru, V.; Deisseroth, K. Structural and molecular interrogation of intact biological systems. *Nature* **2013**, *497*, 332–337.
- (745) Yang, B.; Treweek, J. B.; Kulkarni, R. P.; Deverman, B. E.; Chen, C. K.; Lubeck, E.; Shah, S.; Cai, L.; Gradinaru, V. Single-Cell Phenotyping within Transparent Intact Tissue through Whole-Body Clearing. *Cell* **2014**, *158*, 945–958.
- (746) Huisken, J.; Swoger, J.; Del Bene, F.; Wittbrodt, J.; Stelzer, E. H. K. Optical sectioning deep inside live embryos by selective plane illumination microscopy. *Science* **2004**, *305*, 1007–1009.
- (747) Chen, B. C.; Legant, W. R.; Wang, K.; Shao, L.; Milkie, D. E.; Davidson, M. W.; Janetopoulos, C.; Wu, X. F. S.; Hammer, J. A.; Liu, Z.; English, B. P.; Mimori-Kiyosue, Y.; Romero, D. P.; Ritter, A. T.; Lippincott-Schwartz, J.; Fritz-Laylin, L.; Mullins, R. D.; Mitchell, D. M.; Bembenek, J. N.; Reymann, A. C.; Bohme, R.; Grill, S. W.; Wang, J. T.; Seydoux, G.; Tulu, U. S.; Kiehart, D. P.; Betzig, E. Lattice light-sheet microscopy: Imaging molecules to embryos at high spatiotemporal resolution. *Science* **2014**, *346*, 439.
- (748) Wang, C.; Liu, R.; Milkie, D. E.; Sun, W.; Tan, Z.; Kerlin, A.; Chen, T. W.; Kim, D. S.; Ji, N. Multiplexed aberration measurement for deep tissue imaging in vivo. *Nat. Methods* **2014**, *11*, 1037–1040.
- (749) Ji, N.; Milkie, D. E.; Betzig, E. Adaptive optics via pupil segmentation for high-resolution imaging in biological tissues. *Nat. Methods* **2010**, *7*, 141–147.
- (750) Ji, N. The practical and fundamental limits of optical imaging in Mammalian brains. *Neuron* **2014**, *83*, 1242–1245.
- (751) Hotta, J. I.; Fron, E.; Dedecker, P.; Janssen, K. P. F.; Li, C.; Mullen, K.; Harke, B.; Buckers, J.; Hell, S. W.; Hofkens, J. Spectroscopic Rationale for Efficient Stimulated-Emission Depletion Microscopy Fluorophores. *J. Am. Chem. Soc.* **2010**, *132*, 5021–5023.
- (752) Gustafsson, M. G. L. Surpassing the lateral resolution limit by a factor of two using structured illumination microscopy. *J. Microsc.* **2000**, *198*, 82–87.
- (753) Lacerda, L.; Herrero, M. A.; Venner, K.; Bianco, A.; Prato, M.; Kostarelos, K. Carbon-nanotube shape and individualization critical for renal excretion. *Small* **2008**, *4*, 1130–1132.

- (754) Choi, C. H. J.; Zuckerman, J. E.; Webster, P.; Davis, M. E. Targeting kidney mesangium by nanoparticles of defined size. *Proc. Natl. Acad. Sci. U.S.A.* **2011**, *108*, 6656–6661.
- (755) Kagan, V. E.; Konduru, N. V.; Feng, W. H.; Allen, B. L.; Conroy, J.; Volkov, Y.; Vlasova, I. I.; Belikova, N. A.; Yanamala, N.; Kapralov, A.; Tyurina, Y. Y.; Shi, J. W.; Kisin, E. R.; Murray, A. R.; Franks, J.; Stoltz, D.; Gou, P. P.; Klein-Seetharaman, J.; Fadeel, B.; Star, A.; Shvedova, A. A. Carbon nanotubes degraded by neutrophil myeloperoxidase induce less pulmonary inflammation. *Nat. Nanotechnol.* **2010**, *5*, 354–359.
- (756) Andon, F. T.; Kapralov, A. A.; Yanamala, N.; Feng, W. H.; Baygan, A.; Chambers, B. J.; Hultenby, K.; Ye, F.; Toprak, M. S.; Brandner, B. D.; Fornara, A.; Klein-Seetharaman, J.; Kotchey, G. P.; Star, A.; Shvedova, A. A.; Fadeel, B.; Kagan, V. E. Biodegradation of Single-Walled Carbon Nanotubes by Eosinophil Peroxidase. *Small* **2013**, *9*, 2721–2729.
- (757) Allen, B. L.; Kichambare, P. D.; Gou, P.; Vlasova, I. I.; Kapralov, A. A.; Konduru, N.; Kagan, V. E.; Star, A. Biodegradation of Single-Walled Carbon Nanotubes through Enzymatic Catalysis. *Nano Lett.* **2008**, *8*, 3899–3903.
- (758) Wang, Y. M.; Judkewitz, B.; DiMarzio, C. A.; Yang, C. H. Deep-tissue focal fluorescence imaging with digitally time-reversed ultrasound-encoded light. *Nat. Commun.* **2012**, *3*, 928.
- (759) Katz, O.; Small, E.; Silberberg, Y. Looking around corners and through thin turbid layers in real time with scattered incoherent light. *Nat. Photonics* **2012**, *6*, 549–553.
- (760) Ma, C.; Xu, X.; Liu, Y.; Wang, L. V. Time-reversed adapted-perturbation (TRAP) optical focusing onto dynamic objects inside scattering media. *Nat. Photonics* **2014**, *8*, 931–936.
- (761) Theer, P.; Hasan, M. T.; Denk, W. Two-photon imaging to a depth of 1000 μm in living brains by use of a Ti: Al₂O₃ regenerative amplifier. *Opt. Lett.* **2003**, *28*, 1022–1024.
- (762) Filonov, G. S.; Piatkevich, K. D.; Ting, L. M.; Zhang, J. H.; Kim, K.; Verkhusha, V. V. Bright and stable near-infrared fluorescent protein for in vivo imaging. *Nat. Biotechnol.* **2011**, *29*, 757–761.
- (763) Subach, O. M.; Patterson, G. H.; Ting, L. M.; Wang, Y. R.; Condeelis, J. S.; Verkhusha, V. V. A photoswitchable orange-to-far-red fluorescent protein, PSmOrange. *Nat. Methods* **2011**, *8*, 771–777.
- (764) Chu, J.; Haynes, R. D.; Corbel, S. Y.; Li, P. P.; Gonzalez-Gonzalez, E.; Burg, J. S.; Ataie, N. J.; Lam, A. J.; Cranfill, P. J.; Baird, M. A.; Davidson, M. W.; Ng, H. L.; Garcia, K. C.; Contag, C. H.; Shen, K.; Blau, H. M.; Lin, M. Z. Non-invasive intravital imaging of cellular differentiation with a bright red-excitible fluorescent protein. *Nat. Methods* **2014**, *11*, 572–578.
- (765) Lin, M. Z. Beyond the rainbow: new fluorescent proteins brighten the infrared scene. *Nat. Methods* **2011**, *8*, 726–728.
- (766) Progatzky, F.; Dallman, M. J.; Lo Celso, C. From seeing to believing: labelling strategies for in vivo cell-tracking experiments. *Interface Focus* **2013**, *3*, 20130001.
- (767) Winnard, P. T.; Kluth, J. B.; Raman, V. Noninvasive optical tracking of red fluorescent protein-expressing cancer cells in a model of metastatic breast cancer. *Neoplasia* **2006**, *8*, 796–806.
- (768) Chalfie, M.; Tu, Y.; Euskirchen, G.; Ward, W. W.; Prasher, D. C. Green Fluorescent Protein as a Marker for Gene-Expression. *Science* **1994**, *263*, 802–805.
- (769) Duan, X. J.; Lieber, C. M. Nanoscience and the nano-bioelectronics frontier. *Nano Res.* **2015**, *8*, 1–22.
- (770) Zou, P.; Zhao, Y. X.; Douglass, A. D.; Hochbaum, D. R.; Brinks, D.; Werley, C. A.; Harrison, D. J.; Campbell, R. E.; Cohen, A. E. Bright and fast multicoloured voltage reporters via electrochromic FRET. *Nat. Commun.* **2014**, *5*, 4625.
- (771) Hochbaum, D. R.; Zhao, Y.; Farhi, S. L.; Klapoetke, N.; Werley, C. A.; Kapoor, V.; Zou, P.; Kralj, J. M.; Maclaurin, D.; Smedemark-Margulies, N.; Saulnier, J. L.; Boulting, G. L.; Straub, C.; Cho, Y. K.; Melkonian, M.; Wong, G. K. S.; Harrison, D. J.; Murthy, V. N.; Sabatini, B. L.; Boyden, E. S.; Campbell, R. E.; Cohen, A. E. All-optical electrophysiology in mammalian neurons using engineered microbial rhodopsins. *Nat. Methods* **2014**, *11*, 825–833.
- (772) Gong, Y. Y.; Wagner, M. J.; Li, J. Z.; Schnitzer, M. J. Imaging neural spiking in brain tissue using FRET-opsin protein voltage sensors. *Nat. Commun.* **2014**, *5*, 3674.
- (773) Flytzanis, N. C.; Bedbrook, C. N.; Chiu, H.; Engqvist, M. K. M.; Xiao, C.; Chan, K. Y.; Sternberg, P. W.; Arnold, F. H.; Grdinaru, V. Archaeorhodopsin variants with enhanced voltage-sensitive fluorescence in mammalian and *Caenorhabditis elegans* neurons. *Nat. Commun.* **2014**, *5*, 4894.
- (774) Geng, J.; Kim, K.; Zhang, J.; Escalada, A.; Tunuguntla, R.; Comolli, L. R.; Allen, F. I.; Shnyrova, A. V.; Cho, K. R.; Munoz, D.; Wang, Y. M.; Grigoropoulos, C. P.; Ajo-Franklin, C. M.; Frolov, V. A.; Noy, A. Stochastic transport through carbon nanotubes in lipid bilayers and live cell membranes. *Nature* **2014**, *514*, 612–615.
- (775) Hama, H.; Kurokawa, H.; Kawano, H.; Ando, R.; Shimogori, T.; Noda, H.; Fukami, K.; Sakae-Sawano, A.; Miyawaki, A. Scale: a chemical approach for fluorescence imaging and reconstruction of transparent mouse brain. *Nat. Neurosci.* **2011**, *14*, 1481–1488.